Accurate and Precise 3D T1 Mapping of the Human Liver at 3T Using Widely Available Magnetic Resonance Imaging Methods



Gabriela de Matos Gomes Belsley

St Cross College

University of Oxford

A thesis submitted for the degree of

Doctor of Philosophy

Hillary 2022

Accurate and Precise 3D T1 Mapping of the Human Liver at 3T Using Widely Available Magnetic Resonance Imaging Methods

Gabriela de Matos Gomes Belsley, St Cross College, University of Oxford
A thesis submitted for the degree of Doctor of Philosophy

Abstract

Better diagnostic and treatment methods are needed to counteract the steep increase of liver diseases. A promising non-invasive biomarker for the diagnosis of liver diseases is the longitudinal relaxation time (T_1) of liver tissue, measured through quantitative magnetic resonance imaging. T_1 correlates with liver fibrosis and inflammation. However, non-contrast T_1 mapping is currently restricted to a single slice cross sectioning the liver and uses specialist cardiac imaging sequences that are often unavailable. As such, the main questions addressed in this thesis were: Is it possible to map T_1 across the whole liver using only widely available pulse sequences? If so, can one obtain an unbiased estimate of liver T_1 with sufficient precision for the diagnosis of liver diseases?

To answer these questions, a set of T_1-weighted sequences capable of achieving whole liver coverage was adopted. The large covariance between T_1 and the transmitted magnetic field (B_1^+) highlighted the need for an accurate B_1^+ map. Slice profile effects and several off-resonance based B_1^+ confounders were identified and corrected. Uncorrected, the median B_1^+ error in a phantom was -5.2%, producing a median T_1 error of 10.5%. After applying all corrections, the median T_1 error decreased to -0.3% with an interquartile range of [-2.5 2.1]%.

A theoretical framework was developed to calculate the T_1 variance, including the noise propagated from the B_1^+ map into the T_1 map. This framework was validated *in vivo* and used to find the optimal flip angles that resulted in the highest precision across a range of T_1s and B_1^+ factors observed in the liver at $3\,\mathrm{T}$.

Using scanner-agnostic sequences together with corrections for the confounding factors, a variable flip angle 3D T_1 mapping method was developed requiring 7 breath-holds. A study across 10 healthy volunteers at $3\,\mathrm{T}$ validated the method's accuracy, scan/rescan repeatability and precision. The 3D T_1 maps yielded mean T_1 values that, on average, were 5% lower than alternative single-slice T_1 maps, with a repeatability coefficient of $49\,\mathrm{ms}$ and a median T_1 standard deviation of $31\,\mathrm{ms}$, showing potential to diagnose liver fibrosis.

Acknowledgements

I am very grateful to have received supervision from Dr. Elizabeth Tunnicliffe, Professor Matthew Robson and Professor Damian Tyler. Liz, thank you very much for all that you taught me about MRI Physics, for all the time you spent with me scanning phantoms and healthy volunteers and for your guidance. Matt, without your idea of 3D T1 mapping of the liver this DPhil would not exist. Thank you very much for all your feedback, for teaching me how to do science and for encouraging me to always look at the bigger picture. Damian, thank you very much for your feedback, for your support and for always drawing my attention towards the bigger picture.

Professor Marcel Breeuwer thank you for all that you taught me about science and for that conversation that led me to choose this DPhil.

I am also grateful to everyone at OCMR, all the healthy volunteer's scans in this thesis would not have been possible otherwise. I would like to thank all the members of the Physics group for their interest in my work and feedback. Ferenc, I'd like to especially thank you for all the help you provided with the healthy volunteer's scans, the STEAM sequence and the MOLLI forward simulations. Manny, thank you for your generosity in letting me try out my 3D T1 mapping method on your patients.

I am also grateful to Perspectum for the funding and for letting me use their phantoms. I'd like to thank Matt for facilitating this. Also, many thanks John McGonigle for your constructive feedback.

Being part of the ONBI CDT has been an amazing experience. Thank you very much Professor Peter Jezzard, as well as all the people behind the CDT, for making this possible and for taking such good care of us. I thoroughly enjoyed and learnt a lot from all the lectures I had in my first year. Thanks to the ONBI 2017 cohort for all the intellectually stimulating moments we shared. I am also very grateful to EPSRC for the grant behind this DPhil.

St Cross College has been a wonderful place and it is an honour to be part of this community. The master and all the staff in the college were always extremely polite and helpful. I had the pleasure to meet several enthusiastic, smart and motivated people mostly over St Cross's excellent food. Thank you Cristina, Moss, Zihao, Harkirat, Arnab, Lily and Xrusa for all the conversations and friendship. Professor Achillefs Kapanidis I want to thank you for all your advice and genuine interest in my well-being.

Exploring the UK's nature and countryside while getting to know other outdoors lovers has been amazing. Thanks to Izzy, Chris, Emily and all the members of the Walking Club. During my time at Oxford, I also regained my love for playing the piano. Thank you Daniel.

Emanuel, Rob and Joana thank you for all your support and for our life-long friendship.

Lastly, Mom, Dad, Alex and Freddy thank you$^{\infty}$ for all your love, happiness and support.

Publications

Conference Proceedings

[1] Belsley, Gabriela and Tyler, Damian J. and Robson, Matthew D. and Tunnicliffe, Elizabeth M. Optimal Flip Angle Range for B1+ Mapping at 3T with Slice Profile Correction Using a Dual Angle EPI Sequence. In Proc. Intl. Soc. Mag. Reson. Med. 27, page 4501, 2019

[2] Belsley, Gabriela and Tyler, Damian J. and Robson, Matthew D. and Tunnicliffe, Elizabeth M. A comparison of two B1+ mapping methods for 3D VFA T1 mapping in the liver at 3T. In Proc. Intl. Soc. Mag. Reson. Med. 29, page 3299, 2021

[3] Belsley, Gabriela and Tyler, Damian J. and Robson, Matthew D. and Tunnicliffe, Elizabeth M. Accurate, Precise and Repeatable 3D T1 map of the Liver at 3T using widely Available Pulse Sequences. In Proc. British Chapter Intl. Soc. Mag. Reson. Med., 2021

Contents

List of Figures viii

List of Tables xii

List of Abbreviations xiii

1 Introduction 1
- 1.1 Motivation . . . 1
- 1.2 Outline of Chapters . . . 4

2 Magnetic Resonance Imaging Physics 6
- 2.1 Spin Physics and Precession . . . 6
- 2.2 Quantum Description of Spin 1/2 . . . 8
- 2.3 Rotating Frame of Reference and the Resonance Condition . . . 10
- 2.4 T_1 and T_2 Relaxation . . . 12
- 2.5 Bloch Equation . . . 13
- 2.6 Magnetic Induction and Signal Detection . . . 15
- 2.7 Spatial Encoding in Three Dimensions . . . 16
  - 2.7.1 Frequency Encoding . . . 16
  - 2.7.2 Phase Encoding . . . 17
  - 2.7.3 Slice Selection: Encoding Along Z . . . 19
- 2.8 Image Reconstruction and k-space . . . 21
- 2.9 Pulse Sequences . . . 25
  - 2.9.1 Spin Echo . . . 25
  - 2.9.2 Gradient Echo . . . 28
- 2.10 Quantitative Imaging: T_1 and B_1^+ Mapping . . . 30
  - 2.10.1 Inversion Recovery Spin Echo . . . 30
  - 2.10.2 Saturation Recovery . . . 33
  - 2.10.3 Variable Flip Angle . . . 33
  - 2.10.4 B_1^+ Inhomogeneities . . . 34

3 Identifying, Quantifying and Correcting Confounding Factors Affecting *In Vivo* Liver 3D T_1 maps 37
- 3.1 Introduction . . . 37

3.2 General Methods: Phantoms and Image Acquisition Sequences 39
3.3 B_1^+ Inhomogeneities 41
3.4 B_1^+ Map Confounding Factors 44
3.4.1 Slice Profile Effects 44
3.4.2 B_0 Gradient Through Slice Dephasing 55
3.5 EPI-based B_1^+ Map Confounding Factors 69
3.5.1 Spatial Distortion 70
3.5.2 Chemical Shift Artefacts 76
3.5.3 GRAPPA Fat Ghosts Artefacts 81
3.6 VFA SPGR Confounding Factors: Disruption of the Steady-State Signal . 87
3.6.1 Incomplete Spoiling 87
3.6.2 Spatial Saturation 97
3.7 Accuracy of the Developed 3D T_1 mapping method 103
3.7.1 Phantom 103
3.7.2 *In Vivo* 104
3.8 Discussion 108
3.9 Conclusion 114
3.10 Appendix 115
3.10.1 Gold standard T_1 Mapping Sequence 115
3.10.2 Gold standard B_1^+ Mapping Sequence 115
3.10.3 Derivation of the Error in T_1 due to an Error in the B_1^+ factor . . 118

4 *In Vivo* Liver 3D T_1Mapping Protocol and Processing Pipeline 119
4.1 Image Acquisition 119
4.1.1 B_1^+ Mapping Sequence: 2D GRE-EPI 120
4.1.2 B_0 Mapping Sequence: 2D Double Echo GRE 121
4.1.3 T_1 Mapping Sequence: 3D VFA SPGR 122
4.2 Image Processing Pipeline 124
4.2.1 Data Pre-Processing 126
4.2.2 B_1^+ Mapping Calculation 127
4.2.3 T_1 Mapping Calculation 128
4.2.4 T_1 Map Analysis: ROI Placement Criteria 129
4.3 Appendix 132

5 Optimal FAs for *In Vivo* Liver B_1^+ Mapping and 3D T_1 mapping at $3\,\mathrm{T}$ 137
5.1 Introduction 137
5.2 Theory 139
5.2.1 T_1 Mapping using the VFA SPGR Sequence 139
5.2.2 Min-Max Approach for Combinatorial Optimisation 140
5.2.3 Optimal FAs for T_1 Mapping 140
5.2.4 Optimal FAs for the DAM B_1^+ Mapping 142

5.3 Methods . . . 143
5.3.1 Simulations: Optimal FAs for T_1 Mapping . . . 143
5.3.2 Simulations: Optimal FAs for the DAM B_1^+ Mapping . . . 145
5.3.3 Image Acquisition and Processing . . . 147
5.3.4 Experimental *In Vivo* Precision of the T_1 Maps . . . 148
5.3.5 Experimental *In Vivo* Precision of the B_1^+ Maps . . . 148
5.3.6 Prediction of *In Vivo* T_1 Precision using the CRLB . . . 150
5.4 Results . . . 151
5.4.1 Simulations: Optimal FAs for T_1 Mapping . . . 151
5.4.2 Simulations: Optimal FAs for the DAM B_1^+ Mapping . . . 156
5.4.3 Experimental *In Vivo* Precision of the T_1 Maps . . . 157
5.4.4 Experimental *In Vivo* Precision of the B_1^+ Maps . . . 159
5.5 Discussion . . . 160
5.6 Conclusion . . . 172
5.7 Appendix . . . 173
5.7.1 Overall T_1 Uncertainty from Joining T_1 Distributions from Several ROIs . . . 173

6 Repeatability, Accuracy and Precision of *In Vivo* Liver 3D T_1 Mapping at $3\,\mathrm{T}$ 174
6.1 Introduction . . . 174
6.2 Methods . . . 177
6.2.1 Image Acquisition and Processing . . . 177
6.2.2 Statistical Analysis of the Data . . . 180
6.3 Results . . . 185
6.4 Discussion . . . 188
6.5 Conclusion . . . 200

7 Conclusions and Future Work 201
7.1 Summary . . . 201
7.2 Future Work . . . 205

References 209

List of Figures

2.1 Spin Precession 8
2.2 Energy states of spin 1/2 system in an external magnetic field 9
2.3 Rotation of the magnetisation by a B_1 field. 11
2.4 T_1 and T_2 relaxation 13
2.5 Magnetisation T_1 and T_2 relaxation in the laboratory frame 15
2.6 Frequency encoding schematic 17
2.7 Phase encoding schematic 18
2.8 Image space and k-space 19
2.9 Slice selection 20
2.10 Gradients and k-space coverage 22
2.11 Pulse sequence diagram of a 3D acquisition 25
2.12 Spin echo sequence RF pulse diagram 26
2.13 Main steps in the spin echo sequence 27
2.14 Signal in a spin echo experiment 28
2.15 Main steps in the gradient echo sequence 29
2.16 Inversion recovery spin echo RF pulse diagram 31
2.17 Inversion recovery curve 32
2.18 Variable flip angle spoiled gradient recalled echo signal 34

3.1 B_1^+ and T_1 mapping confounding factors 40
3.2 B_1^+ inhomogeneities effect on the T_1 map 42
3.3 Correlation between T_1 and B_1^+ factor before and after B_1^+ correction . . 43
3.4 Hamming Windowed Sinc slice profile 45
3.5 Water Excitation slice profile 46
3.6 RF pulses and slice-select gradients 47
3.7 Transverse signal as a function of position in z and off-resonance 48
3.8 B_1^+ factor look-up-table 49
3.9 B_1^+ factor look-up-surfaces 50
3.10 Quantification of the error in phantom B_1^+ maps before and after slice profile correction 51
3.11 Quantification of the error in phantom T_1 maps before and after slice profile correction 51
3.12 Slice profile effect on phantom B_1^+ and T_1 maps 52

3.13 Slice profile effect on *in vivo* B_1^+ and T_1 maps using the Hamming Windowed Sinc pulse . . . 53
3.14 Slice profile effect on *in vivo* B_1^+ and T_1 maps using the WE pulse . . . 54
3.15 Residual M_{xy} phase after applying the slice refocusing gradient . . . 56
3.16 Effect of off-resonances through slice on M_{xy} magnitude and phase . . . 56
3.17 M_{xy} magnitude and phase for different B_1^+ factors in the presence of off-resonance variations through slice . . . 58
3.18 Effect of off-resonances through slice on the 2D GRE-EPI DAM ratio as a function of TE . . . 61
3.19 Phase accrual for α and 2α in the presence of a B_0 gradient through slice 62
3.20 B_1^+ factor error as a function of B_0 gradients through slice . . . 63
3.21 Quantification of the error in phantom B_1^+ maps due to B_0 gradients through slice . . . 64
3.22 Phantom B_0 map . . . 64
3.23 Quantification of the error in phantom T_1 maps due to B_0 gradients through slice . . . 65
3.24 B_0 gradient through slice effect on *in vivo* B_1^+ and T_1 maps . . . 67
3.25 *In vivo* T_1 gradient in the slice direction due to B_0 gradients through slice 68
3.26 GRE-EPI pulse sequence diagram . . . 70
3.27 B_0 Map and predicted distortion along the PE direction . . . 72
3.28 Predicted variation in B_1^+ factor along the PE direction due to distortion 73
3.29 Effect of distortion on the *in vivo* GRE-EPI raw data . . . 75
3.30 Effect of distortion on the *in vivo* T_1 maps . . . 76
3.31 Profiles along *in vivo* B_1^+ and T_1 maps before and after distortion correction 77
3.32 Effect of chemical shift artefacts on the *in vivo* GRE-EPI raw data . . . 79
3.33 Correction for the chemical shift artefact on the B_1^+ map . . . 81
3.34 Effect of chemical shift artefacts on the *in vivo* B_1^+ maps . . . 82
3.35 Effect of chemical shift artefacts on the *in vivo* T_1 maps . . . 82
3.36 GRAPPA fat ghosts on the GRE-EPI raw data . . . 85
3.37 Effect of the GRAPPA fat ghosts on the B_1^+ and T_1 maps . . . 86
3.38 Profiles along *in vivo* B_1^+ and T_1 maps with and without GRAPPA fat ghosts . . . 87
3.39 SPGR signal as a function of RF spoiling phase increment . . . 89
3.40 Effect of incomplete spoiling on the SPGR steady-state signal as a function of excitation FA . . . 90
3.41 Incomplete spoiling correction factor as a function of excitation FA . . . 93
3.42 Simulated T_1 error before and after incomplete spoiling correction . . . 94
3.43 Quantification of the error in phantom T_1 maps due to incomplete spoiling 95
3.44 NLLS fit of the SPGR signal without correcting for incomplete spoiling . 95
3.45 NLLS fit of the SPGR signal with a correction for incomplete spoiling . . 96

3.46 Effect of incomplete spoiling on *in vivo* T_1 maps . . . 97
3.47 SPGR pulse sequence diagram with the saturation pulses . . . 99
3.48 Gold standard IR SE T_1 map of the *Calimetrix QC0025* phantom . . . 101
3.49 Interaction of spatial saturation and parallel imaging with the SPGR signal 101
3.50 Quantification of the error on phantom T_1 maps with and without spatial saturation . . . 102
3.51 NLLS fit of the SPGR signal with and without spatial saturation . . . 102
3.52 Accuracy of the 3D T_1 SPGR method on the *FDA4-T1* phantom . . . 103
3.53 *In vivo* T_1 maps shown in the three anatomical planes . . . 104
3.54 *In vivo* T_1 map on a healthy volunteer with ROIs . . . 105
3.55 *In vivo* T_1 map accuracy: evaluation of incomplete spoiling correction . . . 106
3.56 *In vivo* T_1 map accuracy: evaluation of B_1^+ factor bias in the T_1 maps after correcting for all confounders . . . 107
3.57 *In vivo* T_1 map histogram . . . 108
3.58 Gold standard IR SE T_1 map of the *FDA4-T1* phantom . . . 116
3.59 Gold standard B_1^+ map of the *FDA4-T1* phantom . . . 116
3.60 Validation of the gold standard B_1^+ mapping method . . . 117

4.1 2D multi-slice GRE-EPI data . . . 121
4.2 2D multi-slice double echo GRE data . . . 122
4.3 3D SPGR acquisition with DIXON fat/water separation . . . 123
4.4 3D SPGR water-only data . . . 124
4.5 3D SPGR T_1-weighting . . . 124
4.6 Image processing pipeline . . . 125
4.7 Liver Mask . . . 126
4.8 B_0 Map . . . 127
4.9 B_1^+ Map . . . 128
4.10 T_1 Map . . . 129
4.11 Example VFA SPGR data *in vivo* . . . 130
4.12 ROI placement . . . 131
4.13 Liver mask workflow . . . 132
4.14 B_0 map and distortion correction workflow . . . 133
4.15 B_1^+ map corrected for slice profile effects workflow . . . 134
4.16 B_1^+ map corrected for slice profile effects and B_0 gradient through slice workflow . . . 135
4.17 Eliminate chemical shift artefact and outliers workflow . . . 135
4.18 T_1 map with incomplete spoiling correction workflow . . . 136

5.1 SPGR signal with noise . . . 142
5.2 Mapping uncertainties in the DAM ratio into the FA . . . 143
5.3 Monte Carlo simulations of the DAM ratio . . . 147

5.4 Histogram of B_1^+ map values . . . 150
5.5 Example B_1^+ factor bin of the difference between two B_1^+ maps . . . 150
5.6 T_1 CoV as a function of FA number and number of pixels to average to obtain the target T_1 CoV . . . 152
5.7 T_1 CoV as a function of B_1^+ factor for a range of T_1 values . . . 153
5.8 Rationale behind FA choice for T_1 mapping . . . 154
5.9 T_1 CoV decrease by investing FAs in the SPGR or B_1^+ map . . . 155
5.10 B_1^+ factor noise contribution into the T_1 map variance . . . 156
5.11 B_1^+ factor standard deviation as a function of B_1^+ factor values . . . 157
5.12 Percentage deviation in the B_1^+ factor estimate as a function of nominal FA pair . . . 158
5.13 *In vivo* and simulated T_1 CoV as a function of the total number of FAs . 159
5.14 *In vivo* T_1 CoV as a function of SNR . . . 161
5.15 *In vivo* T_1 CoV for varying number of FAs in the B_1^+ map and SPGR acquisition . . . 162
5.16 *In vivo* and simulations B_1^+ factor standard deviations . . . 163

6.1 Healthy volunteer study image acquisition pipeline . . . 178
6.2 Maximum value for VFA SPGR T_1 standard deviation . . . 184
6.3 *In vivo* T_1 median and interquartile range . . . 186
6.4 *In vivo* VFA SPGR T_1 maps . . . 187
6.5 *In vivo* MOLLI and SASHA T_1 maps and histogram of T_1 values for MOLLI, SASHA and VFA SPGR sequences . . . 188
6.6 *In vivo* VFA SPGR T_1 weighted standard deviations . . . 189
6.7 *In vivo* remaining correlation between VFA SPGR T_1 and B_1^+ factor . . . 190
6.8 *In vivo* VFA SPGR T_1 intra-session correlation and Bland Altman plots . 190
6.9 *In vivo* VFA SPGR T_1 inter-session correlation and Bland Altman plots . 191
6.10 VFA SPGR T_1 pixels matching the STEAM voxel . . . 199

7.1 *In vivo* 3D VFA SPGR T_1 maps in a patient with hepatocellular carcinoma 207
7.2 *In vivo* 3D VFA SPGR T_1 maps in a patient with primary sclerosing cholangitis . . . 208

List of Tables

3.1 T_1 error quantification for B_1^+ factor confounding factors 107
3.2 T_1 error quantification for EPI-based B_1^+ factor confounding factors . . . 108
3.3 T_1 error quantification for SPGR confounding factors 109

5.1 Optimal and standard VFA SPGR FA set and the corresponding T_1 CoV . 152
5.2 Comparison between T_1 CoV calculated using the Cramér-Rao lower bound and Monte Carlo simulations 155
5.3 *In vivo* VFA SPGR SNR, T_1 values, B_1^+ factors and B_1^+ map noise 160

6.1 VFA SPGR T_1 inaccuracy 186
6.2 Intra-session and inter-session VFA SPGR T_1 repeatability 191
6.3 VFA SPGR T_1 standard deviation to stratify fibrosis 198
6.4 VFA SPGR T_1 standard deviation to diagnose liver diseases 199

List of Abbreviations

1D, 2D, 3D . . One-, two-, three-dimensional

ACS . . . . . AutoCalibration Signal

ANOVA . . . . One-Way Analysis Of Variance

a.u. . . . . . arbitrary units

B_0 . . . . . Static magnetic field

B_1^+ . . . . . Transmit magnetic field

BW . . . . . Bandwidth

CI . . . . . Confidence Interval

CoV . . . . . Coefficient of Variation

CRLB . . . . . Cramér-Rao Lower Bound

DAM . . . . . Double Angle Method

EPG . . . . . Extended-Phase-Graphs

EPI . . . . . Echo-Planar-Imaging

FA . . . . . Flip Angle

FE . . . . . Frequency Encoding

FLASH . . . . . Fast Low Angle Shot

FoV . . . . . Field-of-View

FS . . . . . Fat Saturation

GE . . . . . Gradient-Echo

GM . . . . . Grey Matter

GRAPPA . . . GeneRalized Autocalibrating Partially Parallel Acquisition

HCC . . . . . HepatoCellular Carcinoma

HWS . . . . . Hamming Windowed Sinc

IQR . . . . . InterQuartile Range

IR . . . . . Inversion Recovery

LoA . . . . . Limits of Agreement

LUS . . . . . Look-Up-Surface

MC . . . . . Monte Carlo

MOLLI . . . . . MOdified Look-Locker Inversion

MRI . . . . . Magnetic Resonance Imaging

M_{xy} . . . . . Transverse magnetisation

M_z . . . . . Longitudinal magnetisation

NAFLD . . . . Non-Alcoholic Fatty-Liver Disease

NLLS . . . . . Non-Linear Least Squares

PBC . . . . . Primary Biliary Cholangitis

PDFF . . . . . Proton Density Fat-Fraction

PE . . . . . Phase Encoding

PI . . . . . Parallel Imaging

PSC . . . . . Primary Sclerosing Cholangitis

RF . . . . . Radio-Frequency

RMSE . . . . . Root Mean Squared Error

ROI . . . . . Region Of Interest

SE . . . . . Spin-Echo

SPGR . . . . . Spoiled Gradient Recalled Echo

SS . . . . . Slice-Select

SSFP . . . . . steady-state free precession

SSR . . . . . Sum of Squared Residuals

STEAM . . . . Stimulated Echo Acquisition Mode

T_1 . . . . . Longitudinal relaxation time

T_2 . . . . . Transverse relaxation time

T_1-**W** . . . . . T_1-Weighted

T_2-**W** . . . . . T_2-Weighted

TE . . . . . Echo Time

TI . . . . . Inversion Time

TR . . . . . Repetition Time

VFA . . . . . Variable Flip Angle

WE . . . . . Water Excitation

WM . . . . . White Matter

1 Introduction

1.1 Motivation

The liver plays a fundamental role in several key metabolic processes essential for life. Failure of liver function is associated with several diseases such as alcohol-associated liver diseases, non-alcoholic fatty liver disease (NAFLD), cirrhosis, and hepatitis. Chronic liver diseases are a global epidemic and are the 11^{th} biggest cause of death worldwide [1]. Therefore, it is essential to develop better ways to diagnose and treat liver diseases. This thesis is dedicated to the development of a robust and widely applicable method of characterising the liver using magnetic resonance imaging (MRI).

The liver is the largest internal organ in the human body, weighing approximately $1.5\,\mathrm{kg}$ and accounting for approximately 2% of total body weight [2]. The liver enables the uptake, storage, and supply of essential nutrients to other organs. For example, bile is produced in the liver and travels to the duodenum to aid in the digestion of fat. Metabolism of proteins, fat, and carbohydrates all take place in the liver. Fat soluble vitamins are stored and metabolised in the liver. The liver also eliminates toxins and drugs from the blood stream [3].

The liver is located in the upper abdominal cavity below the right diaphragm, to which it is attached through the coronary ligaments. It has 4 lobes: the left, right, quadrate,

and caudate lobes. The gall bladder, where bile is stored, lies under the right liver lobe surface. The liver is a highly vascularized organ, receiving 25% of the total cardiac output. The hepatic artery supplies the liver with oxygenated blood, and the portal vein delivers deoxygenated blood and nutrients from the small intestine, supplying 70-75% of the blood in the liver. After the hepatocytes (liver cells) metabolise the nutrient-rich blood and break-down toxins, the blood containing the metabolic by-products flows out of the liver through the hepatic vein into the inferior vena cava [4].

Several liver diseases arise from unhealthy lifestyles such as excessive alcohol consumption, leading to alcoholic-liver diseases, or an unbalanced diet which can result in NAFLD [5]. Approximately two million people die per year worldwide from liver diseases and the rate is expected to increase [6]. The current gold standard for the diagnosis of liver diseases is biopsy as it allows histological assessment of liver morphology including the staging of fibrosis [7]. Fibrosis is characterised by the accumulation of extracellular matrix proteins in the liver and is a hallmark of most liver diseases [8]. However, biopsies have several drawbacks. Biopsies are an invasive procedure, subject to intra and inter-observer variability and are only capable of sampling a small portion of the liver, which can result in a false diagnosis or an understatement of disease severity [9].

MRI has emerged as a non-invasive imaging modality with considerable potential for assessing liver diseases. Contrast-enhanced MRI is implemented in clinical practice, using the gadoxetic acid contrast agent [10]–[12], to assess and localise the remnant liver function in candidates for liver resection, such as hepatocellular carcinoma (HCC) patients. Quantitative MRI without using contrast also has several applications in the diagnosis of liver diseases. Proton-density fat-fraction maps [13], [14] quantify the amount of fat in the liver; an accumulation of 5% or more of fat in the liver is known as steatosis. NAFLD, defined as at least 5% intrahepatic fat in the absence of other liver aetiologies, is a liver disease with increasing prevalence worldwide [15], [16]. Other properties of the liver tissue can be measured with MRI such as the transverse relaxation time (T_2) or the longitudinal relaxation time (T_1). T_2 mapping can measure the iron concentration in

the liver [17], [18], whilst T_1 mapping has shown potential for aiding in the diagnosis and staging of fibrosis and cirrhosis [19]–[21] . Inflammation of liver tissue results in increased T_1 relaxation times in patients with fibrosis and cirrhosis [20], [22].

An inversion-recovery based T_1 mapping method known as MOdified Look-Locker Inversion (MOLLI), originally proposed for T_1 mapping of the myocardium [23], has been successfully applied to the liver [19]. MOLLI T_1 values corrected for the presence of iron in the liver [24] correlate with increasing degrees of liver fibrosis [19]. MOLLI is a highly repeatable and precise T_1 mapping method, but has several drawbacks. It offers limited liver coverage as it is a single slice breath-hold technique. Using single-slice T_1 mapping methods, the diagnosis of HCC or other liver diseases affecting localised areas of the liver [25] are likely to be missed. MOLLI acquisitions are also restricted to modern scanners with access to a cardiac license. Moreover, T_1 values measured with MOLLI are biased [26] by several factors, the largest of which is magnetisation transfer [27].

The aim of the work in this thesis was to develop an alternative T_1 mapping method that overcomes some of the drawbacks of MOLLI and could be deployed in any scanner, independent of vendor. The main goals set during the DPhil work were to:

1. Develop whole liver 3D T_1 maps using only widely available pulse sequences with the aim of deploying the method in multi-vendor scanners, without the need for pulse sequence programming.

2. Obtain an unbiased measurement of liver T_1 values at $3\,\mathrm{T}$ to unlock the possibility of using T_1 as a universal biomarker in the clinic.

3. Develop a T_1 mapping method that is repeatable and has sufficient precision for diagnosis or staging of liver diseases.

Although considerable work has been done developing 3D T_1 maps of the brain [28]–[30], the liver presents several challenges that prevent the direct use of techniques applied to the brain. The most important challenge to overcome is the duration of the acquisitions. For brain imaging, acquisitions can last several minutes, whereas liver

acquisitions should be limited to a reasonable number of short breath-holds, i.e., less than 10 breath-holds each of $15\,\mathrm{s}$ maximum duration. The suppression of fat signal, especially for NAFLD clinical applications, is also important to consider when mapping water liver T_1 values. In addition, the close proximity of the liver to the lungs makes it susceptible to large magnetic field inhomogeneities. All of these challenges were addressed when developing the 3D T_1 mapping method in the liver.

1.2 Outline of Chapters

The thesis is composed of 7 chapters, Chapters 3 to 6 contain the core work undertaken to construct and validate the *in vivo* liver 3D T_1 maps.

Chapter 2 explains the main concepts underpinning MRI from a physics perspective and introduces the field of quantitative MRI.

Chapter 3 contains the groundwork that led to the final method for *in vivo* 3D T_1 mapping. A thorough investigation of the confounding factors affecting the main sequence adopted for T_1 mapping was conducted. The B_1^+ field is the transmit field responsible for rotating the magnetisation and producing a signal. The angle through which the magnetisation is rotated is known as the flip angle (FA). B_1^+ field inhomogeneities in the liver at $3\,\mathrm{T}$ were found to be the largest confounder biasing the T_1 values. Development of an accurate B_1^+ mapping method is therefore crucial for an unbiased T_1. A B_1^+ mapping method using only commercially available sequences was developed and assessed both in phantoms and *in vivo*. Five different confounding factors affecting the B_1^+ map were identified. The errors provoked by the confounders in both the B_1^+ and T_1 map were quantified and corrections were developed and evaluated. Only two of these confounders have been previously reported in the literature in the field of brain T_1 mapping. Two other confounders affecting the T_1 mapping sequence, one previously reported in the brain, were also analysed and corrected. The accuracy of the developed method was evaluated in phantom and metrics were built to evaluate its efficacy *in vivo*.

Chapter 4 presents the final image acquisition and processing pipeline for *in vivo* 3D

T_1 mapping of the liver. This pipeline includes all the corrections developed to calculate the *in vivo* T_1 maps presented in Chapters 5 and 6.

Chapter 5 investigates what are the optimal FAs for B_1^+ mapping and T_1 mapping and how best to distribute the FAs amongst the two maps to obtain the best precision in T_1. A theoretical framework for the variance in the T_1 measurement was developed including the effect of the liver B_1^+ inhomogeneity range at $3\,\mathrm{T}$ as well as the B_1^+ map noise, which has previously been disregarded in the literature. The theoretical variance in T_1 and the optimal FAs were validated with Monte Carlo simulations and *in vivo* data. The algorithm efficiently calculates the FAs and can be extended to any T_1 mapping application, such as contrast-enhanced T_1 maps.

Chapter 6 demonstrates the repeatability, accuracy and precision of the developed T_1 mapping method in a cohort of 10 healthy volunteers. This is a necessary first step towards using the 3D T_1 mapping method in patients with liver diseases and utilising T_1 mapping in multi-centre research studies. The large dimensionality of the data required adapting several statistical metrics to adequately analyse the data.

Chapter 7 summarizes the main conclusions drawn from this work that are important for the accuracy and precision of T_1 values calculated *in vivo* at $3\,\mathrm{T}$, and of relevance for other researchers working in this field. Possible avenues for future work are also put forward and an example of 3D T_1 mapping applied to a HCC patient using the developed method is presented.

2

Magnetic Resonance Imaging Physics

MRI is a medical imaging modality with many clinical applications and is the basis of intensive ongoing research. Understanding the underlying physics of MRI is important to identify artefacts and to optimise MRI parameters during sequence development. This chapter summarizes the physics of MRI based on the textbooks by Brown et al. [31] and McRobbie et al. [32]. It ends with a section on quantitative imaging where sequences for T_1 and B_1^+ mapping are introduced.

2.1 Spin Physics and Precession

Most medical MRI applications image the nuclear spins of the hydrogen atoms due to the abundance of water in the human body. The hydrogen nucleus has a spin $1/2$ as it only has one proton and no neutrons. The magnetic moment ($\vec{\mu}$) associated with the spin is proportional to the spin's intrinsic angular momentum ($\vec{J}$), with a constant of proportionality known as the gyromagnetic ratio (γ):

$$\vec{\mu} = \gamma \vec{J} \tag{2.1}$$

The proton's gyromagnetic ratio is $2.675 \times 10^8\,\mathrm{rad/(sT)}$ or $42.58\,\mathrm{MHz/T}$. The proton magnetic moment in the presence of an external static magnetic field (B_0) experiences a torque force. The torque ($\vec{N}$) is equal to the cross product between the magnetic

moment ($\vec{\mu}$) and the magnetic field ($\vec{B}$):

$$\vec{N} = \vec{\mu} \times \vec{B} \tag{2.2}$$

The torque tries to align the magnetic moment of the proton spin along the magnetic field. The result is a precession of the spin around the axis along which the $\vec{B}$ field is pointing, analogous to the precession of the centre of mass of a gyroscope about the direction of the Earth's gravitational field. A torque will induce a change in the spin angular momentum with time:

$$\frac{d\vec{J}}{dt} = \vec{N} \tag{2.3}$$

Combining Equation (2.1) and Equation (2.2) in Equation (2.3) results in the equation of motion of the spins (Equation (2.4)). Bloch generalised this equation to include relaxation effects.

$$\frac{d\vec{\mu}}{dt} = \gamma\vec{\mu} \times \vec{B} \tag{2.4}$$

Figure 2.1 relates a change in the spin magnetic moment with the angle of rotation relative to the z axis:

$$|d\vec{\mu}| = \mu \sin(\theta)|d\phi| \tag{2.5}$$

The two forms of describing a change in the magnetic moment (Equations (2.4) and (2.5)) result in the angular frequency of precession ($\vec{w}$), known as the Larmor equation:

$$\vec{\omega} = \frac{d\phi}{dt}\hat{z} = -\gamma B\hat{z} \tag{2.6}$$

The minus sign indicates a clockwise precession about the B field. At $3\,\mathrm{T}$, the protons precess at a frequency of $127.7\,\mathrm{MHz}$. The integral of the differential in Equation (2.6) gives the phase of the spin due to its precession about the z axis:

$$\phi(t) = -\omega_0 t + \phi_0 \ , \tag{2.7}$$

where $\omega_0 = \gamma B_0$ is the Larmor frequency and ϕ_0 is the initial angle.

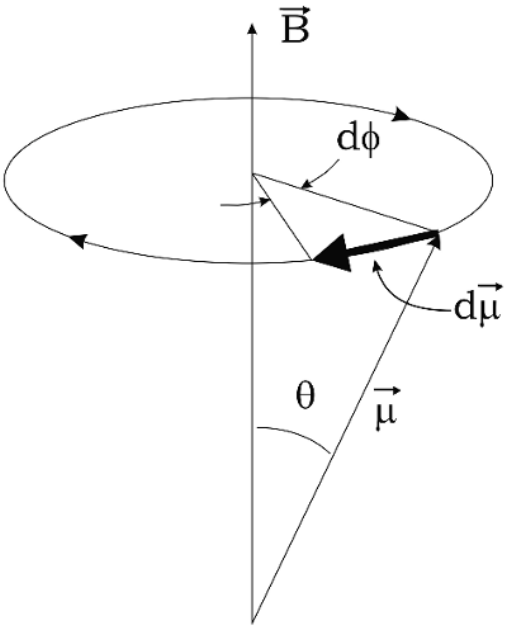


Figure 2.1: Precession of a magnetic moment about an external magnetic field $\vec{B}$. Republished with permission of John Wiley & Sons - Books, from Magnetic Resonance Imaging: Physical Principles and Sequence Design, Brown et al. [31] copyright 2014; permission conveyed through Copyright Clearance Center, Inc.

2.2 Quantum Description of Spin 1/2

A quantum mechanics description of the angular momentum describes the arrangement of the spins in two quantized states: spin up or spin down. The square of the intrinsic angular momentum (S) of each spin can be written as a function of an integer or half-integer spin (s) and Planck's constant $\hbar$:

$$S^2 = s(s+1)\hbar^2 \tag{2.8}$$

The potential energy (E) of a magnetic dipole in the presence of a magnetic field pointing along z is:

$$E = -\vec{\mu} \cdot \vec{B} = -\mu_z B_z = -\gamma m_s \hbar B_z \tag{2.9}$$

where the allowed projections of the spin S along the z axis are $m_s\hbar$. For the proton: $s = 1/2$ and $m_s = \pm 1/2$. An external magnetic field ($\vec{B} = B_0\hat{z}$) applied to S splits the nuclear energy levels in two states (Figure 2.2): parallel to $B_0\hat{z}$ ($ms = +1/2$, lower

energy) or anti-parallel to $B_0\hat{z}$ ($ms = -1/2$, higher energy). The energy necessary for the spin to transition between the two states is equal to the Larmor precession frequency times Planck's constant:

$$\Delta E = \gamma \hbar B_0 = \hbar \omega_0 \tag{2.10}$$

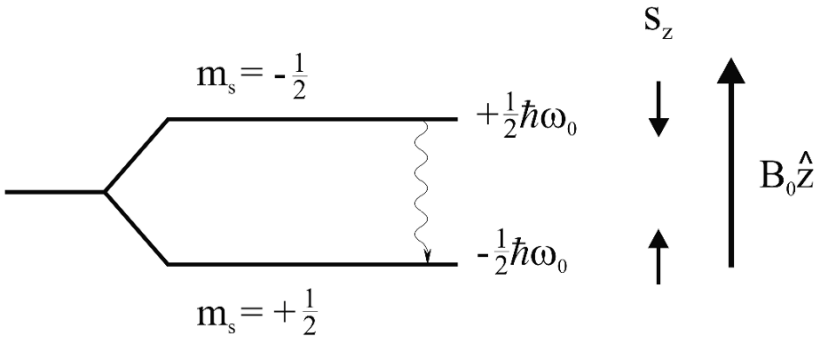


Figure 2.2: A spin $1/2$ system in an external magnetic field $B_0\hat{z}$ can occupy two possible states. The spin can either be parallel to $B_0\hat{z}$ (lower energy state) or anti-parallel to $B_0\hat{z}$ (higher energy state). Republished with permission of John Wiley & Sons - Books, from Magnetic Resonance Imaging: Physical Principles and Sequence Design, Brown et al. [31] copyright 2014; permission conveyed through Copyright Clearance Center, Inc.

Thermal energy in a system prevents the spins from always being in the lowest energy state as it provokes transitions between the two states. In the human body, the thermal energy is given by kT, where k is the Boltzmann constant ($1.38 \times 10^{-23}\,\mathrm{J/K}$). At $37\,^{\circ}\mathrm{C}$ the thermal energy is equal to $4.28 \times 10^{-21}\,\mathrm{J}$. The quantum energy difference between spin up and spin down at $3\,\mathrm{T}$ is $8.46 \times 10^{-26}\,\mathrm{J}$. The Boltzmann distribution gives the relative number of protons in each quantum state:

$$\frac{N_{up}}{N_{down}} = exp\left(\frac{\hbar\omega_0}{kT}\right) \tag{2.11}$$

Since $\hbar\omega_0 << kT$ at $3\,\mathrm{T}$, the fraction of protons in the spin up state is only slightly larger than that in the spin down state:

$$\frac{N_{up} - N_{down}}{N_{Total}} \approx \frac{\hbar\omega_0}{2kT} \tag{2.12}$$

For $3\,\mathrm{T}$, this fraction is 9.9×10^{-6}. This small difference in populations gives rise to the net magnetisation in equilibrium, i.e., pointing along the B_0 field (z axis), that can be manipulated by radiofrequency (RF) pulses.

The magnetisation in a voxel is the sum of the individual magnetic moments of the spins per unit volume:

$$\vec{M_0} = \frac{N_{up} - N_{down}}{\text{Unit Volume}} * \vec{\mu_{up}} = \rho_0 \frac{\hbar\omega_0}{2kT} \frac{\gamma\hbar}{2} \tag{2.13}$$

Fortunately, the proton density (ρ_0) is a large number, there are about an Avogadro number of protons in $9\,\mathrm{cm}^3$ of water tissue, resulting in a measurable signal.

2.3 Rotating Frame of Reference and the Resonance Condition

To facilitate calculations, a new reference frame is defined in MRI which is rotating about the z axis at an angular velocity $\vec{\Omega}$ equal to the Larmor frequency. In this rotating reference frame ($x'y'z'$), the equation of motion of the spins becomes:

$$\left(\frac{d\vec{\mu}}{dt}\right)' = \gamma\vec{\mu} \times \vec{B_{eff}} \ , \tag{2.14}$$

where the magnetic moment is rotated due to the action of an effective magnetic field:

$$\vec{B}_{eff} = \vec{B} + \frac{\vec{\Omega}}{\gamma} \tag{2.15}$$

If $\vec{\Omega}/\gamma = -\vec{B}$, $(d\vec{\mu}/dt)' = 0$, the magnetisation vector appears static in the rotating frame of reference.

The net magnetic moment in equilibrium points along the direction of the B_0 field, i.e., z. Applying a left-circularly polarised RF magnetic field ($\vec{B_1}$) for a short period of time, perpendicular to B_0, will rotate the magnetic moment away from the z axis. The effective magnetic field becomes in a frame rotating at the RF frequency ω:

$$\vec{B}_{eff} = (B_0 - \frac{\omega}{\gamma})\hat{z}' + B_1(t)\hat{x}' = [\hat{z}'(\omega_0 - \omega) + \hat{x}'\omega_1(t)]/\gamma \tag{2.16}$$

When the frequency of the RF field matches the Larmor frequency (ω_0), the motion equation reduces to:

$$\left(\frac{d\vec{\mu}}{dt}\right)' = \vec{\mu} \times \omega_1(t)\hat{x}' \ , \tag{2.17}$$

with the spins precessing about the x' axis in the rotating frame. Tuning the B_1 field to oscillate at the Larmor frequency is known as the resonance condition. Hence, the use of the word *resonance* in MRI.

During the time the B_1 field is on, the spins precess around B_1 and tilt away from the z' axis towards the transverse plane. The amount tilted is known as the FA α:

$$\alpha(t) = \gamma \int_0^t B_1(t')dt' \tag{2.18}$$

A B_1 field on-resonance will be more effective at flipping the spins to the transverse plane than a B_1 field off-resonance (Figure 2.3). The same B_1 field strength off-resonance applied for the same time will not flip the magnetic moment by the same FA, since the effective magnetic field has a component along the z' axis according to Equation (2.16).

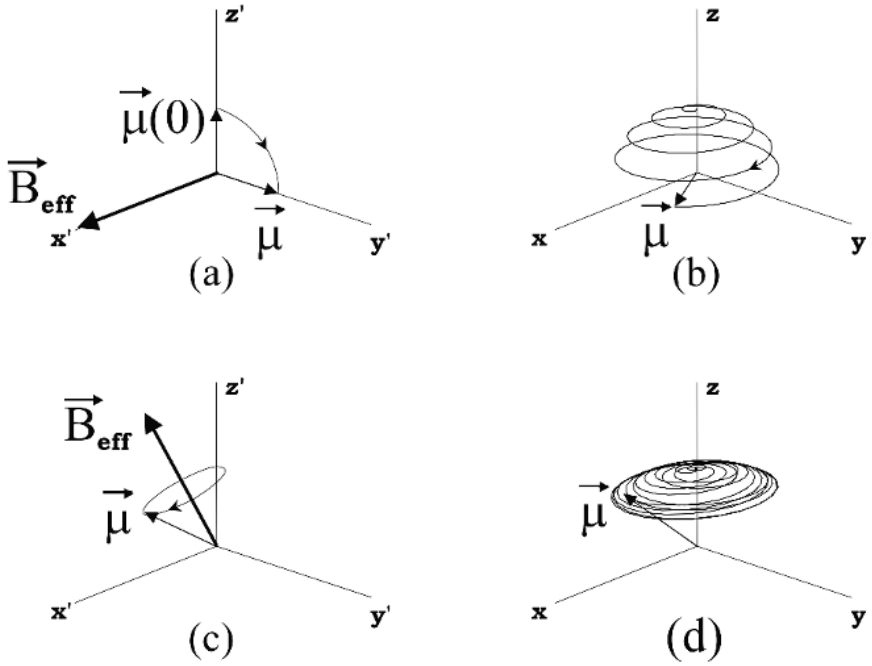


Figure 2.3: A $90°$ flip of the magnetisation for a B_1 field applied on-resonance ((a), (b)) and off-resonance ((c), (d)). In (a) and (c) the primed coordinate system rotates at the Larmor frequency, while (b) and (d) show the spin trajectory in the laboratory frame. The off-resonance frequency for (c) and (d) is $0.85\omega_0$, resulting in a less effective flip. Republished with permission of John Wiley & Sons - Books, from Magnetic Resonance Imaging: Physical Principles and Sequence Design, Brown et al. [31] copyright 2014; permission conveyed through Copyright Clearance Center, Inc.

2.4 T_1 and T_2 Relaxation

When the net magnetic moment is aligned with the B_0 field there is no precession in the laboratory frame. To measure a signal in MRI, the net magnetisation is perturbed from its equilibrium value $M_0\hat{z}$. An RF field tips the spins from alignment with B_0 creating a transverse magnetisation (M_{xy}). As the protons interact with their surroundings, they exchange energy and gradually relax to equilibrium causing the magnetisation to assume its minimum energy state ($M_0\hat{z}$). This process is known as T_1 relaxation or spin-lattice relaxation. The cumulative effect of energy exchange with the lattice results in a growth of the longitudinal magnetisation (M_z) at a rate proportional to the difference $(M_0 - M_z)$:

$$\frac{dM_z}{dt} = \frac{1}{T_1}(M_0 - M_z) \ , \tag{2.19}$$

where T_1 is the characteristic time associated with the relaxation towards equilibrium. The solution of the differential Equation (2.19) is an exponential growth of the initial longitudinal magnetisation $M_z(0)$ back to equilibrium M_0:

$$M_z(t) = M_z(0)e^{-t/T_1} + M_0(1 - e^{-t/T_1}) \tag{2.20}$$

For a $90°$ FA ($M_z(0) = 0$), T_1 is the time needed for the magnetisation to recover to 63% of its equilibrium value.

In addition, after the B_1 field is turned off, the spins start to dephase due to interactions of the spins with each other, known as spin-spin interactions. Spins experience a local magnetic field variation as the magnetic moment of the neighbouring spins adds or subtracts from the main field. Consequently, the spins either precess at a frequency slightly higher or lower than the Larmor frequency and dephase. The phase spread increases linearly with time, with the transverse signal eventually decaying to zero due to total dephasing. This process is known as spin-spin relaxation and it is governed by an exponential decay with a time constant T_2. The differential equation of M_{xy} decay in the rotating frame of reference is:

$$\left(\frac{d\vec{M}_{xy}}{dt}\right)' = -\frac{1}{T_2}\vec{M}_{x'y'} \ , \tag{2.21}$$

with the solution:

$$\vec{M}_{x'y'}(t) = \vec{M}_{x'y'}(0)e^{-t/T_2} \tag{2.22}$$

T_2 corresponds to the time for the magnetisation to decay to 37% of its initial value.

Inhomogeneities in the main magnetic field (ΔB_0) can accelerate T_2 relaxation and are described by a time constant T_2^*. T_2^* is smaller than T_2 (Equation (2.23)). Signal loss due to field inhomogeneities are recoverable using a spin echo sequence.

$$\frac{1}{T_2^*} = \frac{1}{T_2} + \gamma \Delta B_0 \tag{2.23}$$

T_1 is on the order of hundreds to thousands of ms while T_2 is much smaller and on the order of tens of ms for most human tissue (Figure 2.4). T_1, unlike T_2, increases with field strength .

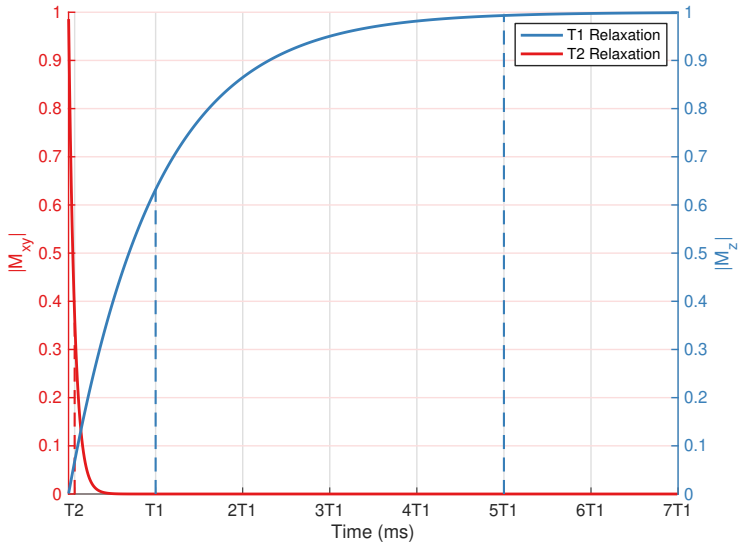


Figure 2.4: T_1 recovery illustrated in blue and T_2 decay illustrated in red for $M_0 = 1$, $T_1 = 1000\,\mathrm{ms}$, $T_2 = 70\,\mathrm{ms}$. T_2 decay is much faster than T_1 relaxation. The rule of thumb for full recovery of the magnetisation corresponding to a time equal to $5T_1$s is also shown.

2.5 Bloch Equation

Combining the two differential equations of T_1 relaxation and T_2 decay with the effective field in the rotating frame results in the equation of motion for the magnetisation,

known as the Bloch equation:

$$\left(\frac{d\vec{M}}{dt}\right)' = \gamma\vec{M}' \times \vec{B}_{eff} + \frac{1}{T_1}(M_0 - M_z)\hat{z} - \frac{1}{T_2}\vec{M}_{x'y'} \tag{2.24}$$

The three components of the Bloch equation in the rotating frame ($x'y'z'$), assuming a constant B_1 field applied along the x' axis, are:

$$\begin{aligned}
\left(\frac{dM_z}{dt}\right)' &= -\omega_1 M_{y'} + \frac{M_0 - M_z}{T_1} \\
\left(\frac{dM_{x'}}{dt}\right)' &= (\omega_0 - \omega)M_{y'} - \frac{M_{x'}}{T_2} \\
\left(\frac{dM_{y'}}{dt}\right)' &= -(\omega_0 - \omega)M_{x'} + \omega_1 M_z - \frac{M_{y'}}{T_2}
\end{aligned} \tag{2.25}$$

The term $(\omega_0 - \omega)$ represents the off-resonance, i.e., deviation of the frequency from the Larmor frequency. On-resonance ($\omega = \omega_0$), the Bloch equations reduce to the relaxation terms and precession of the spins with frequency ω_1. In general, the RF pulses are applied for a short period of time, i.e., the RF bandwidth (BW) is much larger than the relaxation rates $1/T_1$ and $1/T_2$. Therefore, when the RF pulse is on, the relaxation terms can be disregarded. The RF field creates an initial magnetisation with transverse components $M_{x'}(0)$ and $M_{y'}(0)$ and a longitudinal component $M_z(0)$. Once the RF field is turned off ($\omega_1 = 0$), the magnetisation evolves according to:

$$\begin{aligned}
M_{x'}(t) &= e^{-t/T_2}(M_{x'}(0)cos(\Delta\omega t) + M_{y'}(0)sin(\Delta\omega t)) \\
M_{y'}(t) &= e^{-t/T_2}(M_{y'}(0)cos(\Delta\omega t) - M_{x'}(0)sin(\Delta\omega t)) \\
M_z(t) &= M_z(0)e^{-t/T_1} + M_0(1 - e^{-t/T_1}) \ ,
\end{aligned} \tag{2.26}$$

with $\Delta\omega = (\omega_0 - \omega)$.

In summary, M_{xy} precesses in a sinusoidal motion with damping factors given by the T_2 decay. This translates into a clockwise rotation about the z axis in a spiral pattern whose radius exponentially decreases with a time constant T_2. The longitudinal magnetisation increases to its equilibrium value M_0 according to an exponential growth with a time constant T_1 (Figure 2.5).

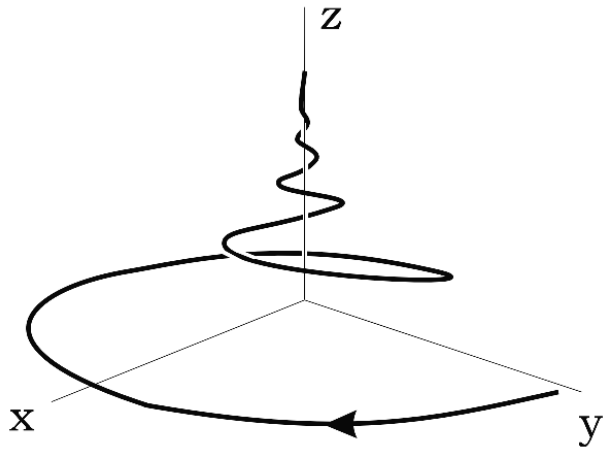


Figure 2.5: Magnetisation trajectory in the laboratory frame simultaneously decaying in the transverse plane (xy) and the longitudinal component (z) regrowing back to equilibrium. The radius of the spirals decrease with the time constant T_2. Republished with permission of John Wiley & Sons - Books, from Magnetic Resonance Imaging: Physical Principles and Sequence Design, Brown et al. [31] copyright 2014; permission conveyed through Copyright Clearance Center, Inc.

2.6 Magnetic Induction and Signal Detection

M_{xy} precesses clockwise in the x-y plane (laboratory frame) with an angle of rotation given by the complex phase of the magnetisation:

$$M_{xy}(t) = M_x(t) + iM_y(t) = e^{-t/T_2} M_{xy}(0) e^{-i\omega_0 t + \phi(0)} \tag{2.27}$$

The spin precession about the B_0 field with angular frequency ω_0, accumulates a phase after a time t. The initial angle of M_{xy}, $\phi(0)$, is determined by the RF pulse.

The precession of the coherent magnetisation in the xy plane, around the external magnetic field B_0, produces a time-varying magnetic flux that induces a voltage in a RF coil, placed close to the body. Detection of the signal is given by Faraday's law of induction where the electromotive force (emf) is proportional to the magnetic flux change with time. The current induced in the coil also produces a magnetic field ($\vec{B}^{receive}$) which opposes the time-varying magnetic field (Lenz's Law):

$$emf = -\frac{d\Phi_B}{dt} = -\frac{d}{dt}(\int \vec{B} \cdot d\vec{S}) \tag{2.28}$$

Electromagnetic theory can be used to re-write the integral over the area of the receiving

coil in terms of the integral of the time varying magnetisation in the volume of tissue. The emf induced in the receive coil is:

$$emf = -\frac{d}{dt}\int d^3r\vec{M}(\vec{r},t)\cdot\vec{B}^{receive}(\vec{r}) \tag{2.29}$$

The time derivative of M_{xy} (Equation (2.27)) is dominated by the Larmor frequency (ω_0 is several orders of magnitude larger than $1/T_2$). Thus, the emf signal is proportional to $\omega_0 M_0$. Since M_0 is proportional to ω_0 according to Equation (2.13), the signal depends quadratically on B_0 and hence the interest in imaging at high field strengths.

2.7 Spatial Encoding in Three Dimensions

2.7.1 Frequency Encoding

B_0 gradients spatially encode the measured signal, allowing the signal to be attributed to a position in the human body from which it originated. Gradients in x,y and z are linear spatial variations in the B_0 magnitude as a function of the x,y and z coordinates, respectively. Note that the direction of B_0 is always along z, just the strength is changing along the different directions of the three-dimensional (3D) coordinate system. The spins will either precess slower than the Larmor frequency (counter-clockwise in the rotating frame), when the gradient subtracts from B_0, or faster when the gradient adds to B_0 (clockwise in the rotating frame). At the centre of the volume imaged, the deviation from the B_0 field is zero, thus the spins continue to precess at the Larmor frequency. The variations due to the magnetic field gradients are much smaller than the static field strength, on the order of tens of mT. For objects with spatial extents of cm, this will lead to frequencies on the order of kHz, while the Larmor carrier frequency is on the order of one hundred MHz.

Consider a one-dimensional (1D) sample extending along the x axis. To encode spatial positions along x, a linearly varying gradient along x is added to the B_0 field:

$$B_z(x,t) = B_0 + x\frac{\partial B_z}{\partial x}(t) \tag{2.30}$$

Consequently, the precession frequency of the spins will also vary linearly with position:

$$\omega(x,t) = \omega_0 + \gamma x G_x(t), \text{ where } G_x = \frac{\partial B_z}{\partial x} \tag{2.31}$$

Because each position in x is now precessing at a certain frequency, there is a correspondence between position and frequency. This process is known as frequency-encoding (FE) (Figure 2.6).

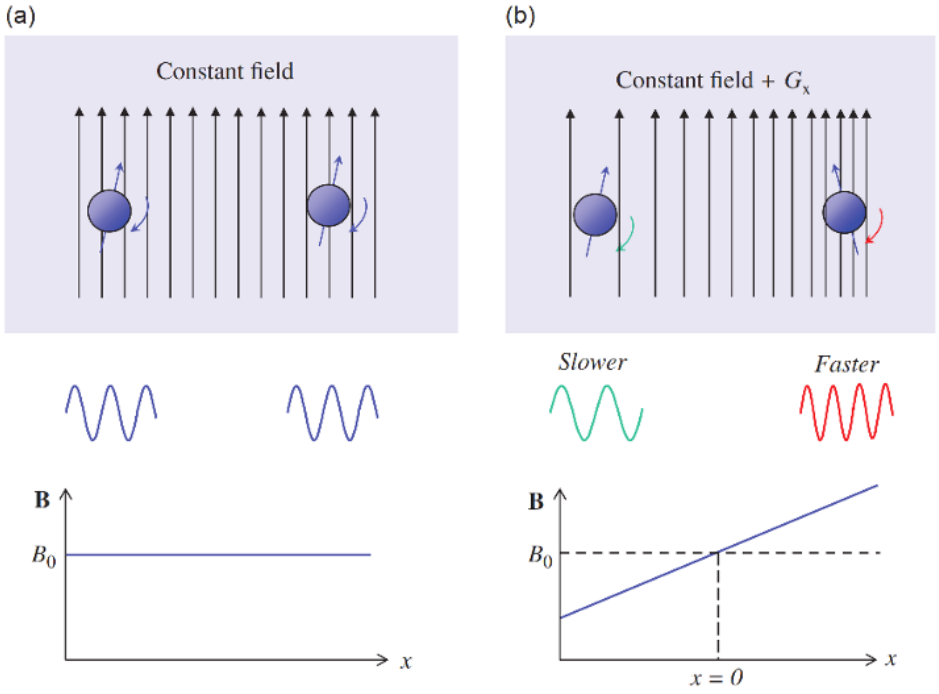


Figure 2.6: Frequency Encoding. (a) In a constant static magnetic field B_0, all nuclei precess at the Larmor frequency independent of their position in x. (b) In the presence of a positive gradient adding to the B_0 field, the spins' precession frequency is modulated according to their position along x. Reproduced from MRI Picture to Proton, McRobbie et al. [32]. Copyright Donald W. McRobbie, Elizabeth A. Moore and Martin J. Graves, 2003, 2007, 2017. Reproduced with permission of The Licensor through PLSclear.

2.7.2 Phase Encoding

Imaging can be extended from 1D to 3D by using three orthogonal gradients under a single RF excitation. A second gradient is applied along the y direction to encode a phase, known as phase-encoding (PE) gradient. The gradient along y is on when the readout gradient along the x direction is off. Therefore, the phase along y is unchanged during the acquisition of the samples along the FE direction. The phase

acquired by the spins due to the PE gradient is:

$$\phi(y) = -y\gamma \int_0^{\tau} G_y(t')dt' = -yk_y \tag{2.32}$$

The signal including both spatial frequencies k_x and k_y is:

$$s(k_x, k_y) = \int\int \left[\int_{z_0-\Delta z/2}^{z_0+\Delta z/2} \rho(x, y, z)dz\right] e^{-i2\pi(k_x(t)x+k_y y)}dxdy \tag{2.33}$$

The range of values collected over k_x and k_y form k-space.

Different features in the image have intensity patterns that can be decomposed into different spatial frequencies. The PE gradient imparts a phase on the spins that varies linearly with the y position (Equation (2.32)). When the spatial frequency k_y of the sinusoidal wave matches the spatial frequency of the proton density, the signal will be maximum for that k_y (Figure 2.7). In summary, the transverse signal is firstly imparted a y-dependent phase due to the action of the PE gradient and subsequently, during the readout time its precession frequency along x is modulated by a FE gradient.

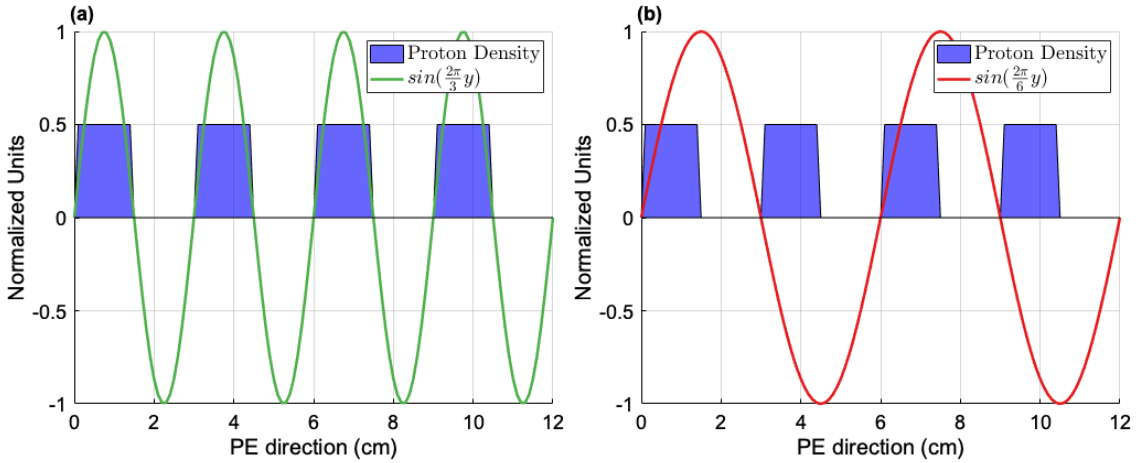


Figure 2.7: Phase Encoding (PE) Schematic. An hypothetical proton density is represented by the blue squares. (a) The sine wave in green oscillates at a spatial frequency, imposed by the PE gradient, of 4 cycles per $12\,\mathrm{cm}$ along the PE direction (y). When the spatial frequency of the sine wave matches the proton density pattern, there is constructive interference and maximum signal. (b) For a sine wave, in red, oscillating at a spatial frequency of 2 cycles per $12\,\mathrm{cm}$ along the PE direction, total destructive interference occurs.

The signal measured in the coil at a specific time t is equal to the two-dimensional (2D) Fourier transform of the spin density at the spatial frequencies $(k_x(t), k_y)$ for all the spins excited in a slice centred at z_0. This process is repeated for a mesh of $(k_x(t), k_y)$

that leads to full coverage of k-space. Figure 2.8 shows the k-space representation of an axial liver slice. The image is decomposed into its spatial frequencies. The main contrast is encoded in the low spatial frequencies forming the k-space centre, while higher spatial frequencies are necessary to represent the edges.

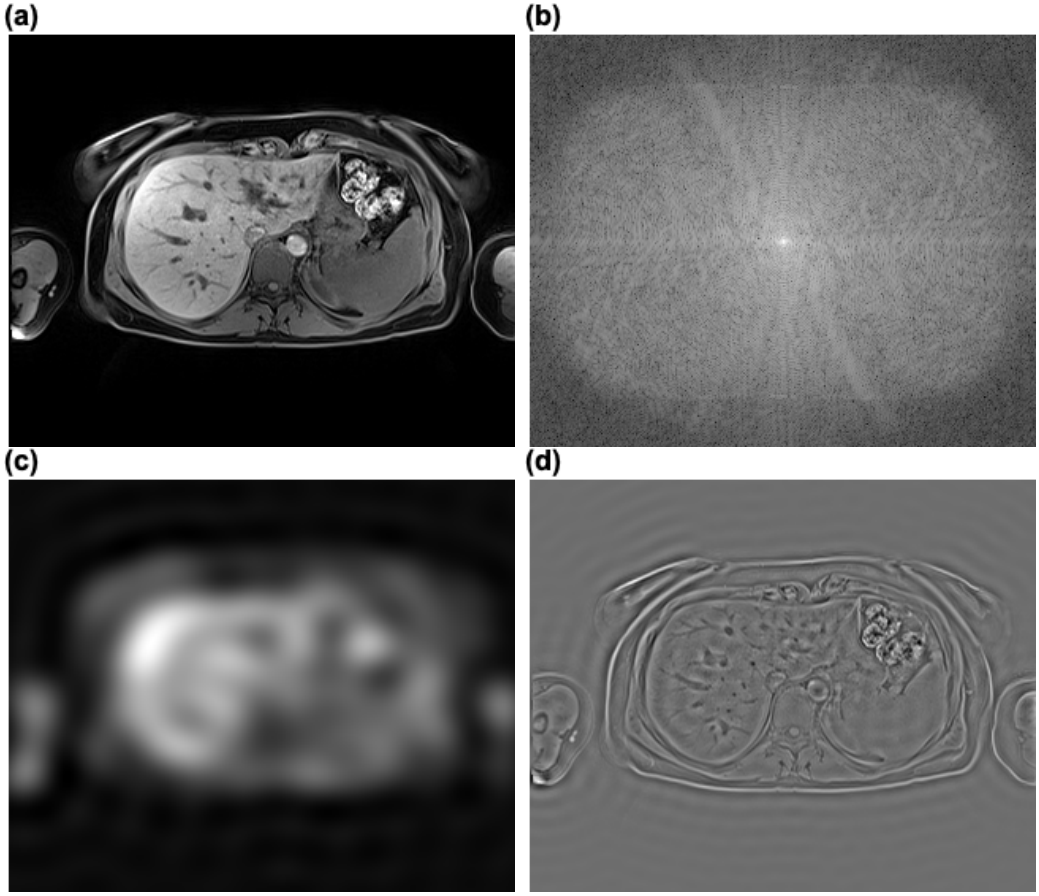


Figure 2.8: (a) T_1-weighted image of an axial slice across the liver and (b) corresponding k-space representation, visually enhanced through a log function. (c) Applying a low pass circular filter to k-space, centred at k=0, extracts the centre portion of k-space. The inverse Fourier transform is a blurred version of (a) showing the bulk intensity of the image. (d) Conversely, applying a high pass circular filter to k-space results in an image containing the edges present in the original image. High spatial frequencies are needed to describe the edges in an image.

2.7.3 Slice Selection: Encoding Along Z

Spatially selective RF pulses only excite a portion of tissue by using a finite BW. A linear B_0 gradient applied at the same time as the RF pulse encodes each position along the slice direction to a specific angular frequency. The gradients are known as slice-select (SS)

gradients. Applying the SS gradient along the z direction gives an axial slice, along the y direction a coronal slice, and along the x direction a sagittal slice. Similar to FE gradients, a SS gradient imposes a linear relationship between position and precession frequency:

$$f(z) = f_0 + \frac{\gamma}{2\pi} G_z z \tag{2.34}$$

To excite a slice centred at z_0, the RF pulse is tuned to a central frequency $f(z_0)$ with a BW of $\frac{\gamma}{2\pi} G_z \Delta z$ proportional to the gradient G_z and the slice thickness Δz (Figure 2.9). Spins outside of the range of frequencies defined by the BW will not be excited by the RF pulse as the resonance condition is not satisfied. Considering a sinc pulse in time, the Fourier transform is a rectangle with a BW equal to the inverse of the time of the first zero crossing in the sinc. Thus, the larger the pulse duration, the shorter the BW of spin excitation and the smaller the slice thickness for a fixed G_z:

$$\Delta z = \frac{2\pi BW_{RF}}{\gamma G_z} \tag{2.35}$$

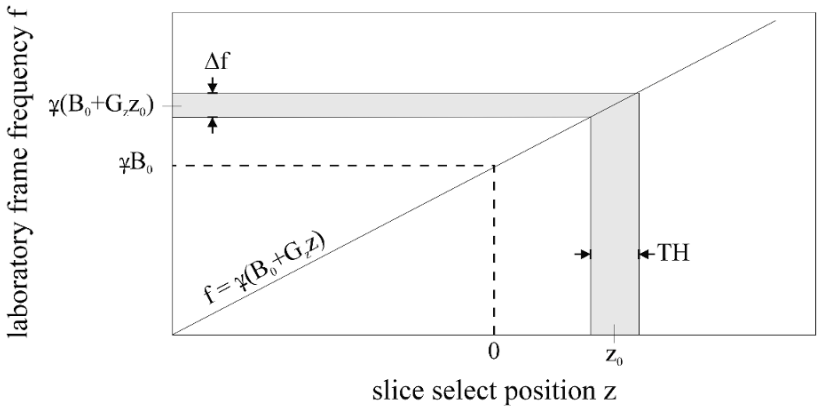


Figure 2.9: A slice-select gradient G_z applied along the z-direction induces a linear change in the spins' precession frequency with position (z) along the slice select axis. The RF transmit bandwidth (Δf) excites a slice of thickness (TH) illustrated by the shaded grey area. To excite a slice centred at z_0, the RF pulse is offset from the static Larmor frequency $\frac{\gamma}{2\pi} B_0$ by $\frac{\gamma}{2\pi} G_z z_0$. Gamma bar is equal to gamma over 2π. Republished with permission of John Wiley & Sons - Books, from Magnetic Resonance Imaging: Physical Principles and Sequence Design, Brown et al. [31] copyright 2014; permission conveyed through Copyright Clearance Center, Inc.

A SS gradient is followed by a rephasing gradient to refocus the dephasing of the spins along the SS gradient direction. For small excitation FAs and an ideal sinc excitation pulse, a refocusing gradient with 50% of the area of the SS gradient and

opposite polarity will rephase all M_{xy} within the slice. For small FAs ($\cos(\theta) \approx 1$ and $M_z \approx M_0$), M_{xy} at the end of the RF pulse ($t = \tau_{rf}/2$) is proportional to the inverse Fourier transform of the B_1^+ field:

$$M_{xy}(\vec{r}, \tau_{rf}/2) = i\gamma M_0 e^{-i\gamma \vec{G}\cdot\vec{r}\tau_{rf}/2} \mathcal{F}^{-1}(B_1^+(t)) \tag{2.36}$$

Assuming a real B_1^+ field, the dephasing is given by $\gamma\vec{G}\cdot\vec{r}\tau_{rf}/2$. A rephasing gradient ($G_{rp}$) with half the area of the dephasing gradient will refocus all the spins:

$$\phi_{G_{rp}} + (-\gamma G_z z \tau_{rf}/2) = 0 \Leftrightarrow G_{rp}\tau_{rp} = \frac{1}{2}(G_z\tau_{rf}) \tag{2.37}$$

For large FAs, M_{xy} is no longer given by Equation (2.36) and consequently a rephasing gradient equal to 50% of the area of the SS gradient will not perfectly refocus the spins, introducing a reminiscent z-dependent phase on M_{xy}. The Bloch equations can be solved numerically to find the slice refocusing gradient area that minimises the phase of M_{xy}.

2.8 Image Reconstruction and k-space

To explain the main features of image reconstruction, consider a 1D object along the x direction. The phase accumulated by the spins for a period of time t after the excitation RF pulse is:

$$\phi(x,t) = -\int_0^t \omega_0 + \gamma x G_x(t')dt' = -\omega_0 t - \gamma x \int_0^t G_x(t')dt' \tag{2.38}$$

The signal detected in the coil is given by:

$$s(t) = \int \rho(x) e^{i(\phi(x,t))} dx = e^{-i\omega_0 t} \int \rho(x) e^{-i\gamma x \int_0^t G_x(t')dt'} dx \tag{2.39}$$

In this expression relaxation is neglected; $\rho(x)$ is the proton spin density one wishes to determine from the signal measured as a function of time. For a signal demodulated at the Larmor frequency, Equation (2.39) is equivalent to:

$$s(k_x) = \int \rho(x) e^{-i2\pi k_x x} dx \ , \tag{2.40}$$

with the spatial frequency $k_x(t) = \frac{\gamma}{2\pi}\int_0^t G_x(t')dt'$. The signal in Equation (2.40) is equal to the Fourier transform of the spin density. Consequently, the spin density can

be recovered by taking the inverse Fourier Transform of the signal. This process is known as k-space reconstruction.

$$\rho(x) = \int s(k_x) e^{+i2\pi k_x x} dk_x \tag{2.41}$$

Coverage of k-space is achieved by tracing a path through the action of gradients that enable all the frequencies that form k-space to be sampled. Two large negative gradients (G_x and G_y in Figure 2.10) move the position in k-space from the centre to the bottom left corner. Turning on k_x, or the read-gradient, during the sampling time Δt, allows to sample all the points in the horizontal or read-direction. The step in the k_x direction is:

$$\Delta k_x = \frac{\gamma}{2\pi} G_x \Delta t \tag{2.42}$$

Traversal of k-space along x in the forward or backward direction is achieved by reversing the polarity of the read-gradient. Turning on k_y for a small period of time τ, when k_x is off, moves the position in k-space in the vertical direction by one line. The step in the y direction is incremented by successive increments in the gradient of ΔG_y:

$$\Delta k_y = \frac{\gamma}{2\pi} \Delta G_y \tau_y \tag{2.43}$$

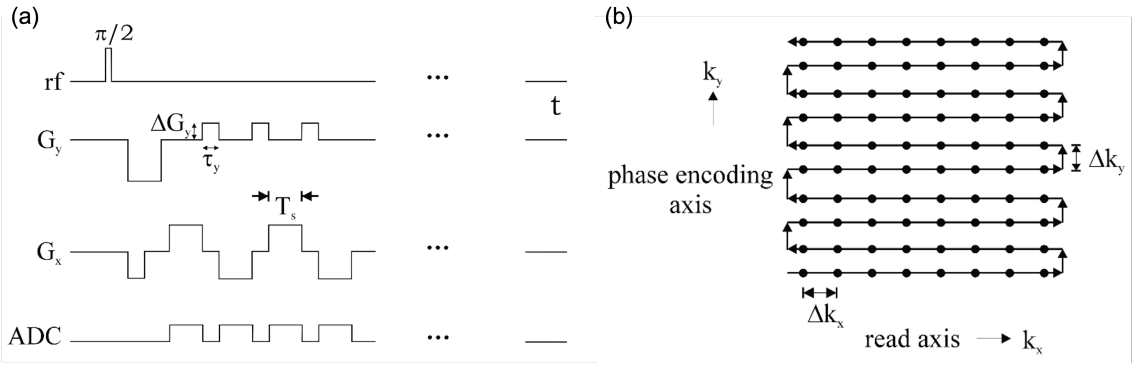


Figure 2.10: (a) Pulse sequence diagram for k-space coverage in 2D using a single RF excitation. G_x is the read gradient that samples the horizontal direction and G_y is the phase-encoding gradient that steps in the vertical direction. (b) Corresponding k-space diagram showing the read axis in the horizontal direction and the phase-encoding axis in the vertical direction. The black dots represent the samples collected in a Cartesian trajectory in k-space. Republished with permission of John Wiley & Sons - Books, from Magnetic Resonance Imaging: Physical Principles and Sequence Design, Brown et al. [31] copyright 2014; permission conveyed through Copyright Clearance Center, Inc.

There is an inverse relationship between spatial frequencies and image space. The field-of-view (FoV) is determined by the smallest frequency step in k-space:

$$\text{FoV}_x = \frac{1}{\Delta k_x} \tag{2.44}$$

The resolution (pixel size) in image space is determined by the maximum frequency sampled in k-space:

$$\Delta x = \frac{\text{FoV}_x}{N_x} = \frac{1}{k_{x,max}} = \frac{1}{\frac{\gamma}{2\pi} G_x N_x \Delta t} \tag{2.45}$$

where N_x is equal to the number of pixels in the x direction. In summary, objects on the order of 1 pixel have the information equally spaced across all frequencies in k-space. On the other hand, nearly constant intensity objects spanning the entire FoV correspond to a narrow range of low frequencies. In conventional imaging, an RF excitation is used to collect each line of k-space. All lines of k-space are usually not collected under a single RF excitation due to T_2^* signal loss. The time between two RF excitations is known as the repetition time (TR). Adjacent points in the PE direction are separated by TR while adjacent points in the FE direction are separated by Δt. The echo time (TE) is the time between the centre of the RF excitation pulse and the echo.

In 2D multi-slice acquisitions, the slices are spaced out across the TR by changing the RF pulse carrier frequency. An interleaved scheme is commonly adopted, where first all the odd slices are acquired followed by the even slices. This avoids slice cross-talk due to the RF pulse excitation profile leaking into the neighbouring slices.

3D imaging is possible by applying a second PE gradient along the slice direction, known as partition-encoding (Figure 2.11). The total time for a 3D image will be equal to $T_{acq} = N_y * N_z * T_R$, where N_y and N_z are the number of PE steps in the y and z direction, respectively. Because of the extra PE gradient along z, the total acquisition time is longer for 3D acquisitions compared to 2D. 2D multi-slice acquisitions differ from 3D imaging as there is an RF excitation for each slice as opposed to a single excitation per volume, or slab, in 3D. 3D presents several advantages relative to 2D multi-slice imaging. Firstly, the slice thickness is controlled in 3D by the step size of the partition-encoding

gradient. Secondly, slice contamination is not an issue, thus there is no need for a slice gap and the slices are contiguous in 3D. Thirdly, TE can be reduced by using RF pulses with shorter time duration or larger BW. Signal loss from T_2^* decay is reduced in the partition encoding direction due to shorter TEs and slice thickness.

The SNR is proportional to the voxel volume and the square root of the total acquisition time ($SNR \propto \Delta x \Delta y \Delta z \sqrt{T_{acq}}$) [33], [34]. In 3D, the total acquisition time is longer compared to 2D by a factor equal to the number of phase encoding steps along z (slice direction). Given the same voxel volume for both acquisitions, there is an SNR advantage for 3D acquisitions. Nevertheless, when 2D acquisitions are interleaved there is T_1 recovery of the magnetisation between subsequent PE steps, thus at least partially recovering the SNR shortfall. Generally, there is an SNR advantage for 3D acquisitions, but it will depend on the T_1 of the tissue being imaged [33].

Periodic motion during the acquisition of the k-space lines manifests in the image as ghost artefacts [35]. Due to the extra PE gradient along the slice direction for 3D, this introduces the possibility for ghosts to appear along this direction. Moreover, Gibbs ringing along the slice direction is an artefact that only affects 3D acquisitions as the images are also Fourier-encoded along the slice direction. Reducing the slice thickness will reduce the Gibbs ringing artefact [33].

The longer acquisition times for 3D compared to 2D acquisitions have the drawback of making 3D acquisitions more prone to motion artefacts. Additionally, temporally localised motion may affect only a few slices in sequential 2D acquisitions, whereas in 3D the whole dataset will be corrupted by motion since data is Fourier encoded along all 3 dimensions [36]. For 3D acquisitions where each PE line is separated by N partitions, a larger susceptibility to ghost artefacts will occur in-plane along the PE direction rather than out-of-plane as the larger time interval between PE lines along y compared to z allows for more opportunity for motion to occur.

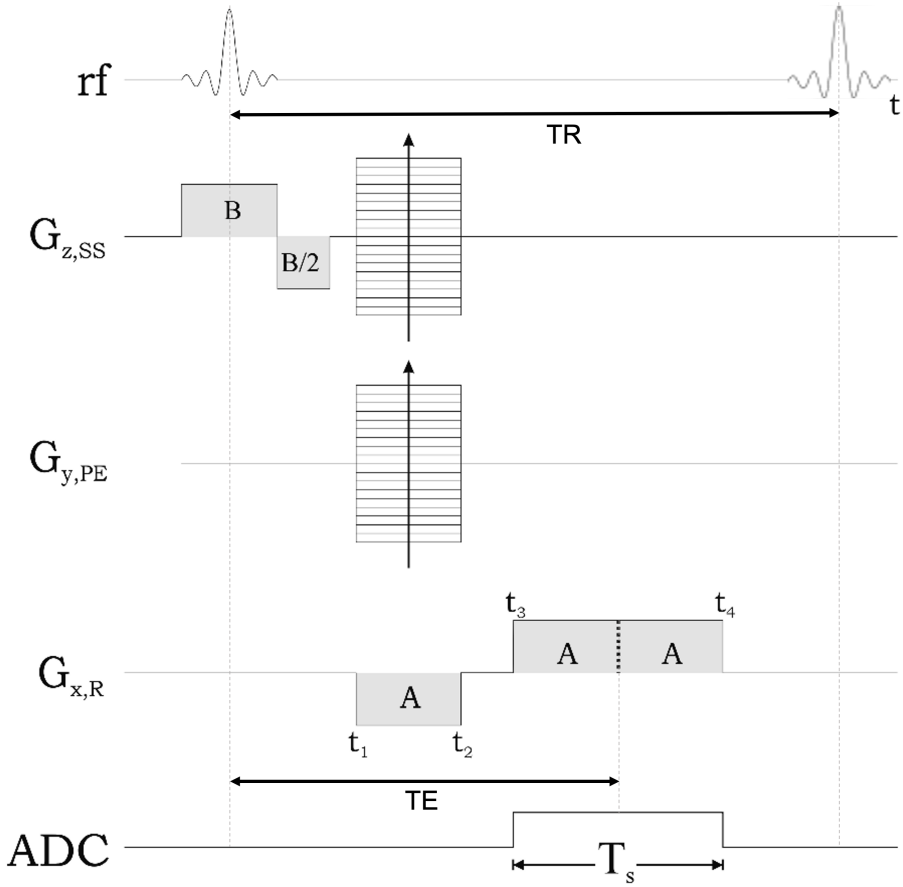


Figure 2.11: Pulse sequence diagram of a 3D acquisition. Two phase-encoding gradients, G_y and G_z, encode the y and z directions respectively and are orthogonal to the read direction encoded by G_x. TE is the time from the centre of the RF pulse until the peak of the echo and TR is the time between two RF excitation pulses. Republished with permission of John Wiley & Sons - Books, from Magnetic Resonance Imaging: Physical Principles and Sequence Design, Brown et al. [31] copyright 2014; permission conveyed through Copyright Clearance Center, Inc.

2.9 Pulse Sequences

2.9.1 Spin Echo

There are two main branches of pulse sequences: spin echo (SE) and gradient echo (GE). SE was invented by Hahn [37] and uses a pair of $90°/180°$ excitation/refocusing pulses (Figure 2.12). The excitation pulse, applied along x', flips the net magnetisation to the xy plane creating a phase coherent M_{xy}. As time evolves, the spins start to dephase due to spin-spin interactions producing a free induction decay (FID) signal. A second RF pulse of twice the magnitude and applied along y' refocuses the dephasing

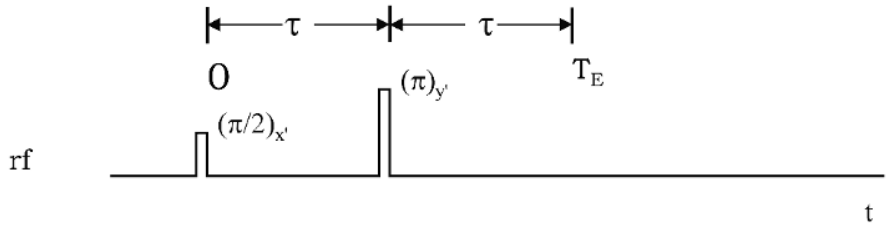


Figure 2.12: Spin echo sequence RF pulse diagram. The π pulse has twice the height of the $\pi/2$ pulse for the same time interval. Republished with permission of John Wiley & Sons - Books, from Magnetic Resonance Imaging: Physical Principles and Sequence Design, Brown et al. [31] copyright 2014; permission conveyed through Copyright Clearance Center, Inc.

spins which results in an echo at time TE. TE is equal to two times the time difference between the excitation and refocusing pulses. The second RF pulse, applied at time TE/2, is known as the refocusing pulse as it inverts the magnetisation about the y' axis; spins that had leading phases have now lagging phases. After time TE, all the spins remaining in the transverse plane refocus producing an echo. The total phase acquired during the SE after the refocusing pulse is:

$$\phi(\vec{r},t) = \gamma\Delta B(\vec{r})\tau - \gamma\Delta B(\vec{r})(t-\tau) = -\gamma\Delta B(\vec{r})(t-2\tau)\ , \tag{2.46}$$

The first term in Equation (2.46) represents the phase accumulated from the $90°$ pulse until the $180°$ pulse. This phase was inverted by the $180°$, hence the positive sign. The second term represents the phase accumulated after the $180°$. The total accumulated phase of the spins is zero at $t = \text{TE} = 2\tau$, independent of the value ΔB or the position $\vec{r}$. All the spins are refocused at TE forming an echo along the y' axis, thus the name spin echo (Figure 2.13).

The FID signal decays according to T_2^* between the excitation and the refocusing pulse. Dephasing due to B_0 inhomogeneities during this period are refocused by the $180°$ pulse. Consequently, the echo amplitude is limited by a T_2 envelope decay rather than T_2^* (Figure 2.14). The sinusoidal oscillations at the Larmor frequency disappear in the rotating frame. Note that the dephasing due to the fluctuating intrinsic local fields from the spin-spin interactions are not refocused as these change on a time scale much faster

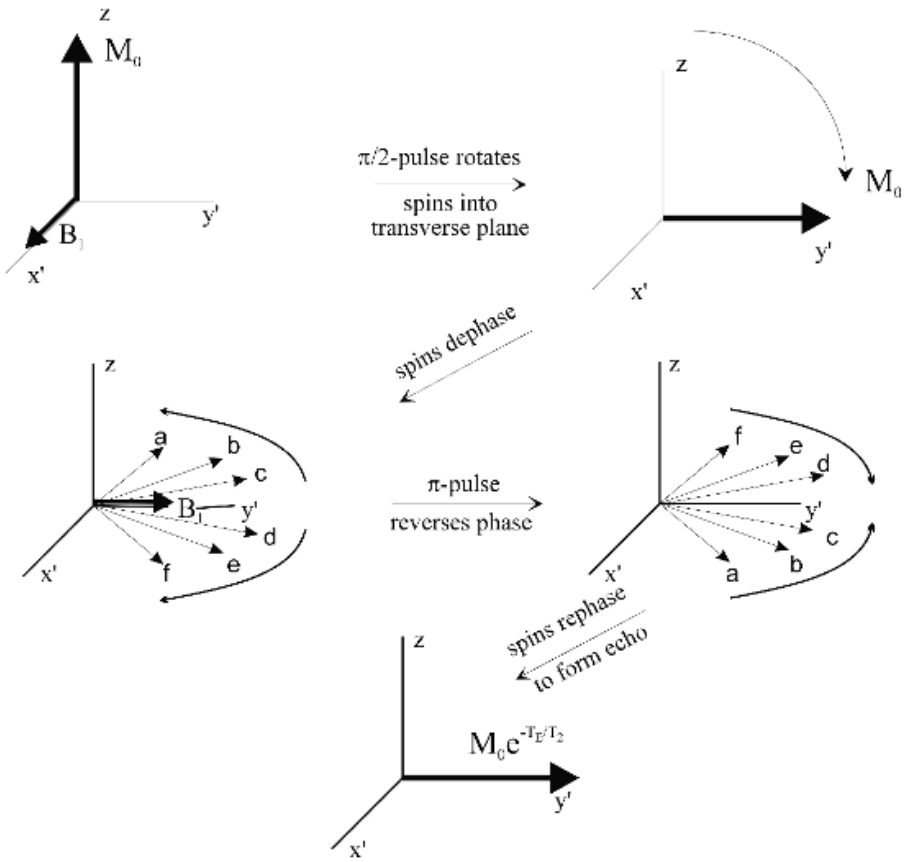


Figure 2.13: Main steps in the spin echo sequence. The longitudinal magnetisation M_0 is rotated by a $90°$ pulse, applied along the positive x' axis, into the transverse plane. The initial magnetisation pointing along y' starts to dephase in the transverse plane. The phase accumulated by the spins is inverted by a $180°$ pulse, applied along the positive y' axis. The spins accumulate phase in the opposite direction and rephase along the positive y' axis forming an echo. Republished with permission of John Wiley & Sons - Books, from Magnetic Resonance Imaging: Physical Principles and Sequence Design, Brown et al. [31] copyright 2014; permission conveyed through Copyright Clearance Center, Inc.

than TE, i.e., the echo is limited by the T_2 decay of the spins. M_{xy} at TE is:

$$M_{xy}(TE) = M_0 e^{-TE/T_2} \tag{2.47}$$

Different versions of SE have been developed to accelerate the acquisition, such as Turbo SE where a train of echoes are collected, after a single RF excitation, by applying successive refocusing pulses. The peak amplitudes of the subsequent echoes will decrease following a T_2 exponential decay. SE produces T_2-weighted (T_2-W) contrast by acquiring images with a long TE and a long TR, to reduce differences in signal due to T_1 recovery and emphasize T_2 decay differences. Tissues with long T_2 appear

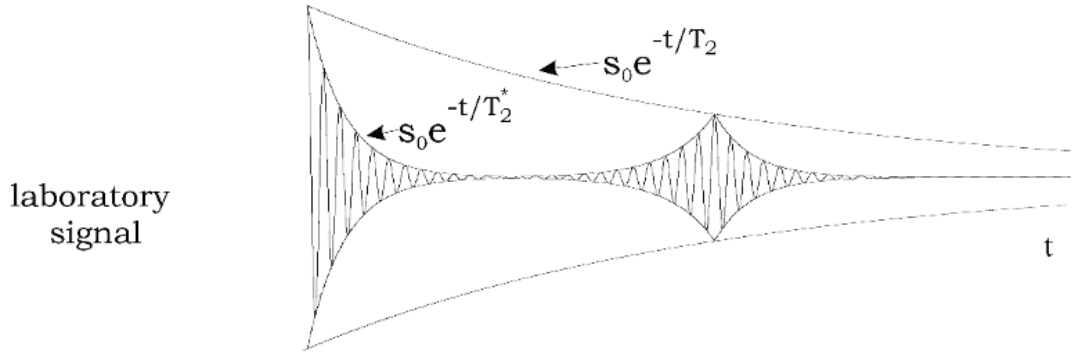


Figure 2.14: Free induction signal decaying with time constant T_2^* and refocused as an echo at time TE. Refocusing of B_0 inhomogeneities by the $180°$ pulse results in an echo whose amplitude is limited by the T_2 envelope. Republished with permission of John Wiley & Sons - Books, from Magnetic Resonance Imaging : Physical Principles and Sequence Design, Brown et al. [31] copyright 2014; permission conveyed through Copyright Clearance Center, Inc.

bright as the magnetisation takes more time to decay than tissues with a short T_2. SE produce T_1-weighted (T_1-W) contrast by acquiring images with a short TR, to emphasize differences in M_z signal between tissues with different T_1 relaxation times, and a short TE to minimise T_2 decay. Proton-density weighted contrast is achieved with a short TE and a long TR to minimise both T_1 and T_2 relaxation.

2.9.2 Gradient Echo

As the name indicates, signals from GE sequences are produced by refocusing of the spins through gradients. A gradient is used in the FE direction, before the readout, to accelerate the dephasing of the spins and subsequently a gradient of equal amplitude but reversed polarity, played during the readout, refocuses the spins resulting in an echo (Figure 2.15). The echo is formed when the rephasing gradient area is equal to the area of the dephasing gradient, i.e., the zero$^{\text{th}}$ moment of the gradient is zero:

$$\int G(t)dt = 0 \tag{2.48}$$

Usually, a rephasing gradient with twice the area of the dephasing is employed such that the echo will occur at the centre of the rephasing gradient. The echo occurs at k-space centre, i.e., k=0. The signal in k-space during the positive rephasing gradient,

between time $t_3 - t_4$ in Figure 2.15, is equal to:

$$s(k) = \int dz \rho(z) e^{-i2\pi k_z} \ , \qquad -k_{\text{max}} < k < k_{\text{max}} \tag{2.49}$$

with $k_{\text{max}} = \frac{\gamma}{2\pi} G(t_4 - t_3)/2$.

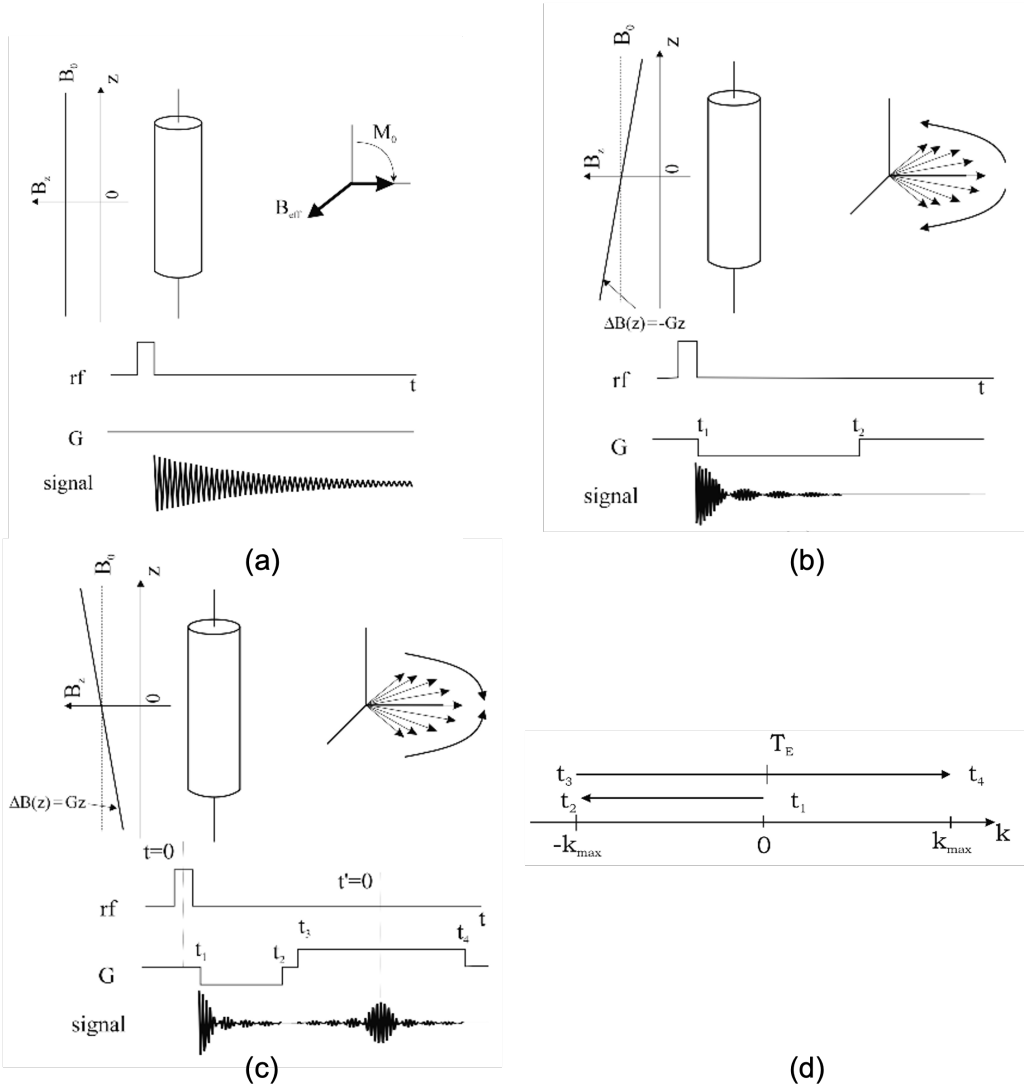


Figure 2.15: Main steps in the gradient echo sequence. (a) Identical to the spin echo, the longitudinal magnetisation M_0 is rotated by a $90°$ pulse into the transverse plane, producing a free induction decay signal shown in the laboratory frame. (b) A gradient along z applied during time interval $t_1 - t_2$ accelerates the spins' dephasing. (c) Applying a gradient of reversed polarity from time t_3 to t_4 recovers the signal loss and produces an echo at time $t' = 0$. (d) Use of the gradients to sample k-space: a negative gradient between $t_1 - t_2$ goes from k=0 to $-k_{\text{max}}$, and the positive gradient between $t_3 - t_4$ travels from $-k_{\text{max}}$ to k_{max}. The echo occurs at $k = 0$ or $t = TE$. Republished with permission of John Wiley & Sons - Books, from Magnetic Resonance Imaging: Physical Principles and Sequence Design, Brown et al. [31] copyright 2014; permission conveyed through Copyright Clearance Center, Inc.

GE sequences refocus the signal loss due to the dephasing gradient. However, the gradient will not refocus B_0 inhomogeneities due to scanner imperfections or tissue susceptibility differences at TE, unlike the π-pulse in SE. Consequently, the signal will experience a faster decay through a time constant T_2^* instead of T_2, limiting the maximum value of TE. GE sequences are faster than SE because the dephasing is manipulated by gradients and the FA, affording shorter TRs.

GE images are primarily used to produce T_1-W images by setting a short TE, to suppress T_2-W, and a short TR. However, any contrast can be generated by manipulating the FA. Small FAs, leave most of the magnetisation in the z axis speeding up the acquisition for successive RF excitations. Low FAs and a short TR will result in PD-W; when TE is increased T_2^*-W images are obtained. High FAs and short TE generate T_1-W images as more magnetisation is flipped to the transverse plane. T_1-W images are commonly used as anatomical scans due to their good contrast between different tissues: fat appears bright (short T_1), water-based tissue appears mid grey (intermediate T_1) and fluid-filled compartments appear dark (long T_1).

2.10 Quantitative Imaging: T_1 and B_1^+ Mapping

In quantitative MRI, the goal is to map a physical property of the tissue from raw MRI-weighted data. The data should be weighted by the physical property of interest. For example, for T_1 mapping the images can have different levels of T_1-weighting by varying parameters such as the inversion time, TR or FA, which can be accomplished by using inversion recovery, saturation recovery or variable flip angle sequences.

2.10.1 Inversion Recovery Spin Echo

Inversion Recovery Spin Echo (IR SE) is considered the gold standard T_1 mapping method. The longitudinal magnetisation is inverted by a $180°$ RF pulse (Figure 2.16), extending the amplitude of M_z recovery by a factor of two compared to a $90°$ excitation pulse. By applying a second RF pulse of $90°$, the magnetisation that recovered along

M_z is flipped into the xy plane producing a FID. The FID is subsequently refocused by a third RF pulse of $180°$ and read as an echo at time TE (Figure 2.17). The time between the first $180°$ inversion and the $90°$ RF pulse is the inversion time (TI), during which the signal undergoes T_1 relaxation.

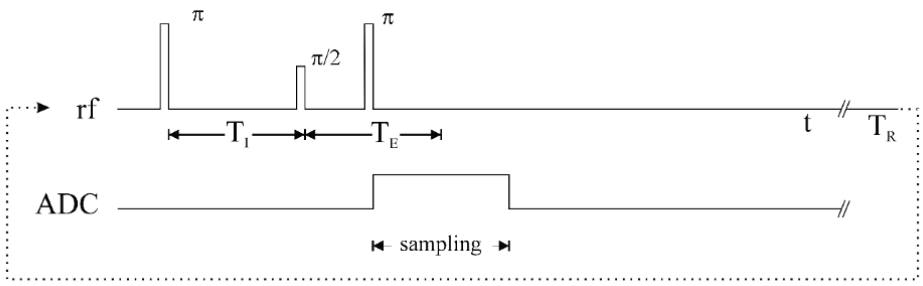


Figure 2.16: Inversion recovery spin echo RF pulse diagram. The π pulse inverts the longitudinal magnetisation. An inversion time TI allows the magnetisation to recover through T_1 relaxation. The $\pi/2$ pulse flips the longitudinal magnetisation to the transverse plane. Varying TI between the π and the $\pi/2$ pulse creates images with different T_1-W. Finally, the third π pulse refocuses the magnetisation to form an echo at time TE. Republished with permission of John Wiley & Sons - Books, from Magnetic Resonance Imaging: Physical Principles and Sequence Design, Brown et al. [31] copyright 2014; permission conveyed through Copyright Clearance Center, Inc.

A large TR (time between two successive inversion pulses) of at least $5T_1s$ is needed for the magnetisation to fully recover before the next $180°$ RF excitation is applied, to collect the next k-space line. This precludes its use *in vivo*. Assuming a $TR > 5T_1$, a perfect inversion and refocusing of the spins, the magnetisation at time TE plus TI is:

$$M_{xy}(\text{TE+TI}) = M_0(1 - 2e^{-\frac{\text{TI}}{T_1}})e^{-\frac{TE}{T_2}} \tag{2.50}$$

A three-parameter fit to Equation (2.50) gives Equation (2.51). A non-linear least-squares (NLLS) fit of the signal as a function of TI provides an estimate of T_1.

$$\text{Signal}(\text{TI}) = a + be^{-\frac{\text{TI}}{T_1}} \tag{2.51}$$

where $a = M_0e^{-\frac{TE}{T_2}}$ and $b = -2M_0e^{-\frac{TE}{T_2}}$.

Look-Locker

Look-Locker [38] is an adaptation of the IR method that overcomes the long recovery period of M_z and thus enables T_1 mapping *in vivo*. In Look-Locker a single $180°$ RF

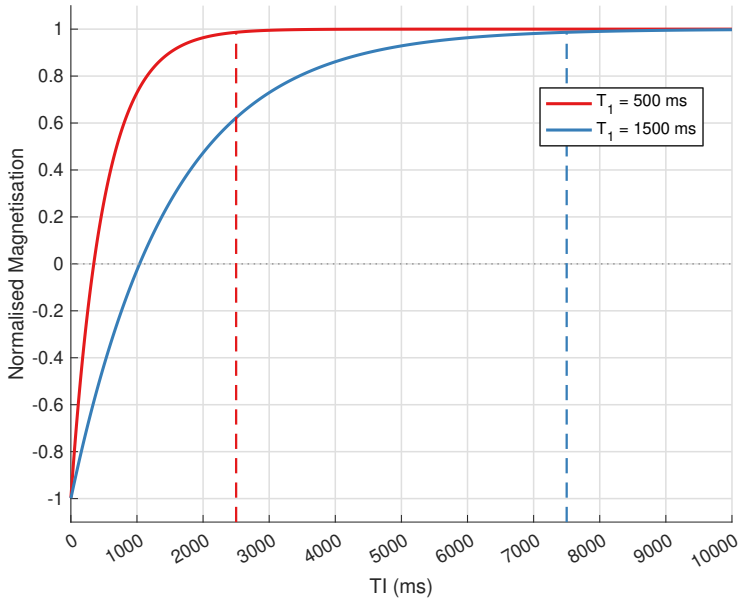


Figure 2.17: Inversion recovery (IR) of the longitudinal magnetisation, normalised by $M_0 e^{-\frac{TE}{T_2}}$, as a function of the inversion time TI in ms. The IR curve for a T_1 of $500\,\mathrm{ms}$ is shown in red and for a T_1 of $1500\,\mathrm{ms}$ is shown in blue. The dashed red line represents M_z at a TI of $2500\,\mathrm{ms}$ $(5 * 500\,\mathrm{ms})$ and the dashed blue line indicates M_z at a TI of $7500\,\mathrm{ms}$ $(5 * 1500\,\mathrm{ms})$.

pulse is applied and the longitudinal magnetisation is sampled at different TIs along the IR curve using small FAs α. This considerably accelerates the IR SE, eliminating the need for a TR of at least $5T_1 s$ per TI sample. However, the small excitation FAs applied every TR will allow for T_1 relaxation during the time TR. This accelerates the recovery of the magnetisation, resulting in a smaller equilibrium magnetisation (M_0^*) than that obtained with IR SE (M_0). The consequence is a shorter T_1 relaxation time, denoted in the literature as T_1^*. A correction is commonly applied to recover T_1 from T_1^* [39]. The magnetisation after inversion is given by:

$$M(t) = M_0^* - (M_0 + M_0^*)e^{-\frac{t}{T_1^*}}, \tag{2.52}$$

which can be fit using three-parameters $(M(t) = A - Be^{-\frac{t}{T_1^*}})$ to determine T_1^* and then T_1 through:

$$T_1 = T_1^*(\frac{B}{A} - 1) \tag{2.53}$$

2.10.2 Saturation Recovery

Saturation recovery sequences for T_1 mapping are similar to IR sequences but use a $90°$ RF saturation pulse instead of a $180°$ inversion pulse. The $90°$ FA saturates the magnetisation into the transverse plane and the magnetisation is read at different saturation recovery times (TS), which is the time between the end of the saturation pulse and k-space centre. The longitudinal magnetisation after the saturation pulse is [40]:

$$M_z = (1 - \eta_{\text{actual}} e^{-\frac{(TS-\Delta)}{T_1}}), \tag{2.54}$$

where $\eta_{\text{actual}} = 1$ corresponds to perfect saturation and Δ is the time interval between the start of the readout and k-space centre. T_1 can be determined through a three-parameter fit of the signal as a function of TS.

2.10.3 Variable Flip Angle

Variable Flip Angle (VFA) using a spoiled gradient recalled echo sequence (SPGR) enables 3D high spatial resolution T_1 mapping within a few breath-holds. RF pulses with small nutation angles are repeatedly applied within a single short TR resulting in a steady-state signal (Equation (2.55)) which is a function of T_1, TR, and the excitation FA θ [41]. The M_0 term includes spin density, coil sensitivities, scanner gain, and T_2^* relaxation. The steady-state limit can be reached for a TR shorter than T_2^* if spoiling is applied to ensure M_{xy} is null before each new RF pulse. Figure 2.18 shows the signal intensity as a function of FA using a short TR of $5\,\text{ms}$.

$$S = M_0 \frac{1 - e^{\frac{-TR}{T_1}}}{1 - \cos(\theta) e^{\frac{-TR}{T_1}}} \sin(\theta) \tag{2.55}$$

T_1 can be estimated from a NLLS fit of the SPGR signal measured at different FA values and a fixed TR. Alternatively, a popular approach to determine T_1 consists in transforming the steady-state equation into a linear equation and using a linear least squares fit (Figure 2.18 (b)). The signal acquired at the different FAs is scaled by the sine and tangent of the FA:

$$\frac{S}{\sin\theta} = e^{\frac{-TR}{T_1}} \frac{S}{\tan\theta} + M_0(1 - e^{\frac{-TR}{T_1}}) \tag{2.56}$$

Using a linear fit, $Y = aX + b$, where $Y = \frac{S}{\sin\theta}$ and $X = \frac{S}{\tan\theta}$, the slope is used to calculate T_1 through:

$$T_1 = \frac{-TR}{\ln\left(e^{\frac{-TR}{T_1}}\right)} \tag{2.57}$$

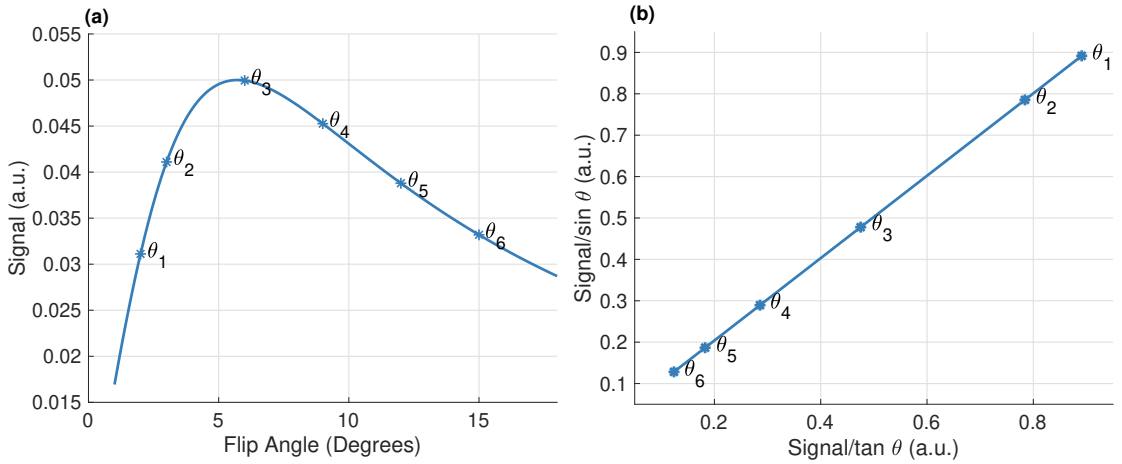


Figure 2.18: (a) Spoiled gradient recalled echo signal as a function of FA (θ) for $M_0 = 1$, TR =5 ms, T_1 =1000 ms. (b) Linear transformation of the signal plotted in (a). Note the larger FAs ($\theta 5 - \theta 6$) on the non-linear curve in (a) are mapped to the beginning of the straight line in (b).

Venkatesan et al. [42] recognised that variations in the transmit RF field and FA miscalibrations affect the accuracy of T_1 estimation using the VFA SPGR sequence. Using this technique requires one to map the true FA exciting the spins through B_1^+ mapping.

2.10.4 B_1^+ Inhomogeneities

The active B_1^+ field is responsible for exciting the spins. The coils responsible for exciting the spins are called transmit coils. The positive sign in the B_1 field refers to the circularly polarised component rotating in the same direction as spin precession. Its distribution can change spatially due to several factors: patient's size and position within the magnet, dielectric and conductive properties of the tissue [43] as well as Larmor frequency [44]. The primary result is a spatial modulation in the signal intensity in both phantom and *in vivo* images [45]. The origin of this modulation can be attributed to two different physical processes. The first is the formation of standing wave patterns due

to the boundaries of the object which reflect the RF waves [44], [46]. For $3\,\mathrm{T}$ imaging, the resonance frequency is $127.7\,\mathrm{MHz}$ and the liver's relative permitivity is 64, resulting in an RF wavelength of approximately $26\,\mathrm{cm}$ [47], which allows for the possibility of standing waves to be formed in the abdomen. This will lead to enhanced fields at the anti-nodes. Even at $1.5\,\mathrm{T}$, the RF wavelength in the liver is approximately $44\,\mathrm{cm}$, which still allows for the formation of standing waves. This suggests it might be important to consider B_1^+ mapping at $1.5\,\mathrm{T}$. However, the standing wave effect is attenuated *in vivo* as the conductivity of biological tissues [44], [46], [48] leads to a decay of the RF wave with penetration depths of $9.3\,\mathrm{cm}$ for the liver at $3\,\mathrm{T}$ [47]. Moreover, this is further attenuated by decreased reflectivity at higher frequencies [45]. The second physical process is the constructive and destructive interference [49] of the propagating RF waves emitted by the multiple transmit elements in array coils. The superposition of the RF fields leads to localised regions of enhanced and diminished B_1^+ fields. This is not a problem at $3\,\mathrm{T}$ when the body coil is used as the transmit coil.

B_1^+ mapping

B_1^+ inhomogeneities provoke intensity modulations, impairing quantitative imaging. Consequently, several schemes have been put forward to map the B_1^+ spatially, enabling correction of the B_1^+ inhomogeneity present at each voxel. B_1^+ mapping imaging methods can be divided into magnitude and phase-based approaches, depending on whether the excitation pulse encodes the actual FA in the magnitude or phase.

Magnitude-based approaches generally take the ratio between two signals to eliminate the signal variations due to spin density, T_2 or T_2^* decay and receive coil sensitivity (B_1^-) as these should not change between the acquisition of the two signals. Magnitude-based approaches for B_1^+ mapping include the double angle method [50], [51], actual flip angle imaging [52], preconditioning RF pulse with a turbo Fast Low Angle Shot (FLASH) readout [53] and a dual refocusing echo acquisition mode [54], among others.

Two phase-based RF mapping methods in the literature are: the Bloch-Siegert shift [55] and a phase-sensitive [56] method encoding the B_1^+ in the phase of the transverse

signal. The main advantage of phase-based B_1^+ map methods compared to magnitude-based methods is the ability to calculate the actual angle over a wider range of nominal FAs ($20^\circ - 180^\circ$). Another important asset, especially when using B_1^+ mapping to correct the FAs in T_1 mapping, is the phase insensitivity to T_1 relaxation effects.

3

Identifying, Quantifying and Correcting Confounding Factors Affecting *In Vivo* Liver 3D T_1 maps

3.1 Introduction

The main research question addressed in this thesis is whether a whole liver coverage T_1 map can be estimated at $3\,\mathrm{T}$ using only widely available pulse sequences, with an accuracy and precision appropriate for clinical applications. This chapter focuses on the confounding factors affecting the accuracy of the T_1 mapping method and the measures taken to mitigate their influence. A discussion of the T_1 mapping precision required in liver applications will be addressed in Chapter 6.

Using widely available pulse sequences ensures that the method is vendor-agnostic and extends the method's applicability beyond research-based facilities to clinical sites that do not have access to state-of-the art sequences. Mapping T_1 relaxation times across the whole liver volume could enable understanding and characterisation of heterogeneous liver diseases as well as improve detection and diagnosis of HCC. Given that liver imaging is usually done under breath-hold conditions, a further requirement was that the whole protocol should be acquired within a reasonable number of breath-holds (less than 10) each of no more than $15\,\mathrm{s}$ duration. All these requirements will facilitate the clinical

availability of robust liver T_1 mapping methods. A sequence that meets these three requirements is the SPGR sequence.

Accuracy of the method is important to enable its wide dissemination across different scanners. If the SPGR T_1 method is to be used clinically, the measurement should not only be precise but also accurate. Different scanner vendors use different MRI building blocks such as RF pulses, shimming procedures and incomplete spoiling methods. If the method is biased due to a mechanism that disrupts the theoretical model of the signal, this bias may have different magnitudes or even opposite directions (over or under-estimation) depending on the sequence implementation. This would result in different T_1s for the same individual measured in two different scanners. Understanding the factors that compromise the accuracy of T_1 is important to be able to move in the direction of using T_1 in the clinic reliably and reproducibly.

A major source of bias in the SPGR T_1 maps at $3\,\mathrm{T}$ are B_1^+ inhomogeneities which cause spatial variations in the true FAs exciting the spins [42]. The B_1^+ correction factor is the ratio between the true FA and the nominal FA prescribed at the scanner. An accurate knowledge of the true FAs is essential for an accurate estimate of T_1 using the SPGR sequence [29]. Thus, it is necessary to acquire an accurate and precise B_1^+ map. The same three requirements of a widely available sequence that provides whole liver coverage within a breath-hold of less than $15\,\mathrm{s}$ also apply to the B_1^+ map, leading to the adoption of the Double Angle Method (DAM) [51] using a gradient recalled echo (GRE) single shot echo-planar-imaging (EPI) sequence.

This chapter starts by demonstrating the importance of correcting for B_1^+ inhomogeneities through analysis of an *in vivo* dataset. The unavailability of an accurate and scanner agnostic B_1^+ mapping method is the main obstacle to implementing a reliable SPGR T_1 mapping method. The adoption of the DAM using a GRE-EPI sequence is subject to at least five confounding factors (Figure 3.1). The first source of B_1^+ bias explored was the effect of slice profile arising from 2D multi-slice acquisitions [57]. A new confounding factor discovered during this work was the variation of B_0 through slice,

which interacts with the slice profile. The remaining three factors are a consequence of using an EPI readout. The DAM requires a TR of $5T_1$s for (near) full recovery of the magnetisation, which makes an implementation using a standard fast SPGR readout infeasible for liver breath-hold acquisitions. EPI is widely available commercially, allowing the DAM to be used for B_1^+ mapping with full liver coverage within two breath-hold acquisitions, each $10\,\mathrm{s}$ long. The disadvantage of EPI is its susceptibility to spatial distortions, chemical shift artefacts and GRAPPA-induced fat ghosts [58]. Assessing the impact of these effects on liver B_1^+ mapping is a novelty of this work. Several corrections were constructed or implemented based on pre-existing algorithms commonly used in neuroimaging. The last two confounding factors affect the steady-state signal of the SPGR sequence: incomplete spoiling and spatial saturation. No mention of the impact of spatial saturation on T_1 mapping using the SPGR sequence was found in the literature.

In this chapter, each confounding factor is considered separately. The study of each factor is presented according to the following structure: a background and motivation section, followed by a description of the methods used to quantify its effect on the T_1 map; where appropriate the developed correction is described and assessed with phantom and *in vivo* data. The corrections either involved changing parameters at the scanner console or constructing MATLAB [59] functions to post-process the data and eliminate the artefact. Flow diagrams of the different functions can be found in the Appendix to Chapter 4 (Section 4.3).

3.2 General Methods: Phantoms and Image Acquisition Sequences

Both phantom and *in vivo* acquisitions were used to study the different confounding factors affecting the B_1^+ and T_1 maps, and to subsequently validate the different correction algorithms developed. Two different phantoms from Perspectum were imaged: *Calimetrix QC0025* and *FDA4-T1*. The *Calimetrix QC0025* phantom consisted of 15 vials: 5 vials had varying T_1s (at $3\,\mathrm{T}$) between $548\,\mathrm{ms}$ and $1429\,\mathrm{ms}$ which were used in this work; 5

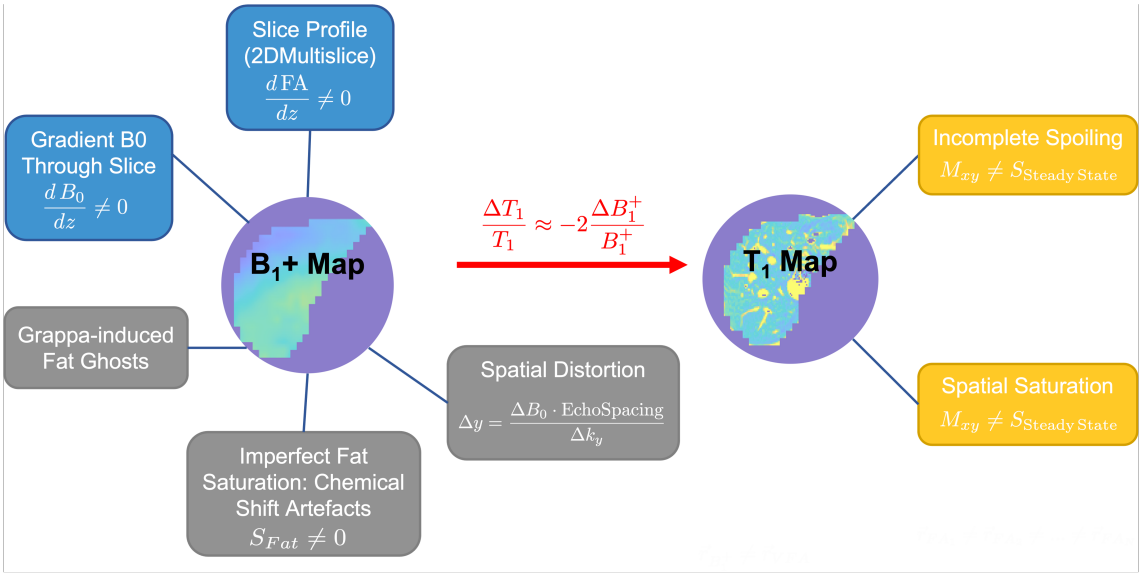


Figure 3.1: Diagram of confounding factors affecting SPGR T_1 maps. Blue and grey rectangles show the factors affecting the B_1^+ map using a dual angle 2D multi-slice GRE-EPI. The grey rectangle confounders arise from EPI artefacts. The relative error from these factors will propagate by approximately a factor of two into the T_1 maps using a VFA SPGR sequence. In yellow are the confounding factors affecting the 3D SPGR sequence.

vials had varying T_2^* values ($5.3 - 21.3\mathrm{ms}$), and the last 5 vials had varying fat fractions (0%-40.1%). The *FDA4-T1* phantom contained 14 vials with T_1s (at $3\,\mathrm{T}$) ranging from $367\,\mathrm{ms}$ to $1699\,\mathrm{ms}$ in steps of approximately $100\,\mathrm{ms}$, an average T_2 of $45\,\mathrm{ms}$ and no fat.

Imaging data were acquired on a $3\,\mathrm{T}$ Prisma Siemens scanner (Siemens Healthineers, Erlangen, Germany), software version E11, using a spinal coil and an 18-channel body coil. Supporting data for this chapter was acquired with the following product sequences: a 2D multi-slice GRE-EPI for B_1^+ mapping, a 2D multi-slice double echo for B_0 mapping and a 3D VFA SPGR for T_1 mapping. Characterising the confounding factors' impact on the T_1 map and evaluating the effectiveness of the corrections developed led to the parameters adopted in the final protocol. Full details of the final protocol are described in Chapter 4. Overnight acquisitions using a gold standard B_1^+ mapping and T_1 mapping sequence were run in the phantoms and are described in Appendix (Sections 3.10.1 and 3.10.2). I was the scanner operator for all the phantom data as well as one *in vivo* dataset that was acquired under the supervision of Dr.Tunnicliffe.

3.3 B_1^+ Inhomogeneities

Background

B_1^+ inhomogeneities result in signal modulations that can degrade the image [45] as well as induce errors in quantitative imaging [60]. The SPGR sequence, adopted for mapping the liver T_1 relaxation in this work, is a steady-state based sequence where the acquired signal magnitude depends on the true local value of the excitation FA. An accurate B_1^+ mapping method is therefore essential for accurate T_1 mapping using the SPGR sequence [29]. *In vivo* B_1^+ inhomogeneities in the liver at $3\,\mathrm{T}$ on a GE scanner varied between 0.59 and 1.13 times the nominal FA [61]. Uncorrected, these B_1^+ errors will propagate into the T_1 maps, with the fractional error in T_1 equal to B_1^+ factor squared minus one [62], e.g., for a B_1^+ factor of 0.6, the relative error in T_1 would be -64%.

Methods

One *in vivo* dataset from a healthy volunteer was used to illustrate the effect of B_1^+ inhomogeneities on the SPGR T_1 map. T_1 maps corrected for B_1^+ inhomogeneities were calculated using the pipeline described in Section 4.2. To calculate the T_1 maps uncorrected for B_1^+ inhomogeneities the same procedure was used, but the SPGR signal was fit to the steady-state model at nominal FAs of [2 2 15 15]$^\circ$.

The correlation between T_1 and B_1^+ was assessed for two single-slice T_1 maps: with and without applying a B_1^+ correction. A mask was constructed to eliminate blood vessels through thresholding. Any pixels with T_1 values above $1150\,\mathrm{ms}$ in the corrected T_1 map were excluded from the correlation plot. This threshold was used to discriminate healthy liver tissue from pixels with partial volume effects from blood [63]. Any pixels with T_1 values below $110\,\mathrm{ms}$ in the uncorrected T_1 map were also excluded. Additionally, liver pixels in the left lobe were also excluded from the analysis as this is a small region near the boundaries of the abdomen with blood vessels. A linear fit of the T_1 versus B_1^+ factor values provided a slope indicating the degree of correlation between T_1 and B_1^+. Multiplying the slope by the range of B_1^+ factor values in the liver gave an estimate

of the B_1^+-related variation in liver T_1.

Results

Without correcting for B_1^+ inhomogeneities, the T_1 map displayed strong variations across the liver (Figure 3.2 (a)). These spatial variations closely resembled the B_1^+ map (Figure 3.2 (b)), indicating a large co-variance between B_1^+ and T_1. Any systematic deviation of the FA from the nominal value set at the scanner can be compensated by a change in T_1 or M_0. After applying the B_1^+ correction to the nominal FAs, the T_1 map was more homogeneous (Figure 3.2 (c)) as expected for a healthy volunteer. The MOLLI T_1 map (Figure 3.2 (d)), which is based on an IR, confirmed the homogeneity of T_1 values across the liver, despite MOLLI underestimating T_1 [26].

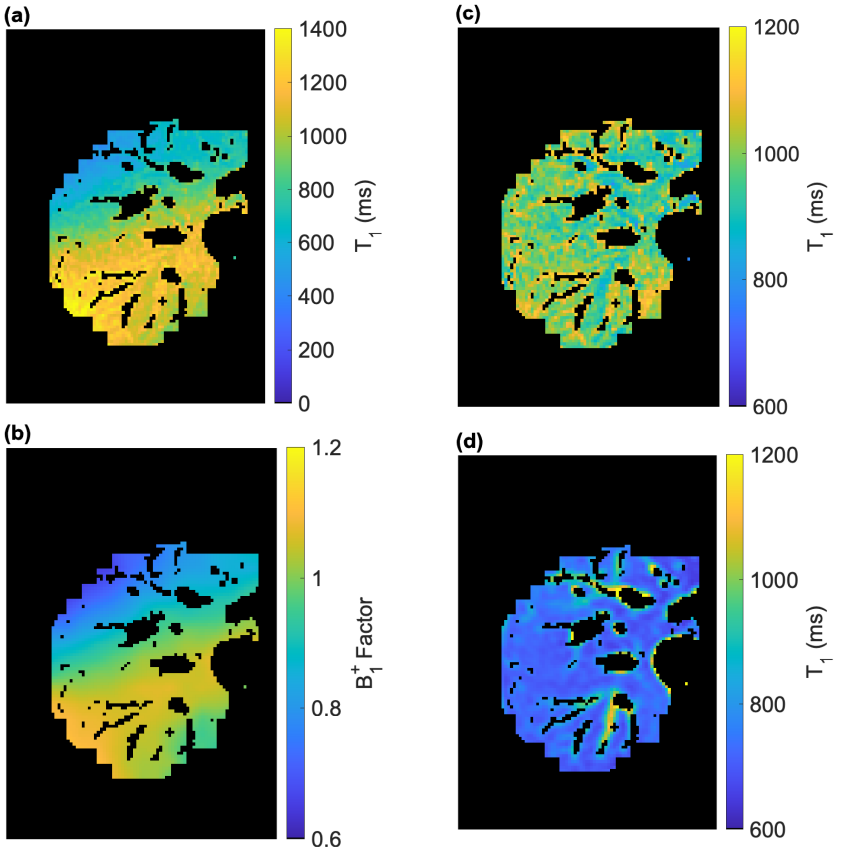


Figure 3.2: (a) *In vivo* T_1 map uncorrected for B_1^+ inhomogeneities, showing strong variations in T_1 especially along the vertical direction. (b) B_1^+ map used to correct the nominal FAs in the SPGR fit resulting in a more homogeneous (c) B_1^+ corrected T_1 map. (d) Corresponding MOLLI T_1 map showing a homogeneous liver T_1. Note that MOLLI underestimates T_1 values. The vessels were excluded from all maps using the thresholding procedure described in the methods.

A large correlation between the uncorrected T_1 and B_1^+ maps is evident in Figure 3.3. The slope of the linear fit to the data gave a gradient in T_1 of $200\,\mathrm{ms}$ per 10% change in B_1^+ factor with a 95% confidence interval (CI) of $[198\ 202]\mathrm{ms}/(10\%\ \Delta B_1^+)$. The correlation coefficient was 0.96 before B_1^+ correction. Correcting for B_1^+ inhomogeneities, the slope reduced significantly, resulting in a T_1 gradient of $2.5\,\mathrm{ms}$ per 10% change in B_1^+ factor with a 95% CI of $[0.5\ 4.5]\mathrm{ms}/(10\%\ \Delta B_1^+)$. The correlation coefficient after B_1^+ correction was 0.042. The average value of the corrected T_1 map was $990\,\mathrm{ms}$; a 10% change in B_1^+ factor resulted in a $200\,\mathrm{ms}$ change in T_1, i.e., a 20% change in T_1. The relative error in T_1 was twice the relative error in B_1^+, consistent with the derivation in Appendix (Section 3.10.3). This highlights the importance of accurately correcting for B_1^+ inhomogeneities.

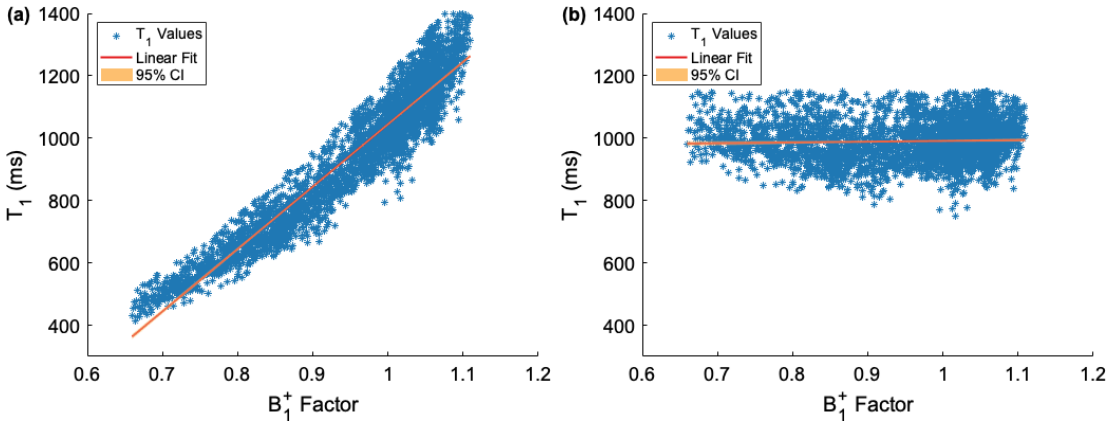


Figure 3.3: Correlation between T_1 and B_1^+ factor for (a) the uncorrected T_1 map and (b) the T_1 map corrected for B_1^+ inhomogeneities from a single slice. A linear fit to the data results in a slope of $2001\,\mathrm{ms}$ with a 95% CI of $[1980\ 2022]\mathrm{ms}$ for the uncorrected T_1 map and a slope of $25\,\mathrm{ms}$ with a 95% CI of $[5\ 45]\mathrm{ms}$ for the B_1^+ corrected T_1 map.

3.4 B_1^+ Map Confounding Factors

3.4.1 Slice Profile Effects

Background

It is necessary to suppress the signal from fat in the B_1^+ map acquisition when using EPI owing to the well-known fat ghost. For this work, two different RF schemes were investigated for the suppression of fat in the B_1^+ map acquisition. The first employed a fat saturation (FS) method [64] by applying a pre-saturation spatially non-selective RF pulse tuned to the fat resonance frequency followed by a strong spoiler gradient to eliminate any transverse fat signal. Immediately after this pulse, the spin magnetisation remaining along the z-axis was excited by a slice-selective RF pulse tuned to the water resonance. The second scheme is known as a 'Water Excitation' (WE) pulse in the Siemens interface and uses a spectrally and spatially selective RF pulse [65] such that only the water signal is excited and the fat signal is not.

Because both pulses are 2D slice-selective, the effect of their slice profile on the accuracy of the acquired B_1^+ maps was studied. The slice profile can be investigated by taking the Fourier transform of the RF pulse. For an infinitely long sinc pulse, the Fourier transform gives a rectangular slice profile, where the FA exciting the spins across the slice is always equal to the FA exciting the spins at slice centre. In practice, RF pulses have a limited time duration, resulting in a deviation of the excitation profile from a perfect rectangle.

For the FS method, the slice selective excitation RF pulse consisted of a sinc function multiplied by a Hamming window, hereafter called a Hamming Windowed Sinc (HWS) (Figure 3.4 (a)). In Fourier space, the resulting slice profile is the convolution of a rectangular pulse with the Fourier transform of the Hamming window function. Consequently, the FA exciting the spins will decrease with the distance from slice centre leading to a non-uniform slice profile (Figure 3.4 (b)). If the FA played out at the slice centre is below $90°$, the free induction decay signal will decrease as one progresses from the slice centre towards the edges of the slice (Figure 3.4 (b) in blue). On the other

hand, if the FA is above $90°$, the signal at slice centre will be smaller than the signal at the slice positions where it reaches $90°$ (Figure 3.4 (b) in green).

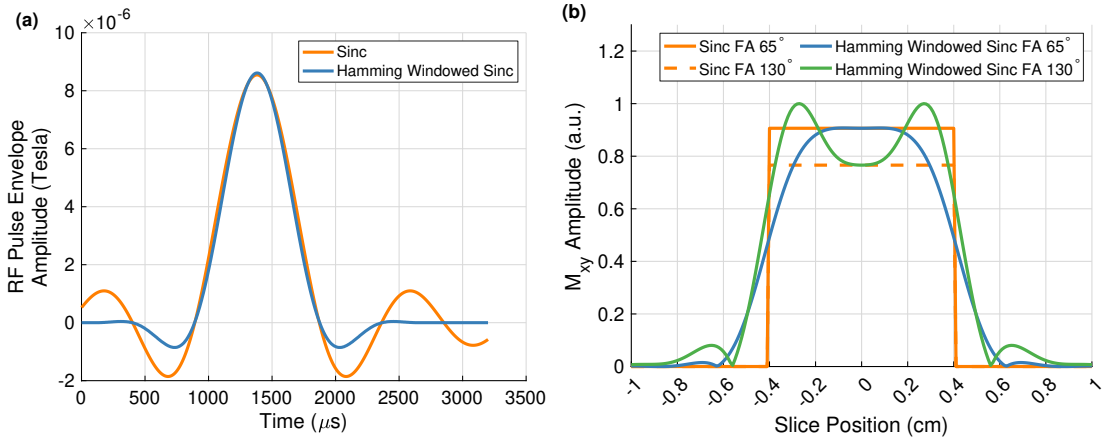


Figure 3.4: (a) Amplitude in Tesla of a Sinc pulse (orange) and a Sinc windowed by a Hamming (HWS) function in (blue) plotted as a function of time. The HWS is used for RF excitation in the Siemens GRE-EPI sequence. (b) Fourier Transform of the Sinc pulse results in a rectangular slice profile for both excitation FAs of $65°$ (orange solid line) and $130°$ (orange dashed line) used in the DAM B_1^+ map. A Fourier transform of the HWS yields a trapezoidal slice profile for the $65°$ excitation FA (blue). The slice profile for a FA of $130°$ (green) achieves maximum signal when the FA decreases to $90°$ (at $-0.27\,\mathrm{cm}$ and $0.27\,\mathrm{cm}$). Magnetisation plotted in arbitrary units (a.u.).

Fat suppression RF Pulses are sensitive to B_1^+ inhomogeneities [66]. Consequently, some residual longitudinal fat magnetisation can persist at the time the HWS RF pulse is applied and result in chemical shift artefacts. In addition, there is T_1 recovery of fat spins between applying the FS pulse and the RF excitation pulse. For the FS scheme employed, the time between the centre of the FS pulse and the centre of the RF excitation pulse was $8.54\,\mathrm{ms}$. With a fat T_1 relaxation at $3\,\mathrm{T}$ of $371\,\mathrm{ms}$ [67], approximately 2.3% of the fat magnetisation will have recovered to equilibrium.

For the WE method, instead of using a RF pulse with a carrier frequency tuned to the fat resonance ($440\,\mathrm{Hz}$ relative to the water signal at $3\,\mathrm{T}$) to saturate the fat signal prior to excitation of the water signal, the excitation RF pulse can be designed so that only the water signal is excited. This is achieved by using a spectral-spatial RF pulse which is spectrally as well as spatially selective [65]. Siemens' implementation for the WE uses three RF pulses with a binomial amplitude ratio of 1:2:1 (Figure 3.5 (a)). It uses an opposed null design where the integral of the signal across the slice position is

zero for the fat signal at $440\,\mathrm{Hz}$ (relative to the water signal) as the real part of the signal has positive and negative lobes that cancel each other to give an overall zero signal (Figure 3.5 (b)). A larger BW without excitation centred at $440\,\mathrm{Hz}$ would be possible by increasing the number of RF pulses [66], with the trade-off of a narrower BW for maximum excitation of water. For Siemens' spectral-spatial pulse, the water passband is $\pm 210\,\mathrm{Hz}$ (FWHM). As a consequence of a broad passband, the null region of the fat signal is very narrow. On-resonance, the fat signal is 2% of the water signal. However, a B_0 inhomogeneity of $+100\,\mathrm{Hz}$ shifts the fat signal into the water passband, resulting in a fat signal that is 31% of the water signal. In conclusion, spectral-spatial pulses are insensitive to B_1^+ inhomogeneities, but they are sensitive to B_0 inhomogeneities.

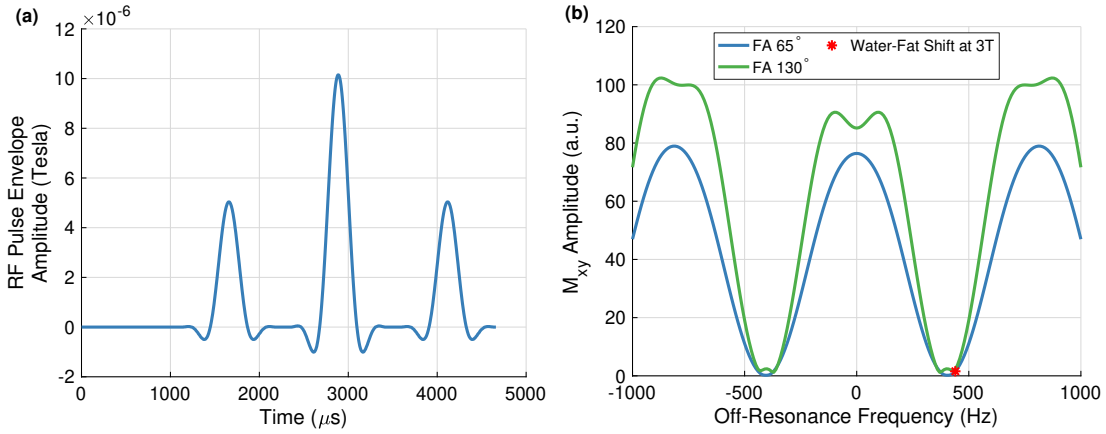


Figure 3.5: (a) Amplitude in Tesla of the Water Excitation (WE) pulse implemented by Siemens used in the GRE-EPI sequence. (b) Transverse magnetisation magnitude for the WE pulse with an excitation FA of $65°$ (blue) and $130°$ (green) as a function of off-resonance in Hz relative to the Larmor frequency. At $3\,\mathrm{T}$, fat is $440\,\mathrm{Hz}$ off-resonance relative to the water signal resulting in a signal close to zero for both FAs (red star). Magnetisation plotted in arbitrary units (a.u.).

Methods

Bloch equations were used to simulate the transverse signal across the slice direction (z) [68]. The two important gradients for Bloch simulation of the transverse signal immediately after RF excitation are the SS gradient and the slice refocusing gradient, applied in the direction of the main magnetic field (z). The Siemens' pulse tool simulator provided RF pulse amplitudes at every $5\,\mu\mathrm{s}$, while the gradients values were sampled

every $10\,\mu s$. Both were interpolated to a common time axis interval of $1\,\mu s$. Figure 3.6 shows that the zeroth moment of the gradient is zero at slice centre for both the HWS and the WE pulses, i.e., the spins are refocused at slice centre.

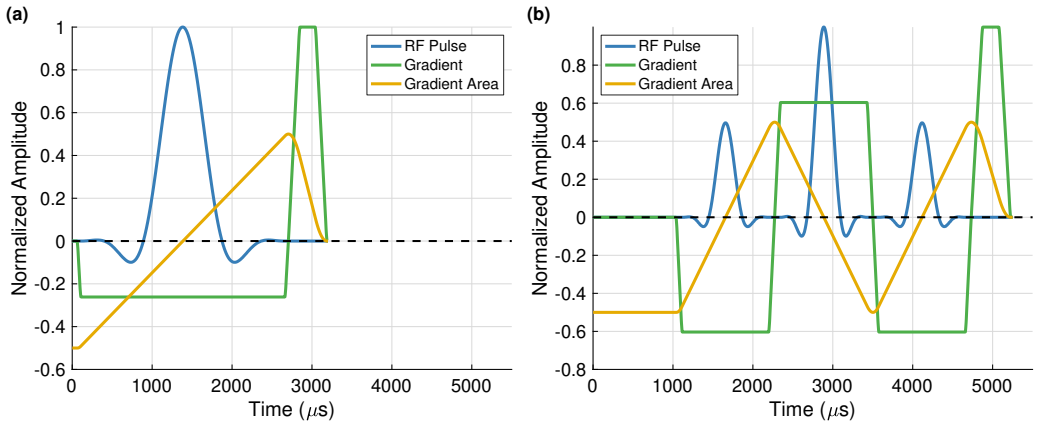


Figure 3.6: Normalised profile of the RF excitation pulse in the temporal domain (blue), the gradient (green) and its corresponding area (yellow) for the (a) Hamming Windowed Sinc and the (b) Water Excitation (WE) RF pulse. Bipolar gradients are used for the WE scheme.

The transverse signal was simulated over a depth of $1.00\,\mathrm{cm}$ extending to either side of the slice centre, in steps of $0.01\,\mathrm{cm}$. The slice thickness was $0.8\,\mathrm{cm}$. The values for T_1 and T_2 relaxation times were $900\,\mathrm{ms}$ and $30\,\mathrm{ms}$, respectively. The relaxation times are a required input to the simulator, but have little effect on the signal calculated immediately after RF excitation in the domain used in this work. To consider the effect of B_0 inhomogeneities on the excitation profile, the signal was Bloch simulated over a range of off-resonance frequencies from $-300\,\mathrm{Hz}$ to $300\,\mathrm{Hz}$ in steps of $100\,\mathrm{Hz}$. The absolute value of the simulated transverse signal, as a function of off-resonance and slice depth, is shown in Figure 3.7 for the FS and the WE schemes. In Figure 3.7, for better visualisation, the absolute signals are shown over a larger spatial and frequency range than were necessary for the simulations.

The DAM B_1^+ mapping [51] takes the ratio between two signals from fully relaxed spins, S_2 and S_1, acquired respectively at nominal FAs 2α and α to estimate the true FA exciting the spins (Equation (3.1)):

$$\frac{S_2(\mathbf{r})}{S_1(\mathbf{r})} = \frac{\sin(2\alpha(\mathbf{r}))}{\sin(\alpha(\mathbf{r}))}\,, \tag{3.1}$$

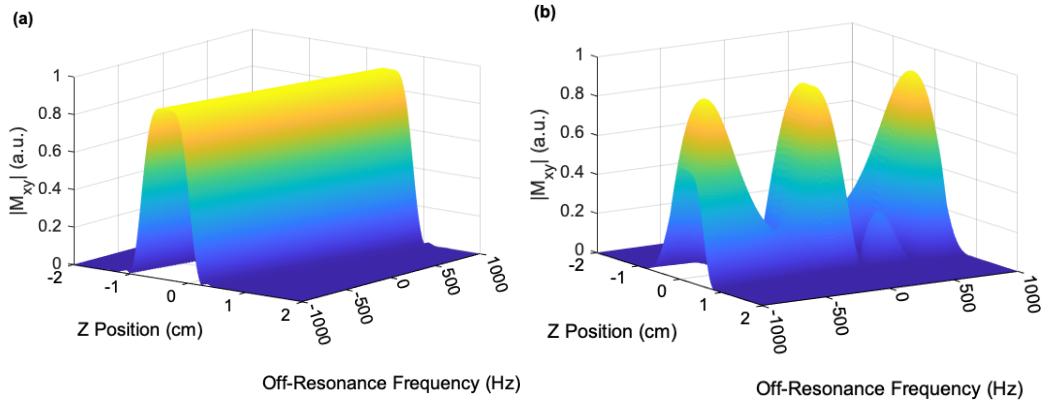


Figure 3.7: (a) Transverse signal in arbitrary units (a.u.) as a function of position along the slice direction in cm and off-resonance frequency in Hz for the (a) Hamming Windowed Sinc (HWS) pulse from the fat saturation scheme and the (b) Water Excitation (WE) RF pulse from the WE scheme. There is a uniform excitation of the spins across the $\pm 1000\,\mathrm{Hz}$ for the HWS, while the WE signal reaches a minimum at the fat-water shift ($440\,\mathrm{Hz}$ at $3\,\mathrm{T}$) and a maximum on-resonance. The frequency is measured relative to the carrier frequency of the RF pulse.

where $\mathbf{r} = (\mathbf{x}, \mathbf{y}, \mathbf{z})$ is the spatial position vector. Taking the ratio of the two signals eliminates the signal dependence on proton density or coil sensitivity. The rule of thumb for full relaxation is to wait a TR larger or equal to $5T_1$ of the tissue of interest. To avoid this long TR, infeasible for a breath-hold acquisition, an EPI readout was adopted. Rearranging trigonometrically Equation (3.1), the FA angle can be mapped by taking the inverse cosine through Equation (3.2).

$$\alpha(\mathbf{r}) = \arccos\left|\frac{S_2(\mathbf{r})}{2S_1(\mathbf{r})}\right| \tag{3.2}$$

In the presence of a non-uniform slice profile, Equation (3.1) (and hence Equation (3.2)) is no longer valid. To correct for slice profile effects the complex transverse signal was integrated across the slice position for each FA, varying between 1° and 360°, and for off-resonance values varying between $-300\,\mathrm{Hz}$ and $300\,\mathrm{Hz}$. The ratio was taken between the absolute value of the integrated complex signal at 2α and α (Equation (3.3)) to generate a B_1^+ look-up-surface (LUS) of the ratio (R) as a function of the FA and the off-resonance frequency.

$$R(\mathbf{r}) = \frac{S_2(\mathbf{r})}{S_1(\mathbf{r})} = \frac{\left|\int dz\,(M_x(z,\Delta f) + iM_y(z,\Delta f)\right|_{2\alpha}}{\left|\int dz\,(M_x(z,\Delta f) + iM_y(z,\Delta f))\right|_{\alpha}} \tag{3.3}$$

The slice profile corrected B_1^+ maps were calculated using the LUS generated off-line. At each pixel, the ratio of the signal acquired at FAs 2α and α was linearly interpolated

on the LUS to obtain the true FA exciting the spins (Figure 3.8). The surface was only interpolated up to the angle of ambiguity, which corresponds to the angle where the first derivative of the ratio changes sign, i.e., where the function is no longer injective. The B_1^+ correction factor is the ratio between the true FA and the nominal FA prescribed at the scanner. It is important to note that for each repetition of the GRE-EPI acquisition, the transmitter frequencies were matched, i.e., the same centre frequency was used for FAs $65°$ and $130°$, and this frequency was also the B_0 map acquisition centre frequency. A flow diagram for the B_1^+ map function corrected for slice profile effects is illustrated in Figure 4.15.

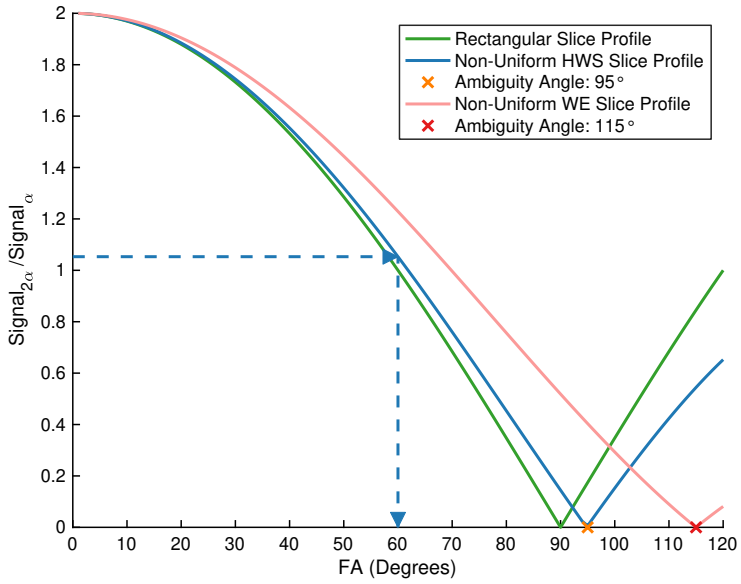


Figure 3.8: Ratio between the signals at 2α and α for three situations: rectangular slice profile (green) and two non-uniform slice profiles using the Hamming Windowed Sinc (HWS) excitation pulse (blue) from the fat saturation scheme and the Water Excitation (WE) pulse (pink) on-resonance. The orange and red crosses represent the ambiguity angles. Without slice profile effects the ambiguity angle is equal to $90°$, with the HWS slice profile the ambiguity angle increases to $95°$, and with the WE it increases to $115°$. The ratio is interpolated (blue dashed arrows) to find the true FA exciting the spins and calculate the B_1^+ correction factor. For the WE pulse, the ratio is linearly interpolated in a look-up-surface (Figure 3.9 (b)) at the off-resonance value given by the B_0 map.

Results

Figure 3.9 shows the B_1^+ LUS for (a) the FS and (b) the WE acquisition schemes. The ratio did not depend on the off-resonance frequency using a HWS excitation pulse

because the pulse is not spectrally selective. Any fat signal not saturated will also be excited into the transverse plane and readout. On the other hand, the WE is a spectrally selective RF pulse. Therefore, the ratio changes as a function of the off-resonance frequency. This required one to know the off-resonance frequency at the time of imaging through the acquisition of a B_0 map.

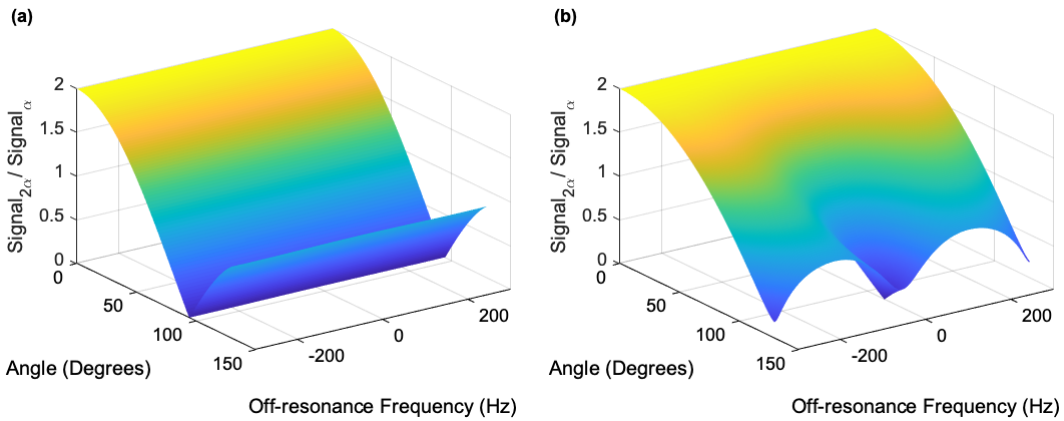


Figure 3.9: Look-up-Surface for B_1^+ correction: ratio between the signal acquired at 2α and α as a function of off-resonance frequency in Hz, ranging from $-300\,\mathrm{Hz}$ to $300\,\mathrm{Hz}$ relative to the Larmor frequency, and FA α varying between $1°$ and $130°$ for the (a) Hamming Windowed Sinc (HWS) and the (b) Water Excitation (WE) pulses. The ratio is constant for the HWS for the plotted range of off-resonance frequencies, while the WE ratio increases as the frequency deviates from on-resonance.

Phantom

Validation of the slice profile correction algorithm was achieved in a phantom by comparing the B_1^+ maps with and without slice profile correction to a gold standard B_1^+ map acquisition (Appendix, Section 3.10.2). Before the correction, the median B_1^+ factor error for the HWS across the 4 slices was -5.2% with a large negative interquartile range (IQR) of [-7.4 -3.7]% (Figure 3.10 (a)). The median B_1^+ factor error was more than two times larger (-12.5%) for the WE RF pulse (Figure 3.10 (b)). Consequently, the T_1 error was larger for the WE RF pulse reaching a median error of 29.0% while the HWS registered a median T_1 error of 10.5% (Figure 3.11). After slice profile correction, the median B_1^+ factor error for the HWS reduced to -1.8% and the median T_1 error to 2.6%. For the WE, the median B_1^+ factor error reduced to 1.9% and the median T_1 error to -5.3%.

B_1^+ maps and corresponding T_1 maps are illustrated in Figure 3.12, before and after

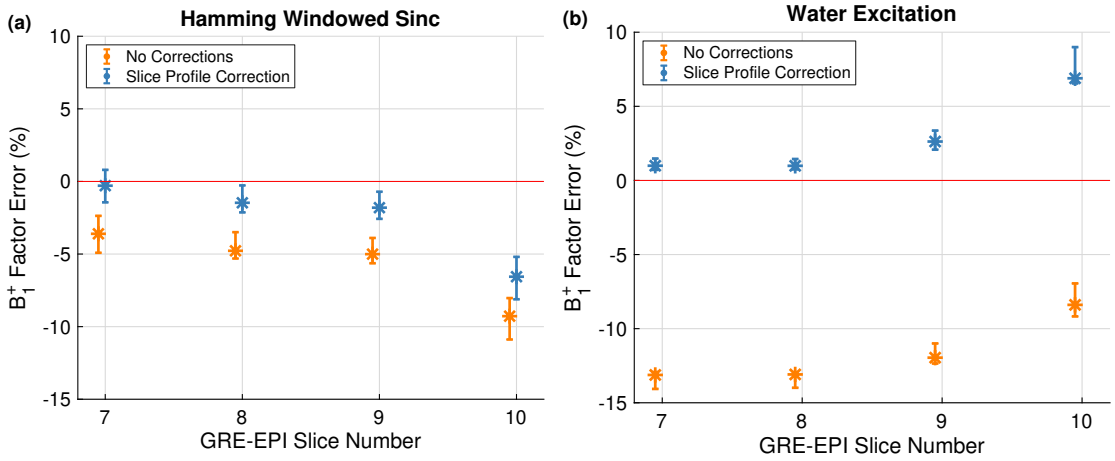


Figure 3.10: Percentage B_1^+ factor error in the *FDA4-T1* phantom B_1^+ map, normalised by the B_1^+ gold standard, without any corrections (orange) and with slice profile correction (blue) for (a) the Hamming Windowed Sinc (HWS) and (b) the Water Excitation (WE) RF pulses for four different GRE-EPI slices, where slice 8 corresponds to the middle slice in the acquisition. The HWS had a median B_1^+ factor error of -5.2% with an interquartile range (IQR) error of [-7.4 -3.7]% before slice profile correction. After slice profile correction, the median B_1^+ factor error was -1.8% with an IQR of [-4.5 -0.5]%. The WE had a median B_1^+ factor error of -12.5% with an IQR of [-13.2 -10.2]% before slice profile correction. After slice profile correction, the median B_1^+ factor error was 1.9% with an IQR of [1.0 4.4]%.

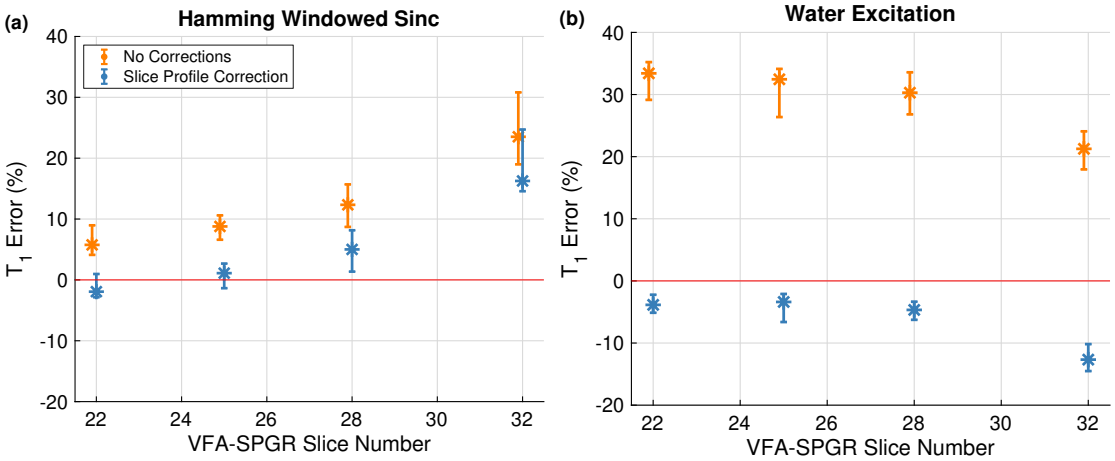


Figure 3.11: Percentage T_1 Error in the *FDA4-T1* phantom T_1 map, normalised by the T_1 gold standard, without any corrections (orange) and with slice profile correction (blue) for the (a) Hamming Windowed Sinc (HWS) and the (b) Water Excitation (WE) RF pulses for four different VFA-SPGR slices, where slice 25 corresponds to the middle slice in the acquisition. The HWS had a median T_1 error of 10.5% with an interquartile range (IQR) error of [6.7 17.5]% before slice profile correction. After slice profile correction, the median T_1 error was 2.6% with an IQR of [-0.4 10.2]%. The WE had a median T_1 error of 29.0% with an IQR of [23.6 33.9]% before slice profile correction. After slice profile correction, the median T_1 error was -5.3% with an IQR of [-7.8 -3.3]%. Note that the SPGR acquisition had 48 slices while the GRE-EPI had only 15 slices for the same FoV. The centre of slice 25 in the SPGR coincided with the centre of slice 8 in the GRE-EPI acquisition.

slice profile correction for the WE RF pulse. The absence of structure in the B_1^+ maps due to the vials, which have a range of T_1 values from $367\,\mathrm{ms}$ to $1699\,\mathrm{ms}$, confirmed that the B_1^+ mapping protocol is T_1 insensitive. Without slice profile correction, there was a clear underestimation of B_1^+ factor which resulted in T_1 overestimation. Moreover, concentrating on the vials within the red ROI (Figure 3.12), representing physiological liver tissue T_1s, the estimated T_1s were almost all above $1300\,\mathrm{ms}$ without slice profile correction. Visually, the FS scheme did not present such a striking overestimation of T_1, but without slice profile correction the median T_1 value was still overestimated by 10.5%.

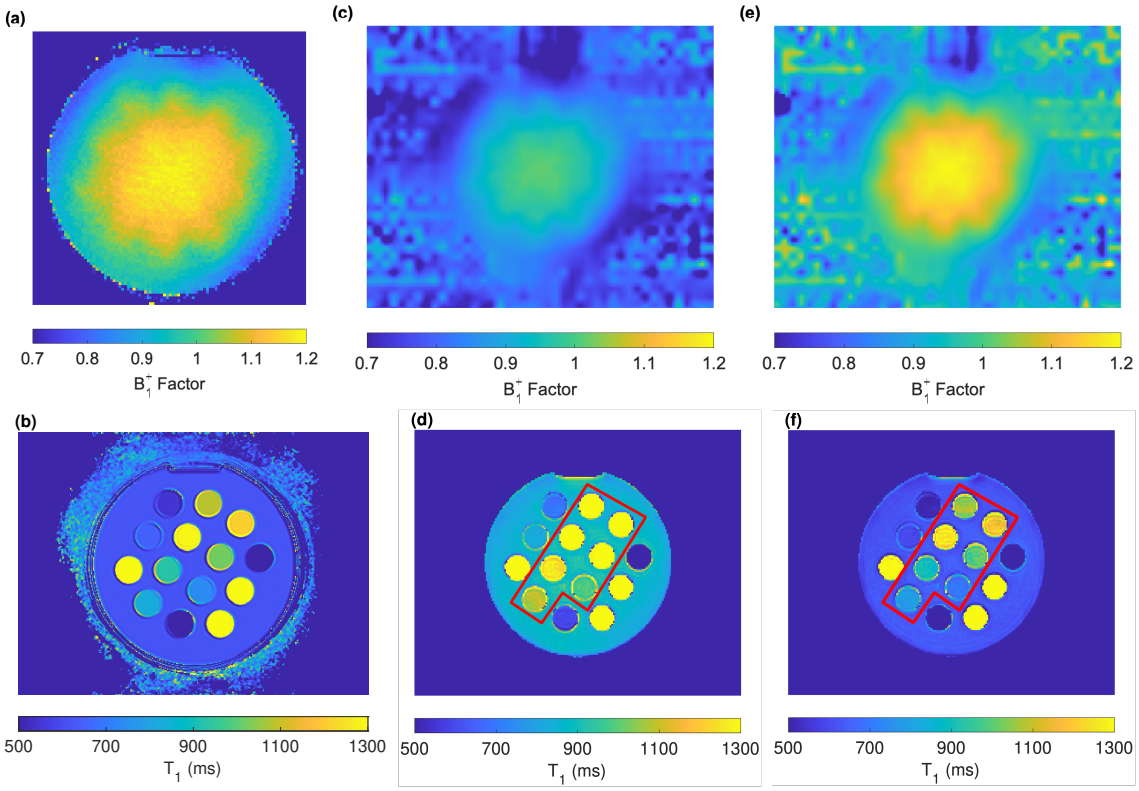


Figure 3.12: Gold Standard (a) B_1^+ map and (b) T_1 map. B_1^+ map for the Water Excitation RF pulse (c) without and (e) with slice profile correction. There is a large underestimation of B_1^+ factor without slice profile correction. Corresponding T_1 maps using the B_1^+ maps (d) without and (f) with slice profile correction to correct the SPGR FAs. Red ROI, containing vials with physiological liver T_1s ($740\,\mathrm{ms}$-$1292\,\mathrm{ms}$), highlighting the difference in T_1 between the two maps, with almost all vials saturated without slice profile correction.

In Vivo

Figure 3.13 shows the impact of slice profile correction on *in vivo* T_1 maps corrected for B_1^+ inhomogeneities using a B_1^+ map acquired with the FS scheme. On average, the B_1^+ map was 3% higher and the T_1 map was 7% lower than the respective values before slice profile correction.

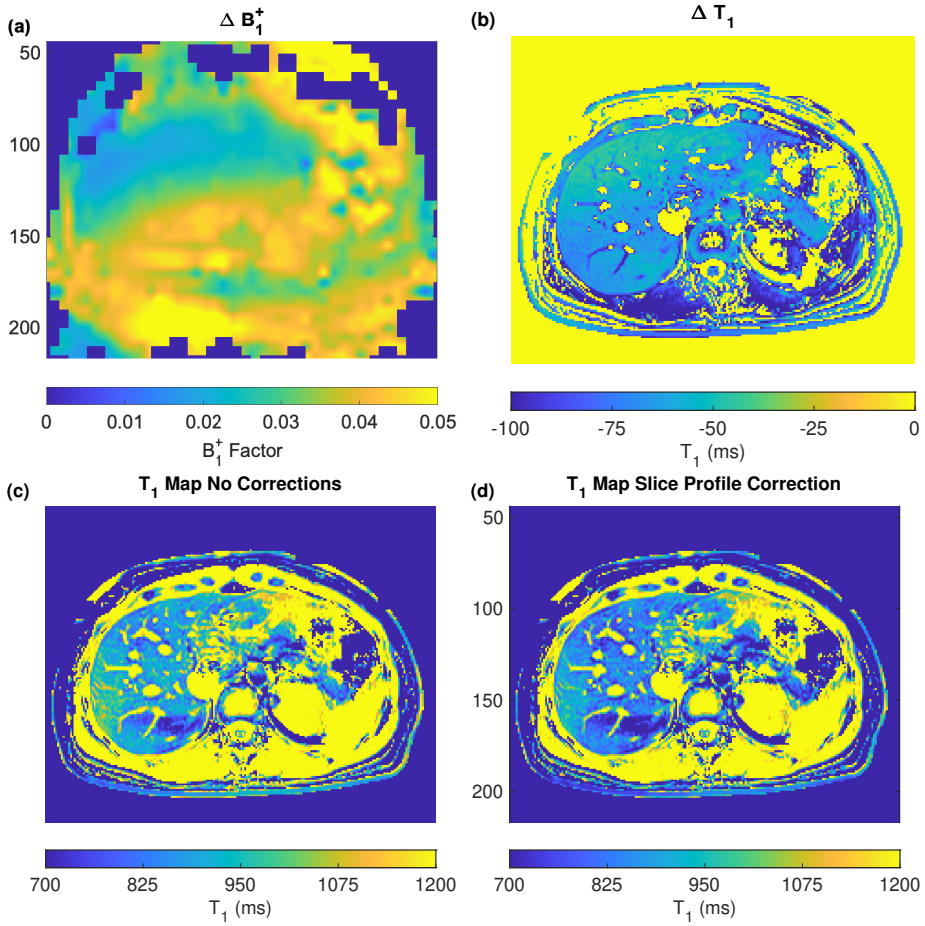


Figure 3.13: (a) Difference between B_1^+ maps using the Hamming Windowed Sinc RF pulse with and without slice profile correction, showing on average a difference of 3% in the liver. (b) Corresponding T_1 map difference. (c) T_1 Map using a B_1^+ map without correcting for slice profile. (d) T_1 Map using a B_1^+ map with slice profile correction. Three circular ROIs of $46\,\mathrm{pixels}$ placed in vessel-free regions of the liver resulted in a mean T_1 of $912\,\mathrm{ms}$ before slice profile correction and $851\,\mathrm{ms}$ after slice profile correction. The dark blue band in rows 160-170 in (d) corresponds to fat chemical shift affecting the B_1^+ map and corresponding to a bright yellow band in (a). This is absent for the Water Excitation T_1 map in Figure 3.14.

Figure 3.14 shows the impact of slice profile correction on *in vivo* T_1 maps corrected for B_1^+ inhomogeneities using a B_1^+ map acquired with the WE RF pulse. On average, the B_1^+ map was 17% higher after slice profile correction and the T_1 map was 44% lower.

Correcting for slice profile when using the WE RF pulse is crucial as confirmed by the significant reduction in T_1 values towards those expected in healthy liver tissue [69].

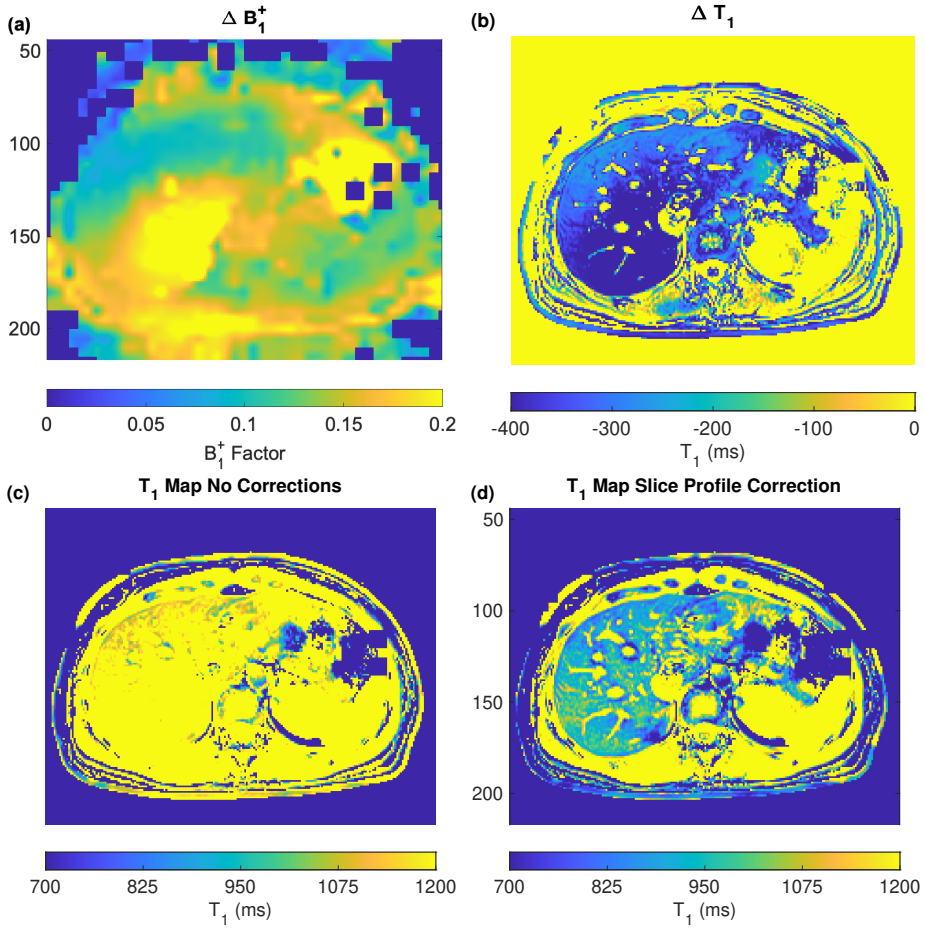


Figure 3.14: (a) Difference between B_1^+ maps using the Water Excitation RF pulse with and without slice profile correction, with B_1^+ factor differences in the liver of on average 16%. The differences are higher in the posterior part of the liver where the B_1^+ factor is larger than 1 as the slice profile has large deviations from a rectangular slice profile. (b) Corresponding T_1 map difference. (c) T_1 Map using a B_1^+ map without correcting for slice profile showing an absurdly high T_1 for a healthy volunteer. (d) T_1 Map using a B_1^+ map with slice profile correction. Three circular ROIs of $46\,\mathrm{pixels}$ placed in vessel-free regions of the liver resulted in a mean T_1 of $1377\,\mathrm{ms}$ before slice profile correction and $961\,\mathrm{ms}$ after slice profile correction.

In conclusion, when using a 2D multi-slice GRE-EPI acquisition for B_1^+ mapping, with either the FS or the WE scheme, slice profile effects can be accounted for by constructing a LUS based on Bloch simulations using the specific RF excitation pulse. The magnitude of the error in the T_1 maps due to slice profile effects depended on the RF excitation pulse as well as the B_1^+ factor, reaching median T_1 errors in the phantom of 10.5% for the HWS and 29% for the WE pulse.

3.4.2 B_0 Gradient Through Slice Dephasing

Background

The liver is the largest internal organ in the body. Situated below the lungs, the liver dome which is closest to the diaphragm is susceptible to large B_0 inhomogeneities from the air-tissue interface, reaching values as large as 200 Hz. The inhomogeneities decrease as the liver extends towards the kidneys. The large variations in B_0 between the dome and the inferior part of the liver create a B_0 gradient in the slice direction when acquiring multiple slices covering the whole liver FoV. The effect of the B_0 gradient on the B_1^+ map is explored in this section.

Considering first the case of a homogeneous B_0 field, there is a residual phase roll that depends on the magnitude of the excitation FA. For small angles, a refocusing SS gradient with half the area of the SS gradient will refocus the magnetisation dephased by the SS gradient and result in an approximately null phase for the transverse magnetisation [31]. However, for angles above 30° the phase accrued during the SS gradient is not completely refocused by the refocusing gradient, resulting in a residual phase roll across the slice (Figure 3.15). The degree of phase accrual will depend on the shape of the slice profile and the slice thickness. The further from slice centre and the larger the angle, the greater the magnitude of the phase accrued. For example, a 130° RF excitation pulse will undergo more dephasing compared to a 65° RF pulse. In summary, the phase varies non-linearly with slice position and excitation FA when the FA leaves the region where the small angle approximation (i.e., FA $\approx \sin(\text{FA})$) can be applied.

During RF excitation, B_0 inhomogeneities along the slice direction impose an additional dephasing of the spins on top of the dephasing from the SS gradient. The dephasing due to B_0 inhomogeneities is not rephased by the slice refocusing gradient. The signal from each RF excitation pulse considering slice profile is given by the integral of the complex signal across the slice position. The magnitude of the transverse signal is unaffected by a constant B_0 offset or a B_0 varying as a function of position through slice (Figure 3.16 (a)). In contrast, a linear B_0 gradient changes the phase behaviour as a function of

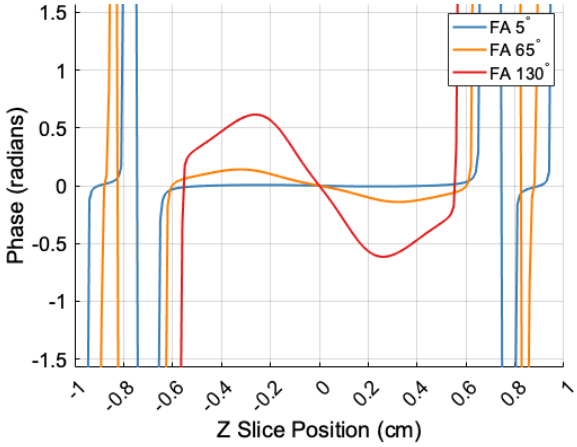


Figure 3.15: Phase of the transverse magnetisation for a Hamming Windowed Sinc RF excitation pulse with FAs of $5°$ (blue), $65°$ (orange) and $130°$ (red) on-resonance. For a $5°$ FA, the phase is very close to zero as a slice refocusing gradient equal to 50% of the magnitude of the slice-select gradient nearly perfectly refocuses the phase accrued by the slice-select gradient. For larger angles, such as $65°$ and $130°$, there is a phase roll that survives the refocusing gradient and this increases with the magnitude of the FA.

distance from the slice centre (Figure 3.16 (b)).

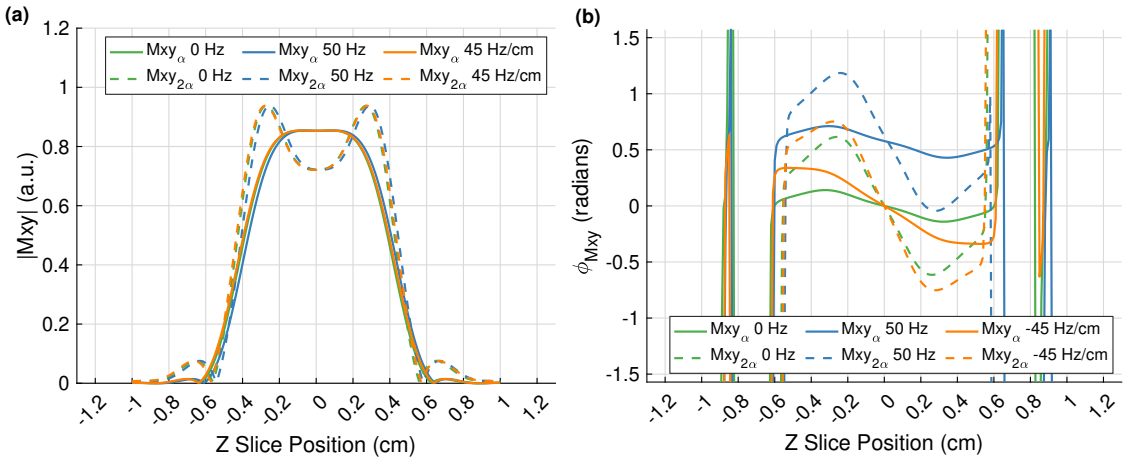


Figure 3.16: Transverse magnetisation in arbitrary units (a.u.) for RF excitation FAs of α equal to $65°$ (solid line) and 2α equal to $130°$ (dashed line) without off-resonance (green), a constant off-resonance of $50\,\mathrm{Hz}$ (blue) and a negative linear gradient in B_0 across the slice of $-45\,\mathrm{Hz/cm}$ (orange). The absolute value of the transverse magnetisation (a) is not affected by these off-resonance values across the slice position. All the lines have the same magnitude, with the blue line shifted horizontally as the frequency is used to encode spatial position in MRI. On the other hand, the phase (b) of the transverse magnetisation varies across the slice profile. For $0\,\mathrm{Hz}$ off-resonance, the phase is larger for 2α (dashed green line) compared to α (solid green line). A constant B_0 off-resonance shifts the phase by a constant offset (blue lines). A linear gradient in B_0 imposes a linear gradient on the phase with a steepness proportional to the linear B_0 gradient. These plots were elaborated assuming a B_1^+ factor of 1. The signals correspond to a time moment immediately after RF excitation.

Consider the following model for the complex signal of a large FA at time TE. To a first approximation, the phase is composed of three different terms (Equation (3.4)): the phase accrued due to the SS gradient that was not refocused ($\phi_{G_z}(z)$); a global phase from a constant off-resonance (ϕ_{B_0}) and a phase that varies with slice position due to a B_0 gradient ($\nabla_z B_0(z)$) across the slice ($\phi_{\nabla_z B_0}(z)$).

$$\phi_{Total}(z) = \phi_{G_z}(z) + \phi_{B_0} + \phi_{\nabla_z B_0}(z) \tag{3.4}$$

The integral of the transverse signal across the slice thickness is given by Equation (3.5), where a(z) is the magnitude of the signal as a function of slice position and the phase terms are those in Equation (3.4).

$$S = |e^{i\phi_{B_0}} \int dz \left(a(z) e^{(i\phi_{G_z}(z) + i\phi_{\nabla_z B_0}(z))} \right)| \tag{3.5}$$

A constant B_0 off-resonance for all the z positions introduces an overall offset in the phase as seen in Figure 3.16 (b) by the blue lines. Because it does not depend on the z position, it does not affect the absolute value of the integrated signal. On the other hand, the B_0 gradient term will impact the absolute value of the integrated signal. Even though the B_0 gradient term is equal for FAs of α and 2α, the B_0 gradient will affect the integrated signal of the 2 FAs differently (Figure 3.16) because of their different slice profiles (the $a(z)$ term) and SS phase accrual (term $\phi_{G_z}(z)$). Since the B_1^+ factor is calculated from the ratio of the integrated complex signal from 2α and α excitation FAs, changes in the ratio due to the B_0 gradient will cause a change in the B_1^+ factor. It is important to note that both the term $a(z)$ and the term $\phi_{G_z}(z)$ will change with the B_1^+ factor (Figure 3.17). Consequently, it is hypothesised that the error in estimating the B_1^+ factor will depend on the magnitude of the B_1^+ factor. Furthermore, free precession of the signal until time TE will increase the z-dependent phase accrued due to the B_0 gradient, amplifying the dephasing effect that was already present at the end of the RF excitation pulse.

In this section, the effect of a B_0 gradient across the slice position on the B_1^+ factor is described. Simulations using linear B_0 gradients across the slice were used to estimate

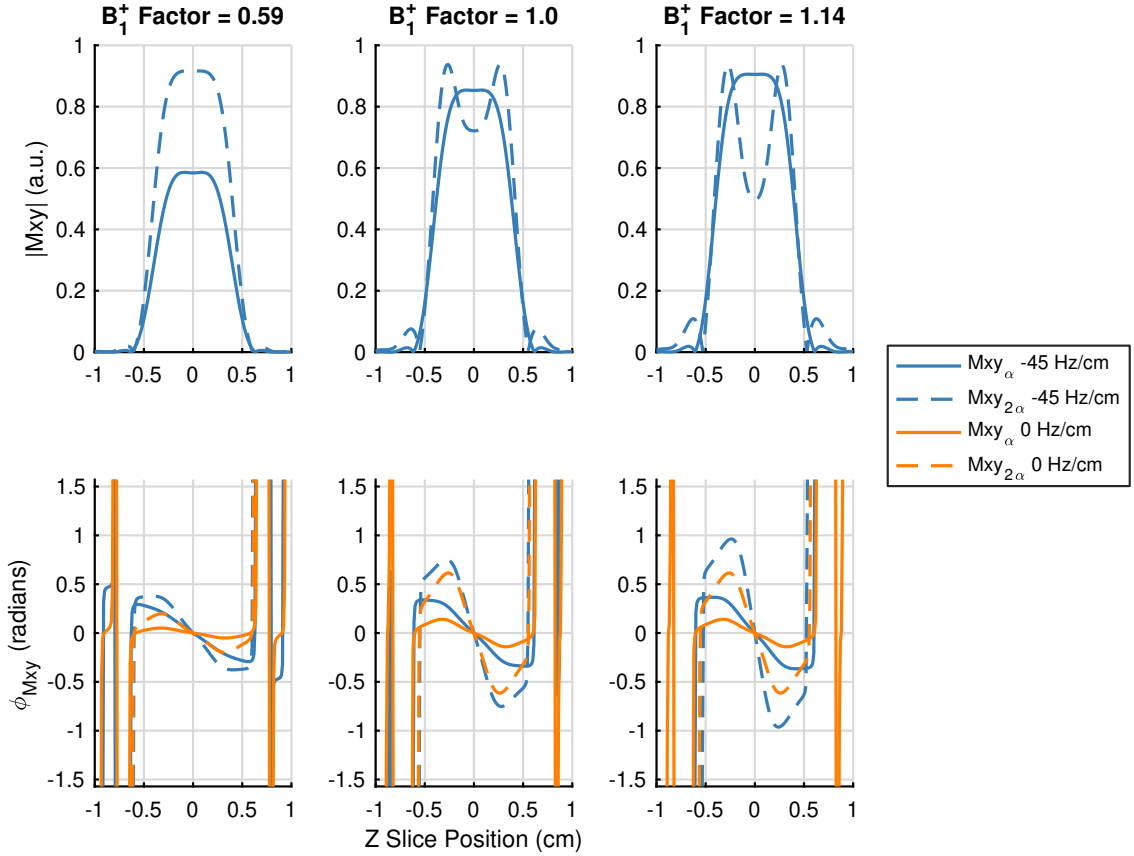


Figure 3.17: Magnitude (first row) and phase plots (second row) for three different B_1^+ factors of 0.59 (first column), 1.0 (second column) and 1.24 (third column) at excitation FAs of α (solid lines) and 2α (dashed lines) for α equal to $65°$ with a B_0 gradient of $-45\,\mathrm{Hz/cm}$ (blue) and $0\,\mathrm{Hz/cm}$ (orange). The transverse magnetisation slice profile changes considerably as the B_1^+ factor increases, with the two peaks for 2α and B_1^+ factor of 1 and 1.24 corresponding to a FA of $90°$. The phase accrual becomes larger as either the FA value or the B_1^+ factor increases. The signals correspond to a time moment immediately after RF excitation.

the error introduced in the B_1^+ map when neglecting this effect. Validation of the predictions were conducted both in phantom and *in vivo*.

Methods

The correction for the B_0 gradient through slice effect on the phantom and *in vivo* data was based on Bloch simulations [68] of the signal including varying off-resonances in the slice direction. To do so, it was necessary to determine the B_0 off-resonance value for each spatial position. The B_0 map was acquired at slice centre positions matching the B_1^+ map acquisition, i.e., at every $1\,\mathrm{cm}$. To determine the B_0 off-resonances at a $1\,\mathrm{mm}$ spatial resolution for each pixel in the B_1^+ map, the B_0 values along the slice direction

with liver tissue were fit to a cubic spline with linear extrapolation [70]. The number of knots in the spline fit was equal to the total number of slices containing liver divided by three and rounded down to the nearest integer. The transverse signal immediately after the RF excitation pulse, calculated with the interpolated off-resonance, was propagated until time TE including free precession at the corresponding off-resonance, and T_1/T_2 relaxation with values of $900\,\mathrm{ms}$ and $30\,\mathrm{ms}$, respectively. Lastly, the complex signal at time TE for each slice was integrated across the slice dimension.

The Bloch simulation implementation details included interpolation of both the SS gradient and the RF pulse to the same time interval of $1\,\mu\mathrm{s}$. The RF pulse was normalised by its area and multiplied by the B_1^+ factor and the nominal FA. Siemens uses the same RF pulse duration and increases the amplitude of the RF pulse for increasing FA values. A T_1 value of $900\,\mathrm{ms}$ and a T_2 value of $30\,\mathrm{ms}$ were used and are close to the average T_1 and T_2 liver values for a healthy population [18], [71]. However, the ratio between the signals at 2α and α during the time between RF excitation and time TE should not be affected by T_1 or T_2 relaxation, since both signals undergo the same relaxation. This insensitivity to relaxation times was confirmed using a Bloch simulation with a linear off-resonance of $20\,\mathrm{Hz/cm}$ and calculating the signal ratio between FAs 2α and α and the corresponding B_1^+ factor. The difference in B_1^+ factors between a T_1 of $1500\,\mathrm{ms}$ or $500\,\mathrm{ms}$ (fixing T_2 to $45\,\mathrm{ms}$) was less than 2×10^{-4}, and the difference in B_1^+ factors between a T_2 of $45\,\mathrm{ms}$ or $5\,\mathrm{ms}$ (fixing T_1 to $1500\,\mathrm{ms}$) was less than 2×10^{-3}. The magnitude of these differences were negligible when using the B_1^+ map to correct the SPGR FAs in the T_1 map calculation. In addition, to test the sensitivity to the step size along the slice direction, the difference in the B_1^+ factor was calculated for step sizes of $1\,\mathrm{mm}$ and $0.1\,\mathrm{mm}$. The difference was less than 10^{-5} and thus a $1\,\mathrm{mm}$ step size was chosen to achieve shorter computation times. Finally, the spatial extension over which the B_0 gradient was simulated along the slice direction was calculated for two cases: between $-2\,\mathrm{cm}$ and $2\,\mathrm{cm}$ and between $-1\,\mathrm{cm}$ and $1\,\mathrm{cm}$, bearing in mind that the distance between adjacent slice centres is $1\,\mathrm{cm}$. The difference in B_1^+ factors was

less than 0.5×10^{-3}, thus a spatial extent of $-1\,\mathrm{cm}$ to $1\,\mathrm{cm}$ was adopted.

Simulations

To study the effect of changes in B_0 across the slice position on the B_1^+ map calculation, the B_0 gradient was varied between $-45\,\mathrm{Hz/cm}$ and $45\,\mathrm{Hz/cm}$, in steps of $5\,\mathrm{Hz/cm}$. In the Bloch simulation of the signal at $2\alpha/\alpha$ of $130°/65°$, three different true B_1^+ factors of 0.59, 1 and 1.15 were used. Here the extreme values correspond to the range of liver B_1^+ factors observed *in vivo* at $3\,\mathrm{T}$ [61]. The ratio between the two transverse signals was interpolated on a LUS (Figure 3.9) to find the excitation FA α. The estimated B_1^+ factor was the ratio between the interpolated FA and the nominal FA of $65°$. The difference between the estimated B_1^+ factor and the true B_1^+ factor gave the error in B_1^+ factor due to changes in the ratio from off-resonance variations across the slice direction.

Phantom and *In Vivo*

The same phantom acquisition used to validate the slice profile correction was used to validate the B_0 correction. For data acquired in phantom or *in vivo*, a NLLS fit was used to find the B_1^+ factor corresponding to the Bloch simulated ratio that best matched the ratio between the images acquired at FA $130°$ and FA $65°$ for each pixel (Equation (3.6)). A flow diagram for the B_1^+ map function with corrections for slice profile effects and B_0 gradient through slice dephasing is illustrated in Figure 4.16.

$$\arg\min_{\{B_1^+\}} (Ratio_{acq} - Ratio_{Sim}(B_1^+, TE, B_0))^2 \tag{3.6}$$

Results

Simulations

Figure 3.18 (a) shows that the ratio between the signals at 2α and α is lower, immediately after the RF pulse excitation, for a negative linear B_0 gradient of $-45\,\mathrm{Hz/cm}$ compared to the ratio simulated with either a constant off-resonance of $50\,\mathrm{Hz}$ or $0\,\mathrm{Hz}$. Furthermore, the ratio decreases as the TE increases. On the other hand, a positive linear B_0 gradient of $45\,\mathrm{Hz}$ results in a larger ratio than on-resonance and the ratio increases as the TE increases (Figure 3.18 (b)).

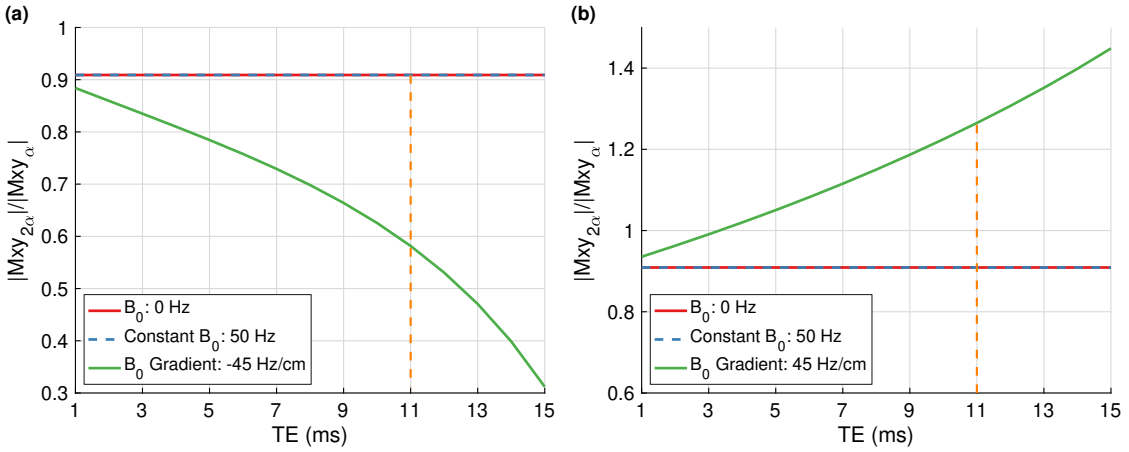


Figure 3.18: Variation in the ratio of the transverse signal at FAs of 2α and α, used for the B_1^+ factor calculation, as a function of increasing TEs. The ratio does not change with TE for a constant B_0 off-resonance (blue dashed line) relative to the on-resonance ratio (solid red line). (a) In the presence of a negative linear gradient in B_0 of $-45\,\mathrm{Hz/cm}$ (green), the ratio decreases monotonically as the spins free-precession time increases. For a TE of $11\,\mathrm{ms}$, used in the B_1^+ acquisition protocol, the ratio is predicted to decrease to 64% of the on-resonance ratio. (b) Conversely, for a positive linear gradient in B_0 of $45\,\mathrm{Hz/cm}$ (green) the ratio increases monotonically as the spins free-precession time increases. For a TE of $11\,\mathrm{ms}$, the ratio is predicted to increase to 139% of the on-resonance ratio. These calculations assumed a B_1^+ factor of 1 with $\alpha/2\alpha$ equal to $65°/130°$.

For the GRE-EPI sequence, the SS gradient was equal to $-5.96\,\mathrm{mT/m}$ which is equivalent to $-2.54\,\mathrm{kHz/cm}$. On-resonance, the phase roll for 2α is larger than α (dashed versus solid orange line in Figure 3.19 (b)). In the presence of a negative off-resonance gradient (blue lines in Figure 3.19 (b)), the pre-existing phase roll is reinforced. The phase difference for the two peaks of the absolute transverse magnetisation for the 2α pulse is 0.92π, very close to the condition for complete destructive interference. This destructive interference reduces the overall integrated complex signal for the 2α pulse. In contrast, for the α pulse the largest contribution comes from a region localised around the slice centre where the phase roll remains small. Consequently, the ratio is less than the ratio on-resonance. The ratio decreases as a function of TE given the signal from the 2α pulse has a larger dephasing, which can be thought of as a shorter T_2^*, thus decaying faster than the signal at FA α. When the off-resonance gradient is of opposite sign to the SS gradient, the phase roll for the 2α pulse is smaller near the slice centre compared to on-resonance (green dashed line versus orange dashed line in Figure 3.19 (b)), resulting in a larger

integrated complex signal for 2α. The phase roll for the α pulse is similar in magnitude, but opposite in sign to the case of the negative off-resonance gradient. The overall effect of a positive off-resonance gradient is an increased ratio compared to on-resonance.

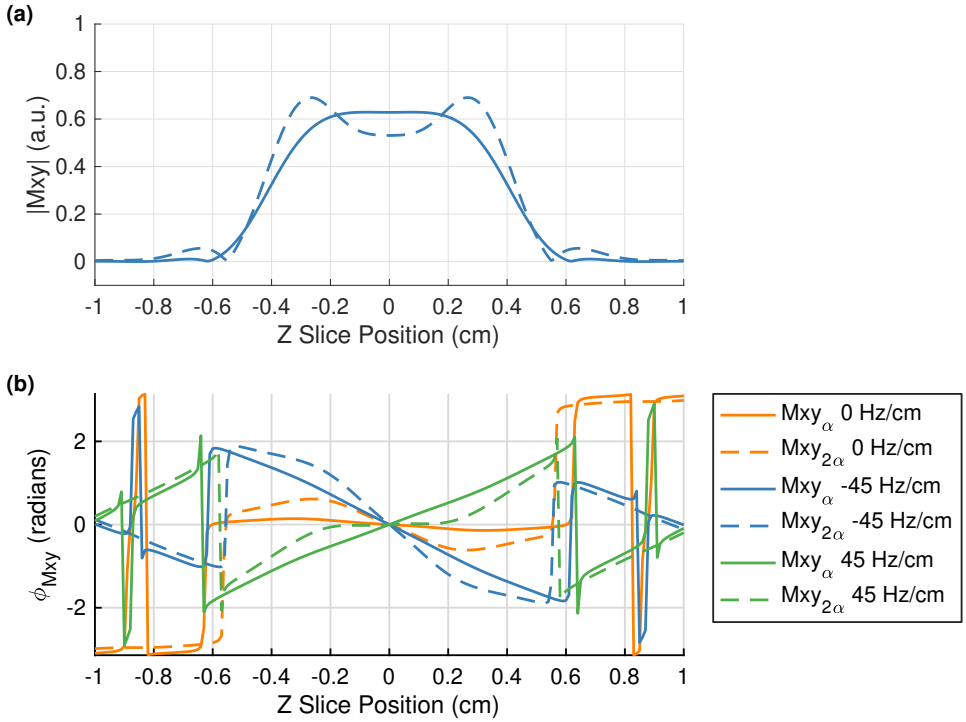


Figure 3.19: (a) Absolute transverse signal for α (blue solid line) and 2α (blue dashed line) for a B_0 gradient in the slice direction of $-45\,\mathrm{Hz/cm}$. (b) Phase in radians for the transverse signal on-resonance (orange) at time TE, with a negative B_0 gradient of $-45\,\mathrm{Hz/cm}$ (blue) and a positive B_0 gradient of $45\,\mathrm{Hz/cm}$ (green). The phase accrual for 2α (dashed orange line) is larger than for α (solid orange line) on-resonance. A negative B_0 gradient across the slice position reinforces the dephasing of the negative slice-select gradient, while a positive B_0 gradient results in a phase accrual in the opposite direction.

A decrease in the ratio induced by the negative B_0 gradient mimics the situation where the B_1^+ factor is larger than 1. Failure to model the varying B_0 across the slice position will result in a B_1^+ factor overestimation (positive error in Figure 3.20) and consequently an underestimation of T_1. Conversely, an increase in the $2\alpha/\alpha$ ratio occurs when the B_0 gradient is of opposite sign to the SS gradient, leading to underestimation of the B_1^+ factor (negative error in Figure 3.20) and T_1 overestimation.

Phantom

Figure 3.21 shows the B_1^+ factor error for the *FDA4-T1* phantom, measured against a B_1^+ gold-standard 3D DAM, before (blue) and after (green) applying the through

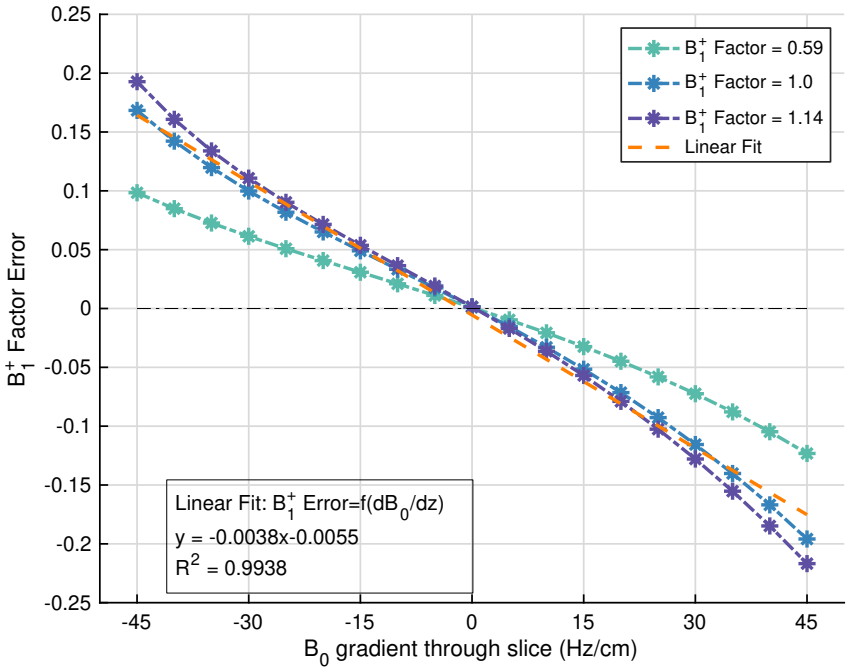


Figure 3.20: B_1^+ factor error as a function of B_0 gradient through slice for three different B_1^+ factors of 0.59 (green), 1.0 (blue) and 1.14 (purple). The error increases for larger absolute B_0 gradients as well as increasing B_1^+ factors. A linear fit (orange dashed line) to the blue curve shows that at a $B_1^+ = 1$, the error in B_1^+ factor scales by approximately 3.8% per every 10Hz/cm variation in B_0 along the slice direction.

slice off-resonance corrections for four different slices. The median error decreased from -1.8% to 0.01%. The IQR using only slice profile correction was [-4.5 -0.5]% and it became approximately three times tighter, [-0.8 0.8]%, after including corrections for the B_0 gradient through slice. Using the WE pulse, including through slice off-resonance corrections resulted in a marginal improvement in the B_1^+ factor error from 1.9% to 1.5%. The smaller uncertainty in the B_1^+ maps with the WE pulse compared to the HWS is noteworthy as illustrated by the smaller error bars in Figure 3.21 (b) compared to (a).

The largest B_1^+ factor error without B_0 gradient through slice correction of -6.6% (blue error bars) occurred for slice 10, which corresponded to the slice with the largest B_0 variations as a function of slice position as shown in Figure 3.22. This slice had the largest reduction in B_1^+ factor error after B_0 gradient through slice correction, reaching a median error of -0.6%.

Figure 3.23 shows the error in T_1 values for the *FDA4-T1* phantom, measured against an IR SE gold standard T_1 method, before and after applying the through slice

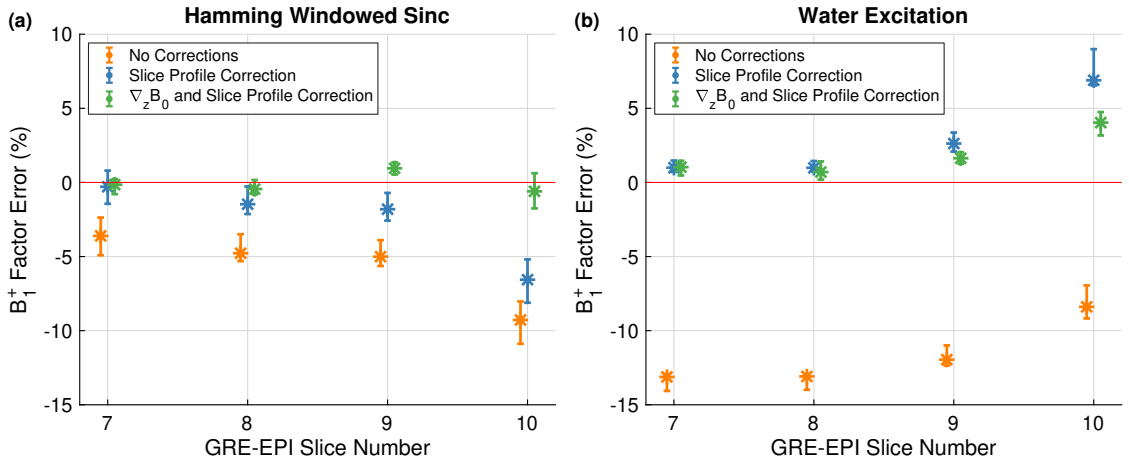


Figure 3.21: B_1^+ factor error in the *FDA4-T1* phantom B_1^+ map, normalised by the B_1^+ factor gold standard value, without any corrections (orange), with slice profile correction (blue) and with B_0 gradient through slice correction added to the slice profile correction (green) for four different GRE-EPI slices, where slice 8 corresponds to the middle slice. (a) The Hamming Windowed Sinc RF pulse had a median B_1^+ factor error of -1.8% with an interquartile range (IQR) of [-4.5 -0.5]% using only slice profile correction. Including the correction for off-resonance variations through slice, the B_1^+ factor error decreased to 0.01% [-0.8 0.8]%. (b) The Water Excitation RF pulse had a median B_1^+ factor error of 1.9% and IQR of [1.0 4.4]% using only slice profile correction; including the correction for off-resonance variations through slice, the B_1^+ factor error decreased to 1.5% [0.7 2.5]%.

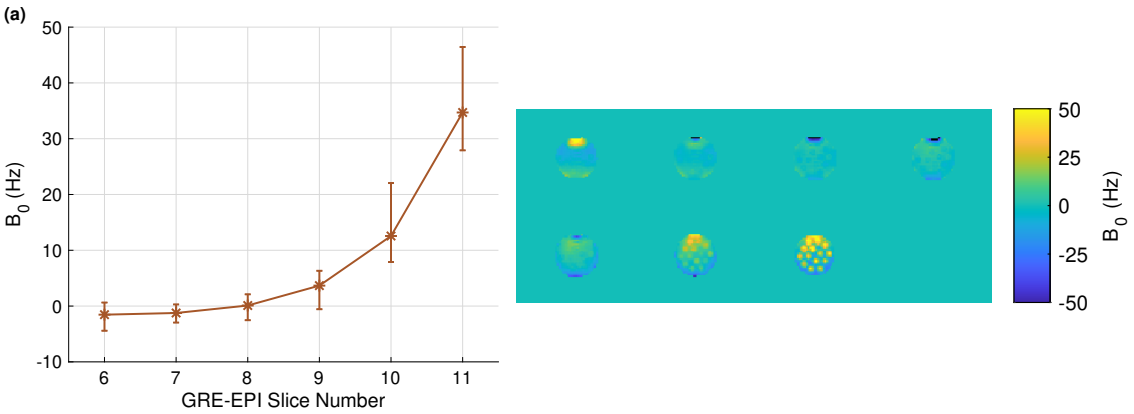


Figure 3.22: Plot of the median B_0 in Hz for slices 6 until 11 in the GRE-EPI acquisition of the *FDA4-T1* phantom. The error bars indicate the associated interquartile range. There is a sharp increase in the off-resonance values as the slice number increases. Slice 10 signal was susceptible to large B_0 variations through slice, as indicated by the steepness of the B_0 line at this position. There was a 9Hz increase in off-resonance between slice 9 and slice 10 and a $22\,\mathrm{Hz}$ increase between slice 10 and slice 11. (b) B_0 maps for slices 5 to 11, with large off-resonance values for slices 10 and 11 as these slices are close to the end of the vials.

off-resonance corrections for 4 VFA SPGR slices matching the GRE-EPI slice locations plotted in Figure 3.21. The median T_1 error decreased from 2.6% to -0.3%, with the sign of the error opposite to the B_1^+ factor error. The IQR using only slice profile correction

was [-0.5 10.2]% and decreased by more than a factor of 2, [-2.5 2.1]%, after including corrections for the B_0 gradient through slice. Slice 10 in the GRE-EPI corresponded to slice 32 in the VFA-SPGR acquisition. This slice had the largest median B_1^+ factor error of -6.6% before B_0 gradient through slice correction and consequently, it also had the largest median T_1 error of 16.3% as illustrated in Figure 3.23 (a) by the blue error bars for slice 32. This error was even larger than the T_1 error of slices 22, 25 and 28 without any corrections, illustrated by the orange error bars. After applying the B_0 gradient through slice correction, the T_1 error decreased by approximately 4.5% compared to only using slice profile correction, emphasising the necessity of developing and applying a B_0 gradient through slice correction. The WE B_1^+ map also showed a decrease in T_1 error after including corrections for the B_0 gradient through slice (green error bars in Figure 3.23 (b). However, there was still a residual negative T_1 bias of -3.9% that propagated from the B_1^+ map. Because of this residual bias, the subsequent confounding factors were investigated using only the FS scheme.

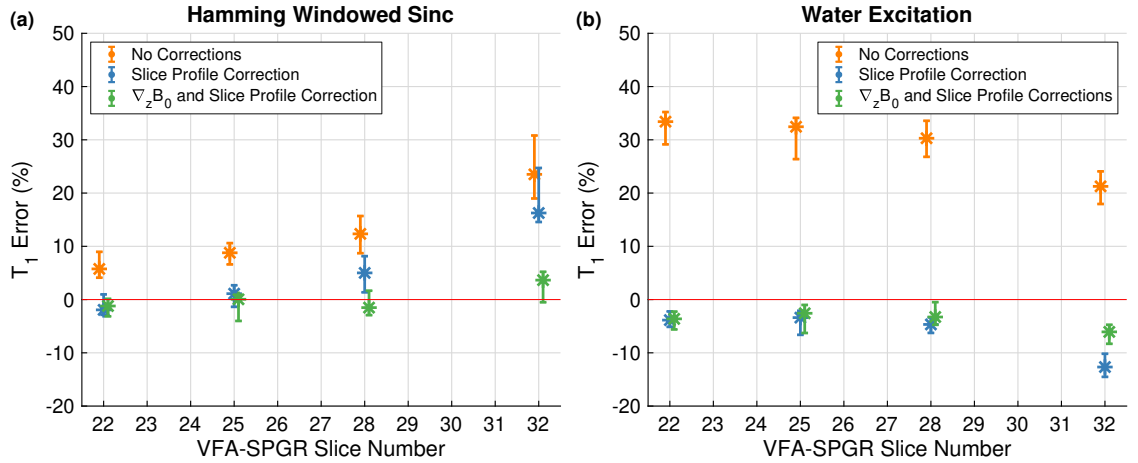


Figure 3.23: Percentage T_1 Error in the *FDA4-T1* phantom T_1 map without any corrections to the B_1^+ map (orange), with slice profile correction (blue) and with B_0 gradient through slice correction added to the slice profile correction (green) for four different VFA-SPGR slices matching the GRE-EPI slices in Figure 3.21, where slice 25 corresponds to the middle slice. (a) The Hamming Windowed Sinc RF pulse B_1^+ map, used to correct the FAs in the T_1 fit, resulted in a median and interquartile range (IQR) T_1 error of 2.6% [-0.4 10.2]% using only slice profile correction; including the correction for off-resonance variations through slice, the T_1 error decreased to -0.3% [-2.5 2.1]%. (b) The Water Excitation RF pulse B_1^+ map resulted in a T_1 map with a median error and IQR of -5.3% [-7.8 -3.3]% using only slice profile correction; including the correction for off-resonance variations through slice the T_1 error decreased to -3.9% [-5.9 -1.7]%.

In Vivo

In vivo T_1 maps without B_0 through slice correction (Figure 3.24 (a)) showed a clear gradient in T_1 values, with lower T_1 values for slices close to the liver dome and increasing T_1 values as the slice number increased. After applying the developed B_0 gradient through slice correction, the T_1 gradient disappeared and the T_1 maps were visually more homogeneous (Figure 3.24 (b)). A red profile crossing the liver along the slice direction showed an 8.8% higher B_1^+ factor without the correction resulting in a 16% T_1 underestimation, for pixels up to slice 29 where the big blood vessel started. The largest variation of B_0 through slice was $-11\,\mathrm{Hz/cm}$ and occurred at slice number 14.

Evaluating further the difference in T_1 for axial slices across the liver with or without the B_0 gradient through slice correction, there was a clear increase in T_1 with slice number when B_0 variations through slice were not corrected (Figure 3.25). Without a B_0 gradient through slice correction, the mean T_1 across all slices was $837\,\mathrm{ms}$, with a coefficient of variation (CoV) of 9.3%. The variations of B_0 through slice reached a maximum of $12\,\mathrm{Hz/cm}$. After applying a B_0 through slice correction to the B_1^+ map, the mean T_1 across all slices increased to $969\,\mathrm{ms}$ and the CoV T_1 decreased to 5%, confirming a more homogeneous liver as observed in Figure 3.24 (b). The T_1 variation over the 25 slices shown in Figure 3.25, determined through a linear fit to the data, was $221\,\mathrm{ms}$ with 95% CI [202 240]ms before the correction and decreased to $4\,\mathrm{ms}$ with 95% CI [-20 28]ms after the correction for a B_0 gradient through slice. In conclusion, these results show the importance of correcting for off-resonance variations through slice to obtain accurate whole-liver T_1 maps when using a 2D multi-slice DAM B_1^+ map.

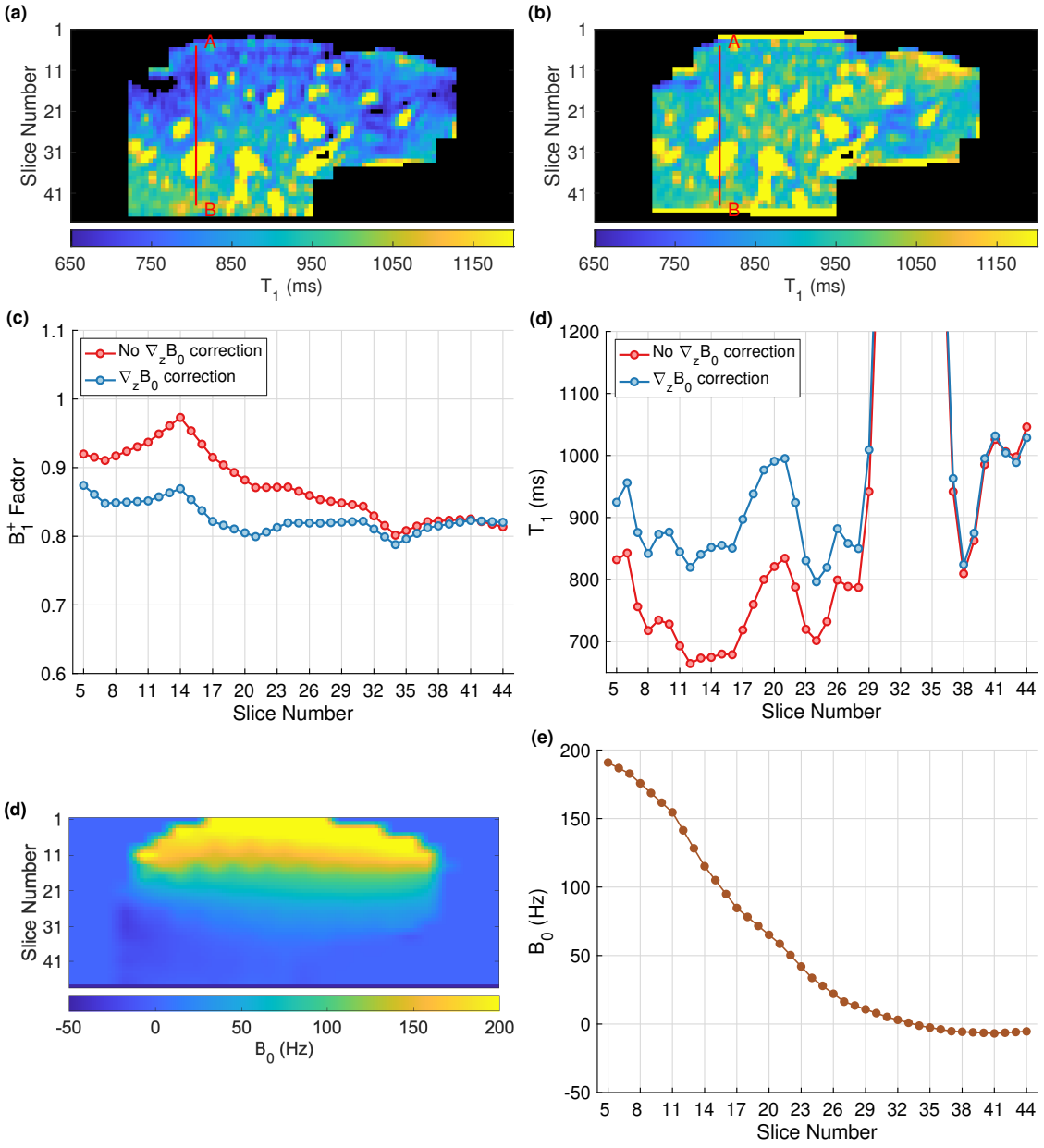


Figure 3.24: (a) Sagittal T_1 Map without the B_0 gradient through slice correction shows a gradient in T_1 as a function of slice number. (b) Applying the developed B_0 gradient through slice correction, the T_1 values at the dome of the liver increased resulting in a more homogeneous T_1 map. The red profile cutting the liver from slice 5 (point A) until slice 44 (point B) is plotted in (c) for the B_1^+ factors and in (d) for the corresponding T_1 values. Without B_0 through slice profile correction, the B_1^+ factor (red) until slice 28 is larger by 8.8% (median) and subsequently, the T_1 is smaller by 16% (median) compared to the T_1 after correcting for B_0 through slice variations (blue). The large T_1 values between slice 29 and slice 37 correspond to a vessel, saturated to yellow in the colormaps. After slice 37, the B_1^+ factors and T_1 values agree as the through slice B_0 variations are negligible. (e) B_0 Map for the same sagittal cut used for the T_1 maps, highlighting large variations in B_0 along the slice direction. (f) B_0 varies smoothly with slice number between $191\,\mathrm{Hz}$, at the top of the liver, to $-5\,\mathrm{Hz}$ at the opposite end of the liver, close to the kidneys.

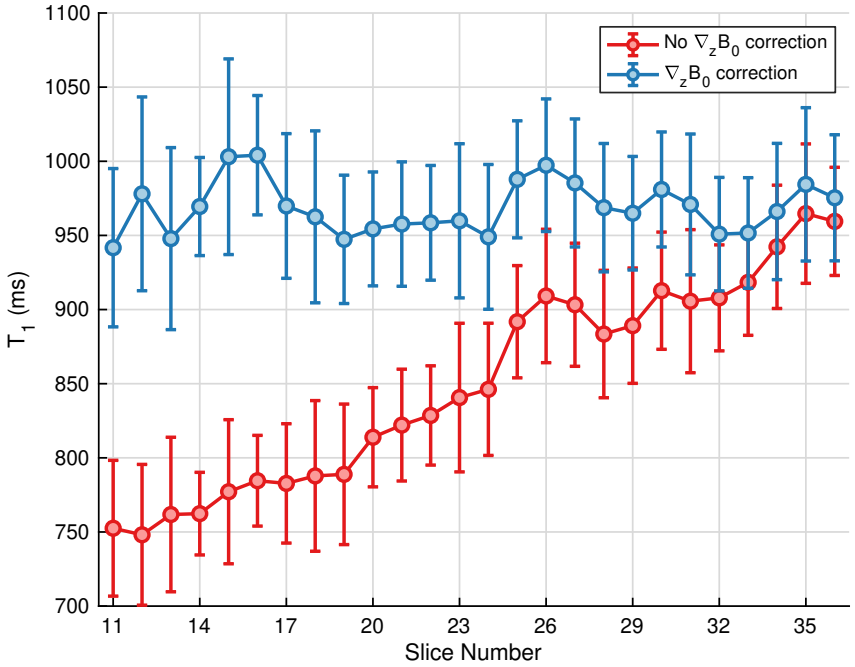


Figure 3.25: *In vivo* T_1 as a function of axial slice number measured from the weighted average of T_1 across three ROIs. ROIs were placed in vessel free areas of the liver on the SPGR image acquired at a FA of $15°$. The average T_1 value using a B_1^+ map without correcting for B_0 through slice variations, in red, shows a steep increase in T_1 from $753\,\mathrm{ms}$ to $959\,\mathrm{ms}$ as the slice number increases. The overall mean T_1 and standard deviation was $837ms \pm 78\mathrm{ms}$. Correcting the B_1^+ map calculation for B_0 through slice variations (blue) results in a more stable T_1 across the liver with an overall mean T_1 and standard deviation of $969 \pm 49\mathrm{ms}$.

3.5 EPI-based B_1^+ Map Confounding Factors

An EPI acquisition presents several differences to conventional image acquisition which result in characteristic artefacts and signal intensity modulations that can affect quantitative imaging if not considered appropriately. The main reason for adopting a single-shot EPI readout for B_1^+ mapping is the need to image a signal that is fully recovered and thus has no T_1 contrast. This is possible through EPI because all the signal acquired results from one single RF excitation pulse. Conversely, in conventional imaging, an RF excitation pulse is applied for every PE line, with each line separated by a time TR. In EPI, prior to the RF excitation pulse, the magnetisation is fully relaxed, pointing along M_z, equivalent to an infinite TR. To acquire all the information from one single excitation, the entire k-space is scanned within one long readout by applying a bipolar oscillatory gradient along the FE direction whilst periodically 'blipping' a PE gradient, which dephases and rephases the spins, generating a train of echoes that sample the entire k-space. The image contrast is determined by the echo time TE necessary to reach the centre of k-space, which is achieved when the sum of the periodic PE pulse 'blips' cancel the PE dephase gradient. To minimise T_2^*-weighting, the TE should be placed to the shortest possible value. To minimise T_2^* blurring, the rate of transversing k-space in the PE direction should be maximised.

The PE gradient in EPI can be either a blip or a constant gradient applied during the whole readout. Its behaviour is analogous to FE in conventional GRE and thus suffers from the same artefacts. Because of the short acquisition time per FE line in EPI, or equivalently large BW, artefacts are negligible along the FE direction. On the other hand, the long readout time along the PE direction in EPI, necessary to collect all the echoes, results in a low acquisition BW in that direction. The BW in the PE is smaller than the BW in the FE by a factor roughly equal to the number of PE lines. The PE gradient strength is comparable to the background B_0 gradient, making EPI particularly susceptible to B_0 inhomogeneities. Consequently, several artefacts can arise along the PE direction: chemical shift, geometric distortion, signal and resolution loss

[58]. In the sections below, each artefact will be reviewed individually and its impact on the B_1^+ map quantified. The pulse sequence diagram for the GRE-EPI sequence using a FS and a HWS pulse is illustrated in Figure 3.26.

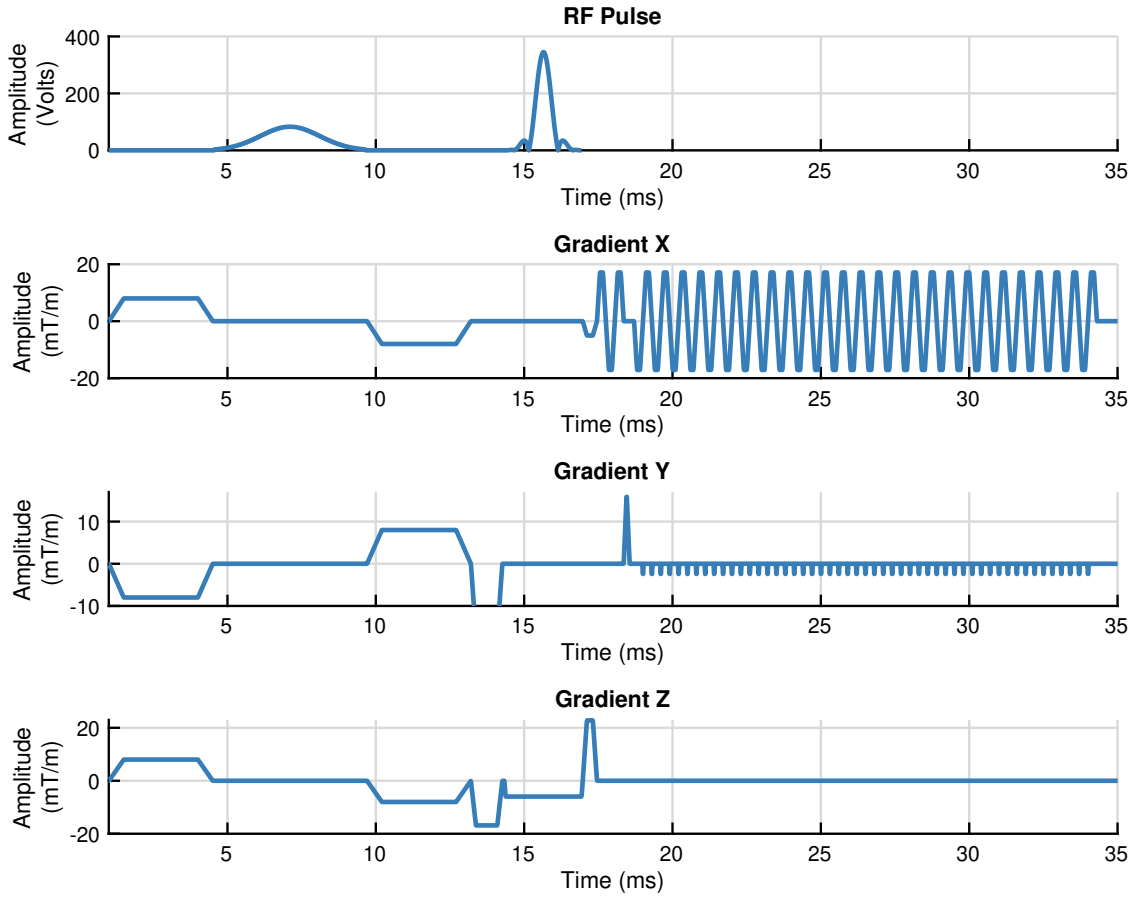


Figure 3.26: Pulse sequence diagram including the RF pulse channel, and the gradients in the three spatial encoding directions. Note that EPI is characterised by a single RF excitation pulse and thus a single slice-select and refocusing gradient (along the z direction) combined with in-plane gradients that allow to read the entire k-space after a single excitation. The gradient in the FE direction (x) is a fast-changing bipolar gradient and the gradient in the PE direction (y) uses small blips to transition between adjacent k-space lines.

3.5.1 Spatial Distortion

Background

In conventional imaging, only the readout direction is affected by distortion artefacts due to B_0 inhomogeneities. In the PE direction, since a new RF excitation pulse is applied between each PE line, a B_0 field inhomogeneity will impose an extra overall constant phase and does not change the phase difference between PE lines [31]. However,

in EPI all k-space data is acquired after a single RF excitation pulse. Any phase error from B_0 inhomogeneities accumulates during the total readout time and thus changes the spacing between PE lines, resulting in shifts along this direction [72]. There is no distortion along the slice encoding direction as the BW of the RF pulses is on the order of kHz (acquisitions with a SS gradient of $5.96\,\mathrm{mT/m}$ and a slice thickness of $8\,\mathrm{mm}$ have a BW of $2\,\mathrm{kHz}$), which is much larger than any off-resonance along the slice direction for a shimmed volume.

The lung-liver interface is a region containing tissues with different magnetic susceptibilities (χ). Consequently, the slices closest to this interface have the largest magnetic field inhomogeneities (Equation (3.7)) and therefore the largest shifts along the PE direction. Because the susceptibility differences vary spatially, there is not a constant shift but instead a geometric distortion. In some areas, there is stretching of the voxel (echo shifted towards the beginning of the EPI readout when the B_0 gradient is of the same sign as the PE gradient) and less signal intensity, while other voxels suffer compression (echo shifted towards the end of the EPI readout when the B_0 gradient is of opposite sign of the PE gradient) and increased signal intensity. The stomach and bowels are also regions in abdominal imaging with large susceptibility differences due to the presence of air-tissue interfaces.

$$\Delta B_0 = (\chi_1 - \chi_2)B_0 \tag{3.7}$$

The distortion (Δy) along the PE direction is given by Equation (3.8) [58]. Distortion increases with the field inhomogeneity (ΔB_0), larger echo spacing and with decreasing PE gradient strength. The increment in k-space along the PE direction Δk_y is equal to the product of the gyromagnetic ratio (γ), the strength of the PE gradient (G_{PE}) and the time the PE gradient is on (τ).

$$\Delta y = \frac{\Delta B_0 * \text{Echo Spacing}}{\Delta k_y}, \quad \text{where } \Delta k_y = \gamma G_{PE} \tau \tag{3.8}$$

Using parallel imaging one travels faster through k-space in the PE direction and can thus reduce distortion by increasing Δk_y through the use of a stronger gradient along

the PE direction. Despite advantages in reducing the distortion artefacts in EPI, parallel imaging was switched off as it induced fat ghost artefacts (Section 3.5.3).

Theoretical Estimate of the Variation in B_1^+ Factor due to EPI Distortion

For our EPI acquisition with a BW per pixel of $3906\,\mathrm{Hz}$, the pixel shift in the FE direction for a $100\,\mathrm{Hz}$ off-resonance is 0.0256 pixels, which is insignificant. On the other hand, the shift in the PE direction is 1.56 pixels (Equation (3.8)), for an off-resonance of $100\,\mathrm{Hz}$, assuming 52 PE lines and an echo spacing of $0.3\,\mathrm{ms}$. Given the pixel size in our EPI acquisition is $7.03\,\mathrm{mm}$, the PE shift is approximately $11\,\mathrm{mm}$. Figure 3.27 (a) shows a B_0 map of the liver for a slice close to the lungs, where there were large susceptibility differences resulting in off-resonances of up to $140\,\mathrm{Hz}$, excluding outliers. According to Equation (3.8) these off-resonances would result in distortions in the PE direction (vertical) of up to $15\,\mathrm{mm}$ (Figure 3.27 (b)).

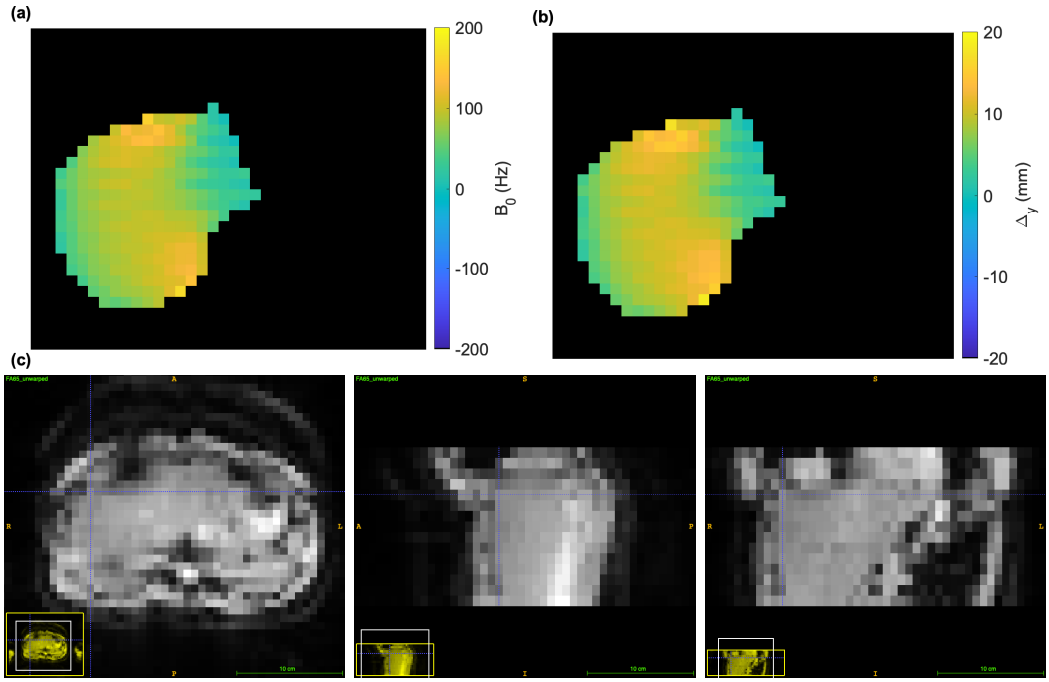


Figure 3.27: (a) B_0 map in Hz for a slice close to the lungs. (b) Shift in the PE direction (vertical) in mm predicted from the B_0 map. The areas with larger B_0 inhomogeneities result in larger shifts along the PE direction. (c) Axial, sagittal and coronal cuts of the GRE-EPI acquisition, after distortion correction, showing the anatomical location of the B_0 map slice.

To decide whether to apply a distortion correction to the EPI data, one should assess the resulting magnitude of the variation in the B_1^+ factor (Equation (3.9)). The average

change in B_1^+ factor along the PE direction (vertical) is 0.05 pixel^{-1} between rows 24 and 27. Pixels in these rows are shifted on average by $7.2\,\mathrm{mm}$ along the PE direction, slightly above one pixel. Thus, Equation (3.9) predicts a variation in the B_1^+ factor of 0.055 (Figure 3.28). The relative error in B_1^+ factor propagates by approximately a factor of two into a relative error in T_1, resulting in T_1 errors of roughly 11%. For a T_1 of $900\,\mathrm{ms}$, an error of 11% corresponds to a bias in measured T_1 of $99\,\mathrm{ms}$ which is larger than the differences in T_1 between different liver fibrosis stages. In conclusion, it is crucial to correct for distortion in the GRE-EPI images before calculating the B_1^+ map.

$$\Delta B_1^+ = \frac{dB_1^+}{dy}\Delta y \tag{3.9}$$

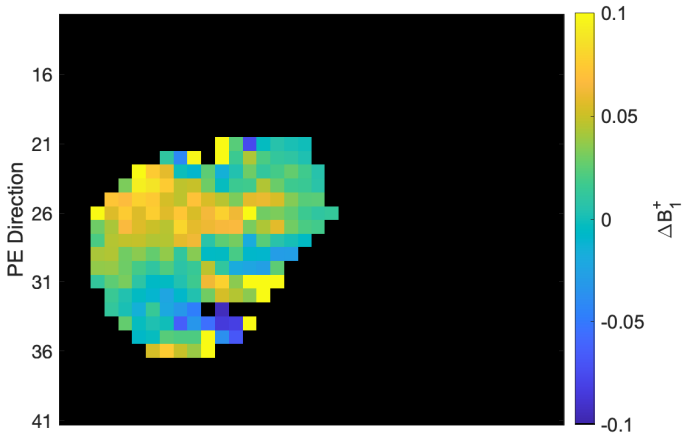


Figure 3.28: Variation in B_1^+ factor along the PE direction (vertical). The variations in the B_1^+ map are larger in the anterior part of the liver, between rows 24 and 27, with an average B_1^+ factor variation of 0.055. The large negative B_1^+ factor variation of almost 0.1 in the posterior part of the liver (rows 33-34) corresponds to fat chemical shift, creating an artificially large variation in B_1^+ factor.

Methods

To minimise distortions in GRE-EPI acquisitions, without resorting to parallel imaging, the remaining adjustable parameter is the echo spacing. Empirically it was found that a BW of $3906\,\mathrm{Hz/pixel}$ yielded the minimum echo spacing of $0.30\,\mathrm{ms}$ on a Siemens $3\,\mathrm{T}$ Prisma scanner without parallel imaging. The k-space increment in the PE direction cannot be increased as this is defined by the abdomen dimensions. A rectangular FoV

(reduced in the PE direction) was chosen to increase the strength of the PE gradient blips and thus minimise distortions and signal loss. In addition, a shim volume including the whole FoV was used to minimise field inhomogeneities.

Given the potentially large errors in T_1 of 11%, it was necessary to apply distortion correction to the GRE-EPI data. A B_0 map was calculated from the phase of the double echo GRE-EPI acquisition. A mask was manually drawn over the liver on the high-resolution VFA SPGR acquired at a FA of $15°$, at slice locations matching the B_0 acquisition, and applied to the GRE double echo after down sampling. The phase data was unwrapped using *fsl* prelude [73], [74]. The liver B_0 map was then interpolated to the GRE-EPI resolution and used to unwarp the GRE-EPI data through the *fsl* distortion correction toolbox *fugue* [72], [73]. A flow diagram of the function written to calculate the B_0 map and correct the GRE-EPI data for distortion is illustrated in Figure 4.14. Using *fugue* instead of *topup* [75] saves the patient one breath-hold, since *topup* requires acquisition of two images with the PE direction reversed. Using PE in the anterior-posterior direction, the fat shifts to the posterior part of the liver, while in the posterior-anterior direction the fat shifts into the anterior part of the liver. Both directions are required by *topup* to unwarp the images, but this results in two locations with chemical-shift artefacts, while *fugue* will just have one.

Results

Figure 3.29 shows the raw GRE-EPI data before and after distortion correction in the sagittal plane. In (a) a shift of the liver dome to the right (posterior direction) was evident when compared to (e) which was not affected by distortion. The shift was a consequence of large off-resonance values of up to $228\,\mathrm{Hz}$ in the dome (d). *Fugue* distortion correction shifted the liver in the opposite direction (b), aligning it with the GRE magnitude (e) data which did not suffer from distortion along the PE direction.

In Figure 3.30 (a) there was a gradient in T_1: with higher T_1 for the initial rows and decreasing towards point B (posterior part of the liver). The initial rows where both the gradient in the B_1^+ factor and the B_0 were largest resulted in the largest

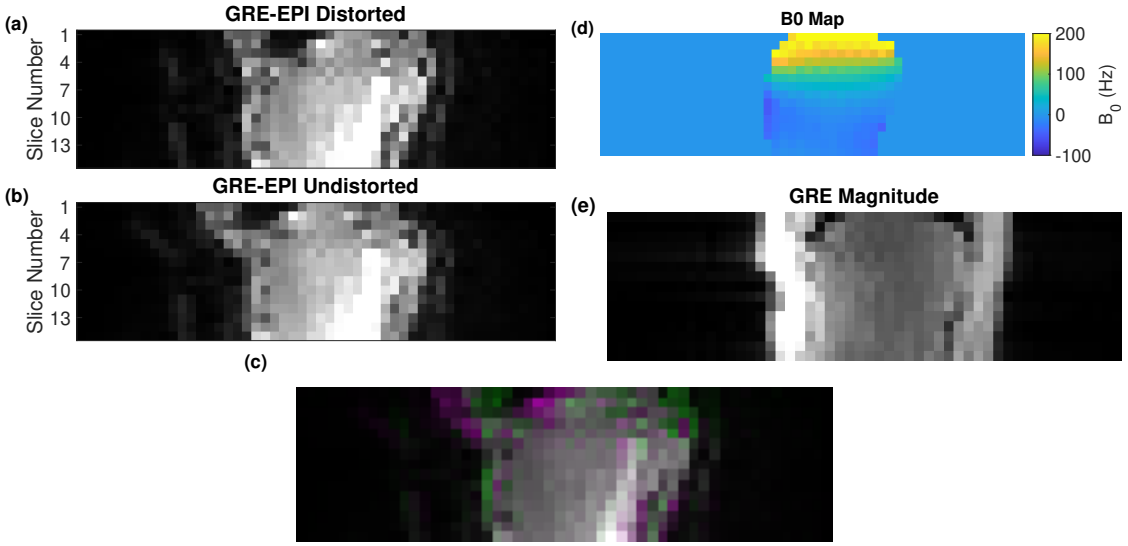


Figure 3.29: (a) GRE-EPI raw signal distorted with the liver dome shifted to the right (posterior direction). (b) GRE-EPI image after *fugue* distortion correction. The liver dome was shifted back to the left (anterior direction), it's true position. (c) Superposition of the distorted gre-EPI in green with the undistorted gre-EPI in magenta. The grey pixels correspond to regions where both images were aligned. The largest misalignment is seen for the first 5 slices where the green and magenta are misaligned. This region corresponds to the areas of largest B_0 inhomogeneities as seen from (d) the B_0 map, ranging from $56\,\mathrm{Hz}$ to $228\,\mathrm{Hz}$ for the first 5 slices. (e) Magnitude image from the B_0 map acquisition which is not affected by distortion. The first pixel corresponding to liver tissue for slice 2 occurs at column 23 for both image (e) and the undistorted GRE-EPI image (b), confirming the distortion correction algorithm was successful.

difference in the B_1^+ factor (Figure 3.28), reflected as a zone of elevated T_1 (Figure 3.30 (a)). A difference of almost 10% in T_1 was observed experimentally, consistent with the theoretical estimates calculated through Equation (3.9). The T_1 map using distortion correction was more homogeneous (Figure 3.30 (b)). A red line across the PE direction in Figure 3.30 was used to plot the B_1^+ map values interpolated to the VFA resolution along with the corresponding T_1 values in Figure 3.31. The mean T_1 value without distortion correction was $1111\,\mathrm{ms}$ and the standard deviation was $54\,\mathrm{ms}$. In contrast, the distortion corrected T_1 profile was more constant overall with an average of $1004\,\mathrm{ms}$ and a standard deviation of $28\,\mathrm{ms}$, excluding rows corresponding to pixels with blood vessels for both maps. The corresponding off-resonance for this region was on average $71\,\mathrm{Hz}$.

After the EPI distortion correction, a right-to-left gradient remained in the upper portion of the T_1 maps. This is likely a consequence of the difficulty of measuring

an accurate B_0 value in an area of low signal (Figure 3.30 (c) and (d)) due to lung tissue. In turn, this affected the accuracy of the B_0 gradient through slice correction resulting in an area of low T_1.

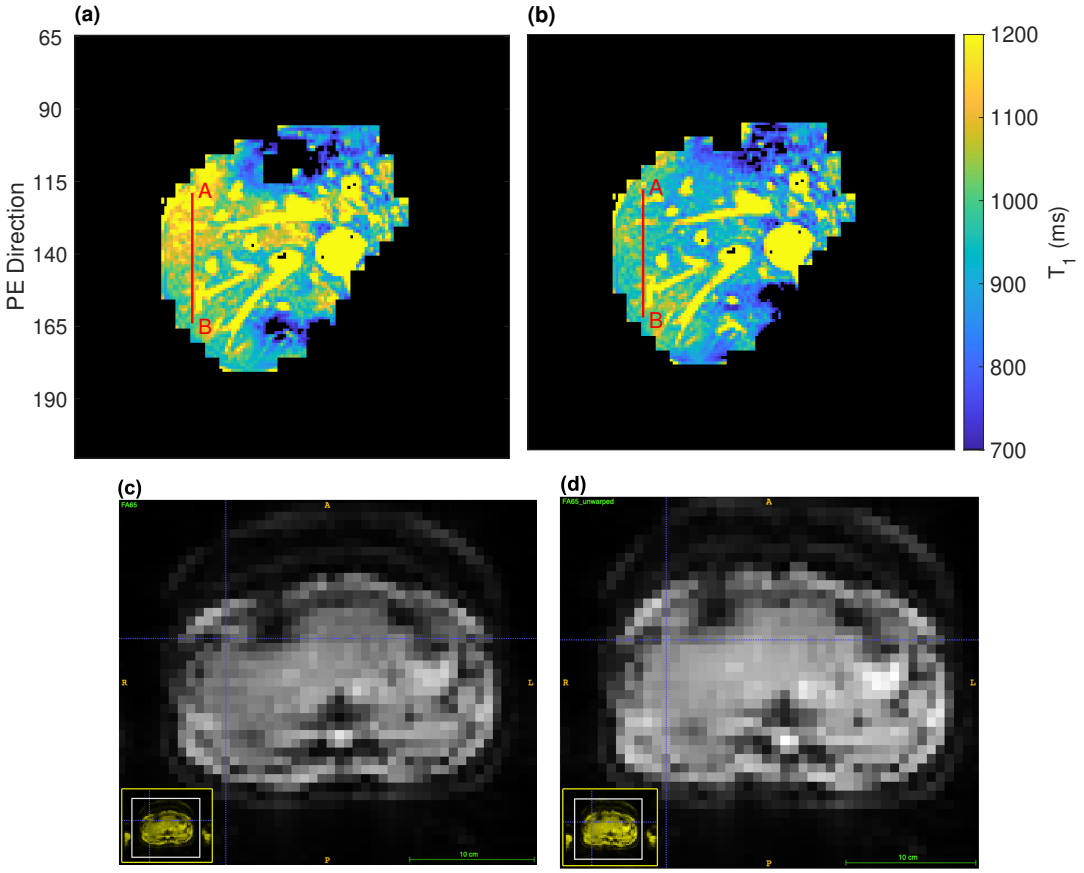


Figure 3.30: Example T_1 maps for a slice close to the lungs including the B_1^+ correction. (a) T_1 maps calculated from GRE-EPI images (a) without and (b) with EPI distortion correction. There is a clear difference between the two T_1 maps. The red profile spans the PE direction (rows) from point A to point B and it is used to assess the difference in B_1^+ factors and T_1 values resulting from applying *fugue* distortion correction. Both maps have the B_1^+ map corrected for slice profile and B_0 gradient through-slice. (c) Distorted and (d) undistorted GRE-EPI images at a FA of $65°$ showing that the black hole in the T_1 maps (above row 115) is a consequence of no signal in the GRE-EPI, preventing the calculation of the B_1^+ factor.

3.5.2 Chemical Shift Artefacts

A fat band in the B_1^+ maps shows up as a rapid localised variation in the B_1^+ factor value and was a clear artefact affecting the T_1 map. This section discusses the origin of the artefact, its impact on the B_1^+ map, and an algorithm that was developed to identify and eliminate the fat band artefact.

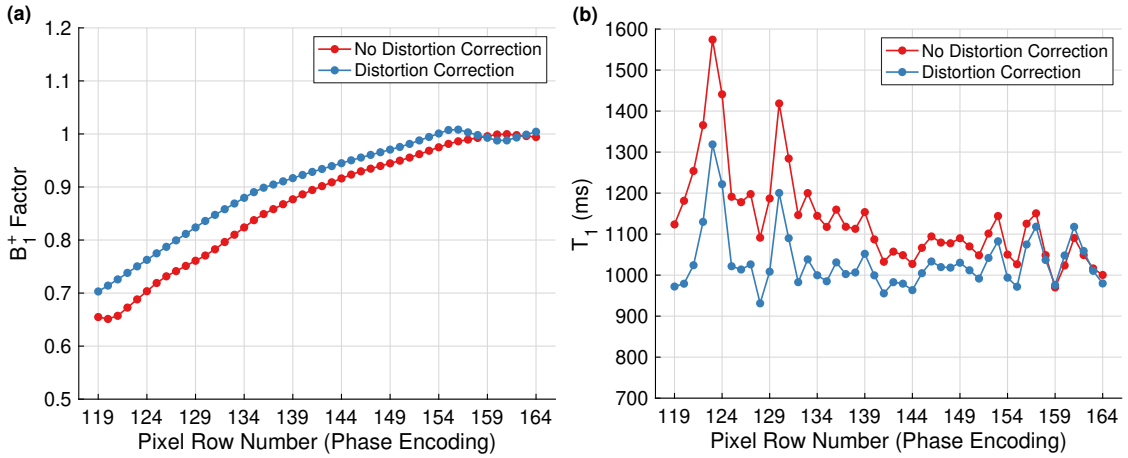


Figure 3.31: (a) B_1^+ factor and (b) T_1 values along the red profile shown in Figure 3.30. There is a large difference in both B_1^+ factor and T_1 between the distortion corrected and non-corrected values, with median differences in B_1^+ factor of -4.4% and in T_1 of 9.7%, slightly more than the double. The median values were calculated excluding pixels corresponding to blood vessels.

Background

Fat precesses at a lower frequency than water, by 3.45 parts per million (σ_{FW}). This results in an absolute frequency difference ($\delta\omega_{FW}$) of approximately $440\,\mathrm{Hz}$ [32] between water on-resonance and fat (Equation (3.10)), at $3\,\mathrm{T}$. This difference in resonance frequencies is also known as a chemical shift.

$$\delta\omega_{\mathrm{FW}} = \gamma B_0 \sigma_{\mathrm{FW}} \tag{3.10}$$

Because in MRI the spatial location is frequency-encoded, a shift in the resonance frequency will result in a shift in image space. Using the BW per pixel, the shift in units of pixels is described by Equation (3.11), being proportional to the main magnetic field strength and inversely proportional to the BW.

$$d_{\mathrm{pixel}} = \frac{\delta\omega_{\mathrm{FW}}}{\mathrm{BW}_{\mathrm{pixel}}} \tag{3.11}$$

The fat-water chemical shift can also be seen as a large off-resonance and therefore as a distortion through the form of a fixed shift. Consequently, the equations used for distortion in Section 3.5.1 are also valid for estimating the shift of the fat signal and the resulting effect on the B_1^+ factor.

Theoretical Estimate of the Variation in B_1^+ Factor due to Fat Chemical Shift

For the GRE-EPI acquisition at $3\,\mathrm{T}$ with the HWS RF excitation pulse, the BW in the FE direction is $3906\,\mathrm{Hz/pixel}$ and in the PE direction it is $64\,\mathrm{Hz/pixel}$. The fat-water off-resonance is small compared to the BW in the FE direction, resulting in a negligible fat signal shift of $1/9^{\text{th}}$ (0.11) of a pixel in the FE, whilst along the PE direction there is a significant shift of $6.7\,\mathrm{pixels}$ which corresponds to $47\,\mathrm{mm}$.

Fat suppression should eliminate the fat signal, but due to B_1^+ inhomogeneities this was not verified and some residual fat signal was still excited by the HWS RF pulse, appearing in the GRE-EPI images (Figure 3.32). The fat from the lower back was shifted into the posterior part of the liver, while the fat in the abdomen shifted outside of the body. The fat can either add constructively or destructively to the water signal, changing the ratio between the signals at $130°/65°$ and thus resulting in inaccurate estimates of the B_1^+ factor which translate into T_1 inaccuracies. Moreover, if there is a misalignment in the breath-hold positions between the two FAs, the area of the B_1^+ map affected by the chemical shift broadens. If the abdomen occupies the whole FoV, the fat of the abdomen that shifts outside of the liver will be wrapped into the posterior part of the liver.

Methods

Similar to distortion, minimising the echo spacing will reduce the fat shift in the PE direction. A FE BW of $3906\,\mathrm{Hz/pixel}$ resulted in the smallest allowable echo spacing of $0.3\,\mathrm{ms}$ on a $3\,\mathrm{T}$ Siemens Prisma scanner. Nevertheless, due to poor fat suppression (Figure 3.32), a post-processing algorithm was constructed to identify and remove the erroneous B_1^+ factor values calculated due to the addition of fat signal to the water signal. First, outlier B_1^+ factor values were identified using the *extrema2.m* function [76]. A threshold criterion was used to triage the identified outliers. If the absolute difference between the outlier B_1^+ factor and the average B_1^+ factor of the surrounding $8\,\mathrm{pixels}$ was larger than 0.075, the B_1^+ pixel was considered a true outlier. The outlier B_1^+ factor values were replaced by values obtained from an interpolation of the Laplacian

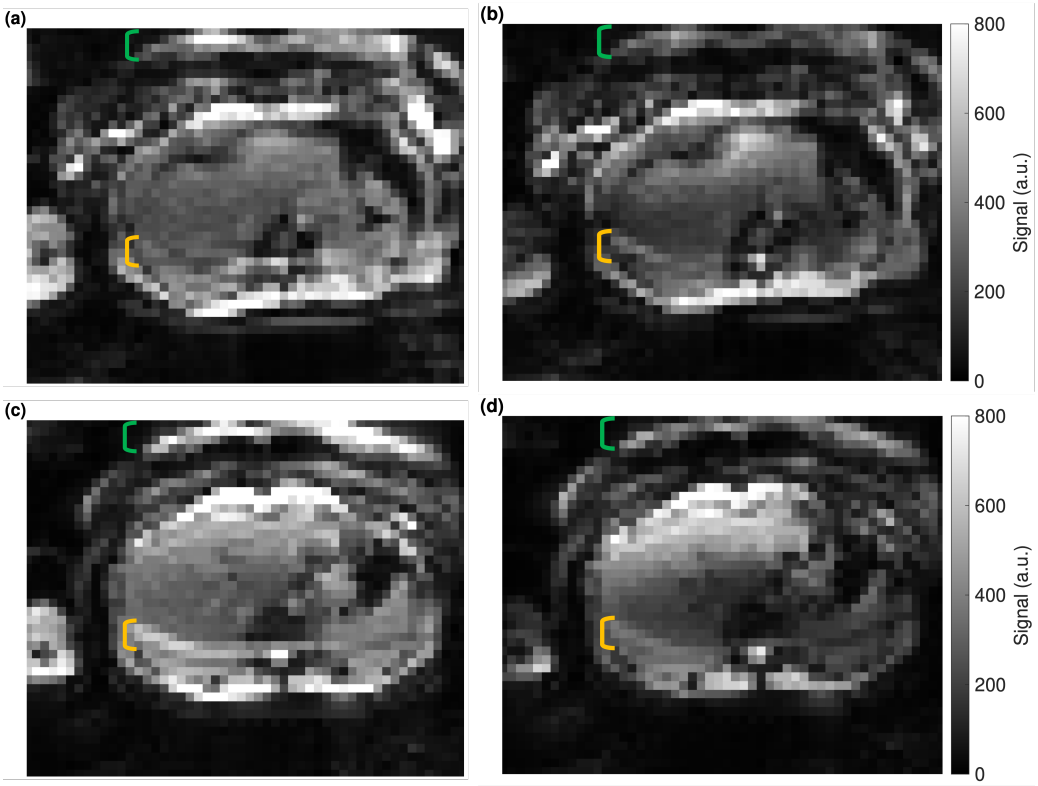


Figure 3.32: Raw GRE-EPI data at a FA of $65°$ (first column) and a FA of $130°$ (second column), for slice 5 out of 15 (first row) and slice 8 out of 15 (second row). In slice 5, the fat adds destructively to the liver water signal for FA $65°$, resulting in lower signal intensity in the fat chemical shift region (yellow square bracket in (a)). Whilst for slice 8, the fat adds constructively to the water signal, showing up as a bright band. The yellow square brackets indicate the fat chemical shift regions. There are also large chemical shifts highlighted by the green brackets, but these shifts are outside of the liver.

evaluated at non-outlier B_1^+ factor values [77].

Having extracted the outliers, the chemical shift band was identified based on the prediction of two B_1^+ factor values for a target pixel in a given column along the PE direction, by approaching the target pixel from either the anterior or posterior direction (Figure 3.33). The fat signal introduces rapid changes in the B_1^+ maps characterised by a localised ridge followed by a depression (Figure 3.34 (a)) or a depression followed by a ridge (Figure 3.34 (d)). The B_1^+ factor prediction was based on an extrapolation using the first and the second derivatives of the B_1^+ map applied to the anterior/forward and posterior/backward direction. The B_1^+ factor predictions were only calculated for pixels below the middle of the liver as the fat band should be physically restricted to this region. The absolute difference between the two B_1^+ factor predictions at each pixel

(Equation (3.12)−Equation (3.13)) was calculated. The fat band was associated with pixels where the largest absolute difference was greater than twice the average absolute difference between the forward and backwards predictions calculated along each column. The start and end rows of the fat band for each column were equal to the location of the two largest absolute differences, provided these locations were not more than $3\,\mathrm{pixels}$ apart. This limited the fat band extent along each column to $3\,\mathrm{pixels}$. The B_1^+ pixels identified as fat band were again replaced by the Laplacian interpolation method [77]. The forward prediction was given by a Taylor expansion up to quadratic terms in the B_1^+ factor:

$$B_1^+(j)_f = B_1^+(j-1) + \left(\frac{dB_1^+}{dy}(j-1)\right)_f \Delta y + \frac{1}{2}\left(\frac{d^2B_1^+}{dy^2}(j-1)\right)_f \Delta y^2\,, \qquad (3.12)$$

where the first derivative was estimated using a backward difference and the curvature was approximated by a central difference:

$$\left(\frac{dB_1^+}{dy}(j-1)\right)_f = \frac{B_1^+(j-1) - B_1^+(j-2)}{\Delta y}$$
$$\left(\frac{d^2B_1^+}{dy^2}(j-1)\right)_f = \frac{B_1^+(j) - 2B_1^+(j-1) + B_1^+(j-2)}{\Delta y^2}$$

The pixel increment Δy equals 1, and j was the index indicating the position of the pixel along the PE direction. An analogous procedure was carried out for the backward prediction:

$$B_1^+(j)_b = B_1^+(j+1) - \left(\frac{dB_1^+}{dy}(j+1)\right)_b \Delta y + \frac{1}{2}\left(\frac{d^2B_1^+}{dy^2}(j+1)\right)_b \Delta y^2 \qquad (3.13)$$

$$\left(\frac{dB_1^+}{dy}(j+1)\right)_b = \frac{B_1^+(j+2) - B_1^+(j+1)}{\Delta y}$$
$$\left(\frac{d^2B_1^+}{dy^2}(j+1)\right)_b = \frac{B_1^+(j+2) - 2B_1^+(j+1) + B_1^+(j)}{\Delta y^2}$$

A flow diagram of the function written to remove the fat band artefact is illustrated in Figure 4.17.

Results

Figure 3.34 shows the B_1^+ map with the fat band as an area of artificially decreased (a) or increased B_1^+ factor (d), and the resulting B_1^+ map after removing the fat band

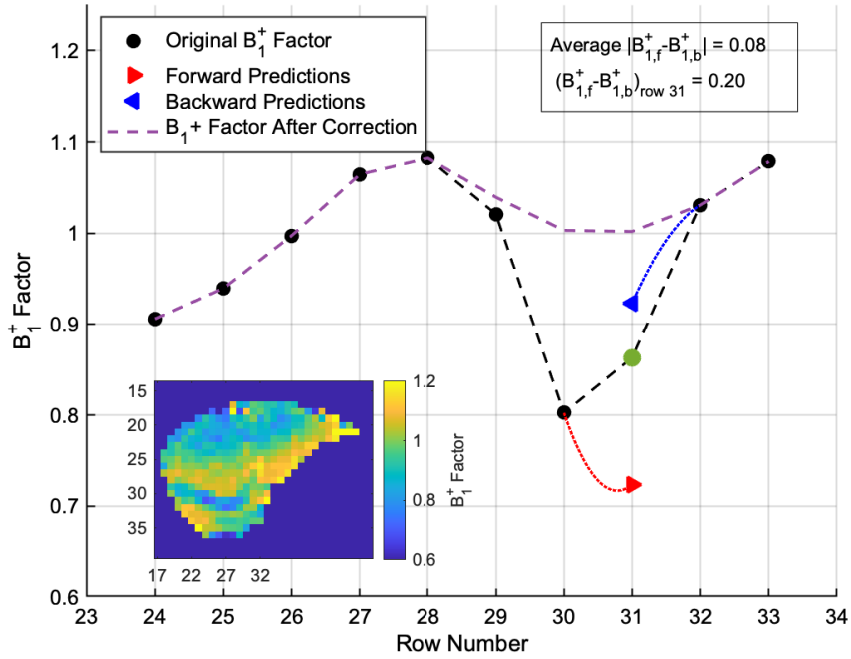


Figure 3.33: Example of the fat correction algorithm applied to column 23 of an *in vivo* B_1^+ map. The black dots correspond to the original B_1^+ factor values. The forward (red triangle) and backward (blue triangle) predictions are calculated for the B_1^+ factor in row number 31 (green dot). The largest absolute difference between the two predictions occurs for row 31 and is equal to 0.2, which is more than two times larger than the average absolute difference of 0.08. The average is calculated over the B_1^+ pixels in rows 24 to 33.

with the proposed algorithm (b, e), for two slices. Quantifying the relative difference in B_1^+ factor before and after removal of the fat band resulted in median variations of -7% for the first slice and +5% for the second slice. These variations in B_1^+ factor resulted in median T_1 relative differences of +15% and -9%, respectively (Figure 3.35).

In conclusion, adequate fat suppression is essential in abdominal imaging, especially when using EPI. When fat suppression methods are insufficient and residual fat signal remains in the images, it is important to quantify and correct the error introduced in the B_1^+ maps.

3.5.3 GRAPPA Fat Ghosts Artefacts

Background

Parallel imaging methods accelerate image acquisition by collecting a reduced number of k-space data points. The spatial resolution is maintained by sampling the same maximum frequency in k-space as when acquiring all k-space lines, but the FoV is

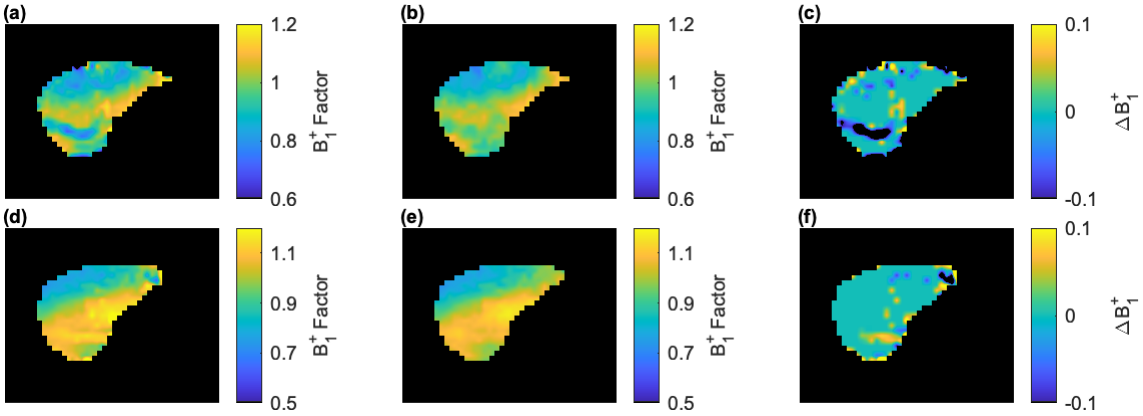


Figure 3.34: B_1^+ maps for slice 14 ((a)-(c), matches slice 5 in Figure 3.32 at the GRE-EPI resolution) and slice 24 ((d)-(f), matches slice 8 in Figure 3.32 at the GRE-EPI resolution) without removing the artificial B_1^+ factor values due to the fat chemical shift (first column), after applying the proposed algorithm to identify and remove the fat band (second column) and the relative difference between the two previous B_1^+ maps (third column). The B_1^+ difference maps highlight the regions identified as fat or outliers by the algorithm. The 75th quantile relative B_1^+ factor difference for pixels lying within the identified fat band is -12.8% for slice 14 and 6.0% for slice 24.

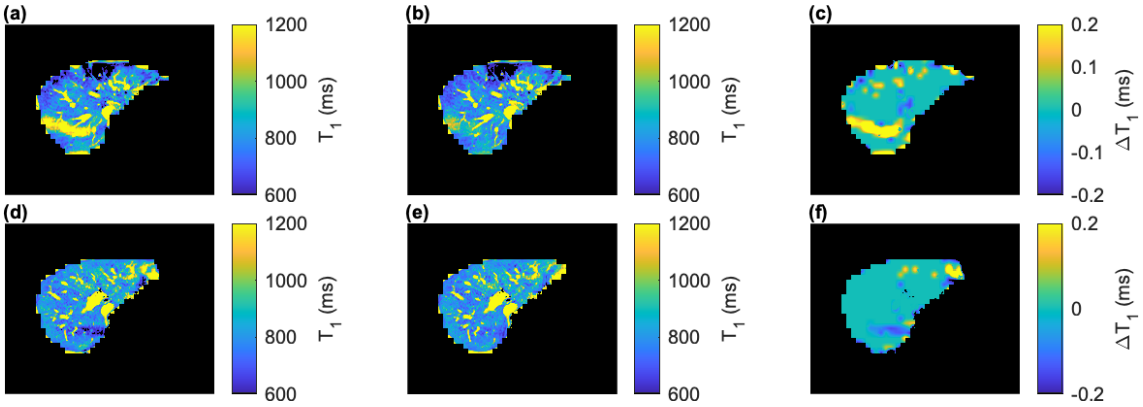


Figure 3.35: T_1 maps calculated for slice 14 ((a)-(c)) and slice 24 ((d)-(f)) without eliminating the fat band from the B_1^+ map (first column), after removing the fat band from the B_1^+ map (second column) and the relative difference between the two previous T_1 maps (third column). The 75th quantile relative T_1 difference for pixels lying within the identified fat band is 32.4% for slice 14 and -11.4% for slice 24.

reduced according to the under-sampling pattern. To overcome the unavoidable aliasing or fold-over artefacts associated with under-sampling k-space, different methods exist to recover the true unfolded image. These methods rely on using spatial information from phased arrays containing multiple channels of independent receiver coils that cover the entire object being imaged. Acceleration is possible by partially replacing spatial encoding, through linear gradients, with the spatial information from each receiver coil.

One acceleration method weighs the single images on a pixel by pixel basis, obtained from each channel, by the coil sensitivity profile for that channel and solves a system of linear equations (SENSE) [78]. Another method, recovers the missing k-space data before reconstruction to image space and is known as the GeneRalized Autocalibrating Partially Parallel Acquisition (GRAPPA) [79], [80]. As the name indicates, it acquires an autocalibration signal (ACS) which is a set of fully sampled central k-space lines, i.e., with a k-space spacing equal to the inverse of the full FoV. A GRAPPA kernel defines the under-sampling pattern in the PE direction. The acquired k-space data in the kernel from the multiple coils are linearly combined through weights to generate the k-space point in the ACS data from a single coil. These weights are subsequently applied to the under-sampled k-space data acquired by each coil to generate the missing k-space points. The weights are shift-invariant [81] but coil specific, i.e., the same weights can be used in under-sampled regions not included in the ACS k-space lines, but each coil has its own set of weights. After the missing k-space data is filled in for each coil, the Fourier transform is applied to generate an image for each coil. The images from all coils are then combined through an array combination method such as the sum of squares to produce a full FoV image.

For the B_1^+ mapping acquisition, the acceleration factor provided by GRAPPA would not help to reduce the acquisition time, as we already make use of EPI, but rather to travel across k-space faster. This would allow a larger Δk_y and a smaller echo spacing and therefore, a reduction in both distortion and chemical shift artefacts in the EPI acquisition as described in the sections above.

Methods

GRAPPA was originally turned on to travel through k-space faster and thus reduce distortion artefacts. However, using GRAPPA with EPI resulted in ghosts spaced by the FoV/(GRAPPA acceleration factor). These ghosts originate from the unsaturated fat signal that suffers a chemical shift in EPI. Because the GRAPPA ACS lines are acquired with a FLASH sequence [82] without EPI readout, the fat signal is not affected

by chemical shift in the PE direction. Therefore, the ACS cannot unfold the aliased fat chemical shift in the under-sampled GRE-EPI acquisition. If there are residual N/2 ghosts in the EPI readout, they will appear at FoV/6 using an acceleration factor of 3 as every odd or even line is now separated by 6 k-space lines.

Note that the ACS lines acquired at the start of the acquisition will perturb the longitudinal magnetisation, i.e., the magnetisation will not depart from a fully relaxed state at the time of the excitation pulse α, unless a TR of more than 5 times T_1 is employed. However, the ACS lines are acquired at the same excitation FA of 4° for both FAs α and 2α, thus it will have no effect when taking the ratio between the signals of FAs α and 2α used to calculate the B_1^+ map. This effect of the GRAPPA reference lines is similar to that of a reset pulse [83] as the magnetisation will depart from the same initial value for both excitation pulses α and 2α.

When turning GRAPPA off, the fat ghosts at FoV/3 disappeared. Using GRAPPA resulted in an inaccurate B_1^+ factor calculation for two reasons: firstly, the fat signal increased or decreased the overall signal as it added constructively or destructively to the water signal which mimicked a variation in B_1^+ factor; secondly, the added fat signal was susceptible to a different B_1^+ field as it was misplaced from a different location in the PE direction due to chemical shift or GRAPPA unfolding artefacts. Another reason for turning GRAPPA off is due to its sensitivity to motion, especially if the ACS lines are acquired at the start, instead of integrated with the EPI readout. Respiratory motion during the ACS lines will result in errors in the coil sensitivity maps and thus residual ghost artefacts due to incorrect unfolding.

In the results section, the relative differences in the B_1^+ map were compared between two acquisitions from the same subject in the same session. The acquisitions used GRAPPA with three times acceleration in the PE direction and two different echo spacings. Using two different echo spacings, the fat chemical shift and its aliased ghosts will undergo different shifts. The ideal comparison would be between one B_1^+ map with GRAPPA on and one with GRAPPA off. However, this dataset was not

collected as the complications arising from using GRAPPA for B_1^+ mapping in the liver at $3\,\mathrm{T}$ were not yet fully understood.

Results

Figure 3.36 shows the raw GRE-EPI data for the same scan session, with GRAPPA on and two different echo spacings: $0.25\,\mathrm{ms}$ (a) and $0.1\,\mathrm{ms}$ (b). With an echo spacing of $0.25\,\mathrm{ms}$, the fat shifted approximately $11\,\mathrm{pixels}$ (green rectangle), while a smaller echo spacing of $0.1\,\mathrm{ms}$ resulted in a fat shift of $4.5\,\mathrm{pixels}$. Aliasing due to GRAPPA with an acceleration factor of three in the PE direction shifted the fat by FoV/3 (yellow rectangle). With $104\,\mathrm{pixels}$ in the PE direction, the shift corresponded to approximately $35\,\mathrm{pixels}$.

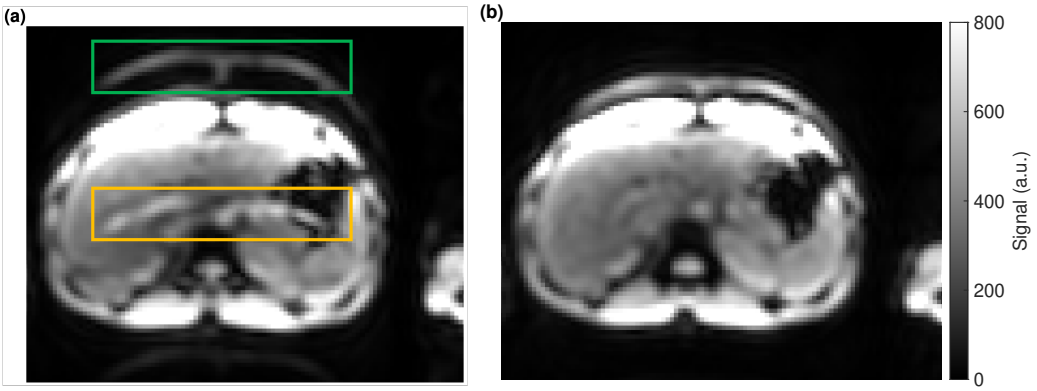


Figure 3.36: Raw GRE-EPI data at a FA of $65°$ with 3 times GRAPPA acceleration in the PE direction and an echo spacing of (a) $0.25\,\mathrm{ms}$ and (b) $0.1\,\mathrm{ms}$. The fat chemical shift, shown by the green rectangle, is aliased into a GRAPPA ghost as shown by the yellow rectangle. With an echo spacing 2.5 times smaller, the fat shifts 2.5 times less in the PE direction in (b) and does not show an aliasing ghost artefact in the same location as the images with an echo spacing of $0.25\,\mathrm{ms}$. Both images are shown without applying distortion correction.

Figure 3.37 shows the B_1^+ maps from the acquisitions with GRAPPA on and an echo spacing of $0.25\,\mathrm{ms}$ (a) and $0.1\,\mathrm{ms}$ (b), together with the corresponding T_1 maps. Profiles cutting the B_1^+ as well as the T_1 maps are shown in Figure 3.38. The maximum relative difference between the B_1^+ profiles for the region corresponding to the unfolded fat chemical shift was $+12.4\%$. The B_1^+ map with an echo spacing of $0.25\,\mathrm{ms}$ was clearly affected by an artefact as the B_1^+ field should vary smoothly as illustrated by the blue curve in Figure 3.38 (a). This B_1^+ factor increase resulted in a T_1 decrease of up to 22%. The T_1 profile corresponding to the red line in Figure 3.38 (b) registered a sudden decrease

in the artefact region with a mean T_1 of $718\,\mathrm{ms}$ between rows 134-141. The mean T_1 for the red curve increased to $895\,\mathrm{ms}$ for rows 142-152, not affected by the artefact, which was closer to the mean T_1 of the blue curve of $940\,\mathrm{ms}$. The $45\,\mathrm{ms}$ mismatch is consistent with a mismatch in the B_1^+ map, which might be a consequence of EPI distortion artefacts that were also not correctly unfolded by the GRAPPA kernel. In conclusion, GRAPPA should not be used in GRE-EPI based B_1^+ maps when fat is poorly suppressed.

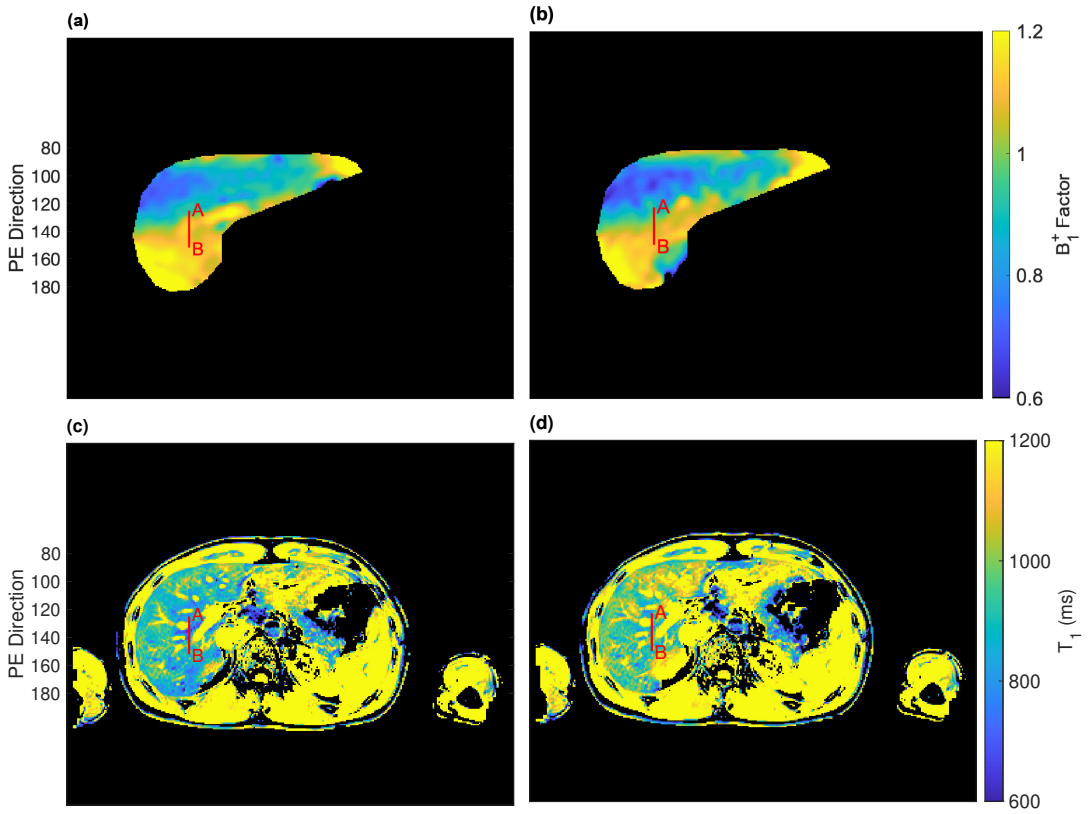


Figure 3.37: B_1^+ map with GRAPPA with three times acceleration in the PE direction and an echo spacing of (a) $0.25\,\mathrm{ms}$ and the corresponding (c) T_1 map. B_1^+ map acquired with and an echo spacing of (b) $0.1\,\mathrm{ms}$ and the corresponding (d) T_1 map. A profile from point A to point B is plotted in Figure 3.38 to evaluate the difference between the two B_1^+ and T_1 maps in the area affected by the unfolded fat chemical shift. The GRE-EPI data underwent distortion correction before calculating the B_1^+ maps. The B_1^+ maps were corrected for slice profile effects, but were not corrected for B_0 variations through slice.

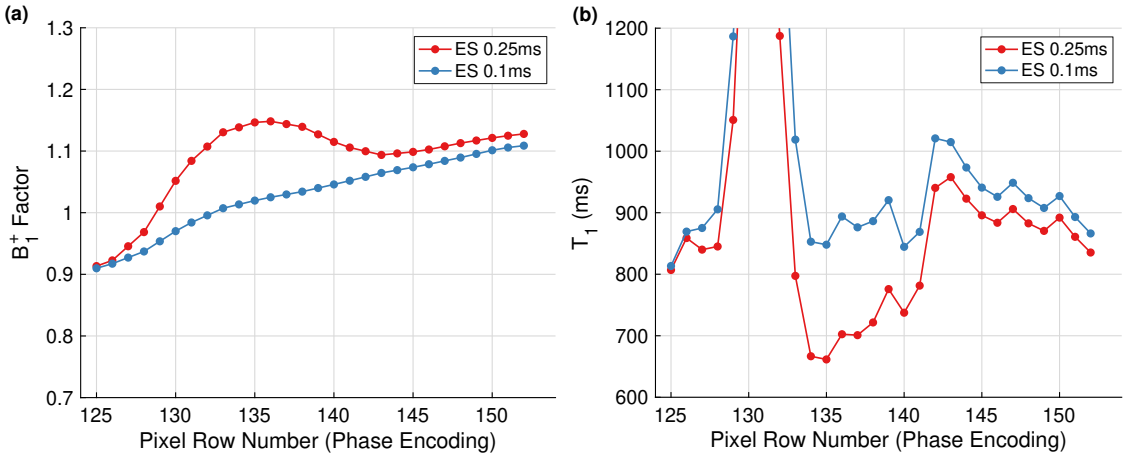


Figure 3.38: (a) B_1^+ factor profiles for an echo spacing of $0.25\,\mathrm{ms}$ in red and an echo spacing of $0.1\,\mathrm{ms}$ in blue. The elevated B_1^+ factor due to the unfolded fat chemical shift is clearly seen. The median B_1^+ factor difference between the two profiles, from rows 134-141, is $+10.6\%$ with a maximum difference of $+12.4\%$. (b) T_1 profiles for an echo spacing of $0.25\,\mathrm{ms}$ in red and an echo spacing of $0.1\,\mathrm{ms}$ in blue. The median T_1 difference between the two profiles, for rows 134-141, is -19.3% with a maximum difference of -22%. Rows 128 to 133 correspond to a blood vessel.

3.6 VFA SPGR Confounding Factors: Disruption of the Steady-State Signal

3.6.1 Incomplete Spoiling

Background

SPGR images are sequences run with a short TR to achieve high temporal resolution. Several RF pulses are applied to drive the longitudinal magnetisation into a steady-state. Given the TR is short compared to T_2, the magnetisation that remains in the transverse plane should ideally be fully dephased before the next RF excitation pulse otherwise, both the transverse and longitudinal magnetisation are driven to the steady-state. If the transverse magnetisation is not set to zero, the steady-state reached will present T_2 contrast and thus deviate from the steady-state signal (Equation (2.55)) which assumes that only the longitudinal magnetisation is affected by the RF pulses. In the liver, assuming a normal iron concentration of $1\,\mathrm{mg/g}$ the T_2 is approximately $22\,\mathrm{ms}$ [24]. Thus, for a TR of $4.1\,\mathrm{ms}$ only 17% of the transverse magnetisation will undergo T_2 decay before the next RF excitation pulse, highlighting the need to spoil the remaining transverse magnetisation.

Several techniques have been proposed to eliminate the transverse magnetisation, known in the literature as spoiling. RF spoiling results in artefact-free images with a T_2 independent steady-state [84]. RF spoiling or RF phase cycling consists in applying RF pulses at each TR interval with a different phase. The spins from each RF excitation pulse will acquire a distinct phase evolution and cancel each other's contribution through destructive interference. The net result is zero coherent transverse magnetisation before each RF pulse. For the magnetisation to achieve steady-state, the RF phase increment needs to be independent of the number of RF pulses. Zur et al. [84] found that a necessary condition for this independence is that the RF pulse phase increments linearly by a constant angle every TR. Furthermore, Zur et al. [84] showed that a phase increment of 117° or 123° results in nearly full cancellation of transverse magnetisation for a large range of physiologically relevant T_1s/TR, T_2s/TR, and excitation FAs between 0° and 90°. Figure 3.39 highlights the importance of a careful choice of the RF phase increment. However, even with a 117° phase increment at an excitation FA of 15°, the signal deviates from the predicted steady-state signal which assumes perfect spoiling. Any deviation of the acquired spoiled GRE signal from the predicted steady-state signal due to incomplete spoiling will result in inaccurate T_1 values when fitting the signal to the steady-state model. On a $3\,\mathrm{T}$ Prisma Siemens scanner the default RF phase increment is 50°. As shown in Figure 3.39, this will result in a signal lower than the steady-state. The lower signal mimics a longer T_1 relaxation resulting in T_1 overestimation (Figure 3.40). In conclusion, a correction for incomplete spoiling is essential for an accurate estimate of T_1 using the VFA SPGR sequence.

Preibisch and Deichmann [85] proposed that RF phase increments of 118.2° or 121.8° give accurate T_1 values for white matter (WM) and grey matter (GM), at a $TR = 7.5\mathrm{ms}$ and optimal FAs of 4° and 18°, but are situated in a region where the slope of T_1 with RF phase increment is large. The authors suggest that any hardware drifts, physiological instabilities, or motion can result in changes of the RF phase increment. For example, they estimated that changes of only 1° result in T_1 variations as high as 9.5%. Those authors

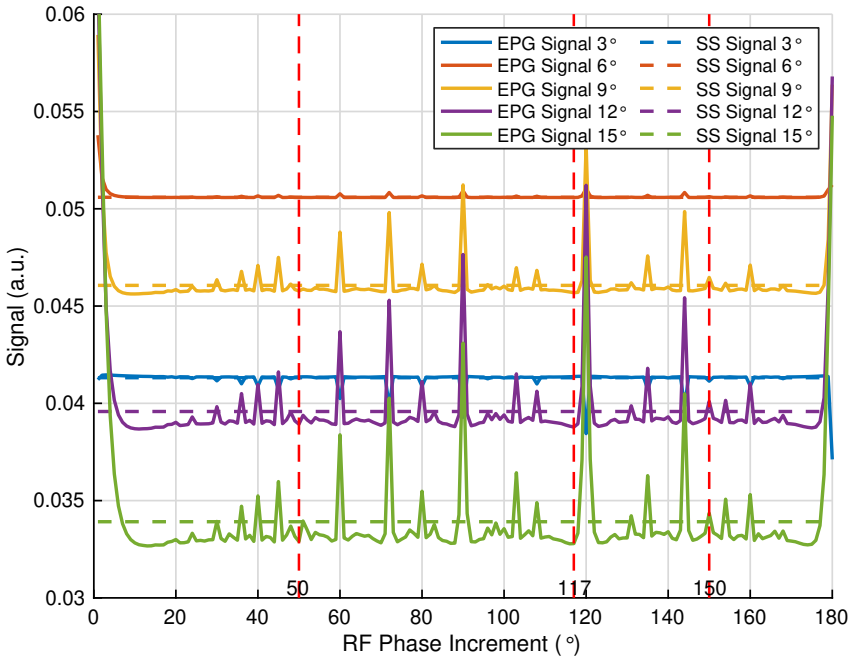


Figure 3.39: SPGR signal dependence on RF spoiling phase increment simulated for FAs of $3°$ (blue), $6°$ (orange), $9°$ (yellow), $12°$ (purple) and $15°$ (green) through the extended-phase-graph (EPG) framework (solid line) and the steady-state (SS) theoretical equation (dashed line) with parameters: $T_1 = 800\,\mathrm{ms}$, $T_2 = 30\,\mathrm{ms}$ and 1500 RF pulses. A careful choice of the RF phase increment is crucial to avoid large deviations of the signal from the theoretical steady-state prediction. The RF spoiling phase increments chosen by the different vendors are highlighted by the vertical red dashed lines: $50°$ for Siemens, $117°$ for GE and $150°$ for Philips.

developed a correction for incomplete spoiling based on an assumed linear relationship between the true T_1 and the T_1 predicted by fitting the incomplete spoiling signal to the steady-state equation. The intercept and the slope varied quadratically with the B_1^+ correction factor, modelled between 0.7 and 1.3, for two FAs of $4°$ and $18°$, a TR of $7.6\,\mathrm{ms}$, and a range of T_1s between $700\,\mathrm{ms}$-$1800\,\mathrm{ms}$. In phantom experiments, the error in T_1 decreased from 12% to less than 1% after spoiling correction. *In vivo*, the T_1 values were still $100\,\mathrm{ms}$ higher than IR EPI reference values. It should be noted that their correction is based on fitting T_1 to a linear form of the steady-state equation obtained using the small-angle approximation.

An alternative correction for incomplete spoiling was proposed by Baudrexel et al. [86]. These authors assume the steady-state signal is valid in the case of incomplete RF spoiling, provided an extra correction is applied to the FA, in addition to the B_1^+ mapping correction. According to the authors, an RF phase increment of $50°$ gave systematic

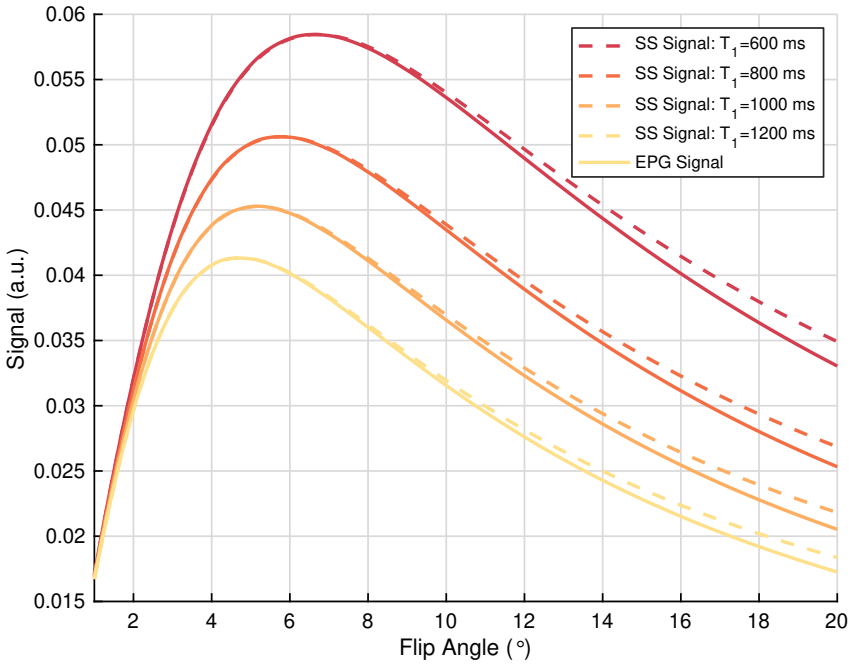


Figure 3.40: SPGR steady-state signal as a function of the excitation FA represented in dashed lines for different T_1 values of $600\,\mathrm{ms}$ (red), $800\,\mathrm{ms}$ (dark orange), $1000\,\mathrm{ms}$ (orange) and $1200\,\mathrm{ms}$ (yellow). Solid lines represent the extended-phase-graph (EPG) signal modelling the effect of incomplete spoiling with matching T_1 colours. The EPG signal was simulated with a $TR = 4.1\,\mathrm{ms}$, $T_2 = 30\,\mathrm{ms}$ and an RF phase increment of $50°$. For these parameters, incomplete spoiling decreases the signal from the steady-state signal, with the deviation increasing as the FA value increases above the Ernst angle.

errors in T_1 as high as 13% in phantom and 24.2% *in vivo* when large FAs of $32°$ were used in the VFA acquisition. After applying the proposed incomplete spoiling correction, the T_1 errors decreased to 0.3% for the phantom, and *in vivo* to 5.2% for WM, and 9.9% for GM. The approach of Baudrexel et al. is in line with the observation that larger excitation FAs, will need larger incomplete spoiling correction factors. However, their observation that the proposed spoiling correction is independent of T_1 does not agree with Figure 3.40 where the deviation between the steady-state and the incompletely spoiled signal changes as a function of T_1.

In this work, a general approach for correcting incomplete spoiling was taken which does not make any underlying assumptions regarding the correction's dependence on T_1 values, nor does it use either the small angle approximation or the linear form of the steady-state equation. The correction is based on extended-phase-graph (EPG) simulations over a range of liver physiological TR/T_1 and TR/T_2 values. EPG gives an

accurate estimate of the echo intensity in the presence of incomplete spoiling [87], and it is used to re-scale the signal to the theoretical steady-state value.

Methods

For the VFA SPGR acquisition, the signal from the outer k-space lines is not acquired in the steady-state. The time to reach k-space centre was $6.9\,\mathrm{s}$, and since TR equals $4.1\,\mathrm{ms}$, it takes approximately 1683 TRs to reach k-space centre. Steady-state is reached after $3T_1$s [31] which would correspond to $4.8\,\mathrm{s}$ for an upper limit T_1 value of $1600\,\mathrm{ms}$ for liver tissue. Thus, the signal acquired near k-space centre should be in the steady-state.

Five important factors affecting incomplete spoiling of the magnetisation are the excitation FAs, the expected T_1 and T_2 range of the tissue of interest, the sequence TR, and the RF phase increment. Considering the default RF phase increment of $50°$ adopted by Siemens Prisma scanners, EPGs [88] were used to simulate the transverse signal for a range of T_1s ($500\,\mathrm{ms}$-$1600\,\mathrm{ms}$ in steps of $100\,\mathrm{ms}$), a range of T_2s ($20\,\mathrm{ms}$-$35\,\mathrm{ms}$ in steps of $5\,\mathrm{ms}$) [18] and a range of excitation FAs ($1°$-$20°$ in steps of $1°$). A fixed TR of $4.1\,\mathrm{ms}$ was used as this allows whole liver coverage within a $15\,\mathrm{s}$ breath-hold. Twenty degrees was used as the maximum FA as it is equal to the product of the maximum FA allowed at the scanner of $15°$ (for a TR of $4.1\,\mathrm{ms}$) and a B_1^+ correction factor of 1.33. The incomplete spoiling correction transformed the acquired signal to the steady-state space. To achieve this, the acquired signal was multiplied by a correction factor equal to the ratio between the theoretical steady-state signal and the simulated EPG signal at the estimated values of T_1 and the true FA. The incomplete spoiling correction was incorporated into the NLLS T_1 fitting procedure following an iterative approach. An initial guess for T_1 was estimated from the ratio between the signals acquired at the two lowest distinct FAs, as these are less affected by incomplete spoiling (Figure 3.40). The initial T_1 estimate together with the B_1^+ corrected FAs were used to interpolate the incomplete spoiling correction factor curves (Figure 3.41), calculated offline for a range of grid points in T_1 and FAs as specified above and a fixed T_2 of $30\,\mathrm{ms}$. The acquired SPGR signal was multiplied by the interpolated correction factor and subsequently fitted

to the theoretical steady-state model to refine the initial T_1 estimate. The incomplete spoiling correction was iterated at each step with the updated T_1 estimate. The iterative procedure stops when the difference between two T_1 estimates was less than $1\,\mathrm{ms}$ or a total of 5 iterations was reached. A flow diagram of the T_1 map function including the correction for incomplete spoiling is illustrated in Figure 4.18.

Because liver T_2 was not measured with the VFA SPGR sequence, it was necessary to use a fixed T_2 value that would give the best overall results for the B_1^+ factor, T_1 and T_2 parameter space observed in the liver *in vivo*. Given a range of physiological T_2s in healthy volunteers varying between $20\,\mathrm{ms}$ and $35\,\mathrm{ms}$ [18], a T_2 value of $30\,\mathrm{ms}$ was found to give the smallest error between the true T_1 and the fitted T_1 including the developed incomplete spoiling correction. This error was always less than 2.8% over the full range of T_2s ($20\,\mathrm{ms}$-$35\,\mathrm{ms}$), T_1s ($700\,\mathrm{ms}$-$1200\,\mathrm{ms}$ [71]) and B_1^+ factors ($0.59 - 1.14$ [61]). The nominal FA set used in the fit was [3 3 15 15]°.

Monte Carlo simulations were used to find the error and standard deviation in T_1 for two sets of FAs and two cases: one without and another case with the incomplete spoiling correction. The first set of FAs was restricted to angles of [2 2 3 4]°, i.e., angles below the Ernst angle for a T_1 of $1200\,\mathrm{ms}$ and TR of $4.1\,\mathrm{ms}$. The second set consisted of [2 2 15 15]°, using the largest FA of $15°$ available at the scanner. The error was simulated over a range of T_2s ($20\,\mathrm{ms}$-$35\,\mathrm{ms}$ in steps of $5\,\mathrm{ms}$) and a range of T_1s ($500\,\mathrm{ms}$-$1600\,\mathrm{ms}$ in steps of $100\,\mathrm{ms}$), with each T_1 and T_2 combination simulated 10000 times. The EPG and the steady-state simulated signals were corrupted with zero mean additive Gaussian noise, corresponding to an SNR of 25 at a nominal FA of $2°$, T_1 of $800\,\mathrm{ms}$ and TR of $4.1\,\mathrm{ms}$. The error was simulated for the largest B_1^+ factor of 1.14 [61] as the error in T_1 due to incomplete spoiling increases with the FA value. The larger the FA, the larger the amount of longitudinal magnetisation flipped to the transverse plane, hence the greater the incomplete spoiling.

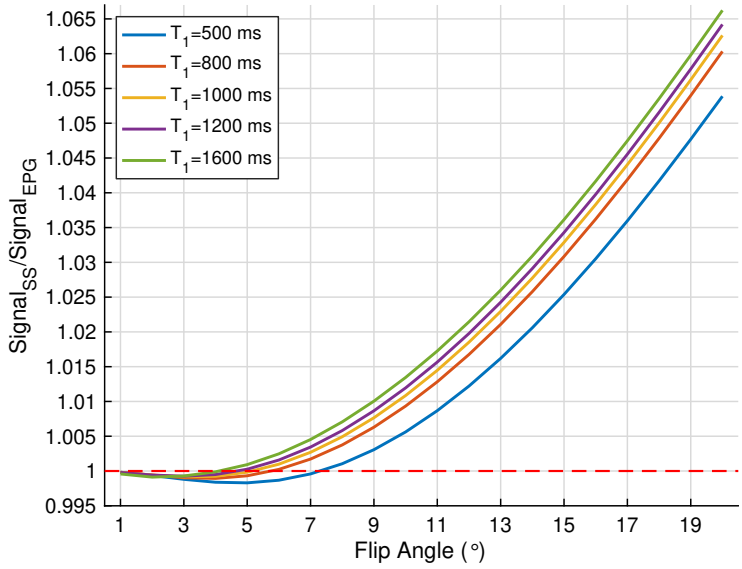


Figure 3.41: Incomplete spoiling correction factor given by the ratio between the theoretical steady-state (SS) signal and the extended-phase-graph signal as a function of the true FA in degrees for a range of T_1s varying between $500\,\mathrm{ms}$ (blue) and $1600\,\mathrm{ms}$ (green). Representative T_1 values, observed in the liver of healthy volunteers, of $800\,\mathrm{ms}$ (orange), $1000\,\mathrm{ms}$ (yellow) and $1200\,\mathrm{ms}$ (purple) are also plotted. This plot shows the correction factor varies with the true FA as well as T_1, hence the iterative procedure for fitting T_1.

Results

Simulations

The T_1 was overestimated when not correcting the signal for incomplete spoiling using the FA set of [2 2 15 15]° with an RF phase increment of $50°$, TR of $4.1\,\mathrm{ms}$ over a range of T_1s ($700\,\mathrm{ms}$-$1200\,\mathrm{ms}$) and a range of T_2s ($20\,\mathrm{ms}$-$35\,\mathrm{ms}$). The relative error in T_1 reached values of 7.7% for a T_1 of $1200\,\mathrm{ms}$ and T_2 of $35\,\mathrm{ms}$ (Figure 3.42). Applying the developed incomplete spoiling correction, the relative error in T_1 was approximately zero for a T_2 of $30\,\mathrm{ms}$, as this was the fixed T_2 adopted for the correction, and it reached extreme values of -2.1% for a T_2 of $20\,\mathrm{ms}$ and +1.3% for a T_2 of $35\,\mathrm{ms}$. The variation in the T_1 errors was about two times larger over the range of T_2 values considered compared to the T_1 error variation over the T_1 range (Figure 3.42). Using FAs below the Ernst angle of [2 2 3 4]° for a T_1 of $1200\,\mathrm{ms}$ and TR of $4.1\,\mathrm{ms}$, the maximum error in T_1 without any incomplete spoiling correction was below 1%. However, using low FAs has the cost of higher T_1 imprecision with a T_1 CoV of 15%. In contrast, using higher FAs of

[2 2 15 15]° improved the T_1 CoV by more than a factor of two (T_1 CoV of 7%).

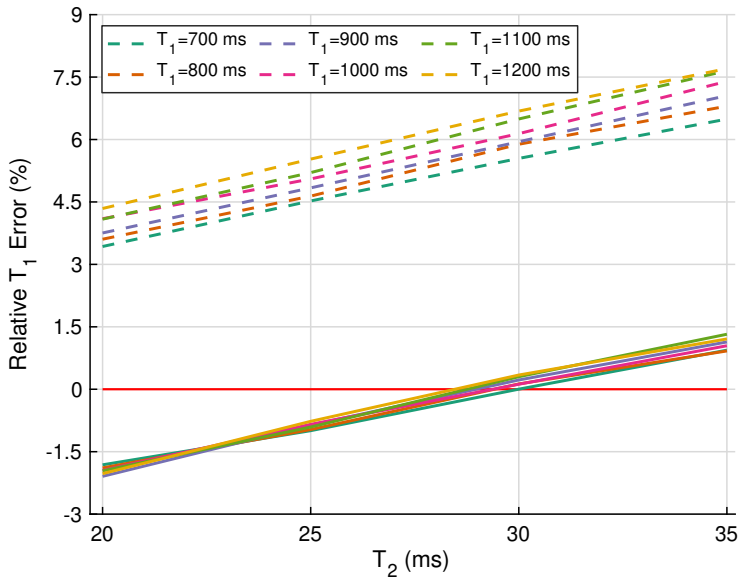


Figure 3.42: Simulated relative error in T_1 (%) due to incomplete spoiling (dashed lines) for a range of true T_1s between $700\,\mathrm{ms}$ and $1200\,\mathrm{ms}$ and a range of T_2s between $20\,\mathrm{ms}$ and $35\,\mathrm{ms}$. The T_1 is always overestimated. The relative T_1 error decreases after applying the incomplete spoiling correction (solid lines).

Phantom

Figure 3.43 shows that the T_1 error in the *FDA4-T1* phantom without incomplete spoiling correction using FAs of [2 2 15 15]° reached a median value of 7.4% with an IQR of [4.4 9.6]% across all vials for the 4 central slices. Using the developed correction, the T_1 error decreased to a median value of -0.3% and a narrower IQR of [-2.5 2.1]%. Using FAs below the Ernst angle of [2 2 3 4]° resulted in unbiased T_1 estimates with a median error of -0.7% without applying the incomplete spoiling correction. The T_1 precision was not affected by the low FAs as the phantom is a system with a high SNR of 103, measured from the difference between two VFA images acquired at nominal FAs of $2°$.

Without correcting the signal for incomplete spoiling, the NLLS fit resulted in a sum of squared residuals (SSR) of 43.0 (Figure 3.44), for one voxel in the phantom. After correcting the signal acquired for incomplete spoiling, the data fitted better to the steady-state model and consequently the SSR decreased to 7.7 (Figure 3.45). For an SNR of 157 at a FA of $3°$, the noise level was 2.2, and the residuals of the fit to the corrected data were all less than or equal to this noise level. With the developed incomplete spoiling correction,

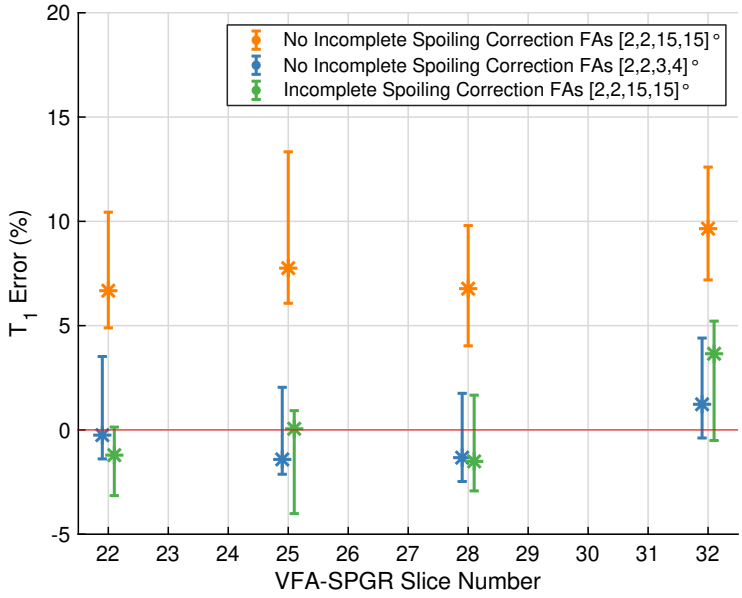


Figure 3.43: T_1 Error in percent, relative to the IR SE, without incomplete spoiling correction to the SPGR signals acquired at FAs of [2,2,15,15]° (orange). The median T_1 error was 7.4% with an interquartile range (IQR) of [4.4 9.6]%. Using the SPGR signal acquired at FAs of [2,2,3,4]° (blue) without incomplete spoiling correction the median T_1 error decreased to -0.7% and the IQR to [-3.8 0.8]%. Applying the incomplete spoiling correction to the signal acquired at FAs of [2,2,15,15]° (green), the median T_1 error was -0.3% with an IQR of [-2.5 2.1]%.

the fitted T_1 was $1016\,\mathrm{ms}$ which was very close to the gold-standard T_1 of $1022\,\mathrm{ms}$.

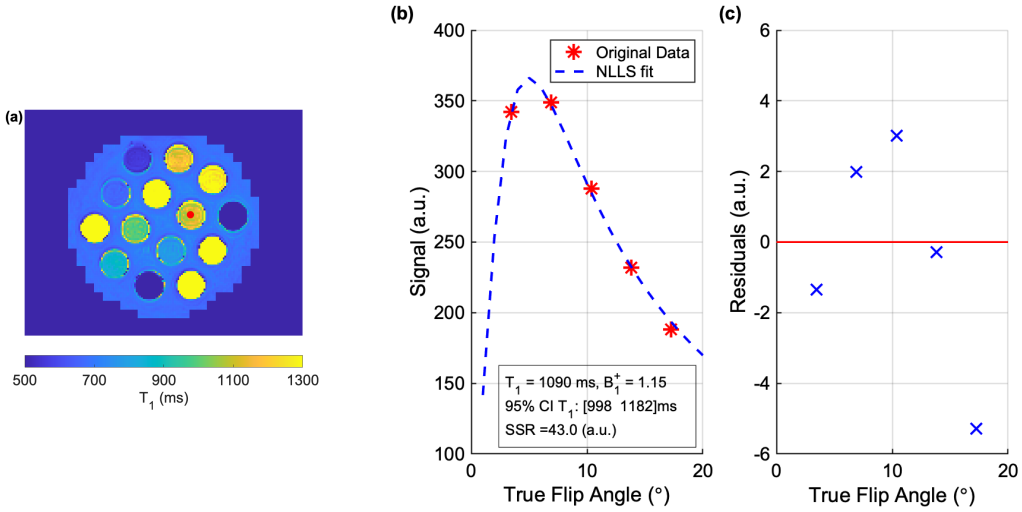


Figure 3.44: (a) T_1 Map of the *FDA4-T1* phantom without correcting for incomplete spoiling. Red point showing the location of the voxel (126,176) used in the analysis of residuals. (b) NLLS fit (dashed blue line) to the acquired data (red stars) without correcting for incomplete spoiling and the corresponding residuals (c). The fitted T_1 was $1090\,\mathrm{ms}$ and the sum of the residuals squared (SSR) was 43.0 (arbitrary signal units). The residuals showed a pattern similar to the steady-state model curve indicating an underlying bias. These data were acquired at nominal FAs of [3 6 9 12 15]°.

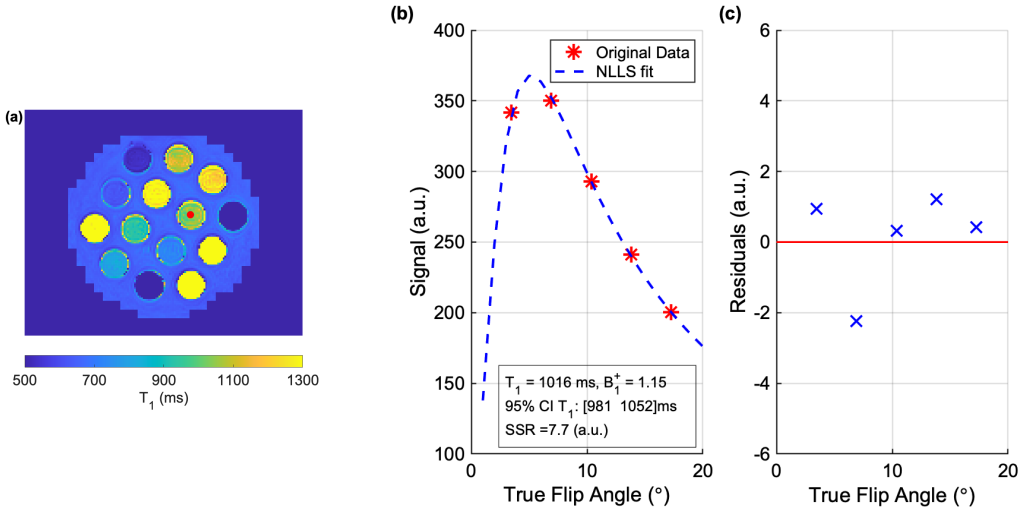


Figure 3.45: (a) T_1 Map of the *FDA4-T1* phantom with incomplete spoiling correction. Red point showing the same voxel analysed in Figure 3.44. Note the change in colour for this vial corresponding to a lower T_1 compared to Figure 3.44. (b) NLLS fit (dashed blue line) to the acquired data corrected for incomplete spoiling (red stars). The residuals (c) are smaller than in Figure 3.44 with a sum of squared residuals (SSR) equal to 7.7. The fitted T_1 was $1016\,\mathrm{ms}$, closer to the gold standard IR SE T_1 of $1022\,\mathrm{ms}$. These data were acquired at nominal FAs of [3 6 9 12 15]°.

In Vivo

The T_1 map *in vivo* uncorrected for incomplete spoiling was on average $51\,\mathrm{ms}$ higher than the corrected map for the posterior part of the liver (Figure 3.46). The anterior portion of the liver had a smaller average difference of $25\,\mathrm{ms}$ as this was a location with a B_1^+ factor less than 1. The posterior part had B_1^+ factors slightly larger than one, resulting in higher excitation FAs and thus more incomplete spoiling.

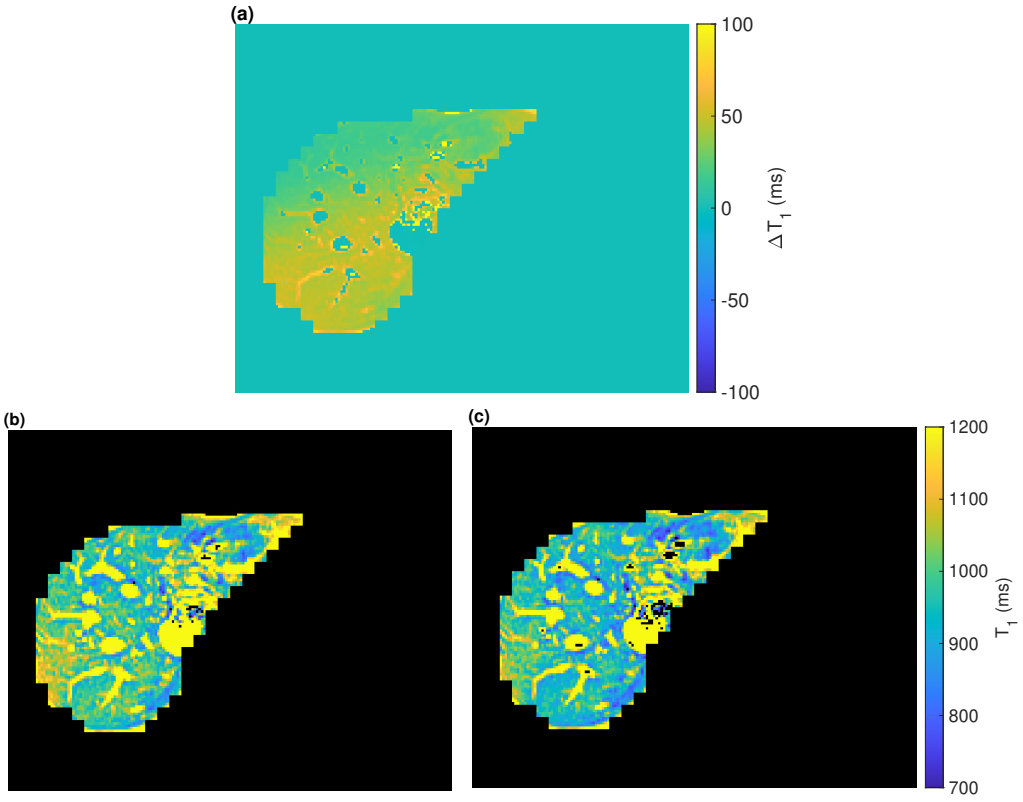


Figure 3.46: (a) T_1 map difference between the (b) T_1 map uncorrected for incomplete spoiling and the (c) T_1 map with the incomplete spoiling correction. The T_1 maps were reconstructed from the SPGR signal acquired at nominal FAs of [2 2 15 15]°.

3.6.2 Spatial Saturation

Background

For fast imaging sequences such as SPGR, where TR is much shorter than T_2 or T_1, steady-state (SS) is achieved by subjecting spins in the imaging volume to a train of RF pulses on-resonance. When the amount of magnetisation tipped to the transverse plane by the RF pulse equals the amount of longitudinal magnetisation recovered through T_1 relaxation during time TR, the magnetisation is said to be in a steady-state. A population of blood spins flowing into the slice will not be subject to the same number of RF pulses as the stationary tissue within the imaging volume. Therefore, the magnetisation of the spins in blood is less saturated and results in a higher signal compared to stationary tissue. Blood moving at a larger velocity through the slice, e.g., blood in the aorta, will result in a larger signal enhancement than slower moving blood, e.g., blood in capillaries. In addition to signal modulation, flowing blood also results in ghosts along

the PE direction known as zipper-like artefacts.

Spatial pre-saturation pulses suppress the signal from tissues outside of the FoV [89]. Its main application is to reduce flow artefacts, respiratory motion artefacts and aliasing artefacts along the PE direction, arising from tissue excited outside of the FoV. Before the imaging RF excitation pulses are played out, spatially selective 90° saturation pulses excite a volume of tissue (slab) surrounding the desired imaging slab. Spins within the FoV are not affected by the saturation pulses as these pulses are played off-resonance. The 90° RF saturation pulses are specially designed to impose maximum phase dispersion on the flipped magnetisation. Nonetheless, to further dephase any remaining coherent transverse signal, large spoiler gradients are used across the three spatial encoding directions. The time between the saturation pulse and the imaging excitation RF pulse should be just a few ms to prevent recovery of the longitudinal magnetisation through T_1 relaxation.

In quantitative imaging, spatial saturation pulses should not interfere with the ability of the magnetisation to reach steady-state. Siemens implements spatial saturation in the SPGR sequence with two RF pulses interwoven into the block of RF excitation pulses used to acquire each PE line which lasts for $148\,\mathrm{ms}$. It was hypothesised that spatial saturation will perturb the steady-state and thus result in an inaccurate estimation of T_1 when fitting the signal to the steady-state model.

Methods

The total duration of a single breath-hold SPGR acquisition per FA was $15.8\,\mathrm{s}$ using Caipirinha [90] parallel imaging with an acceleration factor of 3 along the slice direction. At the start of the acquisition reference lines were acquired for a duration of $2.0\,\mathrm{s}$. The rest of the acquisition time was used to acquire k-space data for each PE line. Starting from the first PE line, it took approximately $6.9\,\mathrm{s}$ to reach the PE line at k-space centre.

The 3D VFA SPGR sequence which runs on the Siemens $3\,\mathrm{T}$ Prisma using VE11 software was simulated by Dr. Iulius Dragonu (Siemens Healthineers, UK), using the parameters described in Section 4.1. The RF pulses and gradients along the three spatial encoding directions were extracted from *dsv* encoded files. Figure 3.47 shows the pulse

sequence diagram corresponding to the block of RF pulses repeated for each PE line. For a total of 260 PE lines, with 3 times acceleration, the block was repeated approximately 86 times during the acquisition. Focusing on the RF pulse channel, there were two saturation pulses at the start of the block followed by 36 slab selective imaging excitation pulses of approximately $0.7\,\mathrm{ms}$ duration. The time interval between adjacent imaging pulses was equal to one TR of duration $4.1\,\mathrm{ms}$. The train of 36 RF pulses, representing 36 partitions, lasted approximately $148\,\mathrm{ms}$ before the next set of two saturation pulses were applied.

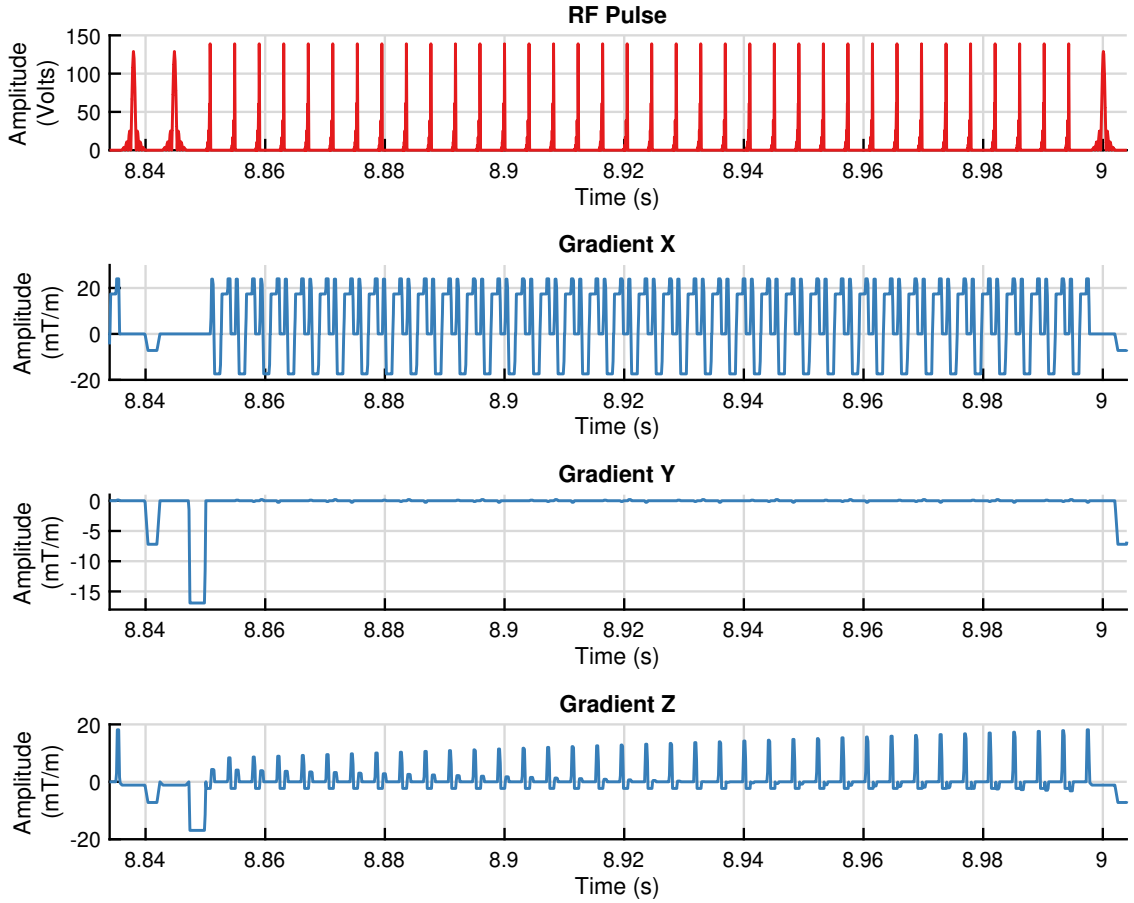


Figure 3.47: Pulse sequence diagram of the 3D VFA SPGR sequence including the RF excitation pulse (red) and the gradients (blue) along the FE (X direction), the PE (Y direction) and the slice encoding direction (Z direction). Only the portion corresponding to k-space centre, almost null PE gradients, is shown for clarity. The RF pulse channel consists of two saturation pulses at the start followed by 36 RF excitation pulses encoding the spatial information for 36 different partitions along the slice encoding direction.

A difference was observed in the T_1 maps reconstructed from signal acquired with parallel imaging on and off. The k-space centre was reached after $6.9\,\mathrm{s}$ with parallel

imaging, which is more than the $3.6\,\mathrm{s}$ needed for a liver tissue with a T_1 of $1200\,\mathrm{ms}$ to reach steady-state. Thus, no difference is expected in the T_1 maps from using parallel imaging. It was hypothesised that the T_1 difference originated from using spatial saturation. To test this hypothesis, phantom data was acquired for the SPGR sequence with FAs of [3,6,9,12,15]°. Each FA was acquired with 4 different combinations of parallel imaging and saturation, named special saturation on the Siemens' console and applied in the foot-head direction:

1. Special Saturation On and Caipirinha On
2. Special Saturation On and Caipirinha Off
3. Special Saturation Off and Caipirinha On
4. Special Saturation Off and Caipirinha Off

The phantom, a *Calimetrix QC0025*, was provided by Perspectum and it consisted of 3 different sets of vials (Figure 3.48). Only the set of vials numbered 1 to 5 corresponding to varying T_1s were used. At the time of this acquisition, the GRE-EPI protocol was not finalised as the different confounding factors were still under study. Therefore, to correct B_1^+ inhomogeneities when fitting the signal, the native B_1^+ mapping sequence on the $3\,\mathrm{T}$ Prisma scanner was adopted. This sequence is based on comparing two fully-recovered TurboFLASH images, one image is acquired with a preconditioning RF pulse and the other without; the signal ratio yields the actual FA of the preconditioning pulse. Imaging parameters were: FoV $= 450 \times 450\mathrm{mm}^2$, matrix $= 32 \times 32$ (interpolated to 64×64), slice thickness of $8\,\mathrm{mm}$, 1 slice, TR/TE $= 10000/1.41\mathrm{ms}$, with FS. The preconditioning RF pulse had a nominal FA of $80°$ and a readout FA of $8°$.

Results

Figure 3.49 confirms that parallel imaging does not affect the signal when saturation was off. On the other hand, with saturation on, large differences exceeding 8% were observed between the SPGR signals with parallel imaging on and off.

Figure 3.50 (a) shows that when saturation was turned on, T_1 differences of on average 10% existed between parallel imaging on and off. On the other hand, when

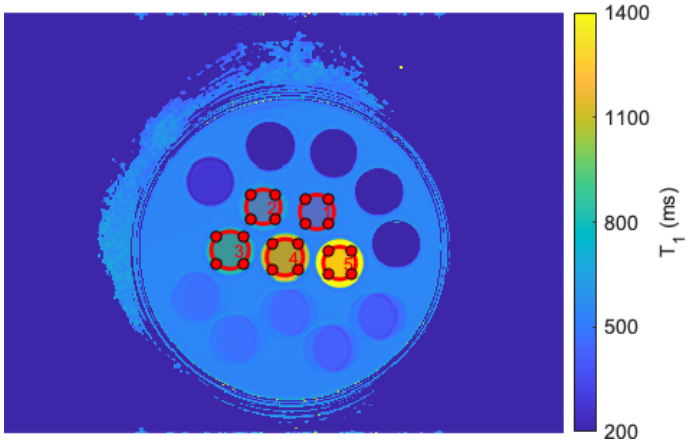


Figure 3.48: Gold standard IR SE T_1 map of the *Calimetrix QC0025* phantom. Vials numbered 1 to 5 correspond to T_1s of $548\,\mathrm{ms}$, $633\,\mathrm{ms}$, $790\,\mathrm{ms}$, $1044\,\mathrm{ms}$ and $1429\,\mathrm{ms}$, respectively. Vials above or below the numbered vials, with varying T_2^* and fat-fractions, respectively were not used in the analysis.

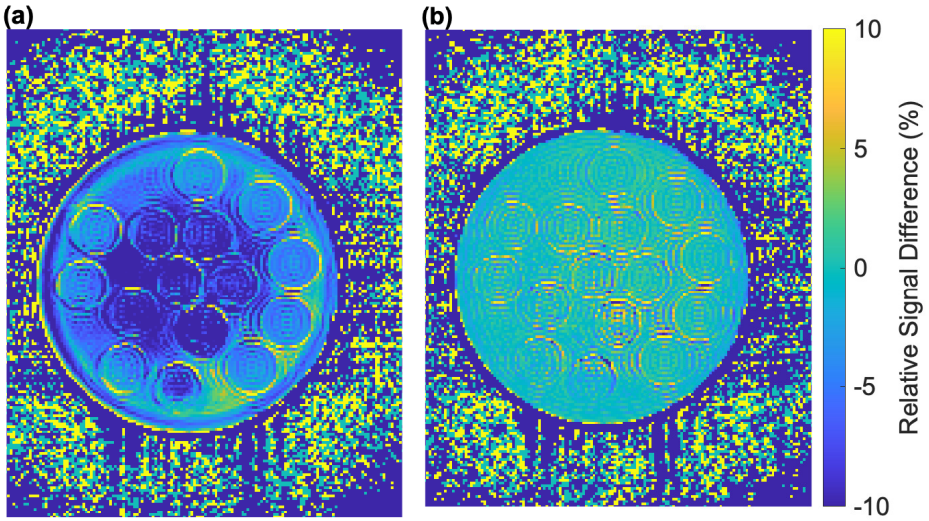


Figure 3.49: Percent difference in SPGR signals between Parallel Imaging (PI) on and off with spatial saturation (a) on and (b) off, normalised by PI off. With spatial saturation, PI on resulted in signals lower by 8% or more relative to PI off, for the 5 vials with varying T_1 values. On the contrary, turning off saturation resulted in small differences between PI on and off.

saturation was off the T_1 values agreed independent of whether parallel imaging was on or off (Figure 3.50 (b)).

When turning saturation off, the SPGR steady-state is achieved regardless of whether parallel imaging is on or off. With saturation on, there is no longer a constant TR between each block of 36 partitions, but instead an $18.6\,\mathrm{ms}$ time interval during which the longitudinal magnetisation growth is larger than the amount of magnetisation flipped by the 3D SPGR excitation pulse. This violates the condition to achieve the SPGR

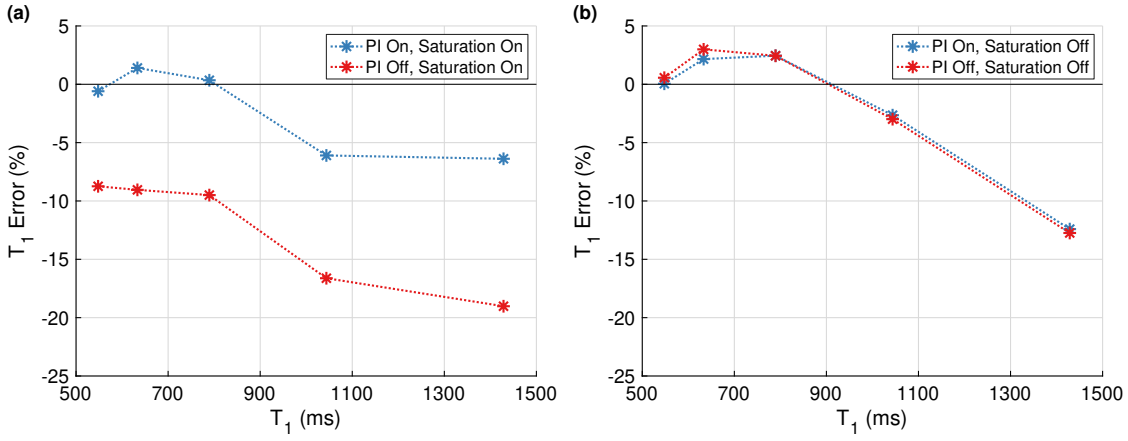


Figure 3.50: T_1 error in percent, relative to the IR SE, with saturation (a) on and (b) off. Blue stars represent parallel imaging (PI) on while the red stars represent parallel imaging off. Using saturation resulted in T_1 differences between parallel imaging on and off of on average 10%. When saturation was turned off, the mean T_1s for the 5 different vials agreed. Note that these T_1 values were corrected for B_1^+ inhomogeneities using the native Siemens B_1^+ map.

steady-state. A further indication that saturation affects the T_1 estimation were the increased residuals observed in the fit when saturation was on (Figure 3.51). In conclusion, saturation pulses perturb the SPGR steady-state magnetisation and should be turned off at the scanner interface. The impact of inflowing blood could be an artefact that requires monitoring.

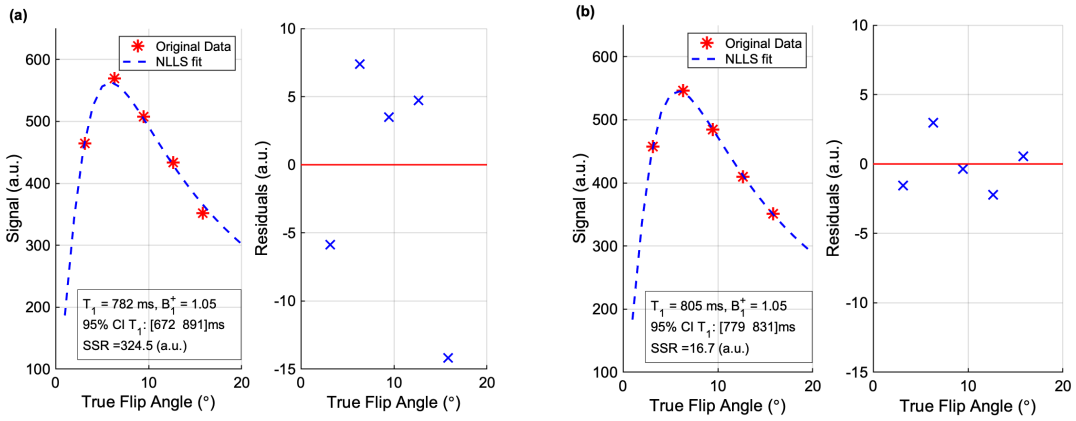


Figure 3.51: (a) NLLS fit (dashed blue line) to the acquired data (red stars) with saturation on and the corresponding residual plot for one pixel (143,111) in the phantom. The sum of squared residuals (SSR) was 324.5. (b) NLLS fit (dashed blue line) to the acquired data (red stars) with saturation off and the corresponding residual plot with a SSR of 16.7.

3.7 Accuracy of the Developed 3D T_1 mapping method

3.7.1 Phantom

Applying all the corrections developed to the SPGR signal resulted in a final T_1 map in the phantom showing an excellent agreement with the gold standard IR SE (Figure 3.52). The weighted least squares linear fit between the SPGR T_1, for all 14 vials across 4 slices, and the gold standard IR SE resulted in a slope of 1.026 with a 95% CI between 1.008 and 1.043. Across the physiologically relevant liver T_1 values at $3\,\mathrm{T}$ (740-1211ms), the IQR relative error was [-2.3 0.4]%. The weighted root mean squared normalised error between the SPGR T_1 and the gold standard T_1 was 2.5%. The weights were equal to the inverse of the SPGR T_1 standard deviation squared. Analysing the residuals between T_1s of $740\,\mathrm{ms}$ and $1211\,\mathrm{ms}$ there was a tendency to underestimate T_1 by $-7\,\mathrm{ms}$ on average, excluding T_1s from slice 32.

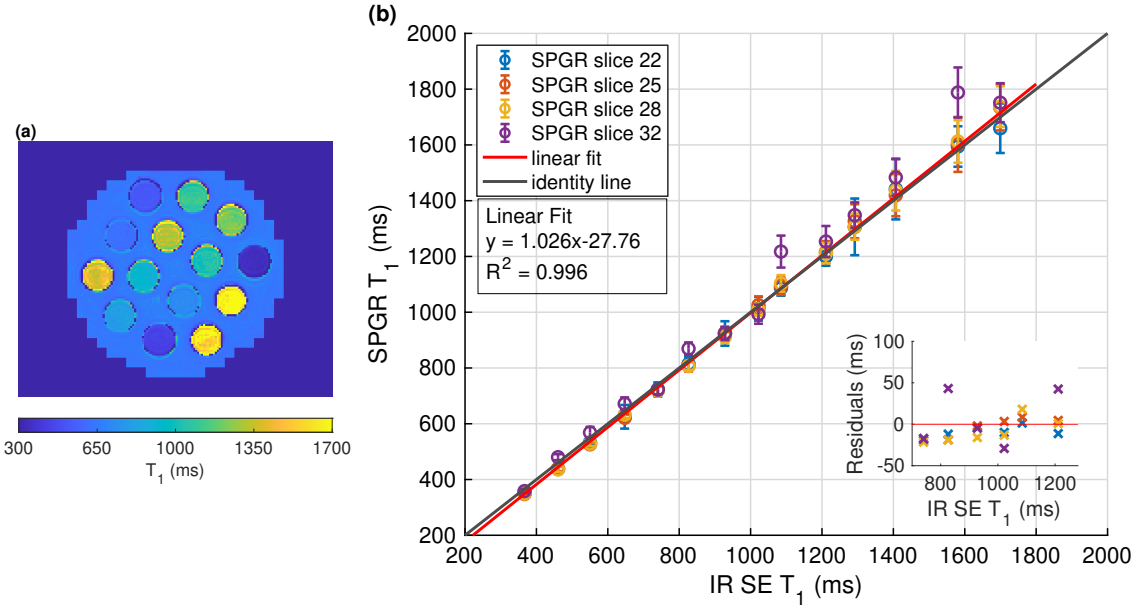


Figure 3.52: (a) Phantom T_1 map for slice 25, middle slice in the SPGR acquisition, after applying all the developed corrections. (b) SPGR T_1 with all the corrections as a function of the T_1 gold standard IR SE in the phantom for 14 different vials across 4 slices. Linear fit, in red, resulted in a slope of $1.026\,\mathrm{ms}$ with an intercept of $-27.76\,\mathrm{ms}$. The R^2 was 0.996.

3.7.2 *In Vivo*

Figure 3.53 shows the SPGR T_1 maps for one healthy volunteer in the three anatomical planes.

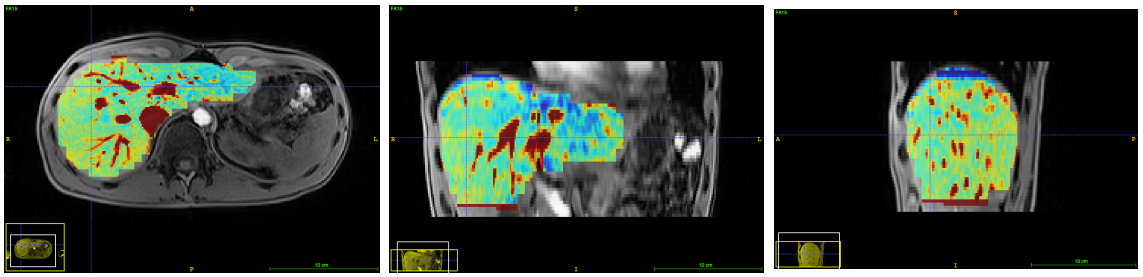


Figure 3.53: Axial, coronal and sagittal planes showing the 3D T_1 map overlaid on the FA $15°$ SPGR image using a colourmap scale [500 1500] ms.

Assessment of the Developed Corrections

In the absence of an *in vivo* gold standard method, it is important to develop tools to assess the effectiveness of the developed corrections. For this purpose, two assessment methods will be presented using one T_1 map from a healthy volunteer (Figure 3.54) with a total of 3036 T_1 values extracted from 22 T_1 map slices where 3 ROIs were drawn according to the criteria in Section 4.2.4.

Incomplete Spoiling Correction

The efficacy of the incomplete spoiling correction can be assessed by the degree to which the data can be modelled by the steady-state equation. For the ideal situation with a VFA SPGR signal which is perfectly described by the steady-state model, the relative difference in T_1, without and with B_1^+ corrections, is predicted to be equal to the B_1^+ factor squared minus one [62]. An accurate method for mapping T_1 should obey Equation (3.14).

$$\frac{\Delta T_1}{T_{1,\text{estimate}}} = \frac{T_{1,(B_1^+=1)} - T_{1,\text{estimate}}}{T_{1,\text{estimate}}} = (B_1^+)^2 - 1\,, \tag{3.14}$$

$T_{1,\text{estimate}}$ is the T_1 map after correcting for all the identified confounding factors, the B_1^+ factor is calculated using all the corrections proposed in this chapter, and delta T_1 is the difference between T_1 without correcting for B_1^+ inhomogeneities and $T_{1,\text{estimate}}$. A

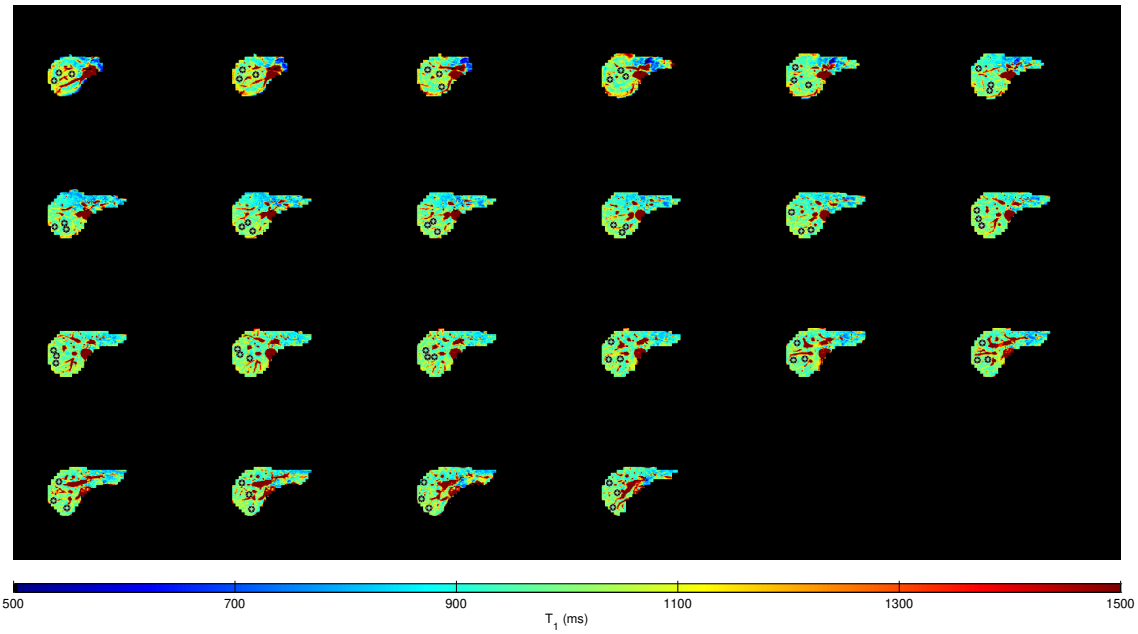


Figure 3.54: In vivo T_1 map in a healthy volunteer with three black circular ROIs drawn in each slice, each ROI contains $46\,\mathrm{pixels}$. Colourmap scale [500 1500] ms.

good agreement was obtained between the *in vivo* data and the theory (Figure 3.55). The theory curve was calculated according to Equation (3.14) and had no free fitting parameters. The linear approximation which corresponds to the rough rule of thumb that the relative error in T_1 equals twice the relative error in B_1^+ factor is applicable for small absolute relative errors in B_1^+ factor of less than 10% (Appendix, Section 3.10.3). In the absence of a gold standard T_1 map *in vivo*, the root mean squared error (RMSE) between the *in vivo* data and the theoretical curve was used as a surrogate for accuracy. The RMSE including a correction for incomplete spoiling was 0.006 while without this correction the RMSE was 0.040.

Assessment of the Remaining B_1^+ Bias in the T_1 Maps

The large co-variance between B_1^+ and T_1 can result in a perfect fit of the data to Equation (3.14) in the presence of an inaccurate B_1^+ map. Equation (3.14) is useful to detect deviations of the signal from the steady-state, but the overall T_1 accuracy should be complemented with another metric that assesses the accuracy of the B_1^+ map. Consequently, the B_1^+-related variation in T_1 metric was developed to infer the residual bias in T_1 due to the B_1^+ factor (Figure 3.56). After applying all the corrections

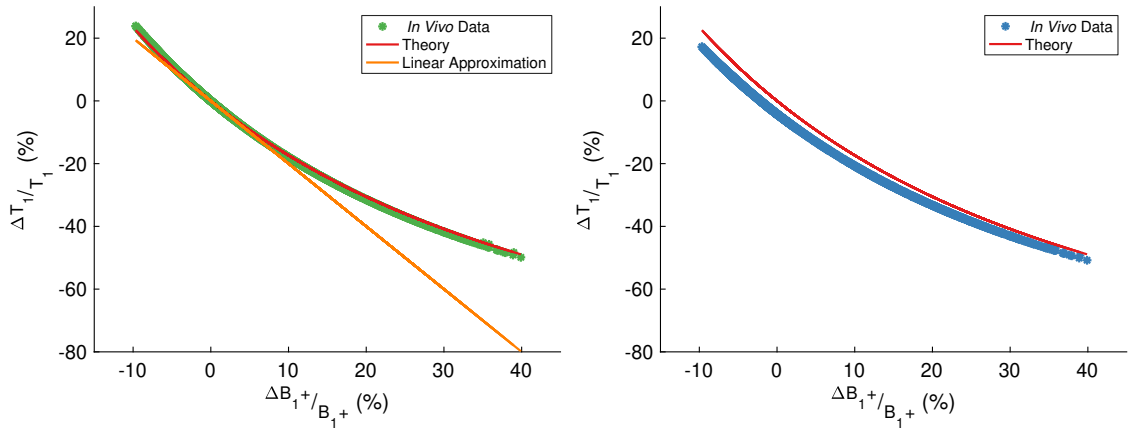


Figure 3.55: Relative difference in T_1 as a function of the relative difference in B_1^+ factor ($(1 - B_1^+)/B_1^+$) for an *in vivo* dataset, illustrated by the green stars, with correction for incomplete spoiling. There are a total of 3036 green stars. The theory line ($\Delta T_1/T_1 = \left(1/(1 + \Delta B_1^+/B_1^+)\right)^2 - 1$) in red is derived from Equation (3.14). The linear approximation curve in orange corresponds to $\Delta T_1/T_1 = -2(\Delta B_1^+/B_1^+)$. The same threshold scheme described in the methods of Section 3.3 was applied across 22 slices with liver. (b) Experimental relative difference in T_1 as a function of the relative difference in B_1^+ factor without correcting for incomplete spoiling is shown in blue.

to the data, the B_1^+-related variation in T_1 was reduced from $781\,\mathrm{ms}$ with a 95% CI $[774\ 788]\mathrm{ms}$ to $-3\,\mathrm{ms}$ with a 95% CI $[-10\ 4]\mathrm{ms}$ containing zero.

3D T_1 Homogeneity

Figure 3.57 shows the improvement obtained after applying all the corrections to the multiple confounding factors. The T_1 distribution with all the corrections was much narrower approximating a normal distribution with a mean of $988\,\mathrm{ms}$ and a standard deviation of $47\,\mathrm{ms}$.

A quantitative assessment of the errors in B_1^+ factor and T_1 arising from the different confounding factors analysed throughout the chapter is summarised in Tables 3.1 to 3.3.

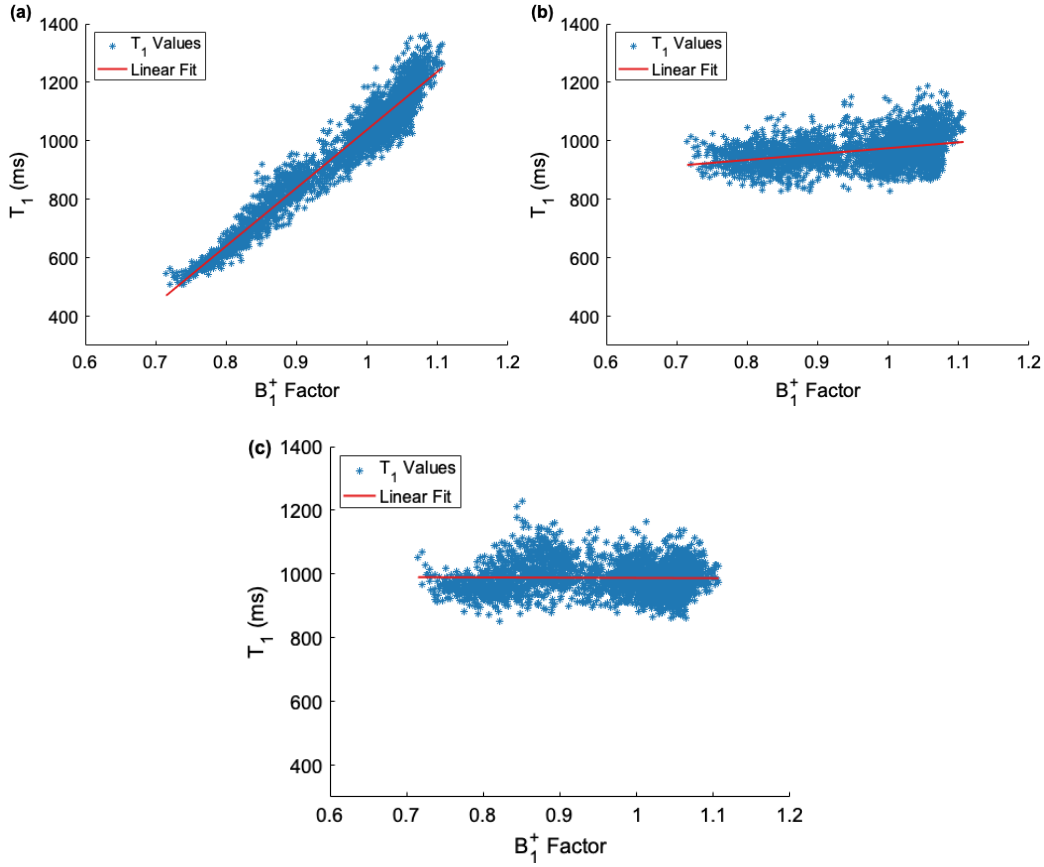


Figure 3.56: Correlation between *in vivo* T_1 and B_1^+ values for (a) the uncorrected T_1 map, (b) T_1 map corrected for B_1^+ inhomogeneities but without correcting for B_1^+ map confounders and (c) the T_1 map with all the corrections proposed in this chapter. The B_1^+-related variation in T_1 was (a) $781\,\mathrm{ms}$ with a 95% CI $[774\ 788]\mathrm{ms}$, (b) $79\,\mathrm{ms}$ with a 95% CI $[71\ 86]\mathrm{ms}$ and with all the corrections (c) it was reduced to $-3\,\mathrm{ms}$, with a 95% CI $[-10\ 4]\mathrm{ms}$ containing zero.

Table 3.1: B_1^+ factor and T_1 error in percentage relative to the B_1^+ gold standard and the IR SE (T_1 gold standard), respectively. The errors are quantified for the two RF pulses, Hamming Windowed Sinc (HWS) and Water Excitation (WE), without applying any corrections and after applying the developed slice profile and B_0 gradient through slice correction. The B_1^+/T_1 errors are quantified across the 14 vials for 4 slices and are reported as median [IQR].

Correction	RF Pulse	Error B_1^+ (%)	Error T_1 (%)
No Corrections	HWS	-5.2 [-7.4 -3.7]	10.5 [6.7 17.5]
	WE	-12.5 [-13.2 -10.2]	29.0 [23.6 33.9]
Slice Profile Correction	HWS	-1.8 [-4.5 -0.5]	2.6 [-0.4 10.2]
	WE	1.9 [1.0 4.4]	-5.3 [-7.8 -3.3]
B_0 Gradient Through Slice Correction	HWS	0.01 [-0.8 0.8]	-0.3 [-2.5 2.1]
	WE	1.5 [0.7 2.5]	-3.9 [-5.9 -1.7]

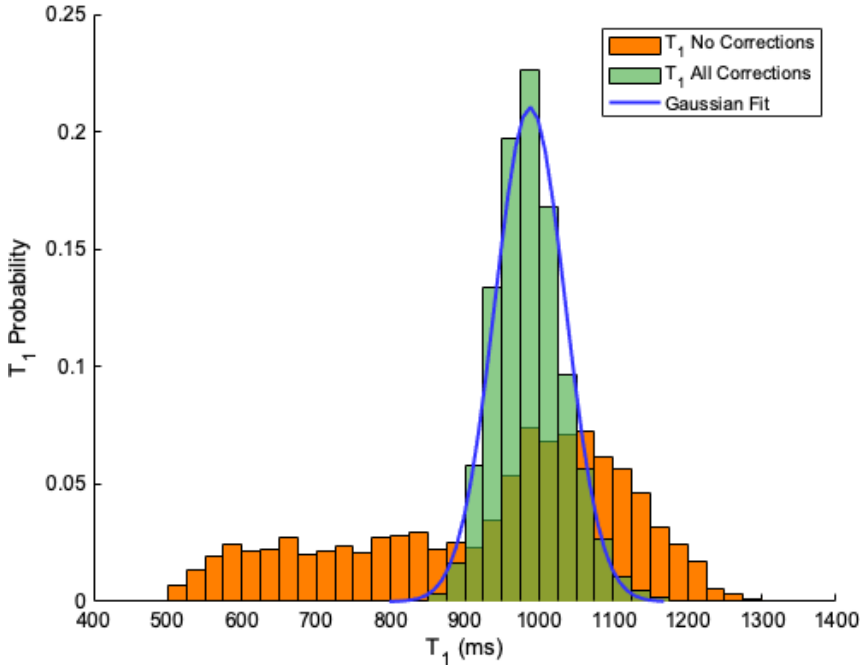


Figure 3.57: T_1 distribution without any corrections (orange) and with all the proposed corrections (green). A Gaussian fit to the green distribution yields a mean T_1 of $988\,\mathrm{ms}$ and a standard deviation of $47\,\mathrm{ms}$. This data was obtained by placing three circular ROIs per slice in vessel free liver regions of an *in vivo* acquisition across 22 slices. Each ROI had $46\,\mathrm{pixels}$ resulting in a total of $3036\,\mathrm{pixels}$.

Table 3.2: Relative difference between the uncorrected and corrected B_1^+ factor and T_1 values, normalised by the respective corrected values, for each EPI-based confounding factor. The B_1^+ factor and T_1 differences are quantified *in vivo* and are reported as median [IQR].

Confounding Factor	$\Delta B_1^+/B_{1,\,\mathrm{corr}}^+$ (%)	$\Delta T_1/T_{1,\,\mathrm{corr}}$ (%)
Distortion	-4.4 [-6.8 -2.8]	9.7 [6.1 15.7]
Fat Chemical Shift	-6.7 [-12.8 -2.2]	15.1 [4.2 32.4]
GRAPPA-induced Fat Ghosts	10.6 [7.5 12.2]	-19.3 [-21.6 -14.2]

3.8 Discussion

The confounding factors affecting T_1 measurements can be divided into two main classes: those affecting the B_1^+ map and those affecting the SPGR signal. Several confounders were found to affect the B_1^+ factor map such as slice profile and B_0 through slice gradients as well as EPI-based artefacts. The widely available SPGR sequence is affected by incomplete spoiling and spatial saturation.

Table 3.3: T_1 error in percentage relative to the IR SE before and after correcting deviations of the SPGR signal from steady-state due to incomplete spoiling or spatial saturation. The T_1 errors are quantified across the 14 vials for 4 slices and are reported as median [IQR].

Confounding Factor	Error T_1 (%) Before Correction	Error T_1 (%) After Correction
Incomplete Spoiling	7.4 [4.4 9.6]	-0.3 [-2.5 2.1]
Spatial Saturation	-0.6 [-6.2 0.6]	0.0 [-5.1 2.2]
Parallel Imaging On		
Parallel Imaging Off	-9.5 [-17.2 -9.0]	0.6 [-5.4 2.6]

Constructing an accurate B_1^+ mapping method is crucial to determine the true excitation FAs in the SPGR acquisition which is essential for an unbiased estimate of T_1. The relative error in T_1 is approximately twice the relative error in B_1^+ factor with an opposite sign (Appendix, Section 3.10.3). This rule of thumb is valid for absolute relative errors in B_1^+ factor less than 7%, above which quadratic corrections have an importance larger than 10% (Figure 3.55). For the *in vivo* case presented in Section 3.3, the B_1^+ factor reached values as low as 0.66. Assuming the B_1^+ factor is 1 is equivalent to a B_1^+ overestimation of $+34\%$, which would result in a T_1 underestimation of 57%.

The lack of a gold standard B_1^+ mapping method was a particular difficulty confronted in this work. The IR SE gold standard T_1 mapping method was initially used to indirectly assess the GRE-EPI B_1^+ map accuracy through its effect on the estimated T_1 maps in phantom studies. However, it was difficult to isolate and quantify the contribution of the B_1^+ factor confounding factors relative to the SPGR steady-state signal confounders into the overall T_1 error. Subsequently, a $4\,\mathrm{h}$ long 3D GRE B_1^+ mapping sequence (Section 3.10.2) was developed by Dr. Tunnicliffe that made it possible to confirm the accuracy of the GRE-EPI B_1^+ map in phantom data. Only then was it possible to confirm that incomplete spoiling was a source of T_1 mapping bias.

B_1^+ Map Confounders

The B_1^+ DAM approach using a GRE-EPI sequence was chosen due to its wide availability and capability of providing whole liver coverage within a $10\,\mathrm{s}$ breath-hold. The

2D multi-slice nature of the acquisition and the use of a GRE sequence make it sensitive to slice profile effects and B_0 variations across the slice direction that affect the B_1^+ factor accuracy. Phantom studies presented in Section 3.4.1 showed that using the HWS a median T_1 error of 10.5% (Figure 3.11 (a)) was incurred when using the DAM without slice profile correction, as is often presented in the literature. An even larger median T_1 error of 29% was assessed for the WE RF pulse (Figure 3.11 (b)). After applying the developed slice profile and B_0 gradient through slice corrections to the phantom data, an accurate T_1 with a median error of -0.3% was obtained for the HWS (Table 3.1). The WE had a significant decrease in the T_1 error, but retained a higher residual error of -3.9%. The sensitivity of the WE signal to off-resonances, as shown in Figure 3.7, could be a possible cause for the remaining error in T_1. In addition to modelling the effect of B_0-variations through slice, the WE signal might be sensitive to in-plane B_0 variations within each pixel. Because of this higher residual error, the WE RF pulse was abandoned for the B_1^+ mapping acquisitions used in the *in vivo* studies presented in Chapters 5 and 6. The HWS was adopted despite the worse performance of FS.

Slice profile effects have been reported in the literature by Parker et al. [57] using a two-point GRE sequence and were compensated by integrating the signal across the slice profile, similar to the procedure used in this work for the GRE-EPI acquisition. An average T_1 accuracy of 1.4% was achieved in a uniform vegetable oil bottle phantom. Their protocol used two different TRs of $1500\,\mathrm{ms}$ and $50\,\mathrm{ms}$ at a fixed FA of $45°$ under a total acquisition time of $19\,\mathrm{min}$. An SPGR acquisition on a $3\,\mathrm{T}$ Prisma scanner was constrained to a maximum TR of $4.1\,\mathrm{ms}$ to achieve whole liver coverage within a $15\,\mathrm{s}$ breath-hold, and the maximum nominal FA achieved at the scanner was $15°$. Despite these constraints, the corrections applied in this work resulted in a better T_1 accuracy in a phantom of on average 0.02%. Lena et al. [91] also corrected for slice profile in 2D VFA T_1 maps acquired at $1.5\,\mathrm{T}$ by Bloch simulating the SPGR signal over the BW of the RF pulse. Phantom data showed errors in T_1 between 40-60% without B_1^+ or slice profile corrections for experimental B_1^+ factors between 0.91 and 0.95. Correcting for both confounders

resulted in T_1 errors between 2% and 12%. The authors concluded that the SPGR slice profile was the main factor underestimating T_1 and corrections for B_1^+ inhomogeneities are less important. However, their study was at $1.5\,\mathrm{T}$ with a small B_1^+ factor range close to 1.

Macroscopic field variations along the slice direction z ($\nabla_z B_0$) have been reported to impact R_2^* and myelin water fraction estimation when using a 2D spoiled multi-gradient-echo sequence [92]. The authors took into account the additional dephasing effect of $\nabla_z B_0$ on the transverse steady-state signal through Bloch simulations and subsequent numerical integration across the slice direction. This procedure is similar to the one used in this work to quantify the effect of $\nabla_z B_0$ on a fully relaxed GRE signal. Qualitatively similar conclusions were reached, namely that $\nabla_z B_0$ can either enhance or diminish the observed transverse signal depending on whether $\nabla_z B_0$ has the opposite or the same sign as the SS gradient, respectively. This signal modulation increases with the magnitude of the excitation FA or equivalently higher B_1^+ factors. Quantitatively, it is hard to draw comparisons since Soellradl et al. [92] focused on the impact that $\nabla_z B_0$ has on R_2^* measurements whereas this work focused on characterising the $\nabla_z B_0$ effect on B_1^+ mapping. For the 2D multi-slice dual angle B_1^+ map it was found that different through slice phase roll behaviours between the signals at FAs α and 2α altered the DAM ratio and led to a B_1^+ factor error that scales by approximately 3.8% per every $10\,\mathrm{Hz/cm}$ variation in B_0 through slice (Figure 3.20). An alternative to the post-processing correction developed in this chapter would be to simply use a SE sequence. SE sequences refocus the signal due to B_0 field inhomogeneities reversing the effect of T_2^* decay. Assessing the potential of using SE to avoid $\nabla_z B_0$ errors in B_1^+ mapping remains as future work.

Beyond slice profile effects, the EPI readout in abdominal GRE acquisitions is also susceptible to confounding factors such as distortion (Section 3.5.1), chemical shift artefacts (Section 3.5.2) and GRAPPA induced-fat ghosts (Section 3.5.3). The large B_0 inhomogeneities present near the diaphragm as well as the distribution of fat present in the human body are difficult to mimic in phantoms and were therefore studied *in vivo*. Uncorrected, these confounding factors provoked notable localised variations in the T_1

maps (Figures 3.30 and 3.35). Upon correction, the T_1 values in the artefact region changed by 10% or more (Table 3.2), resulting in a more homogeneous liver T_1 map.

Distortion correction for B_1^+ mapping has been applied *in vivo* in the brain using a spin-echo stimulated echo approach with a 3D multi-shot EPI at $3\,\mathrm{T}$ [93]. Lutti et al. [93] reported shifts of $8\,\mathrm{mm}$ or larger in areas of large susceptibility difference in the brain. The magnitude of these distortions were similar to those observed in liver slices close to the diaphragm. The authors recommended using parallel imaging to reduce EPI spatial distortions. However, in EPI liver imaging it is also crucial to consider the inevitable large chemical shifts present when fat suppression is not ideal. These shifts can be incorrectly unwrapped when using parallel imaging and result in fat ghosts that interfere with the liver water signal (Section 3.5.3). Even when not using parallel imaging, due to the poor performance of FS, the signal from subcutaneous fat shifts into the liver causing variations in B_1^+ factor as large as 13% (Figure 3.34).

In summary, uncorrected, the confounding factors assessed for the B_1^+ map caused T_1 errors or differences in T_1 larger than or equal to 10% (Tables 3.1 and 3.2). Although errors of this size do not necessarily invalidate clinical application of a method, e.g., MOLLI is known to consistently underestimate T_1 [26], the nature of the different confounding factors in the combined B_1^+ corrected T_1 maps does not allow the use of a single global correction factor to obtain a true T_1 value. This is in part due to the global versus localised nature of the artefacts. However, even an apparently global effect such as slice profile that always overestimates T_1 is affected by the local values of both the B_1^+ factor and B_0 through slice gradient. This calls for pixel-wise corrections. Furthermore, due to the non-linearity of the transverse GRE signal, a global correction in the absence of B_1^+ and B_0 inhomogeneities would vary with the FA pair values. Therefore, in this chapter each confounding factor was carefully assessed, and effective correction schemes were developed.

SPGR Confounders

The presence of incomplete spoiling led to T_1 overestimations with median errors of 7.4% (Figure 3.43); using spatial saturation resulted in a smaller median T_1 error of -0.6% (Figure 3.50) when parallel imaging was on, as required *in vivo* for breath-hold reasons. Applying the proposed corrections to the SPGR signal, the median T_1 error caused by the two confounding factors was reduced to less than 0.4% (Table 3.3). This error is comparable to that achieved in the literature by Baudrexel [86] and Preibisch [85], who recognised the impact of incomplete spoiling on the SPGR T_1 estimate. *In vivo*, both authors used a free-breathing IR EPI as the gold standard T_1, infeasible for liver studies. In Baudrexel et al. [86] the T_1 RMSE reduced from 14.8% to 5.5% after incomplete spoiling correction. In the absence of a gold standard in the liver, an alternative accuracy metric was taken to be the deviation of the experimental data in Figure 3.55 from the theory curve given by Equation (3.14). This metric decreased from 4% to 0.6% after applying the incomplete spoiling correction developed.

Respiration

An additional confounder affecting both the B_1^+ map and the SPGR signal are inconsistent breath-holds. This results in anatomical misalignment between the FAs acquired to calculate either a B_1^+ map or T_1 map. The liver deforms non-rigidly during breathing, requiring affine or non-rigid registration for a good alignment. However, it is not clear whether registration is a good idea in B_1^+ or T_1 mapping due to the B_1^- receive field. The B_1^- and the proton density are assumed to be constant on a pixel-by-pixel basis over the various acquisitions used to determine the B_1^+ factor or estimate T_1. Registration moves the anatomy to a location with a different B_1^- factor resulting in images with mismatching B_1^- factors.

Several attempts of registering the FAs in the B_1^+ map or the SPGR were undertaken with different registration methods using *elastix* [94], [95], including groupwise registration which is state-of-the-art for quantitative imaging [96]. Optimisation of the registration

parameters for the liver at the GRE-EPI and SPGR spatial resolutions was pursued. However, registration was abandoned when analysing a case of no noticeable breath-hold misalignments. The optimised registration framework resulted in differences between registered and non-registered T_1 maps of $50\,\mathrm{ms}$ or higher over more than half of the pixels in a central liver slice. Given the registration should not cause changes in T_1 when the liver is at equal positions for all FAs, it was not included in the processing pipeline.

3.9 Conclusion

In conclusion, an accurate method for mapping T_1 using a 3D SPGR sequence was developed. To accurately measure T_1 it is of paramount importance to accurately correct for B_1^+ inhomogeneities. At $3\,\mathrm{T}$, the B_1^+ factor reached values as low as 0.66 which would induce an error in T_1 of 57%. The confounder with the biggest impact on the dual angle 2D multi-slice GRE-EPI based B_1^+ maps is the effect of slice profile. For the phantom data, slice profile effects accounted for a 7.9% error in T_1 with the FS scheme. Regarding the SPGR signal confounders, a similar size effect of 7.4% was induced by incomplete spoiling . After applying the developed corrections to phantom data, the weighted root mean squared T_1 normalised error between the SPGR T_1 and the gold standard IR SE was 2.5%, for physiologically relevant T_1s in the liver at $3\,\mathrm{T}$ varying between $740\,\mathrm{ms}$ and $1211\,\mathrm{ms}$. *In vivo*, off-resonance effects lead to several artefacts in EPI-based B_1^+ maps. In particular, the unsuppressed shifted fat signal interferes with the water signal resulting in large local variations in B_1^+ factor and consequently T_1. The median T_1 difference between an *in vivo* T_1 map uncorrected and corrected for fat chemical shifts was 15%. Off-resonance gradients through slice also bias the B_1^+ map and resulted in T_1 variations of $221\,\mathrm{ms}$ between the liver dome and the liver slices closest to the kidneys. All the corrections developed taken together, greatly reduced the abrupt variations in T_1 in-plane as well as T_1 gradients in the slice direction leading to more homogeneous *in vivo* whole liver T_1 maps.

3.10 Appendix

3.10.1 Gold standard T_1 Mapping Sequence

Slice-selective IR SE was performed on the phantom using TIs of $25\,\mathrm{ms}$, $50\,\mathrm{ms}$, $75\,\mathrm{ms}$, $100\,\mathrm{ms}$, $200\,\mathrm{ms}$, $300\,\mathrm{ms}$, $400\,\mathrm{ms}$, $600\,\mathrm{ms}$, $800\,\mathrm{ms}$, $1200\,\mathrm{ms}$, $1600\,\mathrm{ms}$, $2300\,\mathrm{ms}$, $3000\,\mathrm{ms}$, $4000\,\mathrm{ms}$ and $5000\,\mathrm{ms}$, a TR/TE $= 9\,\mathrm{s}/12\,\mathrm{ms}$, FoV $= 225\times300\,\mathrm{mm}^2$, matrix $= 144\times192$, a single axial slice of $6\,\mathrm{mm}$ thickness, without acceleration, phase resolution 100%, phase partial Fourier off, interpolation on. The BW was $130\,\mathrm{Hz/pixel}$. All image filters were off.

To calculate the gold standard T_1 map (Figure 3.58), the signal in each pixel was fit using a three-parameter non-linear IR model:

$$S_n = a - be^{\left(\frac{-TI_n}{T_1}\right)}, \tag{3.15}$$

where S_n is the signal intensity, a is the signal at TI $= \infty$, after its full recovery to the equilibrium longitudinal magnetisation M_z, and $a - b$ is the signal at TI $= 0$. Reasonable initial guesses for a is the signal from the largest TI ($5000\,\mathrm{ms}$) and for b is two times the signal at the largest TI. T_1 was initialised to $500\,\mathrm{ms}$. The subscript n denotes the index of the TI, in this case the signal was measured at 15 different TIs. For each fit, the TI corresponding to the minimum signal intensity is determined and all the TIs less than or equal to the TI with the minimum signal intensity are assigned a negative value, i.e., samples which have not reached the null intensity. A second fit is carried out with the minimum signal intensity changed back to positive. The fit with the highest R^2 value is chosen.

3.10.2 Gold standard B_1^+ Mapping Sequence

A 3D non-selective GRE sequence was performed on the phantom to obtain a gold standard B_1^+ map using the DAM. Two acquisitions at nominal FAs of $30°$ and $60°$ were acquired in an interleaved manner to avoid signal drift over time, i.e., PE lines at each partition were acquired for both FAs before moving to the next PE line. Acquisition parameters were: FoV $= 192 \times 192 \times 10\,\mathrm{mm}^3$, matrix $= 48 \times 48 \times 16$,

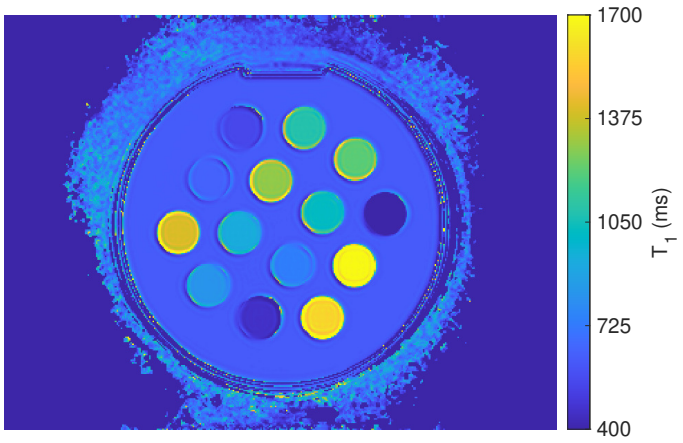


Figure 3.58: Inversion-recovery SE gold standard T_1 map of the *FDA4-T1* phantom with mean T_1s varying between $367\,\mathrm{ms}$ and $1699\,\mathrm{ms}$.

$TR/TE = 10\,\mathrm{s}/2\,\mathrm{ms}$, without acceleration, slice/phase resolution 100%, phase partial Fourier off, interpolation on. The BW was $1000\,\mathrm{Hz/pixel}$. All image filters were off. Slices were acquired in transversal orientation. Given the central slices in 3D acquisitions have a rectangular or ideal slice profile, Equation (3.2) was used to calculate the true FAs exciting the spins in the *FDA4-T1* phantom. Figure 3.59 shows the B_1^+ gold standard maps in the *FDA4-T1* phantom.

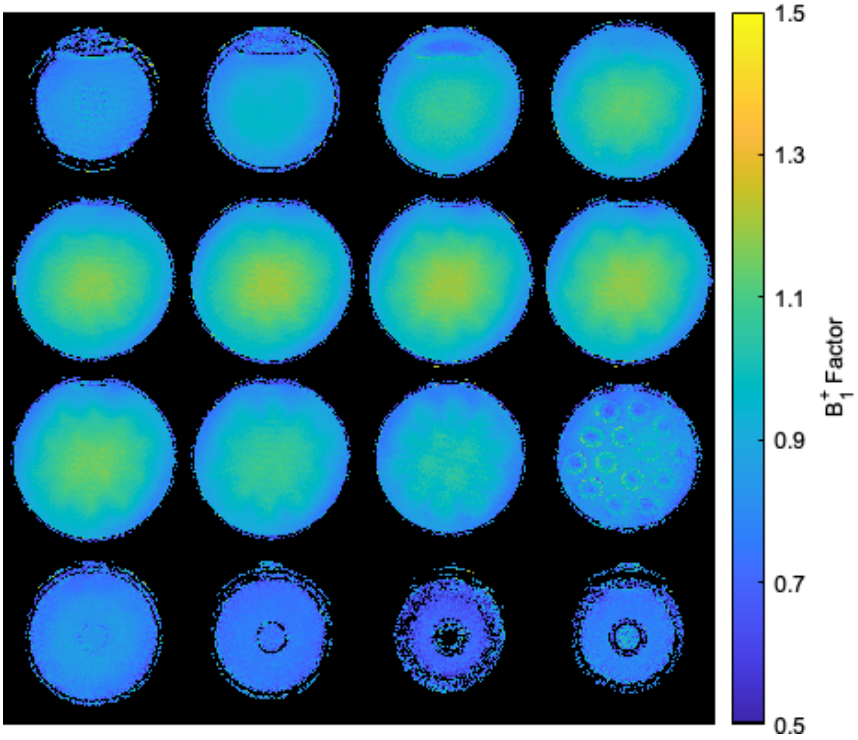


Figure 3.59: B_1^+ gold standard maps of the *FDA4-T1* phantom across 16 slices.

The temperature of the 3D SPGR T_1 mapping protocol and the gold standard B_1^+ and T_1 mapping was monitored overnight using fibre optic probes attached to the surface of the phantoms. For the *Calimetrix QC0025* phantom acquisition, the mean±standard deviation temperature was $23 \pm 0.2\,^{\circ}\mathrm{C}$ over the entire acquisition lasting $17\,\mathrm{h}$ and $40\,\mathrm{min}$. For the *FDA4-T1* phantom acquisition, the mean±standard deviation temperature was $20 \pm 0.4\,^{\circ}\mathrm{C}$ over the duration of $19\,\mathrm{h}$. The magnitude of these temperature variations result in insignificant T_1 changes for $NiCl_2$ filled vials [97]. Stupic et al. [97] measured T_1 variations of 1.3% in a $NiCl_2$ array over a temperature range from $18\,^{\circ}\mathrm{C}$ to $26\,^{\circ}\mathrm{C}$.

To check whether the 3D GRE DAM B_1^+ could be used as the gold standard B_1^+ mapping method in the phantom, the SPGR T_1 map with the FAs corrected by the 3D GRE DAM B_1^+ was compared to the IR SE T_1 map. A good agreement was achieved with the IR SE, as shown in Figure 3.60 with a slope close to the identity line.

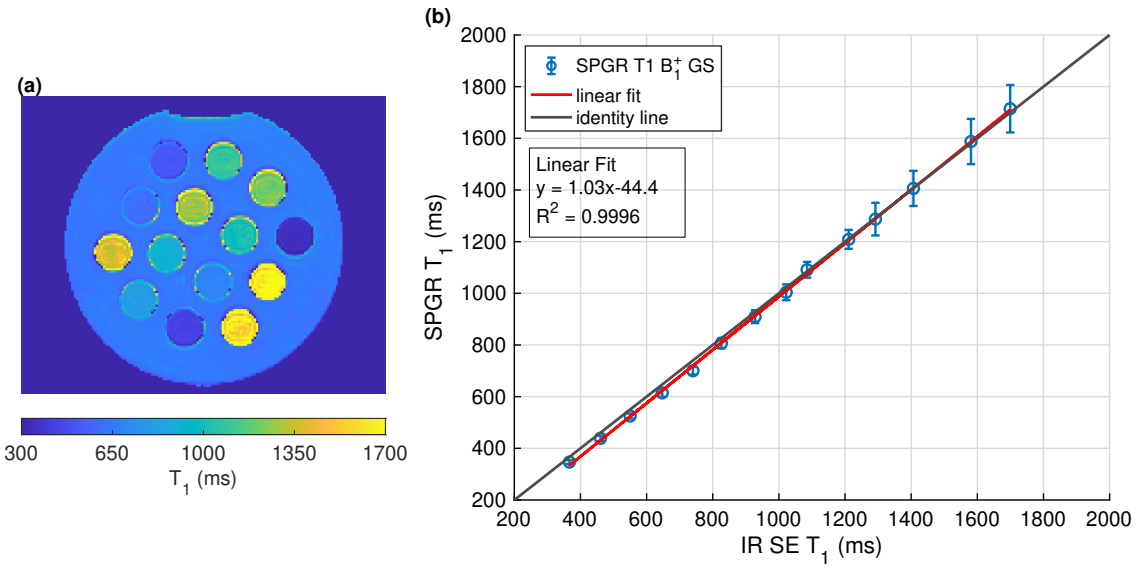


Figure 3.60: (a) SPGR T_1 map with the SPGR FAs corrected by the 3D GRE B_1^+ map. The signal was corrected for incomplete spoiling. (b) Validation of the gold standard B_1^+ mapping method. Linear fit of the SPGR T_1 map to the gold standard IR SE. The slope from the linear fit was 1.03 with a 95% confidence interval between 1.019 and 1.046.

3.10.3 Derivation of the Error in T_1 due to an Error in the B_1^+ factor

A first order Taylor expansion of T_1 was calculated using Helms et al. [62] rational approximation of the Ernst equation for T_1 given by equation $T_{1,\text{app}} = T_{1,\text{true}}(B_1^+)^2$. Starting with $T_{1,\text{est}}(B_{1,\text{est}}^+) = \frac{T_{1,\text{app}}}{(B_{1,\text{est}}^+)^2}$ and expanding about $B_{1,\text{true}}^+$:

$$
\begin{aligned}
T_{1,\text{est}}(B_{1,\text{est}}^+) &= T_{1,\text{est}}\Big|_{B_{1,\text{est}}^+ = B_{1,\text{true}}^+} + \frac{dT_{1,\text{est}}}{dB_{1,\text{est}}^+}\Big|_{B_{1,\text{est}}^+ = B_{1,\text{true}}^+} * (B_{1,\text{est}}^+ - B_{1,\text{true}}^+) \\
T_{1,\text{est}}(B_{1,\text{est}}^+) &= \frac{T_{1,\text{app}}}{(B_{1,\text{true}}^+)^2} - 2T_{1,\text{app}}(B_{1,\text{true}}^+)^{-3}(\Delta B_1^+) \\
T_{1,\text{est}}(B_{1,\text{est}}^+) &= T_{1,\text{true}} - 2T_{1,\text{true}}(B_{1,\text{true}}^+)^{-1}(\Delta B_1^+) \\
\frac{\Delta T_1}{T_{1,\text{true}}} &= -2\frac{\Delta B_1^+}{B_{1,\text{true}}^+}
\end{aligned}
\tag{3.16}
$$

The relative error in T_1 is equal to -2 times the relative error in B_1^+ for small errors in B_1^+, i.e., $B_{1,\text{est}}^+ \approx B_{1,\text{true}}^+$.

4

In Vivo Liver 3D T_1 Mapping Protocol and Processing Pipeline

This chapter describes the final 3D T_1 mapping protocol comprising both the acquisition sequences and the processing algorithms. These sequences were used to acquire the data presented in Chapter 5 and Chapter 6.

4.1 Image Acquisition

All the imaging data were acquired on a $3\,\mathrm{T}$ Prisma Siemens (Siemens Healthineers, Erlangen, Germany) scanner with software version *syngo MR E11*. A spinal coil and an 18-channel abdominal array coil were used for receive and a body coil was used for transmit. All images were acquired in the transverse plane in the head to foot direction, the FE direction was acquired from right to left and the PE direction was acquired from anterior to posterior.

Careful acquisition of the data is essential in quantitative MRI for adequate post-processing. The FoV was positioned to encompass the majority of the liver, including the liver dome. It was defined for the first FA in the SPGR acquisition and then copied for all subsequent FAs. The GRE-EPI (B_1^+ map) and the double-echo GRE (B_0 map) FoVs were defined by copying the image position from the middle slice of one of the VFA

SPGR acquisitions. Therefore, the middle slice location for all the acquisitions matched if the table did not move during the acquisition. The table position was set to 'FIX', i.e., the table position is fixed and does not move between scans. This avoids acquisition of a new adjustment volume and re-shimming. The adjustment volume was slightly larger than the FoV to ensure all slices were shimmed. The same adjustment volume was used for all acquisitions. Between the frequency adjustment in the GRE-EPI and the data acquisition, a pause of $10\,\mathrm{s}$ (approximately the duration of the breath-hold instructions) was applied to ensure the magnetisation fully recovered to equilibrium. Similarly, an interval of at least $10\,\mathrm{s}$ was allowed between the two GRE-EPI acquisitions.

4.1.1 B_1^+ Mapping Sequence: 2D GRE-EPI

On the $3\,\mathrm{T}$ Prisma scanner the pulse sequence used for the DAM B_1^+ mapping was a 2D multi-slice GRE EPI with fat saturation and nominal FAs of $65°$ and $130°$. Acquisition parameters were: FoV $= 450 \times 366\,\mathrm{mm}^2$, matrix $= 64 \times 52$, in-plane spatial resolution of $7 \times 7\,\mathrm{mm}^2$, slice thickness of $8\,\mathrm{mm}$, gap of $2\,\mathrm{mm}$, 15 slices, TE =11 ms, $TR = 10\,000\,\mathrm{ms}$ without acceleration, phase resolution 100%, phase partial Fourier off, interpolation off, with the fast-readout direction in the right-left direction. The BW was $3906\,\mathrm{Hz/pixel}$ to achieve a minimum echo spacing of $0.3\,\mathrm{ms}$ and the slices were acquired in an interleaved scheme. Each FA was acquired during a $10\,\mathrm{s}$ breath-hold. Magnitude (but not complex) data is available from the product sequence. Regarding image post-processing on the scanner: prescan normalise and distortion correction were both turned on. The design of this acquisition ensures that the magnetisation can be approximated to fully recovered, hence the contrast does not depend on T_1 but will depend on the excitation FAs. The lowest spatial resolution possible at the scanner was adopted as the B_1^+ field is expected to vary smoothly across the spatial extension of the liver. At $3\,\mathrm{T}$ the RF wavelength is approximately $26\,\mathrm{cm}$ in the liver [47], which sets the spatial scale of B_1^+ field variations. At a base resolution of 64, the pixel size is $7\,\mathrm{mm}$ and there are roughly $38\,\mathrm{pixels}$ per RF wavelength providing more than adequate spatial sampling of the B_1^+ field variations.

Figure 4.1 shows the GRE-EPI data collected over 15 slices.

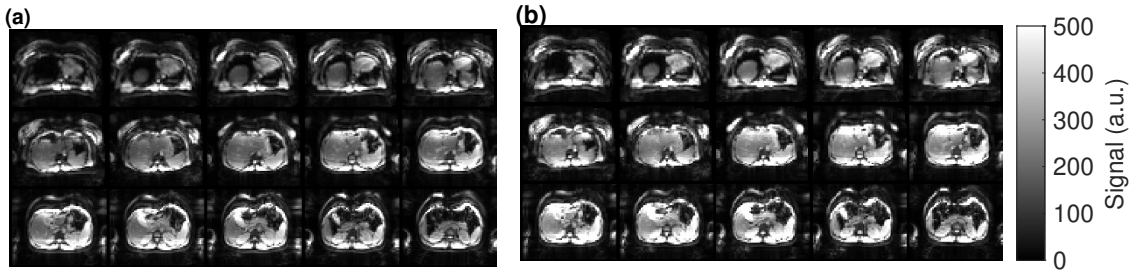


Figure 4.1: 2D multi-slice GRE-EPI data for (a) FA $65°$ and (b) FA $130°$. The white bands of signal above the abdomen correspond to unsuppressed fat signal suffering chemical shift.

4.1.2 B_0 Mapping Sequence: 2D Double Echo GRE

A 2D multi-slice double echo spoiled GRE acquisition with magnitude and phase reconstructed data was acquired to compute a B_0 map. The echo times were $4.78\,\mathrm{ms}$ and $7.17\,\mathrm{ms}$ (at $3\,\mathrm{T}$), TR $=20\,\mathrm{ms}$, FA $=15°$, FoV $= 450 \times 380\,\mathrm{mm}^2$, matrix $= 64 \times 54$, in-plane spatial resolution of $7 \times 7\,\mathrm{mm}^2$, monopolar readout gradients, a BW of $630\,\mathrm{Hz/pixel}$, phase resolution 100%, phase partial Fourier off, interpolation off and readout in the right-left direction. Single band multi-slice with an interleaved scheme was used to acquire 15 slices with a slice thickness of $8\,\mathrm{mm}$ and a gap of $2\,\mathrm{mm}$ to achieve whole-liver coverage. Fat suppression is not necessary as the phase difference for water or fat should be equal and only depend on the off-resonance relative to the Larmor frequency. GRAPPA [80] with two times acceleration was applied in the PE direction and 24 integrated reference lines were used. The acquisition time was $8.6\,\mathrm{s}$ and data were acquired during a single breath-hold. Figure 4.2 shows the phase data for the two TEs acquired over the 15 slices.

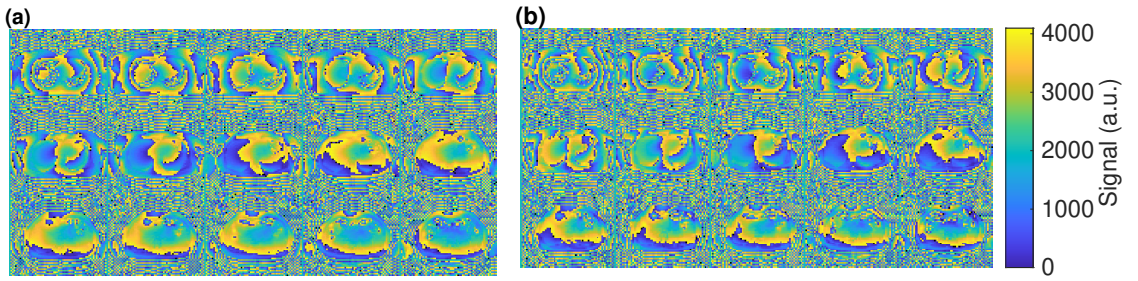


Figure 4.2: 2D multi-slice double echo GRE data for a TE of (a) $4.78\,\mathrm{ms}$ and (b) $7.17\,\mathrm{ms}$. The phase is output by the scanner using a scale between 0 and 4095 (12 bit resolution). The phase is converted to lie between 0 and 2π radians prior to computing the B_0 map.

4.1.3 T_1 Mapping Sequence: 3D VFA SPGR

The T_1 contrast of the liver tissue was obtained through a 3D variable flip angle spoiled gradient recalled echo with DIXON [98] fat/water separation. Acquisition parameters were: FoV $= 450 \times 366 \times 3\,\mathrm{mm}^3$, matrix $= 320 \times 260 \times 48$, spatial resolution of $1.4 \times 1.4 \times 3\,\mathrm{mm}^3$, $TR/TEs = 4.1/[1.23, 2.46]$ ms (at $3\,\mathrm{T}$), phase/slice resolution 75/50%, phase/slice oversampling 30/50%, phase/slice partial Fourier off, interpolation off. Optimal excitation FAs of $2°$, $2°$, $15°$, $15°$ (used in Chapters 5 and 6) and control FAs of $3°$, $6°$, $9°$, $12°$, $15°$ (used in Chapter 5) were employed. Caipirinha [90] was used with an acceleration factor of 3 along the slice direction with 24 separate GRE reference lines. Prescan normalise and distortion correction were turned on. A 3D slab-selective excitation was used. Spatial saturation was turned off as it perturbed the theoretical steady-state signal. The acquisition BW of both echoes was $1040\,\mathrm{Hz/pixel}$. Data were acquired during a breath-hold of $15\,\mathrm{s}$ for each FA.

Fat has a shorter T_1 relaxation time than water, recovering faster to equilibrium. To be able to model the SPGR signal acquired using a single T_1 value corresponding to water-based tissue in the liver, the fat signal was supressed using a DIXON method. At $3\,\mathrm{T}$ fat and water are precessing $440\,\mathrm{Hz}$ off-resonance [32]; DIXON collects two echoes at TEs of $1.23\,\mathrm{ms}$ and $2.46\,\mathrm{ms}$. The shortest TE corresponds to signal collected with fat and water out-of-phase, in pixels with a mixture of fat and water the signal will be reduced. At a TE of $2.46\,\mathrm{ms}$ at $3\,\mathrm{T}$, the fat and water are approximately in-phase, i.e., their signals add up. Water-only images can be generated by taking the average

of in-phase and out-of-phase images. Figure 4.3 shows the 4 images resulting from a DIXON acquisition for the middle slice in the SPGR acquisition. Figure 4.4 shows the water-only images for the 48 slices at a FA of 15°.

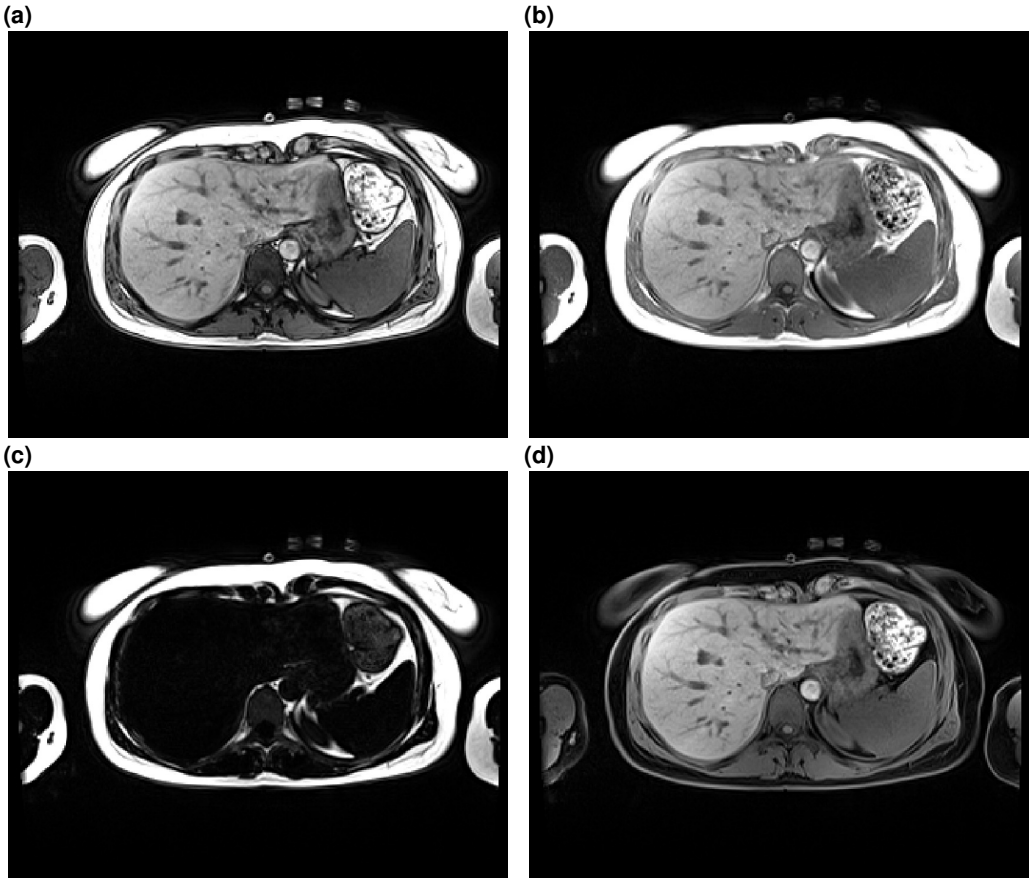


Figure 4.3: 3D SPGR for the middle slice illustrating the output of a DIXON acquisition. (a) Out-of-phase (TE $= 1.23\mathrm{ms}$) data showing clear boundaries between the organs, where the presence of both fat and water in a pixel leads to reduced signal intensity from partial cancellation. (b) In-Phase (TE $= 2.46\ \mathrm{ms}$) data showing enhanced signal from the constructive superposition of fat and water signal. (c) Fat-only image resulting from the subtraction of in-phase and out-of-phase signals. (d) Water-only image obtained from averaging the in-phase and out-of-phase signals.

By acquiring signal at varying excitation FAs and a constant TR of $4.1\,\mathrm{ms}$ one can probe the T_1 contrast in the tissue. The low FAs provide proton density signal, while the higher FAs have a strong T_1-W (Figure 4.5).

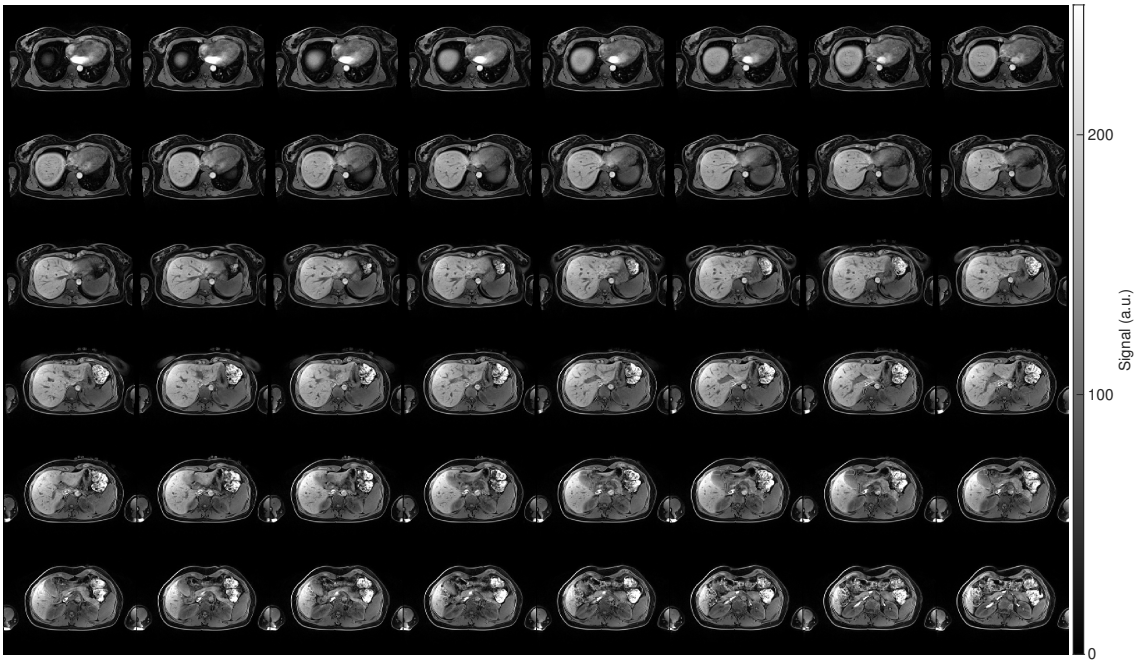


Figure 4.4: 3D SPGR water-only data at a FA of $15°$ collected over 48 slices covering the entire liver volume.

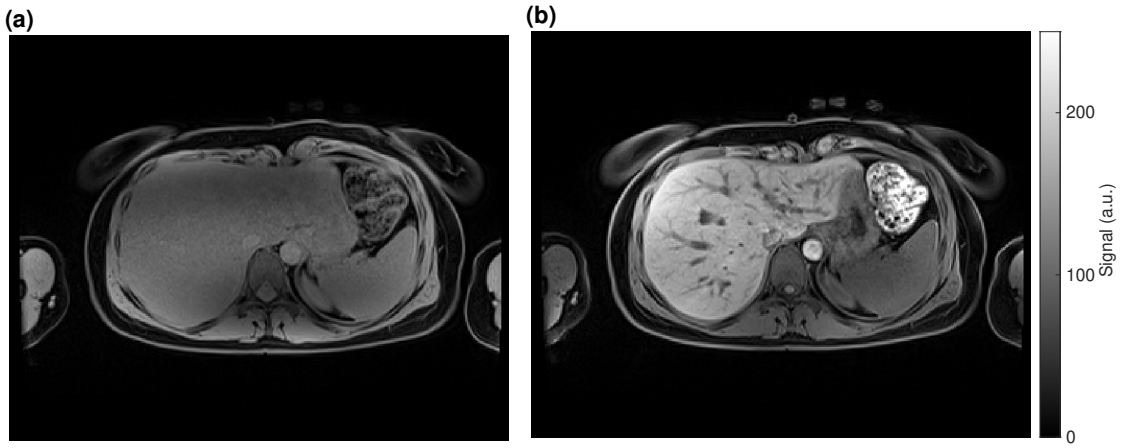


Figure 4.5: 3D SPGR water-only data for the middle slice at a FA of (a) $2°$ and (b) $15°$. FA $2°$ shows an homogeneous image and FA $15°$ is strongly T_1-W showing the liver's dense vasculature.

4.2 Image Processing Pipeline

MATLAB [59] was the programming language chosen to process and analyse the data. Before proceeding with the T_1 map calculation, the acquired data was subject to several checkpoints to avoid using faulty data. First, it was checked whether the only difference between the $65°$ and $130°$ GRE-EPI acquisitions occurred for the FA and

RF pulse field. It was confirmed whether the RF pulse voltage for $130°$ was double the voltage of the $65°$. To carry out the difference between the acquisitions, several fields from the Dicom header and the private headers (ASCONV fields) were extracted: FA, number of RF pulses, RF pulse name and voltages, shim currents, imaging frequency, overall image scaling factor, reference amplitude, 'image position patient', adjustment volume FoV, thickness and position and parallel imaging characteristics. It was verified whether all the acquisitions were acquired with the prescribed nominal FAs and had equal adjustment volume, shim currents, reference amplitude and 'image position patient' fields. In addition, it was verified whether the imaging frequency between the GRE-EPI and the double-echo GRE matched. If the acquisitions passed all the checkpoints, they were apt for B_1^+/T_1 mapping calculation. A flow diagram illustrating the main components of the image processing pipeline used to calculate the T_1 Maps is shown in Figure 4.6. Each component is described in more detail below and complete flow diagrams for each component can be found in the Appendix to this chapter (Section 4.3).

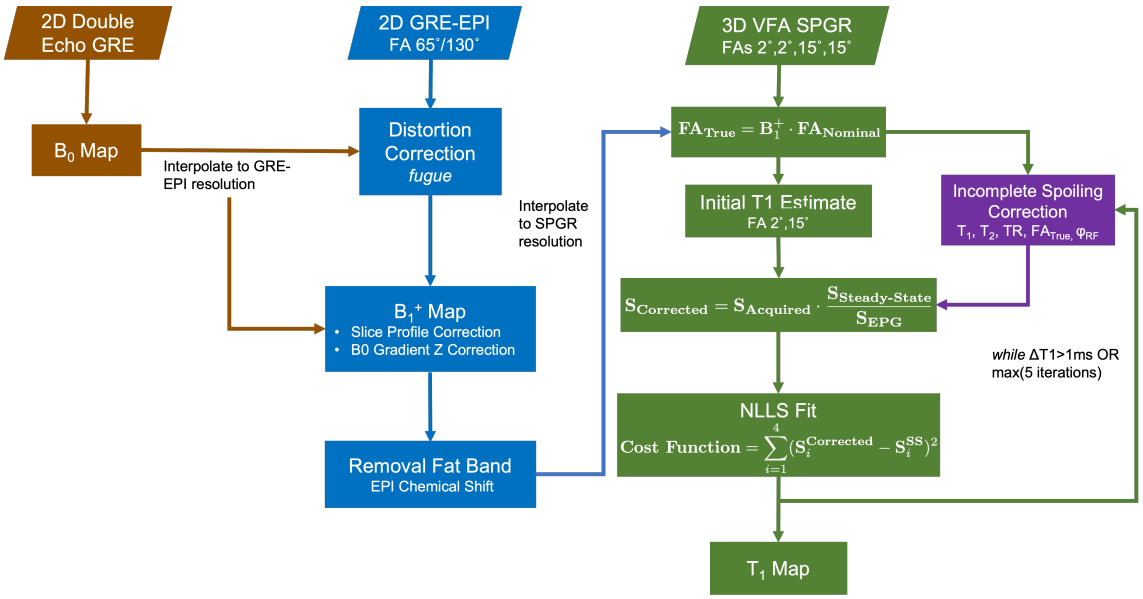


Figure 4.6: Image processing pipeline with three main blocks. The B_0 map (brown block) is used for distortion correction and modelling of B_0 variations through slice of the GRE-EPI images. The blue block corresponds to the B_1^+ map calculation, which is used to correct the SPGR nominal FAs. An incomplete spoiling correction (purple block) calculated from the ratio of the steady state signal and the extended-phase-graph (EPG) simulated signal is applied to the SPGR signal. An iterative non-linear least-squares fit (green block) of the corrected signal to the steady state model is used to estimate the T_1 maps.

4.2.1 Data Pre-Processing

Firstly, a tight mask delineating the liver was defined on the high-resolution SPGR acquired at a FA of 15° (Figure 4.7). Fifteen masks were manually drawn over the liver in the SPGR acquisition for the slices matching the location of each of the 15 slices in the GRE-EPI acquisition.The mask was down-sampled to the double echo GRE acquisition and applied to the magnitude data. Subsequently, the phase data was unwrapped through the *fsl prelude* toolbox [73], [74], using the masked magnitude data, and the B_0 map was calculated through *fsl maths* [73], [74]. The B_0 map was used for distortion correction of the GRE-EPI images and modelling of B_0-variations through slice in the B_1^+ map calculation. The B_0 map was interpolated in-plane to the GRE-EPI resolution as there were two less columns in the GRE-EPI matrix.

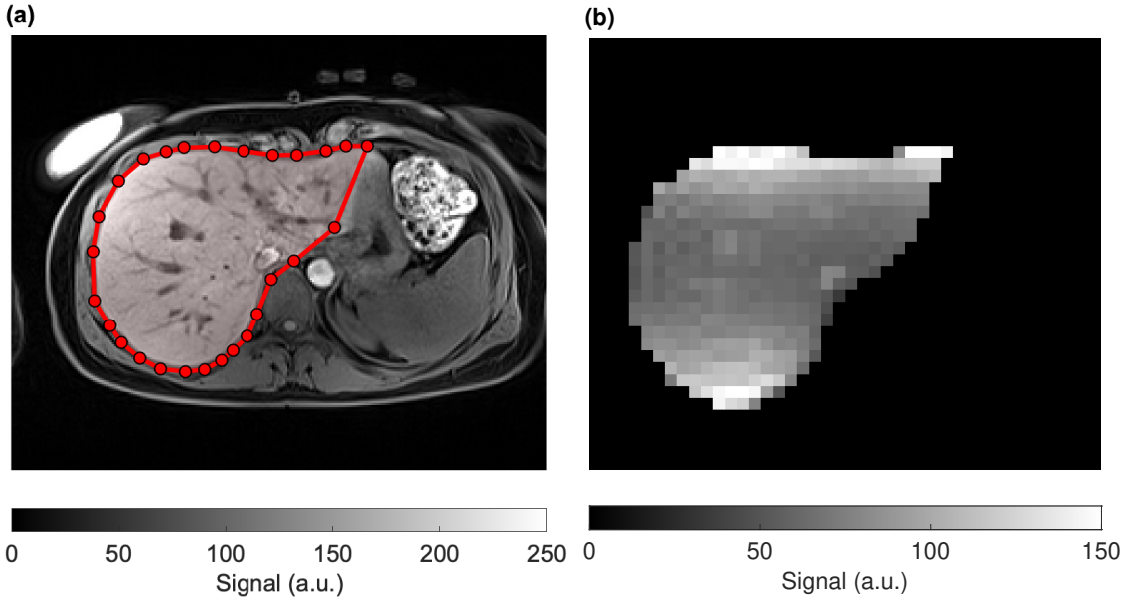


Figure 4.7: (a) Liver mask in red drawn on the VFA SPGR high resolution image at FA 15° (high contrast). This mask was applied to the B_0 and B_1^+ maps. Only the pixels in the B_1^+ map mask were used to calculate T_1, resulting in an automatic liver segmentation of the T_1 maps. (b) Result of the mask applied to one of the magnitude images from the double echo GRE acquisition.

EPI is affected by chemical shift artefacts as well as distortions in the PE direction due to the large readout time and thus small equivalent BW in the slow read direction. The GRE-EPI acquisitions were corrected for distortions through the *fsl fugue* toolbox

[73], [74] using the B_0 map generated [72]. The echo spacing was calculated by taking the inverse of the product of the BW per pixel in the PE direction and the number of PE lines. Figure 4.8 shows an example B_0 map *in vivo*.



Figure 4.8: B_0 Map. Note the large off-resonances of $200\,\mathrm{Hz}$ or higher for the initial slices closest to the diaphragm.

4.2.2 B_1^+ Mapping Calculation

An initial B_1^+ map was calculated with a correction for slice profile effects through a LUS following the procedure described in Section 3.4.1. The resulting B_1^+ map was used as a starting point for the calculation of the B_1^+ map corrected for both slice profile effects and B_0 variations through slice. A NLLS fit was used to find the B_1^+ correction factor corresponding to the simulated ratio that best matched the ratio between the distortion corrected GRE-EPI images acquired at FAs of $130°$ and $65°$. The choice for the FA values is motivated in Chapter 5. The simulated ratio between the signal at $130°$ and $65°$ was computed as follows: the transverse signals at each FA were Bloch simulated [68] across the slice direction, including the off-resonance at each slice position extrapolated from the B_0 map [70]. The complex transverse signal immediately after the RF pulse was propagated until time TE including free precession at the corresponding off-resonance. The complex signals at time TE were integrated across the slice dimension (Equation (3.3)). A detailed description of this procedure is in Section 3.4.2. Fat chemical shifts bias the B_1^+

factor values in the water-liver tissue. The B_1^+ map locations affected by the fat signal shift were identified and removed following the algorithm described in Section 3.5.2.

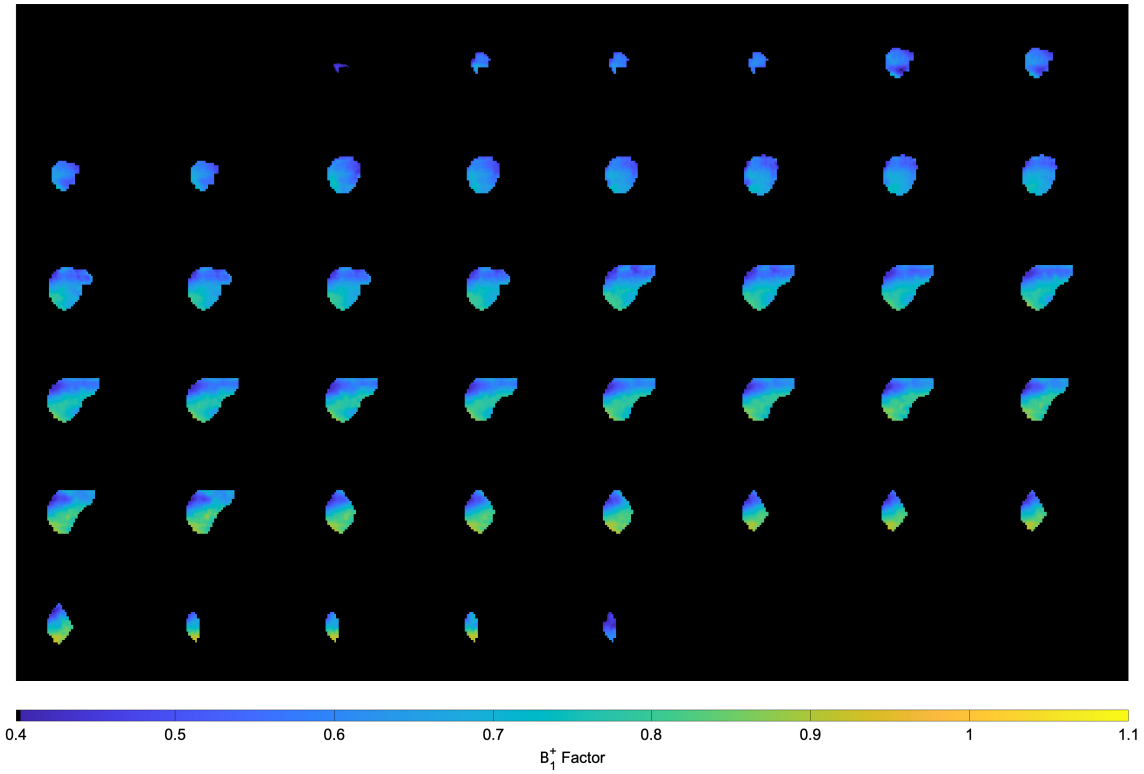


Figure 4.9: B_1^+ Map used to correct the nominal FAs in the VFA SPGR acquisition.

4.2.3 T_1 Mapping Calculation

The B_1^+ map was linearly interpolated along the three dimensions to the same spatial resolution as the SPGR sequence (Figure 4.9). The interpolated B_1^+ factor was multiplied by the nominal FAs to obtain the true FAs. The incomplete spoiling of the transverse magnetisation was calculated through EPG simulations [88] and the correction was equal to the ratio between the steady-state signal and the EPG signal. The SPGR signal acquired at each FA was multiplied by the incomplete spoiling correction. Further details of the incomplete spoiling correction are described in Section 3.6.1. The signal was then fit to the steady-state SPGR function (Equation (2.55)) through a NLLS regression using MATLAB's [59] function *lsqnonlin*. The trust-region reflective algorithm with an optimality tolerance of 1e-10 was used. The starting point for T_1 was calculated from the ratio between the signals acquired at the two lowest distinct FAs, as these are less

affected by incomplete spoiling. A cubic interpolation was applied to the incomplete spoiling correction factor using the starting point for T_1 and the B_1^+ corrected FAs. The M_0 starting point was calculated from the ratio between the signal acquired at the lowest FA and the steady-state equation with the T_1 starting point as input and M_0 of 1. Upper and lower T_1 bounds in *lsqnonlin* were identical to the incomplete spoiling correction T_1 bounds. *lsqnonlin* was iteratively called until the difference between two T_1 estimates was less than $1\,\mathrm{ms}$ or a total of 5 iterations was reached. Typically only 3 iterations were required for convergence. At each iteration the incomplete spoiling correction factor was updated based on the estimated T_1. Figure 4.10 shows the T_1 map output for one healthy volunteer.

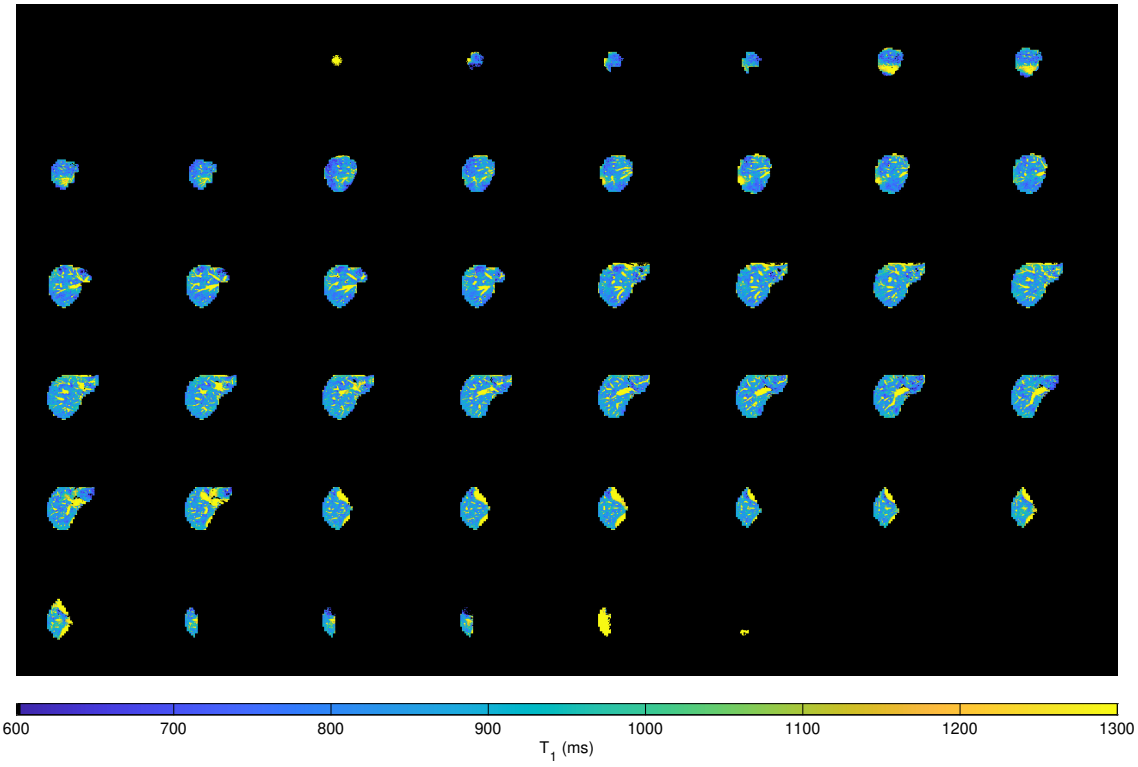


Figure 4.10: T_1 Map in a healthy volunteer spanning the whole liver volume.

4.2.4 T_1 Map Analysis: ROI Placement Criteria

The T_1 maps were analysed using three circular regions of interest (ROIs) per slice, each with a radius of $4\,\mathrm{pixels}$ $(5.6\,\mathrm{mm})$ giving a total of 46 T_1 pixels per ROI. The locations of these ROIs were chosen in the high contrast FA $15°$ SPGR image with a

three-fold criterion in decreasing order of importance: (1) select vessel and bile free areas, (2) select columns corresponding to the central part of the liver, (3) select rows spanning the anterior, centre, and posterior area of the liver. The analysed liver volume was limited to slices where 3 ROIs could be placed following the criteria defined above. In practice, this required starting 8 slices below the first slice in the FoV where the liver dome was clearly visible and stopping 10 slices before the last slice in the FoV where the liver was no longer visible. Figure 4.11 shows an example of a SPGR data set acquired for one volunteer. For this volunteer, the first slice with the liver dome visible was slice 3, adding 8 slices gave slice 11 as the starting slice to place the ROIs. The last slice where the liver could be distinguished from the other organs in the FoV was slice 44. Subtracting 10 slices, resulted in slice 34 as the last slice used to place an ROI. Figure 4.12 shows the ROI placement for slices 11 until 34.

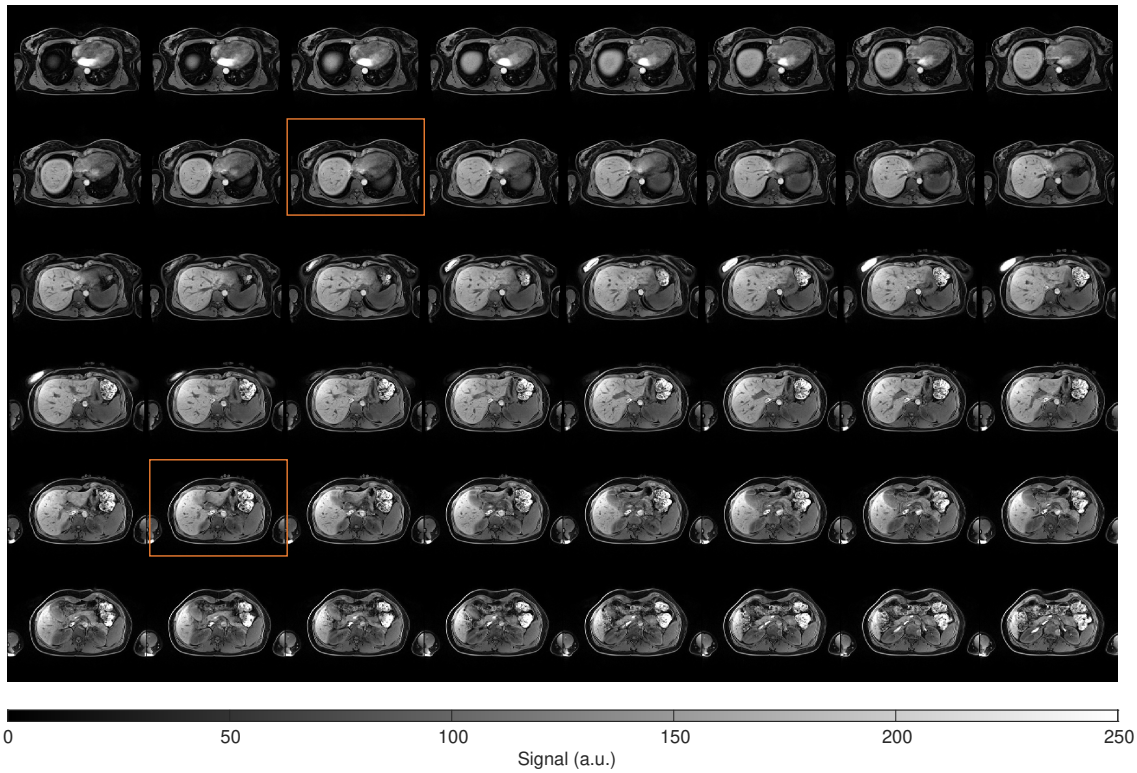


Figure 4.11: Forty-eight SPGR slices acquired for one volunteer. The first slice with the liver dome clearly visible is slice 3, adding 8 slices gives slice 11 (first orange rectangle) as the first slice used to place ROIs. The last slice with liver clearly visible is slice 44, subtracting 10 slices gives slice 34 (second orange rectangle) as the last slice used in the ROI placement. In total, 24 slices of $3\,\mathrm{mm}$ thickness were used for the data analysis of this volunteer resulting in $7.2\,\mathrm{cm}$ of liver.

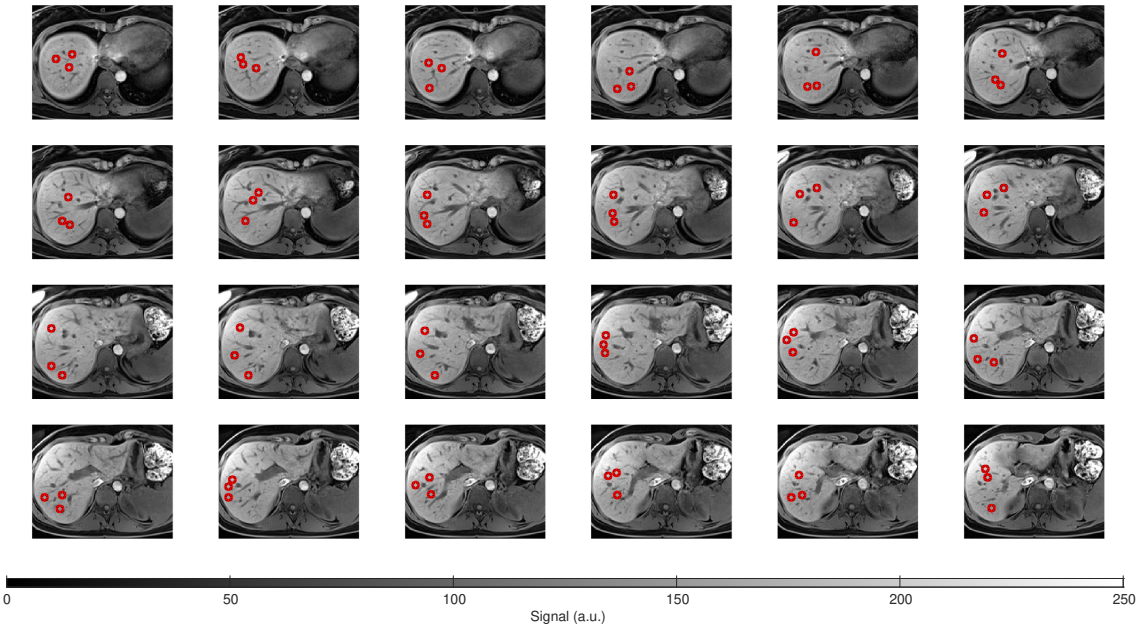


Figure 4.12: ROI placement for the same SPGR data shown in Figure 4.11. Three ROIs, shown in red, were placed for each slice following the criteria described in the text.

4.3 Appendix

This appendix presents flow diagrams corresponding to the main functions in the final image processing pipeline (Section 4.2) to provide a better understanding of how the different functions work together to produce the final T_1 maps. The diagrams are presented in the order that the associated functions appear in the pipeline. The main steps in the processing functions are represented in green, inputs are represented in blue, and the outputs are represented in fuchsia.

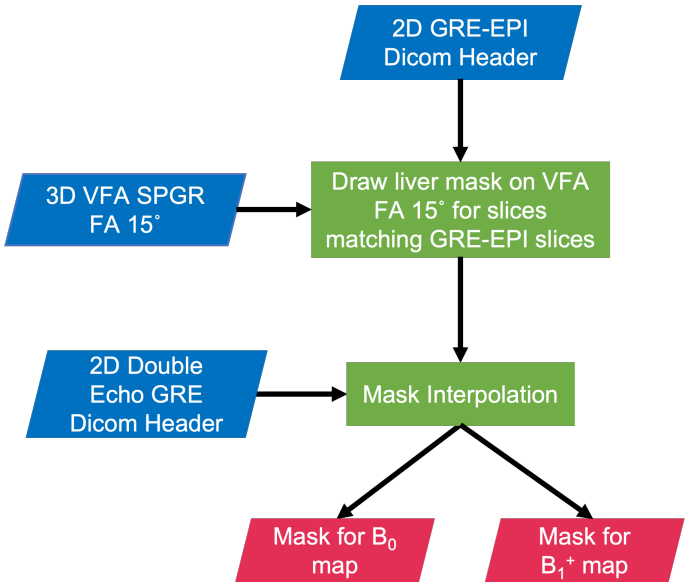


Figure 4.13: Flow diagram to draw a mask surrounding the liver boundaries. The aim is to restrict the B_0 map and B_1^+ map calculation to the liver region. See Figure 4.7 for an example of a mask.

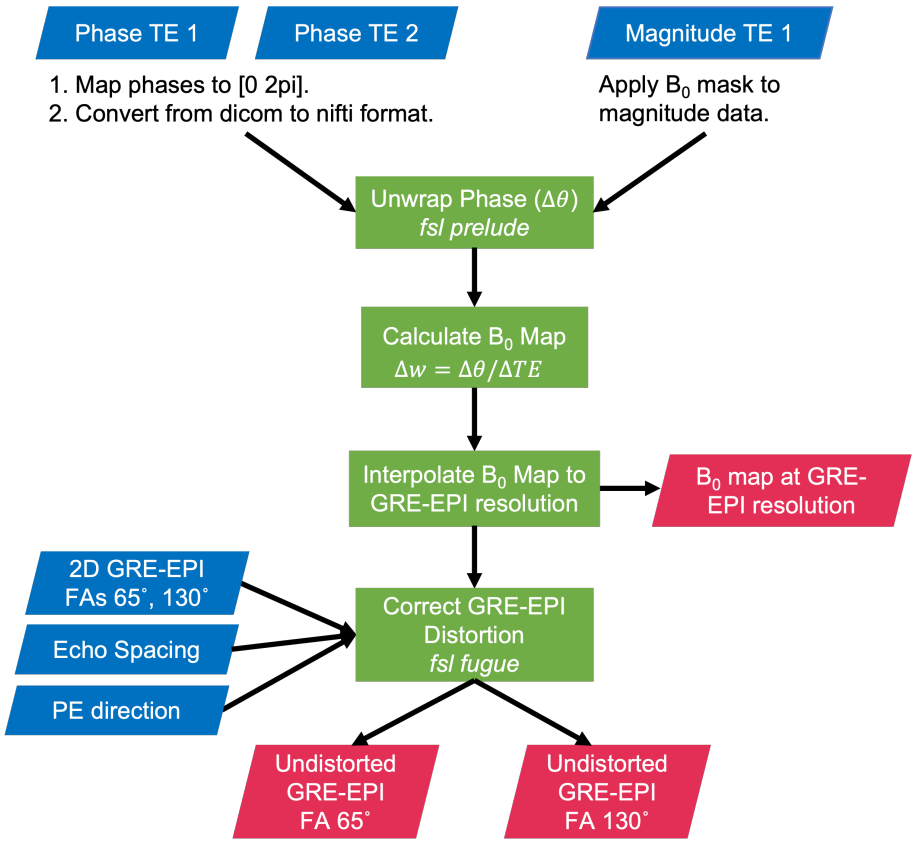


Figure 4.14: Flow diagram to calculate the B_0 map and correct the GRE-EPI data for distortion through *fsl*. For more details see Section 3.5.1.

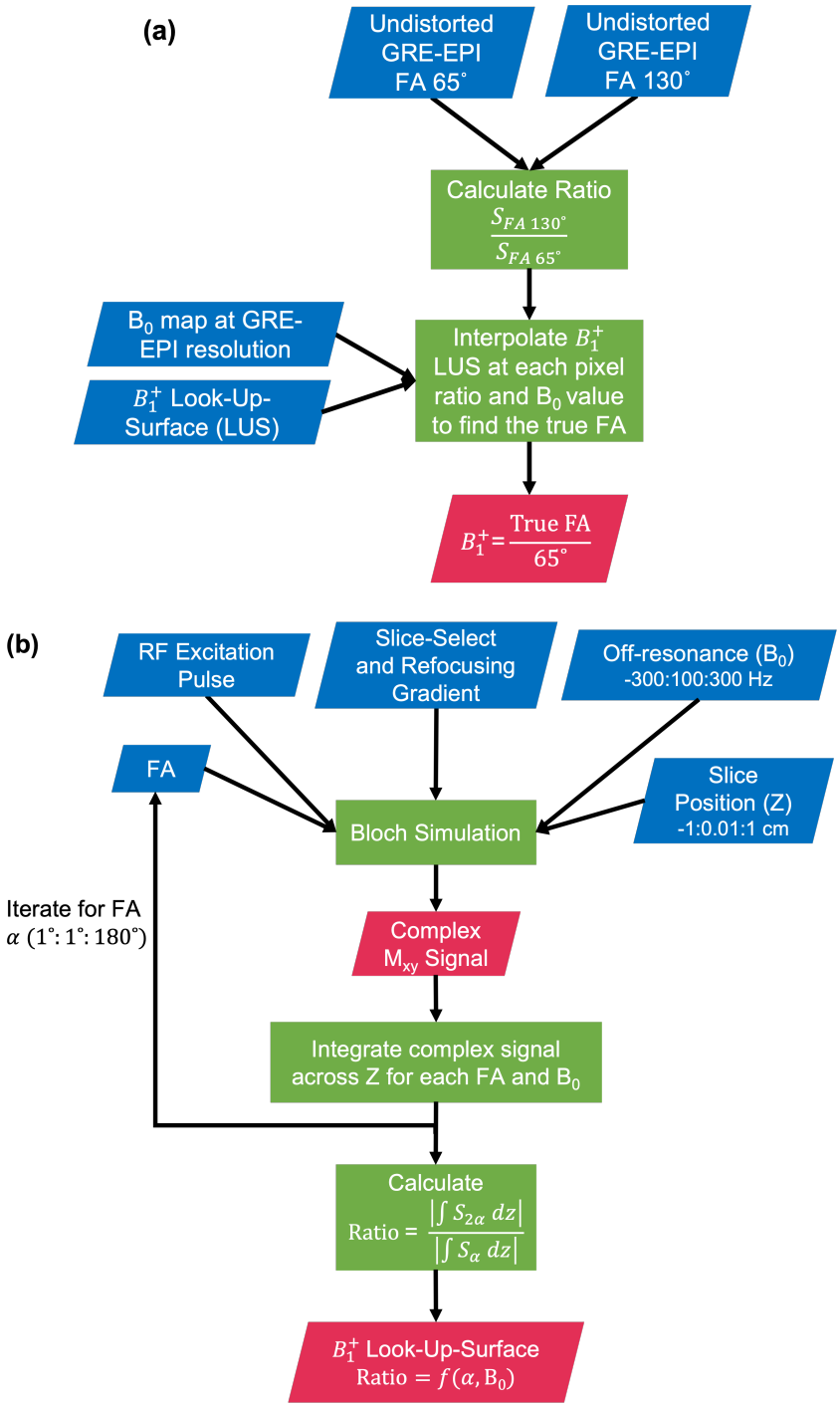


Figure 4.15: (a) Flow diagram to calculate the B_1^+ map corrected for slice profile effects. (b) Flow diagram to calculate the B_1^+ look-up surface used in (a). For more details see Section 3.4.1.

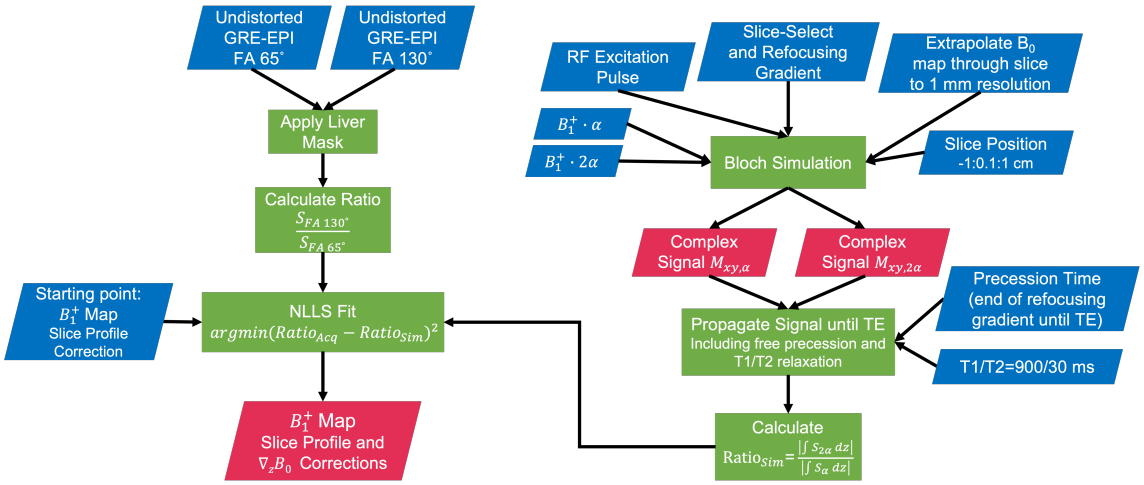


Figure 4.16: Flow diagram to calculate the B_1^+ map corrected for slice profile effects and B_0 gradient through slice dephasing. For more details see Section 3.4.2.

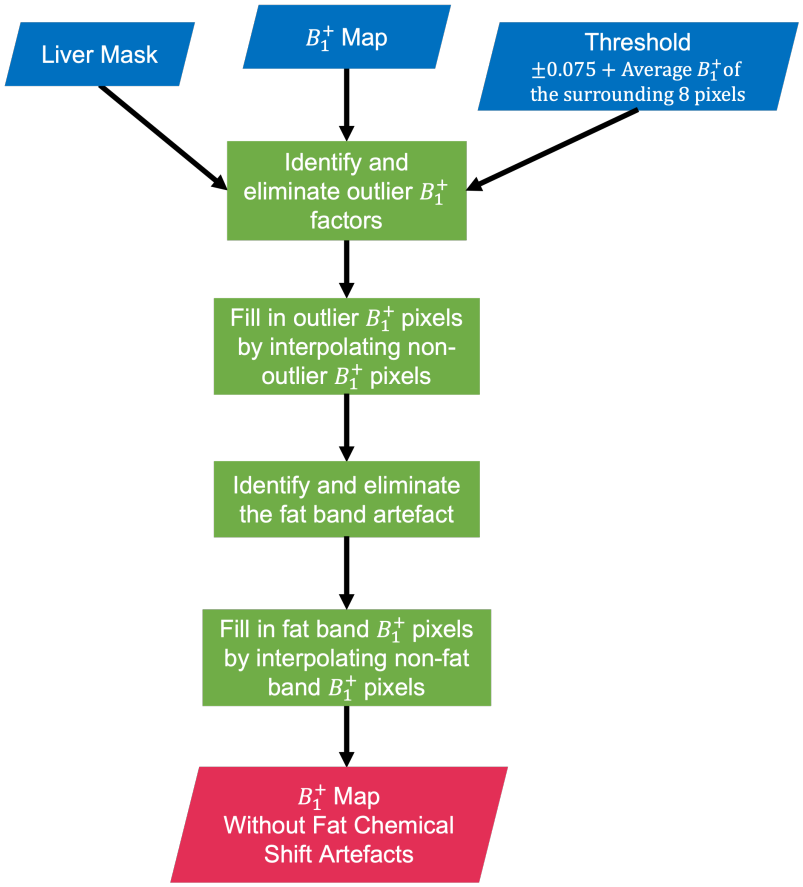


Figure 4.17: Flow diagram to eliminate the fat chemical shift artefact and outliers from the B_1^+ map. For more details see Section 3.5.2.

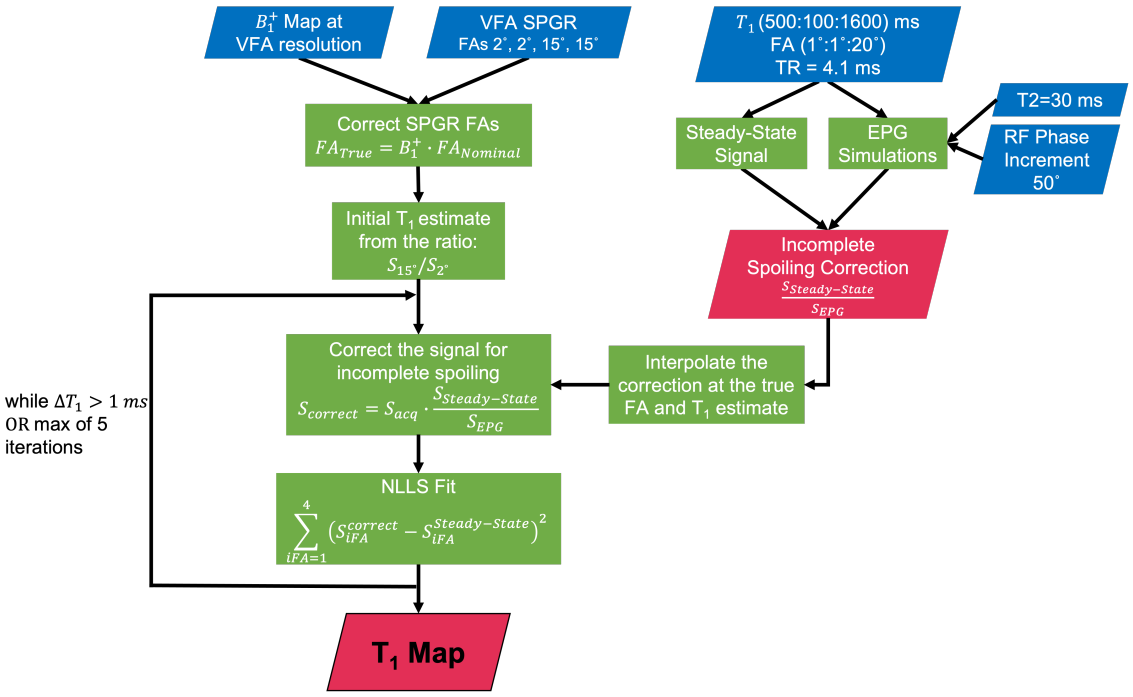


Figure 4.18: Flow diagram to calculate the T_1 map corrected for B_1^+ inhomogeneities using the B_1^+ map with all the corrections (slice profile effects, B_0 gradients through slice and EPI artefacts). The acquired SPGR signal is corrected for incomplete spoiling using extended–phase-graph simulations (see Section 3.6.1 for more details on this correction).

5

Optimal FAs for *In Vivo* Liver B_1^+ Mapping and 3D T_1 mapping at $3\,\mathrm{T}$

5.1 Introduction

The possibility of performing whole-liver T_1 mapping with high precision would enable non-invasive diagnosis, stratification, and treatment of inflammatory liver diseases. This chapter explores the main factors which limit the T_1 precision achievable using the VFA SPGR. This sequence was chosen due to its whole-liver coverage and wide availability on any $1.5\,\mathrm{T}$ or $3\,\mathrm{T}$ commercial scanner.

The VFA SPGR sequence accuracy is strongly dependent on corrections for B_1^+ inhomogeneities [29], [42]. Research using the VFA SPGR sequence in the brain for T_1 mapping recognises this source of inaccuracy [99]–[103]. Research on the liver using this sequence is primarily restricted to contrast studies using gadoxetic acid. Some recent studies are starting to acquire a B_1^+ map together with the VFA SPGR sequence [10]–[12].

The precision of VFA SPGR 3D T_1 mapping will be largely driven by the choice of FAs and TR for the application of interest. The choice of the FAs used for T_1 mapping was first studied by Wang et al. [104] in 1987, where two FAs that minimise the variance in T_1 were found through a numerical search, for a single T_1. Deoni et al. [28] showed that the two optimal angles straddle the Ernst Angle and give a signal equal to 0.71

of the Ernst angle signal. Repeating the two optimal FAs was also shown to result in better T_1 precision compared to using a range of FAs symmetrically sampled around the Ernst angle. This early work, performed at $1.5\,\mathrm{T}$, did not use B_1^+ mapping for FA correction. Scanning at the higher field strength of $3\,\mathrm{T}$ emphasised the need for B_1^+ mapping, as the relative error in T_1 without correcting for B_1^+ inhomogeneities will be equal to the B_1^+ factor squared minus 1 [62]. Cheng et al. [29] concluded that using three FAs, each of which was measured four times, offered the best accuracy and precision for T_1s extending out to $\pm$20% of the target T_1.

Given the need to acquire B_1^+ maps, the noise propagated from the B_1^+ map should also be considered when using the variance of T_1 to find the optimal FAs for the VFA SPGR. For just two SPGR FAs, Helms et al. derived an analytical expression to calculate T_1 [62]. Lee et al. [102] made use of this expression to derive the variance in T_1, including the effect of variance from the B_1^+ measurement through error propagation. However, this approach is limited to two SPGR FAs. In contrast, the approach of Cheng et al. [29] is valid for an arbitrary number of FAs, but relies on the linear form of the SPGR steady-state equation. T_1 can be calculated directly from the slope of the linear form of the steady-state equation and the least-squares fit for the slope has a known analytical expression, which allowed the authors to use error propagation. However, the linear form of the steady-state equation has been shown to result in inaccurate T_1 estimates [105].

The Fisher information matrix allows one to estimate the variance in T_1 for more than two FAs using the non-linear steady-state equation. Lewis et al. [106] determined the optimal SPGR FAs by minimising a cost function given by the variance in T_1 weighted by the joint probability density of M_0 and T_1, extracted from an open-source brain IR dataset. Nataraj et al. [107] used a min-max Cramér-Rao bound to find optimal FAs and TRs for precise T_1 and T_2 estimation through combined SPGR and dual-echo steady-state sequences [108], [109]. The optimisation was carried out over a range of T_1s, T_2 and $\pm 10\%$ B_1^+ inhomogeneities. Although the B_1^+ factor was included in the T_1 variance calculation, the noise in the B_1^+ map was not considered.

The work in this chapter aims to define the optimal FAs for DAM B_1^+ mapping and VFA SPGR that result in a precise estimate of T_1 over a wide range of clinically relevant T_1s and B_1^+ inhomogeneities typically observed in the liver at $3\,\mathrm{T}$. A novelty in our approach for the calculation of optimal FAs is the inclusion of B_1^+ uncertainties. This allowed answering the question: Does one have a higher return in T_1 precision by investing extra breath-holds in the SPGR or the B_1^+ map? An analytical expression of the T_1 variance, including the two sources of noise affecting T_1 precision: VFA SPGR noise and B_1^+ mapping noise is provided. The optimal FA values for a total of two, three, four and five angles were found through a min-max approach to the T_1 CoV calculated across the whole T_1, B_1^+ parameter space of interest. The theoretical framework proposed to calculate the T_1 variance allowed answering three main research questions: How many FAs are required and what are the optimal FAs for a target T_1 CoV that allows one to differentiate fibrosis stages?; How dependent are the optimal FAs on the SPGR SNR?; What is the benefit of using optimal vs uniformly spaced FAs? Experimental validation of the simulations was carried out *in vivo*, across 10 volunteers, and an average precision of $6.2 \pm 1.7\%$ using a set of four standard FAs at $2°$, $2°$, $15°$ and $15°$ was obtained. This was the first time non-contrast 3D T_1 mapping at this level of precision has been reported in the liver at $3\,\mathrm{T}$. A DAM-EPI based B_1^+ mapping permits the use of product sequences, i.e., pulse sequences that are present on all MRI scanners and that are regulatory approved. This should allow any MRI centre to adopt our approach for precise 3D T_1 mapping without requiring pulse sequence programming.

5.2 Theory

5.2.1 T_1 Mapping using the VFA SPGR Sequence

T_1 mapping using the SPGR sequence is based on acquiring data at different FAs to reconstruct the SPGR curve and estimate the T_1 that best fits the data points. The

SPGR signal assuming steady-state is described by Equation (5.1) [110].

$$S_i = M_0 \frac{1 - e^{\frac{-TR}{T_1}}}{1 - \cos(\alpha_i) e^{\frac{-TR}{T_1}}} \sin(\alpha_i)\,, \tag{5.1}$$

where S_i is the acquired (noiseless) signal, M_0 is a numerical constant including the proton density, signal decay due to $T_2^\star$ relaxation and the B_1^- receive sensitivity; TR is the repetition time, T_1 is the longitudinal relaxation time and α_i represents the i^{th} excitation FA.

5.2.2 Min-Max Approach for Combinatorial Optimisation

Min-max is commonly used in optimisation problems to find a robust solution that is optimal for the worst-case over a given parameter range [111]. It finds the FA combination that results in the minimum CoV in B_1^+ or T_1 for the worst-case in the considered parameter range. For the case of optimising T_1 measurements, Equation (5.2) illustrates the min-max approach for the SPGR steady-state sequence.

$$\alpha_{\text{Optimal}} = \arg\min_{\{\alpha\}} \max_{\{B_1^+, T_1\}} CoV_{T_1}(\alpha, B_1^+, T_1, TR, \sigma_{B_1^+}, \sigma_{SPGR}) \tag{5.2}$$

5.2.3 Optimal FAs for T_1 Mapping

Equation (5.2) requires the variance in T_1. During the fitting of the SPGR data to Equation (5.1), M_0 is also an unknown parameter, making the relevant parameter vector $\boldsymbol{\theta} = [M_0, T_1]$. The minimum variance in T_1 is given by the Cramér-Rao lower bound (CRLB) in Equation (5.3) [112]:

$$\sigma_{T_1}^2 \geq [\mathcal{F}^{-1}(\boldsymbol{\theta})]_{T_1,T_1}\,, \tag{5.3}$$

where $\mathcal{F}$ is the Fisher information matrix, defined through Equation (5.4):

$$\mathcal{F}(\theta)_{ij} = -E\left[\frac{\partial^2 \ln p(\mathbf{y}, \mathbf{x}, \boldsymbol{\theta})}{\partial\theta_i \partial\theta_j}\right] \tag{5.4}$$

The function $p(\mathbf{y}, \mathbf{x}, \boldsymbol{\theta})$ represents the likelihood function (Equation (5.5)), which was modelled as a multivariate Gaussian with mean equal to the steady-state signal equation

S. The steady-state signal is a function of the independent variables of the measurement $\boldsymbol{x} = [FA, TR, B_1^+]$. The vector $\boldsymbol{y} = [y_1, y_2, .., y_n]$ represents the measurements acquired at each FA and fixed TR. The total number of measurements acquired is N. σ_i is the total noise associated with the measurement at the i^{th} FA.

$$p(\mathbf{y}, \mathbf{x}, \boldsymbol{\theta}) = \left(\frac{1}{\sqrt{2\pi}}\right)^N \left(\frac{1}{\prod_{i=1}^N \sigma_i}\right) exp\left[-\frac{1}{2}\sum_{i=1}^N \frac{1}{\sigma_i^2}\left(y_i - S_i(\mathbf{x}, \boldsymbol{\theta})\right)^2\right] \tag{5.5}$$

To find the unknown parameters M_0 and T_1, a NLLS approach (Equation (5.6)) was applied, which minimised the sum of squared differences between the signals acquired and the steady-state equation, i.e., the cost function.

$$C(\mathbf{y}, \mathbf{x}, \boldsymbol{\theta}) = \sum_{i=1}^N \frac{1}{\sigma_i^2}(y_i - S_i(x_i, \boldsymbol{\theta}))^2 \tag{5.6}$$

The residuals were weighted by the inverse of the total noise variance in the measurement (σ_i^2). The total noise variance in Equation (5.7) has two contributions: the noise in the SPGR measurement (σ^{SPGR}), which was assumed to be independent of the FA, as well as the uncertainty propagated from the B_1^+ map measurement ($\sigma_{B_1^+}$). This latter uncertainty has been ignored in previous works [29], [106], [107], [113], [114]. Figure 5.1 illustrates the effect of these two noise sources, SPGR and B_1^+, on the SPGR data used to estimate the T_1 value.

$$\sigma_i^2 = \left(\sigma^{SPGR}\right)^2 + \left(\frac{\partial S_i}{\partial \alpha_i^{true}} \alpha_i^{\text{nominal}} \sigma_{B_1^+}\right)^2, \tag{5.7}$$

where $\alpha^{\text{true}} = B_1^+ \alpha^{\text{nominal}}$.

When acquiring a small number of y measurements, the variance in T_1 will be larger than the CRLB. For a NLLS fit, the uncertainty in the fitted T_1 is equal to the CRLB multiplied by the ratio between the cost function and $N - 2$ (Equation (5.8)) [115], where 2 represents the total number of parameters to estimate (T_1 and M_0).

$$\sigma_{T_1}^2 = \frac{C}{N-2}[\mathcal{F}^{-1}(\boldsymbol{\theta})]_{T_1,T_1} \tag{5.8}$$

The factor $N - 2$ represents the number of degrees of freedom in a two-parameter curve using N independent measurements. Note that as the number of measurements

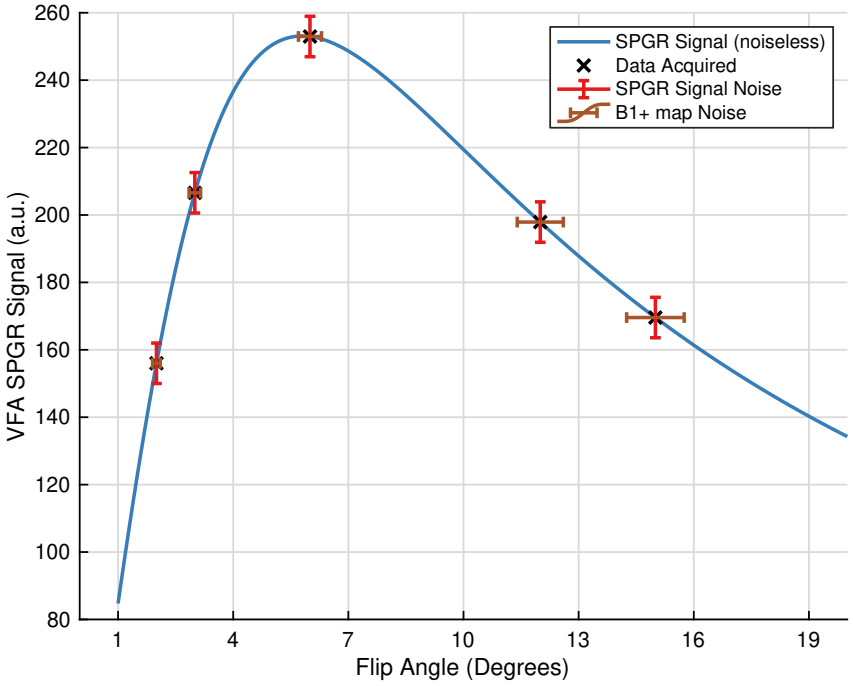


Figure 5.1: Noiseless SPGR signal, represented by the blue curve, for a T_1 of $800\,\mathrm{ms}$, TR of $4.1\,\mathrm{ms}$, M_0 of 5000, and true B_1^+ factor of 1. The noise in the SPGR is shown by the red vertical error bars, while the B_1^+ map noise introduces an uncertainty in the FA, illustrated by the horizontal brown error bars. The noise in the SPGR signal has a standard deviation of 6, which corresponds to an SNR of 26 for a FA of $2°$. The noise in the B_1^+ map has a standard deviation of 5%.

increases, the variance in T_1 tends to decrease towards the CRLB. In the limit where the acquisitions are repeated many times, C follows a chi-square distribution [115]. The mean value of a chi-square distribution is equal to the number of degrees of freedom. Thus, Equation (5.8) reduces to Equation (5.9) when predicting the variance in T_1.

$$\sigma_{T_1}^2 = [\mathcal{F}^{-1}(\boldsymbol{\theta})]_{T_1,T_1} \tag{5.9}$$

5.2.4 Optimal FAs for the DAM B_1^+ Mapping

For the B_1^+ mapping, the DAM approach described in Section 3.4.1 was adopted. Instead of using the FA pair (α, 2α), it was investigated whether another factor k (α, $k\alpha$) resulted in a smaller B_1^+ factor variance. The optimal pair of FAs (α, $k\alpha$) that minimise the variance in the B_1^+ mapping acquisition is found through error propagation

of the noise from FA α and $k\alpha$ according to Equations (5.10) and (5.11).

$$\delta R = |R| * \sqrt{\left(\frac{\delta S_{k\alpha}}{S_{k\alpha}}\right)^2 + \left(\frac{\delta S_{\alpha}}{S_{\alpha}}\right)^2}, \tag{5.10}$$

where $\delta S_{k\alpha}$ represents the signal noise at a FA $k\alpha$ and R is the ratio between the signal at a FA $k\alpha$ and FA α defined in Equation (3.3). Once δR is determined, Equation (5.11) gives an estimate of the variance associated with the B_1^+map. The uncertainty δR is mapped into an uncertainty in the FA α as illustrated in Figure 5.2.

$$\sigma^2_{B_1^+} = \left(\frac{\frac{\delta R}{(\partial R/\partial \alpha)_{\alpha_{\text{true}}}}}{\alpha_{\text{nominal}}}\right)^2 \tag{5.11}$$

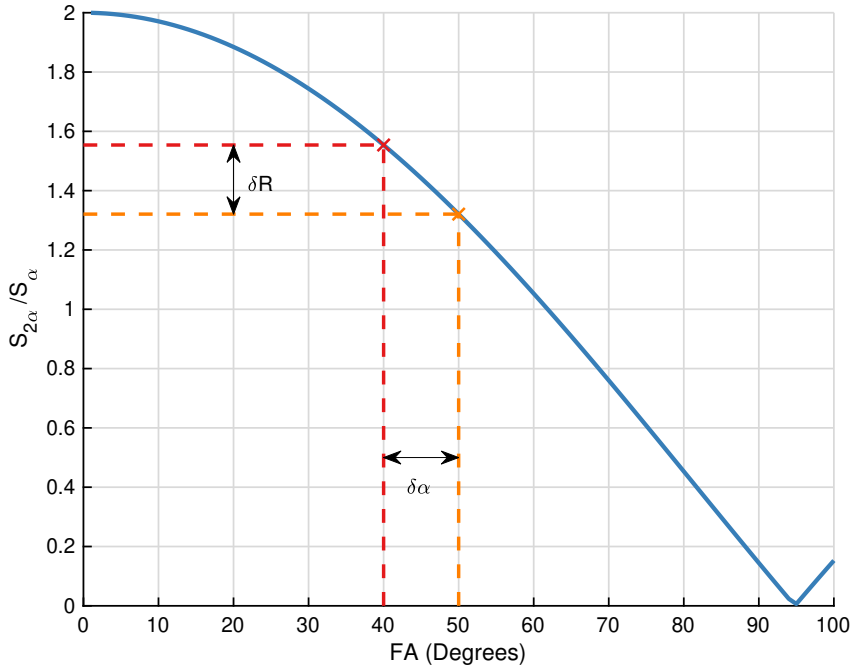


Figure 5.2: Ratio between the signal at FAs $k\alpha$ and α, where k equals 2, for FAs α varying between $1°$ and $90°$. Noise in the signals results in a variation of the ratio (δR) which will correspond to a variation in the FA ($\delta\alpha$). The larger the FA, the steeper the curve. Therefore, for a fixed uncertainty in the ratio, larger FAs yield smaller uncertainties in the B_1^+ factor estimate.

5.3 Methods

5.3.1 Simulations: Optimal FAs for T_1 Mapping

Equation (5.9) was implemented in a custom-built script in MATLAB to find the optimal FAs to run in the VFA SPGR. The five main inputs needed to estimate the

variance in T_1 are the T_1 range, TR, B_1^+ factor range, the associated noise in the B_1^+ map for each B_1^+ factor value, the noise in the VFA SPGR and the (arbitrary) value of M_0.

We are interested in determining liver T_1s in populations at low risk for NAFLD (BMI $< 25\,\mathrm{kg/m^2}$ and PDFF $< 5\%$) and high risk for NAFLD (BMI $\geq 25\,\mathrm{kg/m^2}$ and/or PDFF $\geq 5\%$). Mojtahed et al. [71] showed that MOLLI derived iron corrected (cT_1) values over this population could vary between $573\,\mathrm{ms}$ and $990\,\mathrm{ms}$ (ShMOLLI data acquired at $1.5\,\mathrm{T}$ corrected for iron and mapped to $3\,\mathrm{T}$). A conversion factor given by the ratio of $812\,\mathrm{ms}$ (mean liver T_1 at $3\,\mathrm{T}$ measured with IR SE) [63] to $666\,\mathrm{ms}$ [71] (median cT_1) was applied to the cT_1 limits resulting in a T_1 range between $700\,\mathrm{ms}$ to $1200\,\mathrm{ms}$ at $3\,\mathrm{T}$.

Preliminary SNR measurements indicated a typical SNR at $3°$ of 45 in a healthy volunteer with low BMI, and of 25 in a higher BMI patient with Primary Sclerosing Cholangitis. The simulations use the noise in the signal acquisition as this is constant for different T_1 and FAs combinations. The SNR was converted into a noise value, using average parameters estimated from the liver of the PSC patient: $M_0 = 5000$, $T_1 = 800ms$, nominal $FA = 2°$. Simulations were carried out at noise levels derived from SNRs of 12.5, 25 and 50.

The B_1^+ factor range was limited between 0.59 and 1.14 [61], with 0.05 increments. An array of 4 different uncertainties in B_1^+ factor ranging from 4.6% to 2.3%, decreasing in increments of $1/\sqrt{N}$ with $N = [2, 3, 4]$, were studied to explore the propagation of noise from the B_1^+ maps into the T_1 maps. The highest B_1^+ factor uncertainty of 4.6% was the worst-case across 10 volunteers, corresponding to an SPGR SNR of 19 (nominal $FA = 2°$, $TR = 4.1\,\mathrm{ms}$).

The optimal FAs were found by following the min-max approach applied to the T_1 CoV across the whole T_1 and B_1^+ parameter space. Optimising for the T_1 CoV, instead of the T_1 standard deviation, ensured that the algorithm was not biased towards the high T_1 values. High T_1 values will have a larger standard deviation but equal T_1 CoV to that of a smaller standard deviation at a lower T_1.

One of the clinical applications of the VFA T_1 method would be to differentiate

different stages of liver fibrosis. To achieve this, the T_1 method must have a certain precision. An estimate of the VFA T_1 standard deviation that would allow differentiating between several stages of fibrosis with 90% power at a 5% significance level is carried out in Chapter 6. Table 6.3 shows that the most stringent requirement on the T_1 CoV occurred when classifying individuals with fibrosis between stages 3-4 from those at stages 5-6. A maximum allowable T_1 standard deviation of $38\,\mathrm{ms}$ is necessary to classify correctly the T_1 of a person who has a T_1 equal to the mean T_1 of stage 5-6 ($1025\,\mathrm{ms}$). This leads to a T_1 CoV of 3.7%, which is used in this chapter as the target T_1 CoV.

To validate the theoretical CRLB-based T_1 precision, a Monte Carlo (MC) simulation was carried out over 50 000 iterations. In each iteration, random noise was added to the B_1^+ factor. The noisy B_1^+ factor was used to generate the SPGR signals at each true FA and subsequently these signals were corrupted with Gaussian noise. The SNRs were the same as those used for the CRLB framework. The nominal FAs were equal to the 4 optimal FAs output by the CRLB. The worst-case B_1^+ factor of 0.59, B_1^+ noise of 0.046 and T_1 of $700\,\mathrm{ms}$ were used, consistent with the min-max approach. The fitting parameters, M_0 and T_1, were determined using a NLLS fit to the weighted difference squared between the noisy signal and the steady-state equation. The weights are given by Equation (5.7). The mean and standard deviation of the 50000 T_1 estimates were calculated.

5.3.2 Simulations: Optimal FAs for the DAM B_1^+ Mapping

The optimal FA pairs are the ones that minimise the uncertainty in B_1^+. The uncertainty was calculated using an error propagation approach (Equation (5.11)) and validated through MC simulations. The SNR used for both simulations was 12 at a true FA of $65°$. This corresponded to the 25$^{\text{th}}$ quantile of the *in vivo* SNRs measured in the liver over the 3 central GRE-EPI slices, across 10 healthy volunteers. For each nominal FA pair (α, $k\alpha$), the B_1^+ factor standard deviation was calculated over a range of B_1^+ inhomogeneities varying between 0.59 and 1.15 [61]. The k varied between 1.25 and 4 in steps of 0.25. For both simulations, the nominal FA pair range was limited by one of

two factors: the B_1^+ corrected ambiguity angle of the sine function or the maximum FA achievable at the scanner interface of $130°$. For example, when $k = 2$ and $B_1^+ = 1.15$ the ambiguity angle is reached at a nominal angle of $82.6°$, which gives a FA pair of ($82°$,$164°$). In this case, the scanner will be the limiting factor changing the maximum nominal FA pair to ($65°$,$130°$). The signals were Bloch simulated [68] for a range of FAs, from $1°$ to $360°$, taking into account slice profile effects of the GRE RF pulse.

Using error propagation, the uncertainty in B_1^+ was calculated through Equations (5.10) and (5.11). The ratio was calculated between the simulated signals at $k\alpha$ and α as well as the first derivative of the ratio with respect to the FA α. The ratio and the derivative were interpolated at the true FA. Note that the ratio from the Bloch simulated noiseless signals will always be less than or equal to k. However, noise in the signals can push the ratio to values above k. In these cases, the ratio cannot be interpolated to find the true FA. In the MC simulations, values of the ratio above k were set to 'not a number' (NaN). To include this effect in the error propagation algorithm, the Gaussian distribution of the ratio was also truncated for values above k (Figure 5.3). This resulted in a smaller standard deviation for the ratio than that predicted by Equation (5.10). When the true FA is low or the SNR is small the number of values truncated will increase, which can affect the B_1^+ factor accuracy.

In the MC simulations, for each nominal FA pair and B_1^+ factor 10000 iterations were used to calculate the ratio and estimate the B_1^+ factor standard deviation. The complex Bloch simulated signals were corrected for slice profile effects and corrupted with zero mean additive complex Rician noise, corresponding to an SNR of 12 at a true FA of $65°$. The estimated FA was found by matching the ratio of the noisy signals with an interpolated noise-free off-line ratio, calculated over the k range and true FAs up to the ambiguity angle. The estimated B_1^+ factor is the ratio between the estimated FA and the nominal FA. The B_1^+ factor deviation is the difference between the estimated B_1^+ factor and the true B_1^+ factor.

In both the error propagation and MC simulation, the optimal FA pair was found using a

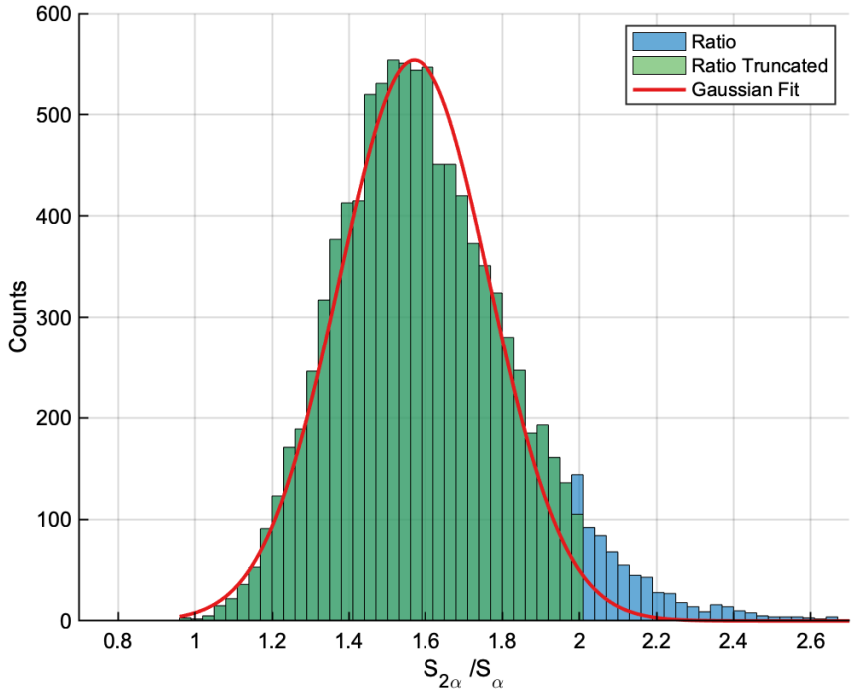


Figure 5.3: Histogram of the ratio between the noisy signals at $k\alpha$ and α (blue), calculated from a Monte Carlo (MC) simulation with α of $65°$, $k = 2$, $B_1^+ = 0.59$, $SNR = 12$ at a true FA of $65°$. MC carried out over 10000 iterations. The green histogram represents the ratio truncated at 2. The red curve is a Gaussian fit to the truncated ratio distribution with a standard deviation used to calculate the uncertainty in the ratio (δR).

min-max approach. The optimal FA pair was the one that achieved the minimum B_1^+ factor uncertainty for the true B_1^+ factor that yielded the highest B_1^+ factor standard deviation.

SNR Calculation

The noise was calculated from the difference between two *in vivo* images obtained under identical conditions at a nominal FA of $2°$ for the VFA SPGR, chosen to minimise the effect of arteries. A nominal FA of $65°$ was used for the GRE-EPI. The difference method yields accurate SNR measurements [116].

5.3.3 Image Acquisition and Processing

To validate the simulations, imaging data were acquired from 10 healthy volunteers on a $3\,\mathrm{T}$ Prisma Siemens (Siemens Healthineers, Erlangen, Germany) scanner. The imaging acquisition sequences are outlined in Section 4.1. *In vivo* data was collected by myself and Dr.Mozes, I designed the data acquisition, Dr Mozes controlled the scanner and I supported

all the acquisitions and ensured data were collected correctly. B_1^+ and T_1 map calculations were performed according to the image processing pipeline described in Section 4.2.

5.3.4 Experimental *In Vivo* Precision of the T_1 Maps

T_1 maps for each run were analysed by placing ROIs according to the criteria defined in Section 4.2.4. The estimated T_1 for each subject was calculated as a weighted sum of the T_1s extracted from each ROI selected in each slice according to Equation (5.12). In this equation, $\mathsf{N}_{\mathsf{Slices}}$ is the total number of slices, $\mathsf{N}_{\mathsf{ROIs}}$ is the total number of ROIs chosen per slice and $\mathsf{N}_{\mathsf{Pixels}}$ is the total number of pixels per ROI. The weights for each ROI were given by the inverse of the standard error in the mean squared. Weights apportioned a smaller contribution from the ROIs where the T_1 was less precise to the overall mean T_1 measured at each slice.

$$w\mu_{T_{1,\mathsf{Subject}}} = \frac{\sum_{s=1}^{\mathsf{N}_{\mathsf{Slices}}} \sum_{r=1}^{\mathsf{N}_{\mathsf{ROIs}}} \sum_{p=1}^{\mathsf{N}_{\mathsf{Pixels}}} w_{s,r}\, T_{1_{s,r,p}}}{\sum_{s=1}^{\mathsf{N}_{\mathsf{Slices}}} \sum_{r=1}^{\mathsf{N}_{\mathsf{ROIs}}} \mathsf{N}_{\mathsf{Pixels}} w_{s,r}}, \tag{5.12}$$

where $w_{s,r} = \frac{\mathsf{N}_{\mathsf{Pixels}_{s,r}}}{\sigma^2_{s,r}}$. The sum over p runs over the N pixels in a given ROI, the sum over r runs over the different ROIs in a given slice and the sum over s runs over the slices in a given acquisition.

The weighted T_1 standard deviation was calculated for each subject using Equation (5.13), at the pixel level. The same weights from Equation (5.12) were used.

$$w\sigma_{T_{1,\mathsf{Subject}}} = \sqrt{\frac{\sum_{s=1}^{\mathsf{N}_{\mathsf{Slices}}} \sum_{r=1}^{\mathsf{N}_{\mathsf{ROIs}}} \sum_{p=1}^{\mathsf{N}_{\mathsf{Pixels}}} w_{s,r}(T_{1_{s,r,p}} - w\mu_{T_{1,\mathsf{Subject}}})^2}{\sum_{s=1}^{\mathsf{N}_{\mathsf{Slices}}} \sum_{r=1}^{\mathsf{N}_{\mathsf{ROIs}}} \mathsf{N}_{\mathsf{Pixels}} w_{s,r}}} \tag{5.13}$$

The SNR for each subject was calculated from the sum of the SNRs calculated for each ROI and weighted by the T_1 variance within each ROI.

5.3.5 Experimental *In Vivo* Precision of the B_1^+ Maps

The acquisition of two B_1^+ maps, within each run, enabled the calculation of the B_1^+ map precision. The B_1^+ map precision is one of the required inputs to validate the CRLB

framework. The 3 ROIs selected in each slice of the SPGR acquisition were applied to the two B_1^+ maps interpolated to the SPGR resolution. The mean B_1^+ factor for each ROI was calculated from the B_1^+ map used in the T_1 map calculation. Subsequently, a histogram of the B_1^+ factor values within the masked B_1^+ maps was constructed with B_1^+ factor bins of width equal to 0.1 (Figure 5.4). Provided each bin contained more than $25\,\mathrm{pixels}$ with a B_1^+ factor different from zero in both repetitions, the B_1^+ factor uncertainty was calculated by taking the standard deviation of pixel-wise differences between the two binned B_1^+ maps and dividing by the square root of two. The B_1^+ factor uncertainty for each ROI was given by the B_1^+ factor standard deviation of the bin containing the mean B_1^+ factor of the ROI.

The B_1^+ pixels in-plane were five times larger than the SPGR pixels in both length and width. Thus, an ROI of $46\,\mathrm{pixels}$ in the SPGR corresponded to approximately two B_1^+ pixels. Two observations can be drawn from this calculation. It is reasonable to assume the B_1^+ factor is homogeneous within an ROI of $46\,\mathrm{pixels}$. Secondly, the B_1^+ factor standard deviation should not be calculated from the difference between two ROIs at the SPGR resolution as the B_1^+ map only had two pixels. To have more than two B_1^+ map pixels in the calculation of the B_1^+ factor standard deviation, the B_1^+ map values within the liver were binned. Binning allowed to characterise the random noise in the B_1^+ map as a function of the local B_1^+ factor. Note that noise in the B_1^+ map decreases monotonically as the B_1^+ factor increases.

In vivo B_1^+ factor uncertainties were also calculated at the GRE-EPI resolution to validate the theoretical error propagation used to estimate the B_1^+ factor standard deviation. Instead of using ROIs, the B_1^+ factor uncertainty was calculated across all GRE-EPI slices within manually drawn liver masks. The masked B_1^+ factors were separated into bins and the standard deviation was calculated as described above (Figure 5.5). Theoretical error propagation to predict the B_1^+ factor standard deviation *in vivo* were calculated using the mean B_1^+ factor within each bin and a whole-liver SNR estimated from two distortion-corrected GRE-EPI acquisitions at nominal FAs of $65°$. A global

SNR was used instead of an SNR per B_1^+ factor bin as the SNR was approximately constant over the B_1^+ factor bins for each volunteer.

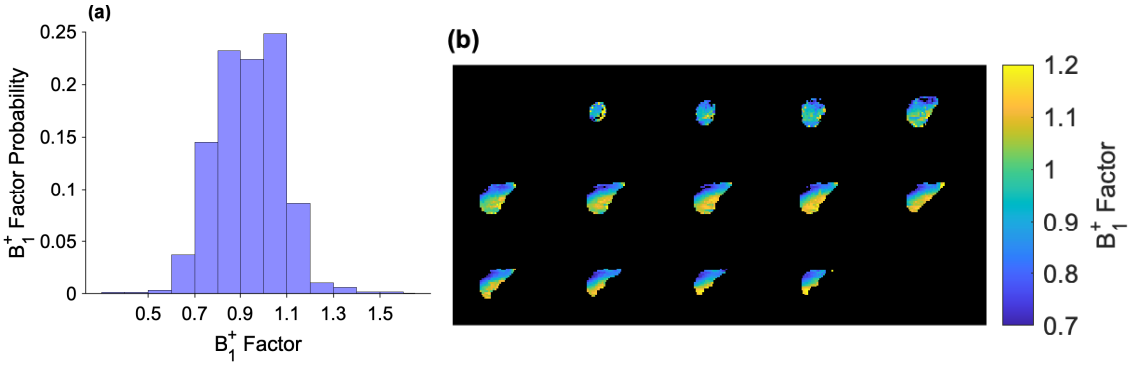


Figure 5.4: (a) Histogram of the B_1^+ factor values (bin width of 0.1), extracted from all the (b) B_1^+ map slices calculated for a healthy volunteer.

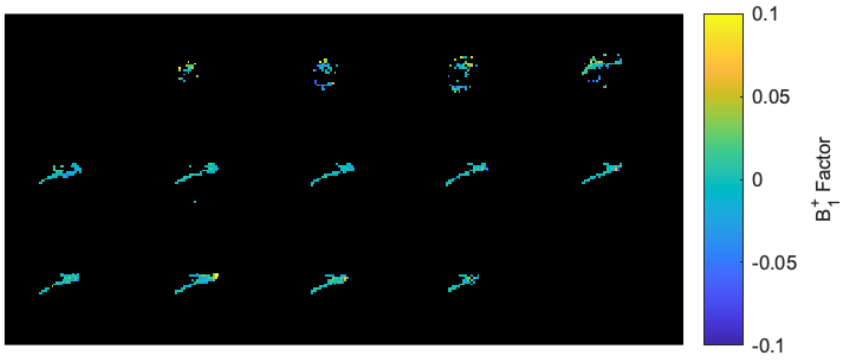


Figure 5.5: Difference between two B_1^+ maps, acquired within the same session under the same conditions, for B_1^+ factors within bin $0.8 - 0.9$.

5.3.6 Prediction of *In Vivo* T_1 Precision using the CRLB

After acquiring the data, the simulations were run again to compare the CRLB derived T_1 CoV against the experimental weighted T_1 CoV for each subject. An estimate for the variance in T_1 was calculated for each individual ROI defined in each slice. The corresponding M_0 and T_1 were set to the experimental mean value within each ROI. The mean B_1^+ factor and the associated uncertainty for each ROI were calculated as described in Section 5.3.5. The noise in the SPGR was calculated for each ROI through the method of differences. These were the main inputs necessary to simulate the variance in T_1 for each ROI. A final T_1 variance for each subject was calculated from the weighted

ROI T_1 variances through Equation (5.14).

$$w\sigma_{T_1,\text{Simulations}} = \sqrt{\sum_{r=1}^{N_{\text{ROIs}}} w_r(\sigma_r^2 + (\mu_r - w\mu_{\text{Subject}})^2)} \tag{5.14}$$

The derivation of Equation (5.14) is found in Section 5.7.1 (Appendix).

5.4 Results

5.4.1 Simulations: Optimal FAs for T_1 Mapping

Figure 5.6 (a) shows how the precision varies with the total number of FAs for three SNR cases. For the lowest SNR, the four optimal FAs that minimised the worst-case T_1 CoV were $2°$,$3°$,$15°$,$15°$. However, to calculate the SPGR SNR *in vivo* a repetition at the lowest FA was needed. Hence, it was decided to use FAs of $2°$,$2°$,$15°$,$15°$ *in vivo*, hereafter referred to as the standard 4 FAs. For a total of 2 SPGR FAs the standard 2 FAs set was $2°$,$15°$; the 3 FAs set was $2°$,$2°$,$15°$ and the 5 FAs set was $2°$,$2°$,$2°$,$15°$,$15°$. The predicted T_1 CoV for the standard FAs was compared against that of the optimal FAs as well as against five uniformly spaced FAs of $3°$,$6°$,$9°$,$12°$,$15°$. Using five optimal FAs at the highest SNR, the desired T_1 CoV represented by the dashed orange line was not achieved and therefore it was necessary to average T_1 pixels (Figure 5.6 (b)). The number of pixels to average was calculated assuming that the uncertainty in the measurement is dominated by random Gaussian noise, thus it represents a lower bound in the presence of other sources of error.

The worst-case imprecision corresponded to the lowest B_1^+ factor (0.59) and the lowest T_1 value ($700\,\text{ms}$) in the B_1^+/T_1 parameter space. Figure 5.7 shows how the precision varies for the different T_1s and B_1^+ factors that can be measured in an *in vivo* liver at $3\,\text{T}$. The T_1 CoV increased with the T_1 value measured and with deviations from a homogeneous B_1^+ factor.

Table 5.1 shows the simulated T_1 CoV obtained when using an optimal set of two, three, four, and five FAs, together with the standard FA set, using the min-max approach across a T_1 range of $700\,\text{ms}$ to $1200\,\text{ms}$ and an unbiased B_1^+ factor varying between 0.59

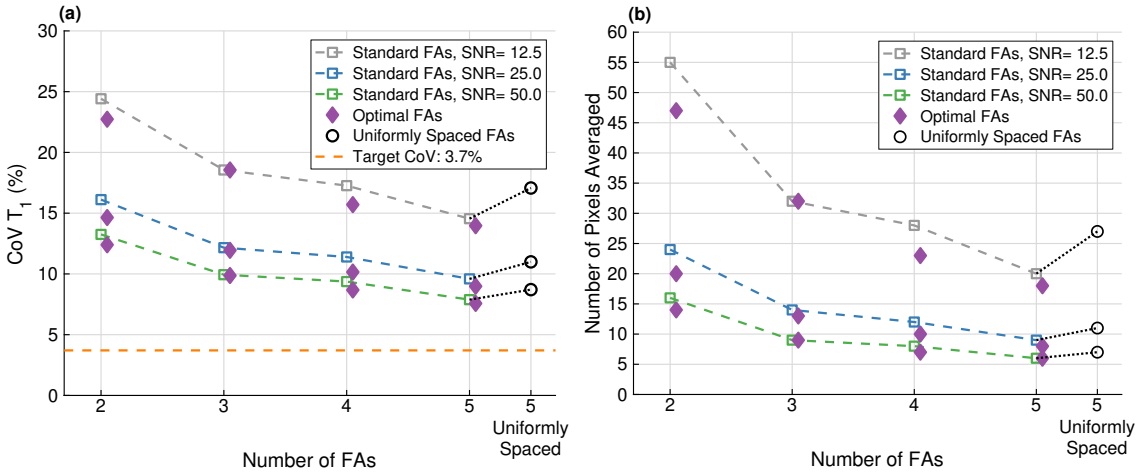


Figure 5.6: (a) CoV in T_1 as a function of the number of FAs used to estimate T_1 for three different SPGR SNRs of 12.5 (grey), 25 (blue) and 50 (green), at the largest B_1^+ factor standard deviation of 4.6%. Standard FAs (hollow squares) are compared against optimal FAs (purple diamonds) and five uniformly spaced FAs (black hollow circles). Target T_1 CoV of 3.7% to differentiate fibrosis stages represented by the dashed orange line. (b) Minimum number of pixels to average to obtain the target T_1 CoV of 3.7% for the same SNRs and FAs described in (a). All SNRs were defined at a true FA of $2°$ degrees, $TR = 4.1\,\text{ms}$, $T_1 = 800\,\text{ms}$ and $M_0 = 5000$.

and 1.14 with a constant B_1^+ factor uncertainty of 4.6%, for three different SNRs.

Table 5.1: T_1 CoV for the optimal and standard set of 2, 3, 4 and 5 FAs, for three different SNR values of 12.5, 25 and 50 (measured at a true FA $2°$, $TR = 4.1\,\text{ms}$, $T_1 = 800\,\text{ms}$ and $M_0 = 5000$) and the largest B_1^+ factor standard deviation of 4.6%. The T_1 CoV for each case corresponds to the worst-case scenario within a T_1 parameter space varying between $700\,\text{ms}$ and $1200\,\text{ms}$ and a B_1^+ factor varying between 0.59 and 1.14.

Number of FAs	SNR	Optimal FA Set (°)	T_1 CoV (%) Optimal FA set	T_1 CoV (%) Standard FA Set
2	12.5	[3 13]	22.7	24.4
	25	[3 15]	14.6	16.1
	50	[4 15]	12.4	13.3
3	12.5	[2 2 15]	18.6	18.6
	25	[3 3 13]	11.9	12.2
	50	[3 3 14]	9.9	9.9
4	12.5	[2 3 15 15]	15.7	17.3
	25	[3 4 15 15]	10.2	11.4
	50	[4 5 15 15]	8.7	9.4
5	12.5	[2 2 4 15 15]	14.0	14.5
	25	[3 3 3 15 15]	9.0	9.6
	50	[3 3 4 15 15]	7.6	7.9

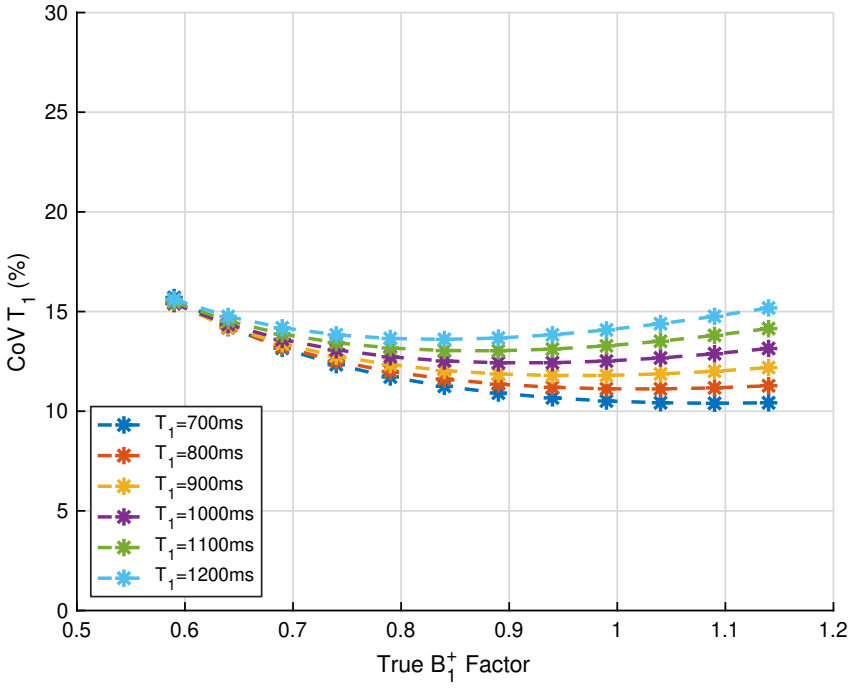


Figure 5.7: Simulated CoV in T_1 as a function of T_1 and B_1^+ parameter space for four optimal FAs with a B_1^+ factor standard deviation of 4.6%, and an SNR of 12.5 measured at a true FA of 2°, $TR = 4.1\,\mathrm{ms}$, $T_1 = 800\,\mathrm{ms}$ and $M_0 = 5000$. The smallest B_1^+ factor of 0.59 and the smallest T_1 of $700\,\mathrm{ms}$ were responsible for the largest T_1 CoV of 15.7%, while a B_1^+ factor of 1.09 and T_1 of $700\,\mathrm{ms}$ gave the smallest T_1 CoV of 10.4%. At the lowest B_1^+ factor, the T_1 CoV is nearly independent of T_1, whilst for the largest B_1^+ factor the T_1 CoV increases with T_1.

The CRLB-based algorithm always chose a set of low and high FAs, independent of the range of SNR or total number of FAs. The two unknown parameters in the steady-state SPGR equation are M_0 and T_1. Figure 5.8 (a) shows that the signal at low FAs is insensitive to T_1 variations. For FAs below 2°, the SPGR curves at different T_1s are all superimposed. This is consistent with the low angle limit of the SPGR steady-state curve which is equal to $M_0\alpha$. The lowest FA will be the least sensitive to T_1, but at the cost of lower SNR which scales linearly with the FA in the low angle regime. The algorithm takes into account the effects of SNR, B_1^+ factor range and noise and generally chose low FAs of 2° or 3°. Conversely, the role of the high FAs is to determine T_1. For FAs above the Ernst angle the signal varies considerably with T_1. Figure 5.8 (b) shows the first derivative of the signal with respect to T_1 for a range of FAs. The min-max approach minimises the T_1 variance for the worst-case scenario. From Figure 5.7, the largest variance in T_1, for a B_1^+ factor of 1, was obtained at the largest T_1 of $1200\,\mathrm{ms}$.

Figure 5.8 (b) explains why the variance in the estimation of T_1 increases with the T_1 value; the absolute value of the slope is lowest at the highest T_1 value. Taking a min-max approach, the best T_1 precision will be obtained when the true FA is at the maximum absolute first derivative. For a T_1 of $1200\,\mathrm{ms}$, the absolute value of the slope is maximum at $8.2°$. Given the lowest B_1^+ factor of 0.59, this leads to a nominal FA choice of $13.9°$, which approximates the values chosen by the algorithm to determine T_1.

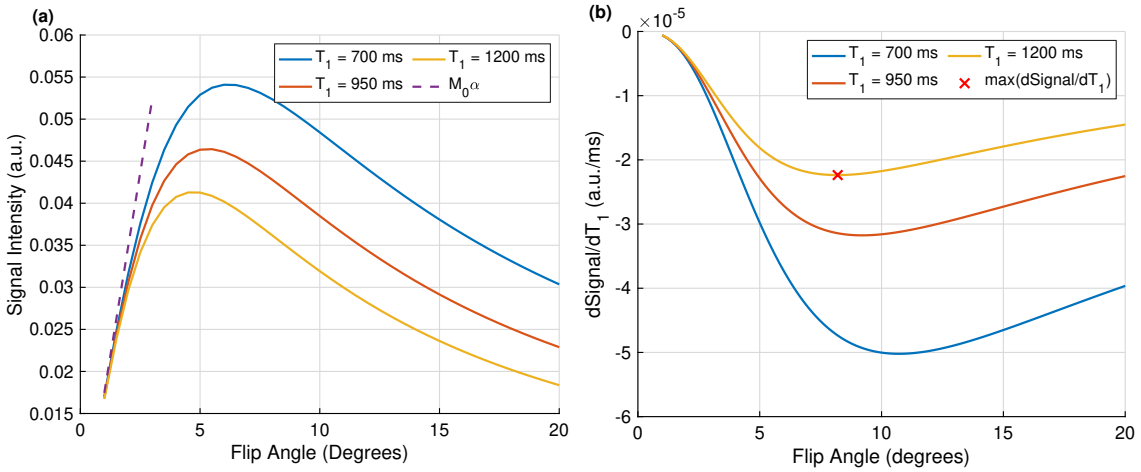


Figure 5.8: Rationale for FA choice. (a) SPGR signal as a function of nominal FA for three different T_1 values of $700\,\mathrm{ms}$ (blue), $950\,\mathrm{ms}$ (orange) and $1200\,\mathrm{ms}$ (yellow). The low FA is used to determine M_0 as it is insensitive to T_1, i.e., all the SPGR curves coincide for FAs that lie between $1°$ and $2°$. (b) First derivative of the SPGR signal with respect to T_1, for a B_1^+ factor of 1, at three different T_1 values of $700\,\mathrm{ms}$ (blue), $950\,\mathrm{ms}$ (orange) and $1200\,\mathrm{ms}$ (yellow). Taking into account only SNR, the highest T_1 precision will occur where the absolute value of the first derivative is largest, which is at $8.2°$ (red cross) for a T_1 of $1200\,\mathrm{ms}$. For the lowest B_1^+ factor of 0.59, this translates into a nominal FA of $13.9°$.

Figure 5.9 shows how the precision in T_1 depends on the noise in the SPGR acquisition and the noise in the B_1^+ map. The T_1 CoV changed more rapidly by increasing the number of SPGR FAs rather than B_1^+ map FAs, i.e., noise in the SPGR is the limiting factor for the T_1 map precision. The only exception occurred at the highest SNR of 50 for 3 SPGR FAs and 2 B_1^+ map FAs, where it was slightly more advantageous to invest in B_1^+ map FAs. As the SNR increased, the horizontal component of the gradient vectors started to increase, indicating that the SNR in the B_1^+ map starts to have a larger weight in the T_1 map precision.

Figure 5.10 shows that the percentage of T_1 map variance due to B_1^+ factor noise

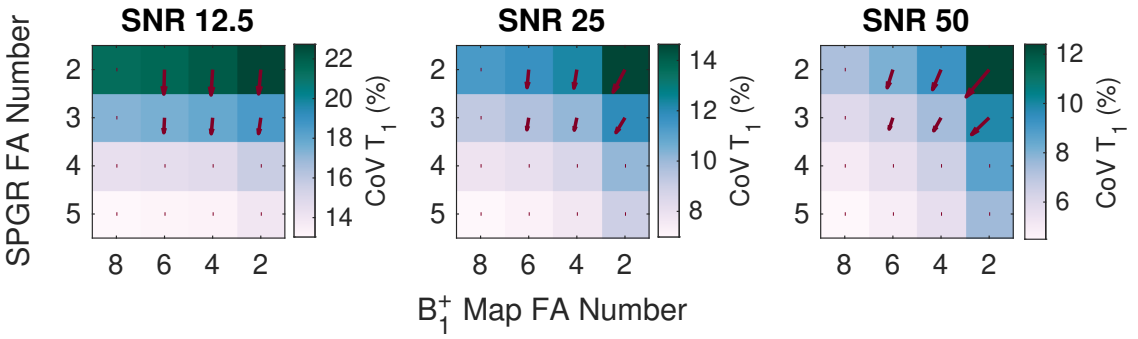


Figure 5.9: T_1 CoV for different total number of VFA SPGR and B_1^+ map FAs. The vertical component of the vectors represents the decrease in T_1 CoV by investing 2 FAs in the SPGR acquisition, while the horizontal component represents the decrease in T_1 CoV from investing 2 FAs in the B_1^+ map. There is almost always a higher return in T_1 CoV when increasing the number of SPGR FAs compared to the number of B_1^+ map FAs. This is indicated by a change in colour when stepping in the vertical direction compared to a change in shading when stepping in the horizontal direction as well as nearly vertical vectors. It is only best to invest in B_1^+ FAs for the case of 3 SPGR FAs and 2 B_1^+ FAs at the highest SNR. SNRs correspond to a true FA of 2°, $TR = 4.1\,\text{ms}$, $T_1 = 800\,\text{ms}$ and $M_0 = 5000$. The B_1^+ factor noise for 2 FAs was equal to the worst-case B_1^+ factor noise of 4.6%.

depends on the B_1^+ factor, the T_1 range, the SPGR noise and the noise in the B_1^+ map. As the SPGR SNR increased and the B_1^+ factor decreased, the relative percentage of B_1^+ factor noise in the T_1 variance increased. The noise in the B_1^+ map was characterised by three different levels of B_1^+ factor standard deviation which differed by successive factors of square root 2.

The CRLB framework was validated by comparing the predicted T_1 CoV values against those obtained from MC simulations for 4 optimal FAs (Table 5.2).

Table 5.2: Comparison between T_1 CoV calculated using the CRLB and MC simulations for 4 optimal FAs at three different SNR levels: 12.5, 25 and 50. The SNR corresponds to a true FA =2°, $TR = 4.1\,\text{ms}$, $T_1 = 800\,\text{ms}$ and $M_0 = 5000$. For these calculations, the min-max approach was followed by adopting a B_1^+ factor of 0.59 and T_1 value of $700\,\text{ms}$. The B_1^+ factor standard deviation was 4.6%. 50000 iterations were used for the MC simulations.

SNR	Optimal FAs (°)	CRLB T_1 CoV (%)	Monte Carlo Simulations T_1 CoV (%)
12.5	[2 3 15 15]	15.70	15.65
25	[3 4 15 15]	10.15	10.16
50	[4 5 15 15]	8.68	8.65

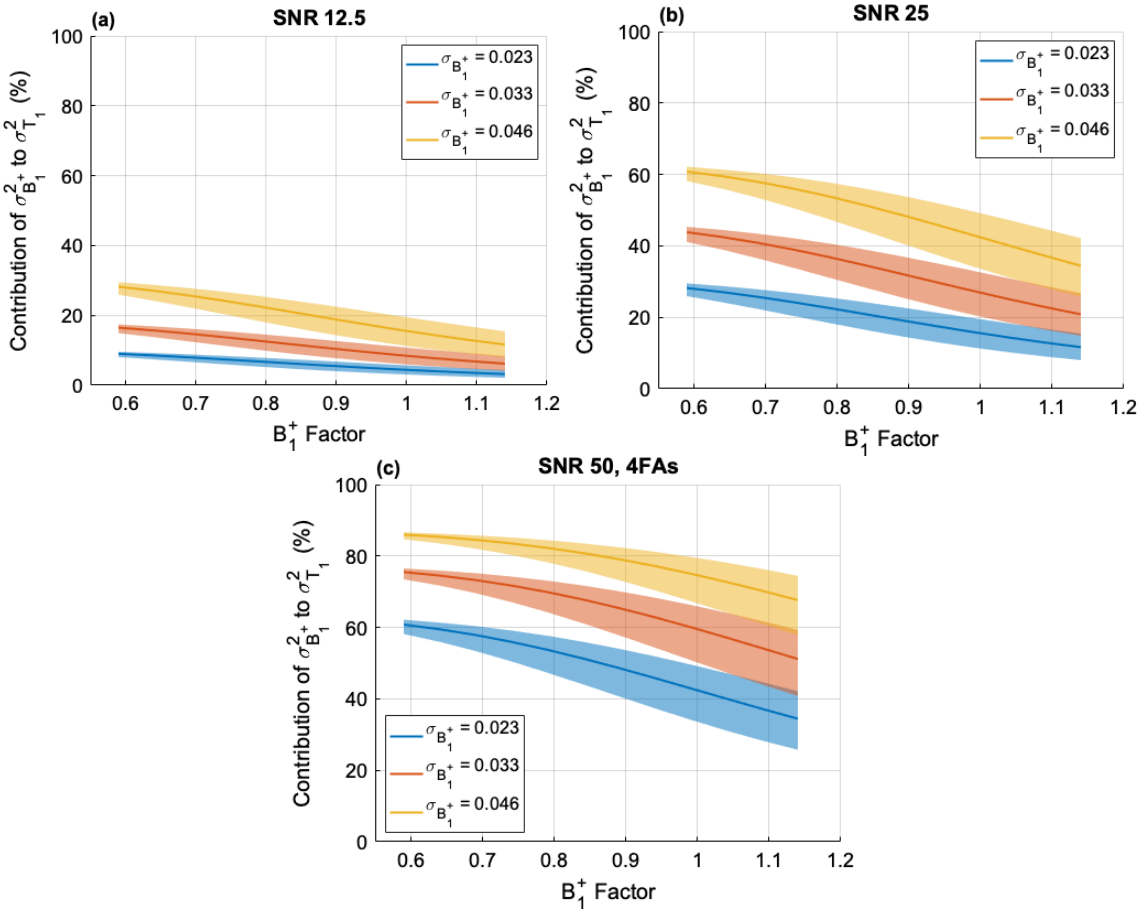


Figure 5.10: B_1^+ factor noise contribution into the T_1 map variance in percentage, for 4 standard SPGR FAs, at three different SNR levels of 12.5 (a), 25 (b) and 50 (c). The solid lines show the variation in the B_1^+ factor noise contribution for a T_1 of 900ms, while the shaded region denotes the spread in the B_1^+ factor noise contribution over the full range of T_1 values, varying between $700\,\text{ms}$ and $1200\,\text{ms}$. Each plot, corresponding to a different SPGR SNR, shows three different levels of B_1^+ factor standard deviation of 0.023 (blue), 0.033 (red) and 0.046 (yellow). The SNRs correspond to a true FA of $2°$, $TR = 4.1\,\text{ms}$, $T_1 = 800\,\text{ms}$ and $M_0 = 5000$.

5.4.2 Simulations: Optimal FAs for the DAM B_1^+ Mapping

Results from the error propagation of the B_1^+ factor uncertainty (Figure 5.11) agreed with MC simulations (Figure 5.12). Both methods found that the nominal FA pair of $65°$ and $130°$ resulted in the minimum B_1^+ factor standard deviation, using the min-max approach. The optimal numerical k factor between the two B_1^+ map FAs was 2. For an *in vivo* SNR of 12, measured at a nominal FA of $65°$, the B_1^+ factor standard deviation was 0.158 from the MC simulations, and 0.158 from the error propagation, for the worst-case B_1^+ factor of 0.59. Figure 5.11 shows that the uncertainty in B_1^+ factor

decreased rapidly as the B_1^+ factor increased.

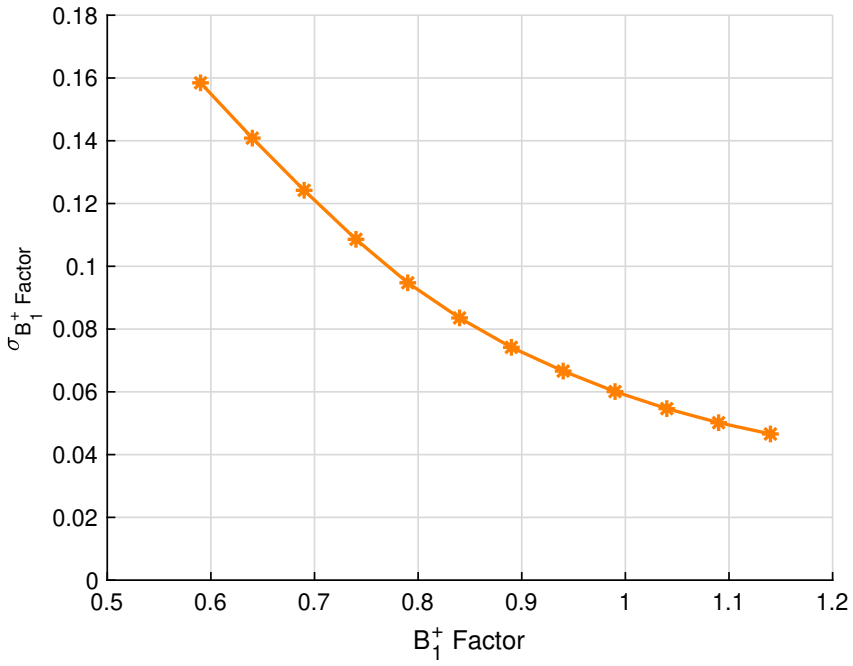


Figure 5.11: B_1^+ factor standard deviation as a function of B_1^+ factor values in the liver (at $3\,\mathrm{T}$) for $k = 2$ and a nominal FA pair of [65°,130°]. The largest B_1^+ factor standard deviation was 0.158 and occurred for the lowest B_1^+ factor in the liver of 0.59. This curve was calculated using an SNR of 12 corresponding to the 25$^{\text{th}}$ quantile measured across 10 volunteers at a nominal FA of $65°$.

Figure 5.12 shows the deviation of the estimated B_1^+ correction from the true B_1^+ factor for each pair of FAs, using a fixed k of 2, for the two extreme B_1^+ factors of 0.59 and 1.15, and a B_1^+ factor of 1. The angle of ambiguity for a B_1^+ factor of 1 is $95°$. Therefore, the smallest B_1^+ factor is expected to reach the ambiguity angle at $161°$ and the largest B_1^+ factor at $83°$. Slight deviations from these angles in Figure 5.12 are a result of noise in the signal at α and 2α.

5.4.3 Experimental *In Vivo* Precision of the T_1 Maps

Figure 5.13 shows how the T_1 CoV varied *in vivo* as the number of standard FAs increased from two to five. For a total of 5 standard FAs, to avoid an extra breath-hold by collecting a third SPGR signal at a FA of $2°$, a FA of $3°$ from the uniformly spaced FA set was used. A close agreement existed between the T_1 CoV obtained *in vivo* and the T_1 CoV simulated using the proposed algorithm.

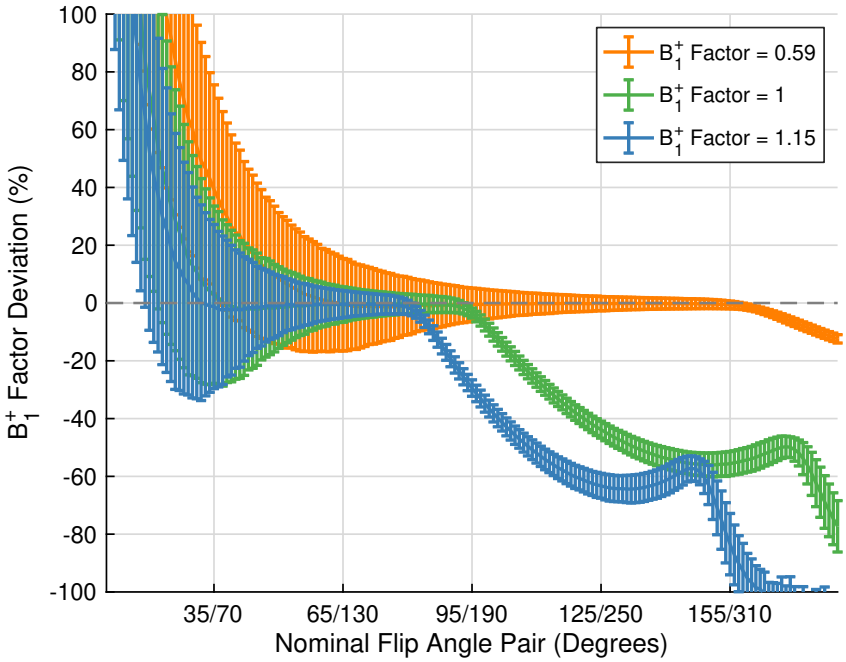


Figure 5.12: Percentage deviation in the B_1^+ factor estimate as a function of nominal FA pair for a B_1^+ factor of 0.59 (orange), a B_1^+ factor of 1 (green) and a B_1^+ factor of 1.15 (blue). Data from Monte Carlo simulations with 10000 iterations and Bloch simulated signal with added complex Rician noise and taking into account slice profile effects. The B_1^+ factor error is above 2% for nominal FAs of $58°/116°$ or lower at a B_1^+ factor of 0.59 due to low SNR. The B_1^+ factor error also deviates from 0% once the nominal FA pairs reach the ambiguity angle, which is reached first for a B_1^+ factor of 1.15 at a nominal FA pair of $83°/166°$.

The average SPGR SNR, B_1^+ map noise, mean T_1 and mean B_1^+ factor, all weighted by one over the squared standard error of the mean T_1 within each ROI, are shown in Table 5.3 for each volunteer. A large range of SNRs was observed from 19 to 59 and the mean B_1^+ map noise varied between 0.8% and 4.6%. The mean T_1 varied between $775\,\mathrm{ms}$ and $1050\,\mathrm{ms}$ and the mean B_1^+ factors between 0.62 and 0.96. All of these values, except SNRs above 50, are within the parameter space range used in the simulations. Figure 5.14 shows the T_1 CoV experimentally decreased as the SNR increased, illustrating the large range of SNRs in the cohort of imaged volunteers.

The research question of whether a larger decrease in T_1 CoV is obtained by investing extra-breath holds in the B_1^+ acquisition or the SPGR acquisition was answered *in vivo* by comparing the blue and grey curves shown in Figure 5.15 to the orange curve. It was always better to add extra breath-holds to the SPGR acquisition for the B_1^+/T_1 parameter space observed in the liver at $3\,\mathrm{T}$. Investing breath-holds in the B_1^+ map

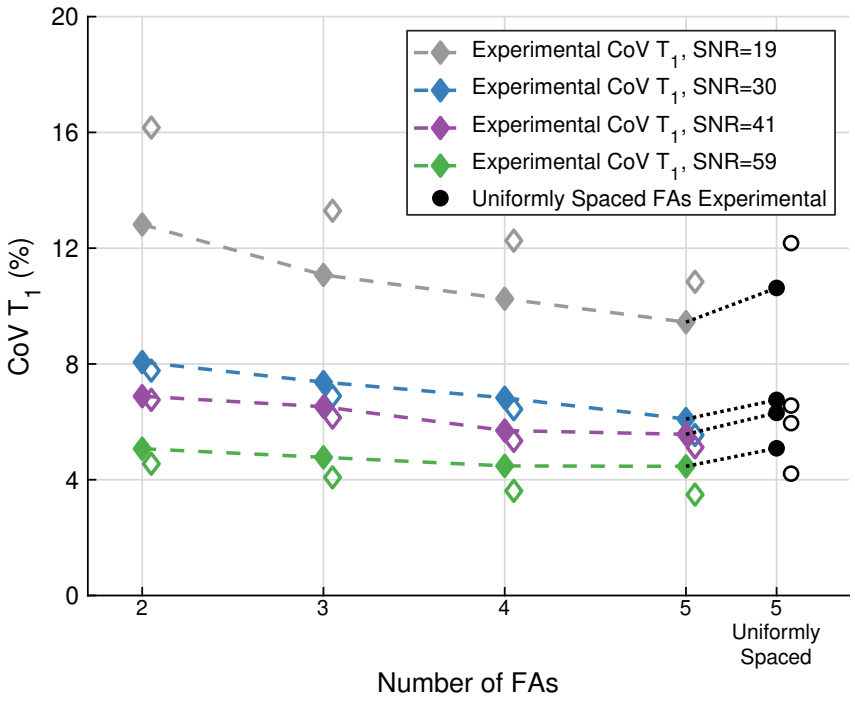


Figure 5.13: Experimental CoV in T_1 as a function of the total number of FAs used to estimate T_1 for four volunteers with different SPGR SNRs of 19 (grey), 30 (blue), 41 (purple) and 59 (green). The standard FAs in sets of 2, 3, 4, and 5 total FAs were [2,15]°, [2,2,15]°, [2,2,15,15]° and [2,2,3,15,15]°, respectively. The results using five uniform FAs of [3,6,9,12,15]° are depicted in black. The filled markers represent the experimental T_1 CoV, while the hollow markers, adjacent to the filled markers, correspond to the simulated T_1 CoV using the experimental M_0, T_1, B_1^+ factor, SPGR SNR and B_1^+ factor standard deviation obtained *in vivo* per ROI.

was actually counter-productive in three cases.

5.4.4 Experimental *In Vivo* Precision of the B_1^+ Maps

Figure 5.16 shows the *in vivo* experimental B_1^+ factor uncertainty and the error propagation predicted uncertainty for each B_1^+ factor bin of the whole liver volume B_1^+ maps, for each of the 10 volunteers.

Table 5.3: Characterisation of SPGR SNR, T_1, B_1^+ factor and B_1^+ factor noise parameter space for each volunteer. The SNR is calculated from the difference of two distinct SPGR images acquired at a nominal FA of $2°$. The mean, minimum and maximum are reported for the T_1, B_1^+ factor and B_1^+ factor noise. The mean values are within the bounds defined in the simulations.

Volunteer	SPGR SNR	T_1 (ms) Mean [Min Max]	B_1^+ Factor Mean [Min Max]	B_1^+ Factor Noise Mean [Min Max]
1	44	809 [619 1070]	0.914 [0.691 1.077]	0.028 [0.009 0.099]
2	30	822 [621 1054]	0.713 [0.521 0.846]	0.012 [0.002 0.055]
3	52	1050 [743 1319]	0.937 [0.764 1.020]	0.030 [0.011 0.074]
4	51	947 [795 1177]	0.892 [0.765 1.101]	0.016 [0.004 0.063]
5	59	985 [853 1230]	0.959 [0.761 1.086]	0.012 [0.004 0.027]
6	34	775 [594 1007]	0.809 [0.529 1.003]	0.022 [0.008 0.041]
7	41	793 [603 978]	0.922 [0.699 1.164]	0.016 [0.007 0.037]
8	19	926 [626 1341]	0.621 [0.474 0.741]	0.046 [0.023 0.079]
9	26	798 [607 1091]	0.836 [0.619 0.998]	0.026 [0.012 0.044]
10	53	970 [802 1157]	0.927 [0.723 1.064]	0.008 [0.002 0.020]

5.5 Discussion

SPGR is a powerful sequence to get 3D whole liver coverage within a breath-hold. While it is well known that the accuracy of the T_1 maps generated with this sequence is strongly dependent on the accuracy of the B_1^+ maps, what is less appreciated in the literature is how the precision of the T_1 maps are influenced by the B_1^+ map precision. In this work, we presented a quantitative model based on the Fisher information matrix to predict the variance in T_1 considering both the noise in the SPGR acquisition and the noise in the B_1^+ maps. We identified the optimal set of FAs for the SPGR sequence using a min-max optimisation approach on the T_1 variance, calculated with our model, across an extended range of T_1s, spanning values observed in populations at low and high risk for NAFLD, and a range of B_1^+ factors observed in the *in vivo* liver at $3\,\mathrm{T}$. Simulations were used to explore the robustness of the FA choice to variations in SNR, to compare the optimal FAs to standard and uniformly spaced FAs, and to understand the influence of the B_1^+ precision on the T_1 precision. The simulation results were validated

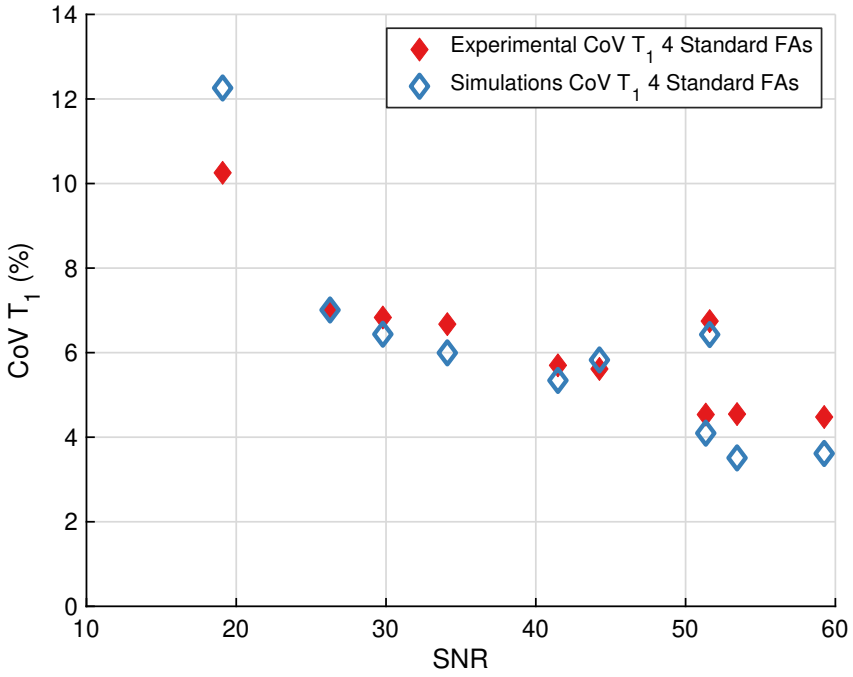


Figure 5.14: Experimental CoV in T_1 as a function of SNR for the 10 volunteers. The experimental T_1 CoV is shown in filled red diamonds, and the simulated T_1 CoV in hollow blue diamonds for the 4 standard FAs of [2,2,15,15] degrees. As the SNR increases the T_1 CoV decreases both experimentally and using the developed simulations algorithm. Only volunteer 3, with an SNR of 53, had an increase in T_1 CoV relative to the volunteer with the previous lowest SNR. Volunteer 3 had the largest mean T_1 of $1050\,\mathrm{ms}$ and Figure 5.7 shows that T_1 CoV increases as T_1 increases. The simulated T_1 CoV is in close agreement with the experimental T_1 CoV, except for the lowest SNR case.

in vivo in 10 volunteers. The close agreement between the experimental data and the simulations is a strong indicator that the proposed model can be used to characterise the T_1 variance and subsequently estimate optimal FAs.

Optimising FA Choice in SPGR Improves T_1 Map Precision and Can Save Breath-Holds

Our results demonstrate it is worthwhile investing in FA choice as a smaller T_1 CoV was achieved compared to uniformly spaced FAs, and it will avoid unnecessary breath-holds. Using a uniform spacing FA set of 3,6,9,12,15 degrees resulted in a higher T_1 CoV than using only 4 optimal FAs (Figure 5.6) or 4 standard FAs *in vivo* (Figure 5.13). This is in agreement with Cheng et al. [29] and Lewis et al. [106] which confirmed that optimal FAs outperformed the same number of arbitrarily chosen FAs. Our results go one step further by showing that you can outperform the arbitrarily chosen FAs

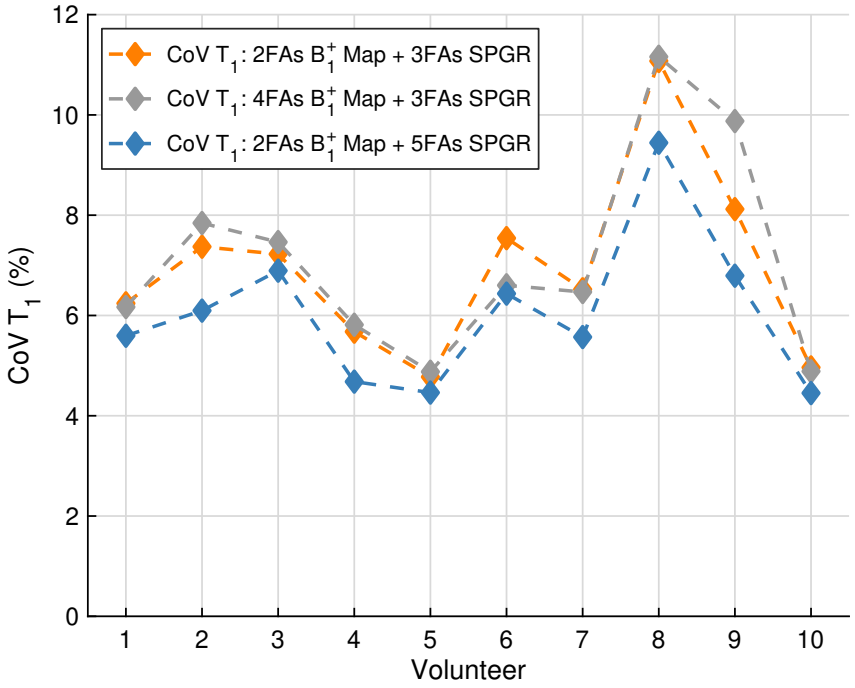


Figure 5.15: Experimental CoV in T_1 using as a reference case 2 FAs in the B_1^+ map and 3 standard FAs in the SPGR acquisition (orange). Investing 2 more FAs in the B_1^+ map results in the grey curve, while investing 2 more FAs in the SPGR acquisition gives the blue curve. The *in vivo* data confirms the conclusions drawn from the simulations results (Figure 5.9) that it is best to invest FAs in the SPGR acquisition rather than the B_1^+ map. This occurs within the parameter space explored for all 10 volunteers.

with one fewer FA in the optimal FA set.

The close agreement between the simulated T_1 CoV, using the proposed Fisher information algorithm, and the experimental data (Figure 5.13) for 4 volunteers with SNRs differing by as much as a factor of 3 supports the validity of our theoretical model. The largest disagreement in T_1 CoV between the experimental data and the simulations was observed for the volunteer with the lowest SNR. This volunteer had the largest B_1^+ map noise with a mean of 4.6%, almost 2.5 times higher than the average B_1^+ map noise of the other volunteers. This was a consequence of the volunteer falling asleep and free-breathing during the acquisition. Due to large liver misalignments between the two B_1^+ maps, the method of the differences between two B_1^+ maps might have overestimated the B_1^+ map noise present in the single B_1^+ map used in the experimental T_1 map calculation. Looking at the GRE-EPI raw data, there were large misalignments of more than $1\,\mathrm{cm}$ between FAs, with simultaneous positive and negative misalignments

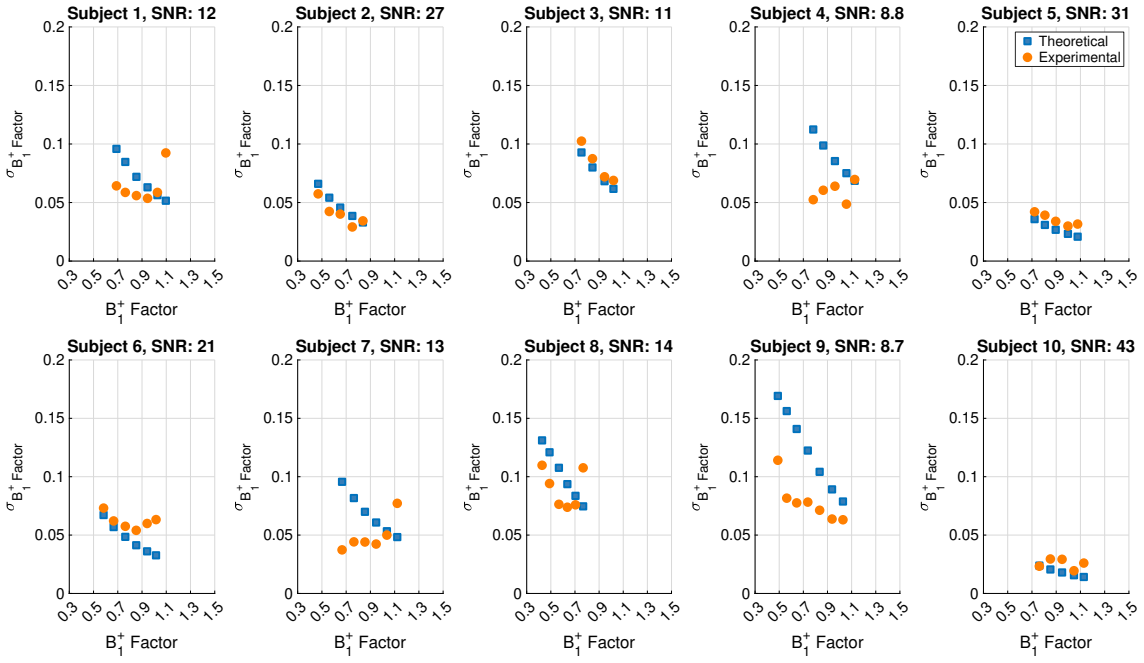


Figure 5.16: Experimental B_1^+ factor standard deviations (orange circles) as a function of the number of B_1^+ factor bins across the whole liver volume for each volunteer. Theoretical standard deviations in B_1^+ factor (blue squares) were estimated from the GRE-EPI SNR, calculated from the difference between two GRE-EPI images acquired at a nominal FA of $65°$. Experimental standard deviations were estimated from the difference of two B_1^+ maps at the GRE-EPI resolution. Volunteers 2, 5 and 10 had the lowest noise magnitude and it was constant across all B_1^+ factor bins, showing a good agreement between experimental and theoretical B_1^+ factor standard deviations.

along the slice direction between two repeated acquisitions.

Table 5.1 provides the MR Physicist studying the liver T_1 at $3\,\mathrm{T}$ with some useful FA sets for different SNRs plausible *in vivo* and a TR that can achieve whole liver coverage. When optimising the acquisition for contrast T_1 mapping, the variance in T_1 benefits from higher FAs as lower T_1s lead to larger Ernst angles.

Influence of SPGR SNR on FA Choice

A rough knowledge of the *in vivo* SNR is helpful, but not a determining factor in finding the optimal FAs using our approach. We have shown that using the same standard FAs for all SNRs resulted in minimal increases in T_1 CoV compared to the optimal FAs found for each SNR. The largest difference in T_1 CoV between the standard and optimal FAs was 1.7% in absolute terms, or less than 8% in relative terms, for 2 FAs at the lowest SNR (Figure 5.6). For the liver parameter space at $3\,\mathrm{T}$, repeating two FAs to

create a standard FA set is a robust and nearly optimal strategy.

Investing FAs in the VFA SPGR or the B_1^+ Map?

The strong co-variance of T_1 with the B_1^+ factor might motivate one to invest breath-holds in repeating the B_1^+ acquisition to improve T_1 precision. However, the effect of the B_1^+ map noise on the T_1 map precision depends on the magnitude of the B_1^+ factor noise, the SPGR SNR, B_1^+ factor and T_1 range (Figure 5.10). At the lowest SPGR SNR of 12.5 ($FA = 2°$, $TR = 4.1\,\mathrm{ms}$, $T_1 = 800\,\mathrm{ms}$ and $M_0 = 5000$), B_1^+ factor had a minor effect on the T_1 CoV. The standard deviations in the B_1^+ map had a larger impact on the T_1 CoV as the SPGR SNR increased. Simulation results showed that increases in the B_1^+ factor noise favoured an overall increase in the value of the optimal FAs. Our simulations (Figure 5.9) and experimental data (Figure 5.15) showed that acquiring two extra FAs in the SPGR provided a larger reduction in T_1 CoV than repeating the B_1^+ acquisition. Investing two extra FAs in the B_1^+ map without changing the SPGR FA set should reduce the T_1 CoV. However, our experimental data (Figure 5.15) showed an opposite trend, with overall equal or higher T_1 CoVs using 4 FAs for the B_1^+ map. This suggests that other sources of uncertainty in the B_1^+ map are larger than the decrease in noise one expects from repeating the B_1^+ acquisition. One hypothesis is the added opportunity for breath-hold misalignments between the four B_1^+ FAs, resulting in higher variance in the B_1^+ map.

B_1^+ Map Precision

We also explored the optimisation of B_1^+ mapping precision using standard product sequences and taking the ratio of two fully recovered GRE signals acquired at FAs α and $k\alpha$. A min-max approach confirmed that using a k factor of 2 resulted in the smallest B_1^+ factor variance over a B_1^+ factor range observed in the liver at $3\,\mathrm{T}$. The maximum uncertainty in the B_1^+ factor occurred at the smallest B_1^+ factor of 0.59, as it leads to the lowest SNR (Figure 5.11). MC simulations confirmed the theoretical uncertainty from error propagation. Both methods showed that the FA pair $65°/130°$ minimised the uncertainty in the B_1^+ factor for the worst-case B_1^+ inhomogeneity of 0.59. From the

MC simulations (Figure 5.12) we concluded that the FA lower bound is influenced by the SNR, while the upper boundary is determined by the lack of phase data from this product sequence and the magnitude of the B_1^+ factor inhomogeneity. In our system, the largest nominal FA available at the scanner console of $130°$ was the limiting factor as the angle of ambiguity with the largest B_1^+ factor of 1.15 is $83°$, with 2α equal to $166°$.

The error propagation simulations showed that the B_1^+ factor standard deviation decreased as the B_1^+ factor increased (Figure 5.11). Therefore, the uncertainty in the experimental B_1^+ maps was calculated for binned B_1^+ maps. Only one B_1^+ map was binned to avoid artificially low B_1^+ standard deviations. The experimental standard deviations in the B_1^+ factor generally agreed with the theoretical predictions based on the GRE-EPI SNR. Volunteers 2, 5 and 10 had experimental standard deviations in all B_1^+ factor bins below 5% (Figure 5.16), except for the lowest B_1^+ factor bin for volunteer 2. For these three subjects, the noise estimated from the two GRE-EPI acquisitions at FAs of $65°$, hereafter named FA65 and FA65R, was always below 20 and constant across the B_1^+ factor values as expected. The remaining volunteers had experimental B_1^+ factor standard deviations above 5% and the experimental values were often lower than the theoretical predictions. There were large signal differences between FA 65 and 65R, and consequently, higher noise levels by factors of 3-7 compared to those of volunteers 2,5 and 10. In addition, the noise was not constant but varied with the B_1^+ factor from the anterior to the posterior part of the liver. This suggests that noise sources other than the intrinsic hardware noise and patient loading were present. The largest differences in signal between the two FAs of $65°$ occurred for blood vessels, gall bladder and the chemical shift of unsaturated fat in regions of B_1^+ factors above 1. Furthermore, large differences were concentrated around the edges of the liver, suggesting a misalignment between the two acquisitions from different expiratory breath-holds. Liver dome misalignments were confirmed by visual inspection of the raw data. The B_1^+ map seems to be more immune to breath-hold misalignments than the signal. Possibly misregistration results in non-random noise between the different GRE-EPI acquisitions. However, error propagation

assumes the noise is uncorrelated, treating misalignment-derived differences as originating from random unbiased noise sources. This might explain the larger B_1^+ factor standard deviations for the simulations compared to the experimental data.

Boudreau et al. [101] measured *in vivo* standard deviations in B_1^+ factor across 6 healthy volunteers using a SE-EPI DAM and obtained on average a standard deviation of 1.57% for an SNR of 130 ± 30. Our experimental B_1^+ factor standard deviation, without binning, ranged from 4.1% to 23.0% for SNRs of 48 and 15 (for a signal at $90°$), respectively.

Note that the experimental uncertainty in the B_1^+ factor in Table 5.3 is lower than that shown in Figure 5.16. In Table 5.3 the uncertainty was calculated from B_1^+ maps interpolated to the VFA SPGR resolution as this is the resolution of the T_1 maps. Five pixels in the VFA T_1 map resolution corresponded to $1\,\mathrm{pixel}$ at the B_1^+ map resolution, thus sharing the same B_1^+ factor and noise. Therefore, the B_1^+ factor standard deviation in Table 5.3 is lower.

Comparison to the Literature

The search for optimal FAs using the SPGR sequence started in 1987 where Wang et al. [104] presented an analytical expression for the T_1 variance, derived from the linear form of the SPGR signal using error propagation. In agreement with our results, they also emphasised the benefits of optimising the SPGR FAs to reduce scan time compared to arbitrarily chosen FAs, without any cost to the T_1 precision. Limitations of this analytical model include the consideration of a single T_1, validity of the expression for only 2 FAs, absence of B_1^+ inhomogeneities and relying on a linear least-squares fit. Although Deoni et al. [28], [114] offered an empirical analytical expression for the 2 optimal FAs that avoids a time-consuming numerical search, the expression suffers from the same limitations as listed for Wang et al. Both authors recognised that when using more than 2 FAs, the uncertainty in the fitted T_1 does not benefit from a range of FAs but instead from repeating the 2 optimum FAs.

The approach by Lee et al.[102] is unsuitable for more than two FAs. The authors

comment in their discussion that according to their expression for T_1 variance using more than 2 different FAs will increase the T_1 variance. Contrary to Lee et al., our results indicate as expected that increasing the number of distinct FAs results in a decreased T_1 CoV. Lee et al. assume that the different noise contributions to the T_1 variance from the SPGR signal and the B_1^+ map are independent. Our experiments using the CRLB agree with this independence. However, in the Lee et al. formulation, the contribution due to the noise in the B_1^+ map is independent of the SPGR FA values. Their expression reduces to a variance in T_1 from the B_1^+ map noise given by $\sigma^2_{T_1} = \sigma^2_{B_1^+} \cdot (-2 \cdot \mathrm{TR} \cdot \frac{T_1}{B_1^+})$. As a result, if one were to use Lee's algorithm to find the optimal SPGR FAs, an increase in B_1^+ map noise would not change the FA values. On the other hand, our CRLB algorithm includes in the weighting factor of the cost function a B_1^+ factor noise term that varies with the SPGR FA. As a result, the optimal FAs chosen by our algorithm increase with increasing values of B_1^+ factor noise, keeping all other factors constant. This happens even in situations where the min-max approach chooses the same B_1^+/T_1 for the worst-case T_1 CoV. Based on the B_1^+ map noise and SPGR noise independence, Lee et al. performed experimental measurements that suggest that the noise in the B_1^+ map and the noise from the individual SPGR signals, both propagated with similar weights into the T_1 map variance. For our liver parameter space at $3\,\mathrm{T}$, the relative contribution of the B_1^+ map noise into the T_1 variance varied significantly with the B_1^+ factor and with the SNR of the SPGR acquisition (Figure 5.10). For the lowest SNR, the variance in T_1 was dominated by the SPGR noise. Even for the largest noise in the B_1^+ map, the percentage of T_1 variance due to the B_1^+ variance was always less than 25%. For the largest SNR, there was an inversion of roles with the B_1^+ factor noise dominating the T_1 variance over the SPGR noise. As the B_1^+ factor decreased, the percentage of the T_1 variance due to the B_1^+ map variance increased. The dispersion in the relative contribution of B_1^+ factor noise over the range of liver T_1s increased as the B_1^+ factor increased.

Cheng et al. [29] proposed the adoption of 3 angles for the SPGR extracted from 2 sets of optimal FA pairs, one optimal for the minimum T_1 and the other for the

maximum T_1. While this approach agrees with our findings that the largest T_1 CoV is obtained for the extreme T_1s (Figure 5.7), their method did not take into account either inhomogeneities or noise in the B_1^+ factor measurement in their calculation of the T_1 variance. Out of the 4 optimal FAs, the authors advise dropping one of the lowest FA. Our results suggest, that for a narrower range of T_1s found in the liver at $3\,\mathrm{T}$ and B_1^+ ranges, the optimal set of three FAs uses two low FAs (Table 5.1). One possible reason is that the SPGR curve is steeper for the low angles (Figure 5.8). This agrees with findings of Schabel et al. [113] who state that the "error is largely determined by the smaller of the two FAs and is comparatively insensitive to changes in the larger angle". It should also be noted that in the Cheng et al. [29] paper the variance in T_1 is inversely proportional to M_0 squared. This is incorrect given that for the case of 2 FAs the T_1 can be calculated from the ratio of the signals, which is independent of M_0.

Choosing the set of FAs that minimises the T_1 CoV for the B_1^+/T_1 combination with the maximum T_1 CoV, will ensure that the T_1 CoV will always be equal or better to this value. Other authors have used different approaches to take into account the large range of T_1s, as is required in liver applications, when calculating the optimal FAs. For example, Schabel et al. [113] calculated the two optimal FA pairs over a range of T_1s by minimising the integral of the mean relative error in T_1. Lewis et al. [106] expanded the selection of optimal FAs to more than two and weighted the T_1 variance by the joint probability density estimate of M_0 and T_1. These alternative approaches might provide a lower T_1 CoV on average, but will result in larger T_1 CoVs for $T_1\mathrm{s}/B_1^+$ factors near the extremes compared to the min-max approach. Another advantage of min-max is the elimination of starting points in the multi-dimensional search for the optimal FAs. The method of Lewis et al. suffered from choosing erroneous local minima depending on the choice of starting point.

Similar to Lewis et al.[106], our results also suggest using two angles on either side of the Ernst angle in the steeper portion of the SPGR curve. However, in contrast to their results, our min-max approach did not necessarily choose to repeat low or high FAs (Table 5.1). The authors reported worse rat ex-vivo T_1 CoVs by 2-3% compared to FAs

calculated using Deoni's formula, for SNRs above 5. The authors suggested that B_1^+ inhomogeneities are the cause of Deoni's FAs outperforming their optimal FAs. The authors did not consider B_1^+ variations during FA selection. In our case, the T_1 CoV of 2 optimal FAs selected using Deoni's criteria ($\alpha = \cos^{-1}\left(\frac{0.71^2 e^{-TR/T_1} \pm (1-e^{-2TR/T_1})\sqrt{1-0.71^2}}{1-e^{-2TR/T_1}(1-0.71^2)}\right)$) increased the simulated T_1 CoV by 4.2%, 2.9% and 1.9% for SNRs of 12.5, 25 and 50 respectively in our liver $3\,\mathrm{T}$ parameter range. Repeating Deoni's FA pair resulted in T_1 CoV increases of 3.3%, 2.3% and 1.4% compared to the 4 optimal FAs found using our approach, for SNRs of 12.5, 25 and 50, respectively. Furthermore, even though Lewis et al. reported that their standard deviation was 20-50 times larger than the bias in simulation data, there was a statistically significant increase in ex-vivo T_1 as the magnitude of the FAs increased, which suggests this could have arisen from incomplete spoiling. Finally, these authors also stated that the T_1 variance was dependent on the joint T_1 and M_0 distribution. In our results, changing M_0 did not affect the T_1 variance; the term $[\mathcal{F}^{-1}(\boldsymbol{\theta})]_{T_1,T_1}$ is independent of M_0.

Similar to our method, Nataraj et al. [107] used the CRLB to find optimal scan parameters through a min-max approach restricted to two SPGR FAs. The authors considered variations in the B_1^+ factor but disregarded the effect of noise from the B_1^+ map on the T_1 precision. Their optimal scan parameters for SPGR consisted of a low and a high FA of [$5°$, $15°$] and a larger TR of $12.2\,\mathrm{ms}$ than our TR of $4.1\,\mathrm{ms}$. Using a larger TR decreases T_1 CoV as it increases the SPGR first derivative with respect to the FA for angles below the Ernst angle, and increases the Ernst angle and therefore the signal and SNR. We were restricted to a maximum TR of $4.1\,\mathrm{ms}$ in our system to achieve whole liver coverage within a 15s breath-hold, but in systems where a higher TR is permitted this should be utilised. Their simulations resulted in a $28\,\mathrm{ms}$ T_1 standard deviation at SNRs between 105-122. Their posterior WM T_1 CoV for one healthy volunteer varied between 8-10% for 2 SPGR FAs of [$5°$, $15°$] and a $TR = 12.2\,\mathrm{ms}$. For a 2 FA acquisition with a smaller TR of $4.1\,\mathrm{ms}$, experimentally we achieved a T_1 CoV of almost half (5%) for our highest SNR *in vivo* of 57, which is approximately half of their SNR. The absence of direct comparison between their theoretical framework and the acquired phantom or

in vivo T_1 standard deviations does not allow validation of their method.

Recent work at $7\,\mathrm{T}$ [117] where the B_1^+ variation is particularly large, studied FA choice and RF pulse shape and duration for precise and unbiased T_1 estimates of the whole brain. Their criterion for choosing the optimal FAs was based on the mode of the apparent Ernst angle. By following this procedure, the authors are essentially using the mode of the B_1^+ inhomogeneities which will be close to 1. Therefore, their approach for optimal FA choice disregards B_1^+ variations. However, as they emphasise B_1^+ variations are one of the main sources of systematic errors in VFA T_1 mapping and become more important as the field strength increases, with variations in their study between -70% and +30% of the nominal FA. Their T_1 CoVs using two FAs for WM and cortical GM were 7.1% and 8.8%, respectively. In our work with two optimal FAs, we achieved T_1 CoVs varying between 5.1% and 12.8% depending on the *in vivo* SNR (Figure 5.14). At 7T it is not clear whether better T_1 precision could be achieved as we expect the SNR to increase, but there will also be an increase in the B_1^+ inhomogeneities and liver tissue T_1 which contribute towards larger T_1 CoVs.

This is the first time non-contrast-enhanced 3D T_1 mapping has been reported in the liver at $3\,\mathrm{T}$. Although several groups have presented contrast-enhanced liver 3D T_1 maps [10]–[12], [118], T_1 precision is usually overlooked as they are measuring large differences in T_1, of approximately 50% or larger, between pre- and post-contrast T_1 maps. However, relying solely on pre-contrast T_1 maps for clinical diagnosis and monitoring of liver diseases will benefit from attaining the best precision possible.

Nevertheless, Dietrich et al.[119] explored the possibility of using a single FA after contrast injection that minimised the statistical error in T_1. The post-contrast FA always lay above the Ernst angle defined at a given T_1/TR. A single FA is feasible when using the M_0 estimate from the pre-contrast T_1 mapping acquisition. To neglect statistical error from the M_0 estimate, the authors acquired a large set of 13 FAs uniformly spaced by increments of $2.5°$. Fewer FAs could have been used if the authors had also optimised the FA choice pre-contrast, reducing susceptivity to motion artefacts. Although B_1^+

mapping was acquired, B_1^+ spatial variations were not considered in the post-contrast FA optimisation which will certainly result in different FA values. A wide post-contrast T_1 range between $2629\,\mathrm{ms}$ and $137\,\mathrm{ms}$ was considered and the optimal post-contrast FA was the average of the FAs that resulted in a minimal statistical error for each T_1. The disadvantage of averaging, compared to the min-max, are larger T_1 uncertainties for the extreme T_1s.

Final Remarks on the Proposed Framework

Our approach offers several advantages. An analytical expression characterising the variance in T_1 was developed that considers a large range of T_1 and B_1^+ factors without any approximations, simplifications, or making use of the linear form of the SPGR signal. Importantly, the analytical expression is computationally inexpensive. It overcomes the time-consuming burden of MC simulations, which can be prohibitive when including large ranges of T_1, B_1^+ factors and nominal FAs (in our case this resulted in a 9-dimensional search space with 5 FAs). SPGR is used in several applications for T_1 mapping, including contrast. Our method applies to any research using the SPGR signal for T_1 mapping, regardless of body part imaged or B_1^+ mapping method adopted. Note that our approach uses the CRLB, which assumes there is no bias in the measurement of T_1. Therefore, any errors in the T_1 due to uncompensated B_1^+ inhomogeneities, incomplete spoiling or slice profile in 2D acquisitions should be carefully considered and corrected.

An important factor affecting the precision of the B_1^+ and T_1 maps is consistency in the expiratory breath-hold positions. Our ten volunteers cohort contained extreme cases: three volunteers had very consistent breath-holds; one volunteer fell asleep and consequently was free-breathing throughout the acquisition; the rest had visually misaligned liver domes for some of the GRE-EPI and SPGR acquisitions. Nevertheless, the extreme free-breathing case had a T_1 CoV only 2.3 times greater than the highest SPGR SNR case, demonstrating inherent robustness to our optimised method.

5.6 Conclusion

A whole liver 3D T_1 mapping using 4 optimised FAs was achieved *in vivo* at $3\,\mathrm{T}$ using product sequences with an average T_1 CoV of $6.2 \pm 1.7\%$ across 10 volunteers using a total of 7 FAs, 4 standard SPGR FAs ($15\,\mathrm{s}$ each), 2 B_1^+ FAs ($10\,\mathrm{s}$ each) and 1 B_0 map FA ($8.6\,\mathrm{s}$). We developed a theoretical framework to compute the T_1 variance that incorporates both the effect of noise from the VFA SPGR signal and the B_1^+ map as well as the range of B_1^+ factors and T_1s observed in the liver at $3\,\mathrm{T}$. This framework allows one to efficiently identify optimal FA values as well as determine the total number of SPGR measurements needed to achieve a certain T_1 CoV threshold. Validation of several predictions of this framework was achieved *in vivo* at $3\,\mathrm{T}$.

5.7 Appendix

5.7.1 Overall T_1 Uncertainty from Joining T_1 Distributions from Several ROIs

Consider the case of N ROIs. The distribution of T_1 values within each ROI is modelled as a Normal distribution, each with a mean value μ_j, and a standard deviation σ_j:

$$P_j(x) = \frac{1}{\sigma_j\sqrt{2\pi}} \exp\left[\frac{-(x-\mu_j)^2}{2\sigma_j^2}\right] \tag{5.15}$$

where j is the index running over the number of ROIs.

The weighted mean value of the union of N distributions is:

$$\mu = \sum_{j=1}^{N} w_j \mu_j \tag{5.16}$$

The weights for each distribution are proportional to one over its variance:

$$w_j = \frac{\left(1/\sigma_j^2\right)}{\sum\limits_{j=1}^{N} 1/\sigma_j^2} \tag{5.17}$$

The weights are normalised so their sum is equal to unity.

The weighted variance of the union of N distributions is:

$$\sigma^2 = \sum_{j=1}^{N} w_j \int_{-\infty}^{\infty} P_j(x)(x-\mu)^2 = \sum_{j=1}^{N} w_j \int_{-\infty}^{\infty} dx\ \frac{(x-\mu)^2}{\sigma_j\sqrt{2\pi}} \exp\left[\frac{-(x-\mu_j)^2}{2\sigma_j^2}\right] \tag{5.18}$$

To carry out the integral for each of the distributions, the substitution $s = x - \mu_j$ was used:

$$\begin{gathered} \int_{-\infty}^{\infty} ds\ \frac{(s+\mu_j-\mu)^2}{\sigma_j\sqrt{2\pi}} \exp\left[\frac{-s^2}{2\sigma_j^2}\right] \\ = \frac{1}{\sigma_j\sqrt{2\pi}} \left\{ \int_{-\infty}^{\infty} ds\ s^2 \exp\left[\frac{-s^2}{2\sigma_j^2}\right] + \int_{-\infty}^{\infty} ds\ (\mu_j-\mu)^2 \exp\left[\frac{-s^2}{2\sigma_j^2}\right] \right\} \\ = \frac{1}{\sigma_j\sqrt{2\pi}} \left\{ \sqrt{2\pi}\sigma_j^3 + \sqrt{2\pi}\sigma_j(\mu_j-\mu)^2 \right\} \end{gathered} \tag{5.19}$$

The resulting weighted variance for N distributions is:

$$\sigma^2 = \sum_{j=1}^{N} w_j \left(\sigma_j^2 + (\mu_j-\mu)^2\right) \tag{5.20}$$

This formula was used to calculate the variance from the N T_1 distributions corresponding to the N ROIs.

6

Repeatability, Accuracy and Precision of *In Vivo* Liver 3D T_1 Mapping at $3\,\mathrm{T}$

6.1 Introduction

Quantitative MRI liver studies have shown that non-contrast liver T_1 may be a promising novel biomarker for aiding in the diagnosis and treatment of liver diseases as increases in liver T_1 correlate with liver fibrosis and inflammation. T_1 mapping has been carried out on patients, spanning paediatric to elderly populations, with different liver aetiologies including NAFLD [19], [21], [71], [120], NASH, cirrhosis [22], [121], chronic liver diseases [122]–[124], portal hypertension [125]–[127], HCC [128]–[130] and autoimmune liver diseases [131], [132] such as autoimmune hepatitis, autoimmune sclerosing cholangitis, primary sclerosing cholangitis (PSC) and primary biliary cholangitis (PBC).

Adoption of a method in clinical practice requires high repeatability and reproducibility. Repeatability represents the agreement between replicate measurements over a short period of time under a set of conditions. These conditions include using the same measurement procedure, the same operators, the same measuring system, the same operating conditions, and the same physical location [133]. Reproducibility is also a measurement of agreement between replicate measurements, but under a different set

of conditions than repeatability. The repeated measurements could be carried out at different locations, by different operators or with different measuring systems [133].

MOLLI [120], [134], SASHA [135], [136] and IR-SE-EPI [20], [121] have been shown to be highly repeatable and reproducible in vitro and *in vivo*. Despite MOLLI's and SASHA's high repeatability, these methods have one big limitation: they are restricted to imaging a single slice at a time. It is not efficient to acquire the whole liver volume when each slice requires a separate breath-hold. Whole Liver T_1 mapping would be advantageous to characterise fibrosis and inflammation across the entire organ. In particular, the main application benefiting from 3D T_1 mapping would be diffuse liver diseases, such as PSC or PBC, as well as HCC. The phenotype of diffuse liver diseases is characterised by areas of normal T_1 adjacent to areas of increased T_1 which may be restricted to areas of the liver that are not imaged using single slice methods. In addition, HCC screening will unquestionably miss tumours if whole-liver coverage is not used. The second limitation of using MOLLI for T_1 mapping is that MOLLI requires a relatively modern scanner with a cardiac license, limiting its deployment. In addition, MOLLI gives a biased T_1. Several effects contribute to an inaccurate T_1 [26]. Magnetisation transfer effects are the biggest factor responsible for MOLLI T_1 underestimation ($-170\,\mathrm{ms}$ for $T_1 = 1175\,\mathrm{ms}$ and $T_2 = 54.4\,\mathrm{ms}$ using a tan/tanh inversion pulse and MOLLI scheme 5-(1)-1-(1)-1) [27]. Other factors are sensitivity to T_2 in the balanced steady-state free precession (SSFP) readout ($\sim -45\,\mathrm{ms}$ for a $T_2 = 45\,\mathrm{ms}$, $T_1 = 1000\,\mathrm{ms}$), imperfect inversion efficiency, off-resonance effects on the SSFP readout ($\sim -40\,\mathrm{ms}$ for $B_0 = \pm 100\,\mathrm{Hz}$, FA of $35°$, $T_1 = 1000\,\mathrm{ms}$), and FA error in the SSFP readout with a smaller error for lower angles at the expense of reduced SNR and thus precision ($\sim -10\,\mathrm{ms}$ for a variation in FA from $30°$ to $35°$, $T_1 = 1000\,\mathrm{ms}$) [26]. In addition, the presence of fat and water in the same voxel result in MOLLI T_1 overestimation ($\sim 21\%$ overestimation for 20% fat fraction, at $3\,\mathrm{T}$ with a $TR/TE = 2.14/1.07\,\mathrm{ms}$) [137], and the presence of iron decreases T_1 (1.5% increase in hepatic iron concentration results in ∼29% decrease in T_1) [24]. For the latter two effects, correction factors have been developed [24], [138].

Unlike MOLLI, the saturation-recovery method SASHA gives an accurate measure of T_1 in the heart [40], making it a good candidate to be used as an *in vivo* gold standard T_1 method in the liver. However, SASHA is also a single slice T_1 method. On the other hand, 3D IR-SE EPI with multiple TIs can achieve whole liver coverage [20] using a free-breathing approach through respiratory triggers [139]. Both SASHA and multi-TI 3D IR-SE-EPI are not available as product sequences which prevents their immediate widespread clinical use and adoption.

The aim of the work described in this thesis was to design a whole-liver T_1 mapping method that uses sequences that are widely available on any scanner independent of the manufacturer. This will facilitate widespread clinical use of the method (no pulse sequence programming or research agreements required), and enable the comparison of T_1 values in multi-centre studies as well as in pharmaceutical drug trials using different scanners in multiple countries. To demonstrate its potential use to the liver community, we need to assess the repeatability and reproducibility performance of the developed methods in vitro and *in vivo*. Repeatability is important as the method should not be affected by the positioning of the patient in the MRI scanner or any hardware or software dependent biases. *In vivo* repeatability is the key research question addressed in this chapter.

Additionally, two other research questions are addressed in this chapter: (1) is the method accurate *in vivo*? and (2) provided the method is repeatable under identical testing conditions, is the method precise enough to stratify liver diseases? Accuracy of the method in measuring the true T_1 would be important to allow for universal cut-off values to be developed and applied clinically in the stratification and monitoring of liver diseases. This would facilitate dialogue between clinicians and increase the utility of liver T_1 as a universal biomarker in clinical practice, similar to the clinical role of blood serum used in the calculation of the enhanced liver fibrosis score [140]. In addition, understanding the confounding factors affecting the method's accuracy is important to avoid false diagnoses, as could be the case in analysing myocardial MOLLI T_1 values in regions of off-resonances [26]. Moreover, the method should have a precision that

allows a two-fold goal: differentiate different stages of liver disease as well as monitor T_1 changes of a single patient in longitudinal studies or during treatment. Previous studies have mainly focused on the use of T_1 for the diagnosis and stratification of liver disease or changes in T_1 following administration of a drug treatment [122], [140]. Another area of clinical interest is the longitudinal monitoring of liver disease progression. This is the most demanding application in terms of precision when for example the patient is at the borderline between two Ishak fibrosis scores. Ideally, the method should also allow flexibility to provide an increased precision if needed.

6.2 Methods

6.2.1 Image Acquisition and Processing

Imaging data were acquired in ten healthy volunteers (5 female and 5 male) on a $3\,\mathrm{T}$ Prisma Siemens (Siemens Healthineers, Erlangen, Germany) scanner, using a spine array coil and an 18-channel abdominal array coil. The pipeline is illustrated in Figure 6.1. The study was designed to assess the repeatability of 3D T_1 mapping, therefore the volunteer was scanned twice in visit one. Between run 1 and run 2 the volunteer was asked to step out of the scanner, rest for approximately 3 minutes, and then go back into the scanner to acquire repeated data. In a second visit, approximately one week later, the volunteer was re-scanned only once with the same sequence scheme. Images for all sequences were acquired in the transversal plane with PE direction anterior–posterior. *In vivo* data was collected by myself and Dr. Ferenc Mozes, I designed the data acquisition, Dr. Mozes controlled the scanner and I supported all the acquisitions and ensured data were correctly collected.

A multiple-TR multiple-TE stimulated echo acquisition mode (STEAM) single-voxel magnetic resonance spectroscopy sequence [141] was used as the gold standard T_1 *in vivo*. Thirty ^{1}H single-average spectra were acquired in a $20 \times 20 \times 20\ \mathrm{mm}^3$ voxel placed on the left lobe of the liver, avoiding vessels and bile ducts. Twenty-two spectra were collected with a fixed TE of $10\,\mathrm{ms}$ and varying TRs of [— 350 2000 325 1500 300 1250 275 900 250

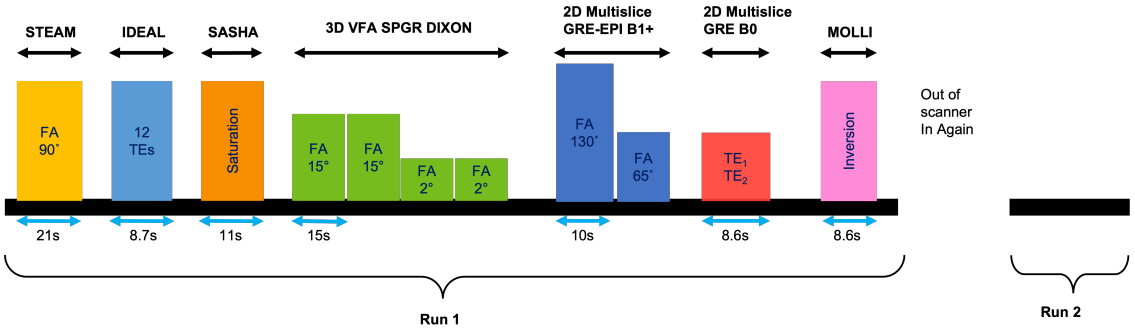


Figure 6.1: Imaging sequences acquired in the healthy volunteer repeatability study.

700 225 550 200 500 175 450 150 400 600 800 1000] ms to calculate T_1. The remaining eight spectra were collected with varying TEs of [15 20 25 30 50 70 90 110] ms and large TRs of [1002.5 1005 1007.5 1010 1020 1030 1040 1050] ms to calculate T_2. The three slice-selective excitation pulses had a nominal FA of $90°$. Data were acquired within a single $21\,\mathrm{s}$ breath-hold. A 3D Shim followed by a frequency adjustment were applied before running the STEAM sequence. The thirty spectra were fit using a MATLAB version of the advanced method for accurate, robust and efficient spectral (AMARES) fitting algorithm [142], [143] to extract the peak amplitudes which were subsequently fitted to a non-steady signal given by Equation (6.1) [141]. In Equation (6.1), n is the index for each spectral peak, $\tau_n = (TR_n - TE_n/2) - TM$ is the time interval between the third $90°$ STEAM FA and TR. The mixing time (TM) is the time between the 2nd and 3rd $90°$ pulses and it was equal to $5\,\mathrm{ms}$. α is the STEAM excitation FA, and M_n corresponds to the longitudinal magnetisation at each nnth spectrum. MATLAB's *lsqcurvefit* function was used to calculate an *in vivo* gold standard T_1 with starting values for the parameters $[M_0, T_1, T_2, \alpha]$ equal to [Signal$_{n=1}$, $0.8\,\mathrm{s}$, $0.04\,\mathrm{s}$, $\pi/2$ rad], respectively.

$$S_n = M_n\, e^{-TE_n/T_2}\, \sin(\alpha)\,, \tag{6.1}$$

where $M_n = M_{n-1}\, e^{-\tau_n/T_1}\, \cos(\alpha) + M_0 \left(1 - e^{-\tau_n/T_1}\right)$.

T_2^* and proton density fat-fraction (PDFF) were calculated from a LiverMultiscan (Perspectum Ltd, Oxford, UK) multi-echo T_2^*-Iterative Decomposition of Water and Fat with Echo Asymmetry and Least-Squares Estimation (IDEAL) [144] protocol with imaging parameters: FA of $3°$, TR $= 15\,\mathrm{ms}$, 12 TEs varying between $1.1\,\mathrm{ms}$ and

$13.2\,\mathrm{ms}$ incremented in steps of $1.1\,\mathrm{ms}$, FoV $= 440 \times 399\,\mathrm{mm}^2$, matrix $= 128 \times 116$, 5 slices with a thickness of $10\,\mathrm{mm}$ and a gap of $5\,\mathrm{mm}$, no fat suppression, bipolar gradient, a BW of $1560\,\mathrm{Hz/pixel}$ for all echoes, phase resolution 100%, phase partial Fourier off, interpolation on and no acceleration. 2D multi-slice data was acquired sequentially within a single $8.7\,\mathrm{s}$ breath-hold. T_2^* and PDFF maps were calculated for each volunteer using a magnitude-only approach [145] for the third slice in the acquisition, cross-sectioning the portal vein.

Inline SASHA T_1 maps were acquired with a work in progress protocol (WIP1041B) with the following imaging parameters: FoV $= 360 \times 270\mathrm{mm}^2$, matrix $= 128 \times 96$, in-plane spatial resolution of $2.8 \times 2.8\,\mathrm{mm}^2$, single slice $8\,\mathrm{mm}$ thick, TR/TE=2.77/1.39 ms, nominal readout FA of $45°$, phase resolution 96%, phase partial Fourier off, interpolation off, no fat suppression, no acceleration and BW of $1085\,\mathrm{Hz/pixel}$. Eleven images, one without magnetisation preparation and the other 10 with a non-selective saturation pulse with a $600\,\mathrm{ms}$ saturation recovery time were acquired. Data was acquired within a single $11\,\mathrm{s}$ breath-hold. SASHA T_1 maps were not acquired for the first two volunteers in runs 1 and 2.

The VFA SPGR sequence, the GRE-EPI sequence for B_1^+ mapping, and the double-echo GRE sequence for B_0 mapping are described in Section 4.1. The image processing pipeline to process the corresponding raw data is described in Section 4.2.

MOLLI T_1 maps were acquired with a LiverMultiscan (Perspectum Ltd, Oxford, UK) protocol with the following imaging parameters: FoV $= 440 \times 330\mathrm{mm}^2$, matrix $= 192 \times 144$ (interpolated to 384×288), in-plane spatial resolution of $2.3 \times 2.3\,\mathrm{mm}^2$. single slice $8\,\mathrm{mm}$ thick, TR/TE=2.6/1.05 ms, phase resolution 100%, phase partial Fourier factor of $6/8$, no fat suppression, nominal readout FA of $35°$, BW of $965\,\mathrm{Hz/pixel}$ and GRAPPA with two times acceleration in the PE direction and 24 integrated reference lines. Seven TIs were collected with a non-selective adiabatic IR RF pulse and a readout scheme synchronised with the volunteer's R-wave from their electrocardiogram. The first of five samples started with a minimum TI of $100\,\mathrm{ms}$ and the subsequent four TIs were

separated by the volunteer RR interval (100, 100+RR, 100+2RR, 100+3RR, 100+4RR); the last two samples were acquired at TIs of 180 and 260 ms. Data was acquired within a single $8.9\,\mathrm{s}$ breath-hold. Complex data from the first 5 TIs were fit to an IR model with a Look-Locker correction to obtain an off-line MOLLI T_1 map.

6.2.2 Statistical Analysis of the Data

T_1 maps for each run were analysed by placing ROIs according to the criteria defined in Section 4.2.4. The estimated T_1 for each subject was calculated as a weighted mean of the T_1s extracted from each ROI selected in each slice according to Equation (5.12).

Evaluating Inaccuracy

Inaccuracy or systematic errors are given by the difference between the average experimental measurement and its true value, determined using a gold standard method [133]. STEAM was chosen as the gold standard T_1 method *in vivo*. The inaccuracy was calculated by taking the relative difference between the whole liver weighted VFA SPGR T_1 and the gold standard STEAM T_1, averaged over all runs and volunteers (Equation (6.2)). A second VFA inaccuracy measurement was calculated from the relative difference between the mean VFA T_1 and the STEAM T_1, using only VFA pixels within the spectroscopy voxel. STEAM T_1 is a single value measured from one voxel, thus no weighting was used. In addition, systematic relative differences between the measured weighted VFA T_1 ($w\mu_{T_1}$) and the two alternative T_1 methods (SASHA and MOLLI) were calculated using Equation (6.2). The MOLLI and the SASHA T_1 values corresponded to weighted mean T_1 values from the 3 ROIs defined within the single slice acquired.

$$\delta_{\mathsf{inaccuracy}} = \frac{1}{\mathsf{N}_{\mathsf{Volunteers}} \cdot \mathsf{N}_{\mathsf{Runs}}} \sum_{v=1}^{\mathsf{N}_{\mathsf{Volunteers}}} \sum_{u=1}^{\mathsf{N}_{\mathsf{Runs}}} \frac{w\mu_{T_{1_{v,u}}} - T_{1,\mathsf{reference}_{v,u}}}{T_{1,\mathsf{reference}_{v,u}}} \tag{6.2}$$

To calculate the VFA T_1 accuracy using the MOLLI T_1 maps as the reference T_1, it was necessary to forward simulate the VFA water T_1 into a MOLLI T_1 using a Bloch equation simulation [138], as MOLLI is known to underestimate T_1 [146]. Three VFA slices, each of $3\,\mathrm{mm}$ thickness, fit within a single-slice MOLLI acquisition of $8\,\mathrm{mm}$

thickness. Consequently, the mean VFA water T_1 from the 9 ROIs drawn on the 3 VFA slices matching the MOLLI slice location were used as the T_1 input to the Bloch simulator [138]. Additional inputs consisting of the B_0 value for each ROI, T_2^* and PDFF were respectively used to correct the MOLLI simulated signal for off-resonances, iron [24] and fat [137]. The signal was also corrected for magnetisation transfer effects [27]. Other inputs included MOLLI sequence-specific components such as the exact inversion RF pulse, gradients and the SSFP readout pulse. The simulated transverse signal was fit to an IR curve. The output was a Look-Locker corrected simulated MOLLI T_1, which was compared to the acquired MOLLI T_1 data.

Evaluating T_1 Homogeneity across the Liver

In healthy volunteers, the T_1 values are expected to be homogeneous across the liver parenchymal tissue. The homogeneity of the measured T_1 values across the liver was assessed by calculating the dispersion of the weighted mean T_1 values at an ROI level through Equation (6.3). In this equation, the sum over r runs over the different ROIs in a given slice and the sum over s runs over the slices in a given acquisition. $\mathsf{N}_{\mathsf{Slices}}$ is the total number of slices and $\mathsf{N}_{\mathsf{ROIs}}$ is the total number of ROIs chosen per slice.

$$\left(w\sigma_{\mu_{T_1}}\right)_{\mathsf{ROI}} = \sqrt{\frac{\sum_{s=1}^{\mathsf{N}_{\mathsf{Slices}}}\sum_{r=1}^{\mathsf{N}_{\mathsf{ROIs}}} w_{s,r}(\mu_{T_{1_{s,r}}} - w\mu_{T_{1,\mathsf{Subject}}})^2}{\sum_{s=1}^{\mathsf{N}_{\mathsf{Slices}}}\sum_{r=1}^{\mathsf{N}_{\mathsf{ROIs}}} w_{s,r}}}, \tag{6.3}$$

where $w_{s,r} = \frac{\mathsf{N}_{\mathsf{Pixels}_{s,r}}}{\sigma^2_{s,r}}$.

If random Gaussian noise dominates the measurement, the T_1 standard deviation at an ROI level ($w\sigma_{\mu_{T_1}}$) should be lower than the standard deviation of the T_1 distribution calculated at the pixel level ($w\sigma_{T_1}$) by the square root of the number of T_1 pixels averaged in each ROI. Conversely, if this is not the case, there are non-Gaussian noise sources present in the T_1 map (Equation (6.4)). Each of these sources of error were quantified for each run. The dispersion of T_1s at the pixel level for all the ROIs defined in each

slice, across all slices, was defined by Equation (5.13).

$$\left(w\sigma^2_{\mu_{T_1}}\right)_{\text{ROI}} = \frac{\left(w\sigma^2_{T_1}\right)_{\text{Pixel, Gaussian Noise}}}{\text{N}_{\text{Pixels}}} + \left(w\sigma^2_{T_1}\right)_{\text{Pixel, Non-Gaussian Noise}} \tag{6.4}$$

Quantifying B_1^+ Factor Induced Bias in the T_1 maps

B_1^+ factor bias in the T_1 maps was a source of systematic error we strived to minimise. The remaining correlation between T_1 and the B_1^+ factor was computed for all the mean T_1s and B_1^+ factors within each ROI for each run. The correlation coefficient follows a t-distribution with $n-2$ degrees of freedom [147]. The null hypothesis that there is no relationship between T_1 and B_1^+ factor was thus tested through a t-test statistic at a significance level of 0.05. The slope of the linear regression between T_1 and B_1^+ factor indicated the strength of the relationship between the two variables (Equation (6.5)). A B_1^+-related T_1 variation ($\Delta T_{1_{B_1^+}}$) is given by the product of the slope (b), from the linear fit between T_1 and B_1^+ factor, and the range of B_1^+ factor values (ΔB_1^+) observed across the liver (Equation (6.6)).

$$\mu_{T_1} = a + b\mu_{B_1^+} \tag{6.5}$$

$$\Delta T_{1_{B_1^+}} = b\Delta B_1^+ \tag{6.6}$$

The 95% CI in the B_1^+ related T_1 variation (Equation (6.7)) was calculated using a t-test statistic with 2 degrees of freedom at a significance level of 0.05 [148].

$$b\Delta B_1^+ \pm t_{(0.05/2,\text{N}_{\text{ROIs}}-2)} \times \Delta B_1^+ \times \sqrt{\frac{s^2}{\sum_{i=1}^{\text{N}_{\text{Slices}}}\sum_{j=1}^{\text{N}_{\text{ROIs}}}(\mu_{B_{1_{i,j}}^+} - \mu_{B_{1_{\text{Run}}}^+})^2}}\,, \tag{6.7}$$

where s^2 is the residual variance of the linear fit between the mean T_1 and mean B_1^+ factor.

Evaluating Precision

The method's precision in measuring T_1 was calculated from a one-way analysis of variance (ANOVA) of the mean T_1s from run 1 and run 2 across the 10 subjects,

where the groups are the subjects. The within-subject variance ($\sigma^2_{\text{within-subject}}$) represents the measurement error, assuming there is no physiological variation in T_1 between the two measurements. The measurement error is equal to the residual mean square error in an ANOVA table. The precision or repeatability coefficient (RC) is 1.96 standard deviations of the measurement error times square root two as we have two measurements for each subject (Equation (6.8)) [149]:

$$\text{RC} = 1.96\sqrt{2}\sigma_{\text{within-subject}} \tag{6.8}$$

Target VFA T_1 Standard Deviation for Liver Applications

The ability to stratify different stages of fibrosis or to distinguish a healthy liver from a diseased liver using T_1 will depend on the measurement standard deviation. Consider two normal distributions (Figure 6.2), where the first one (blue curve) corresponds to a no fibrosis population and the second one (red curve) corresponds to the probability distribution of T_1 measured using the developed VFA method for an individual with a true T_1 equal to the mean T_1 of a fibrosis Ishak 1-2 group [19]. The allowed maximum standard deviation was defined by satisfying two criteria (Equation (6.9)). Firstly, a critical T_1 value was defined such that 5% (blue shading) of the population in group 1 had a T_1 value that surpassed the critical value. The critical T_1 value is 1.65 standard deviations to the right of the mean of group 1. Secondly, the VFA measurement should be above the critical T_1 value with 90% probability (red shading). The z statistic corresponding to 90% probability of T_1 being above the critical value is 1.28 standard deviations to the left of the mean VFA T_1 distribution.

$$\sigma_{\text{VFA}} = \frac{\mu_{\text{group}_1} + 1.65\sigma_{\text{group}_1} - \mu_{\text{VFA}}}{-1.28} \tag{6.9}$$

The allowed maximum standard deviation in Equation (6.9) was calculated for different liver diseases and used as a metric to assess the feasibility of the developed T_1 method to differentiate between different stages of liver disease (Tables 6.3 and 6.4).

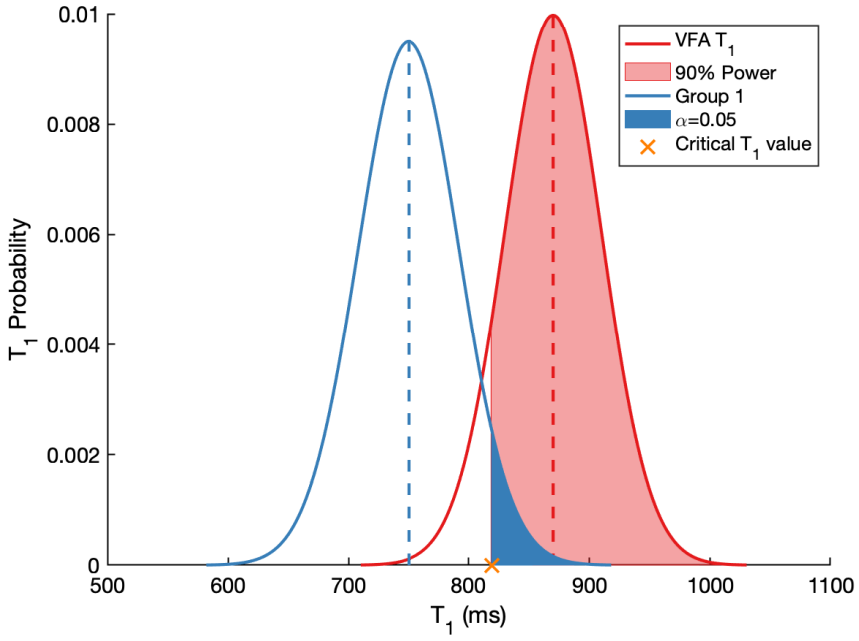


Figure 6.2: Gaussian T_1 distributions corresponding to two different fibrosis groups one wishes to differentiate using a VFA T_1 measurement. Group 1, in blue, has a mean T_1 of $750\,\mathrm{ms}$ denoted by the blue dashed line and a standard deviation of 42 ms. This characterises the no fibrosis population in Banerjee et al. [19]. Group 2, in red, corresponds to an experimental distribution of measuring T_1 with the VFA method from an individual with a T_1 value equal to the mean of Ishak 1-2 group. The mean VFA T_1 is $870\,\mathrm{ms}$ and the T_1 standard deviation should allow the VFA mean T_1 to be allocated with 90% power to the red distribution. The critical T_1 value (orange cross) is 1.65 standard deviations from the mean of group 1, i.e., the probability that a T_1 value from group 1 is above the critical T_1 is only 5%. The critical value and the 90% power define where the blue area intercepts with the red area and thus the maximum value for the standard deviation of the VFA T_1 measurement.

Evaluating Repeatability

To assess intra-session repeatability, the difference in the weighted mean of run 1 and run 2 was analysed. We took the null hypothesis to be that the mean difference between the weighted mean T_1s ($\Delta\mu_{T_1}$) of the two runs was equal to zero. The 95% CI for the mean difference between the weighted mean T_1s of the two runs is given by Equation (6.10) [149].

$$\Delta\mu_{T_1} \pm t_{(0.95,\mathrm{N_{subjects}}-1)}\frac{\sigma_{\Delta\mu_{T_1}}}{\sqrt{\mathrm{N_{subjects}}}}, \tag{6.10}$$

where $\Delta\mu_{T_1} = w\mu_{T_{1,\mathrm{Run_1}}} - w\mu_{T_{1,\mathrm{Run_2}}}$ and t is the Student's t distribution with a significance level of 0.05 and 9 ($\mathrm{N_{subjects}} - 1$) degrees of freedom. If the probability of the CI including zero is less than 0.05 then we reject the null hypothesis, i.e., the probability of observing the data if the null hypothesis were true is very unlikely. For normally distributed

differences, 95% of the observations should lie within the limits of agreement (LoA), i.e., 1.96 standard deviations away from the mean difference.

Pearson correlation coefficients between run 1 and run 2, and a linear regression slope close to 1 with a narrow 95% linear fit CI assessed the agreement in measured T_1 between the two runs. The same procedure was used to assess inter-session repeatability between run 1 and run 3 as well as the repeatability of STEAM, SASHA and MOLLI T_1.

6.3 Results

Figure 6.3 compares the VFA T_1 B_1^+ corrected for the 3 runs acquired for each of the 10 volunteers. In general, the 3 runs agreed well overall; the differences between the 3 runs for the 10 subjects were all below $31\,\mathrm{ms}$, except for volunteers 3, 4 and 9. The *in vivo* gold standard STEAM T_1 (grey) and two alternative methods for liver T_1 mapping, MOLLI (pink) and SASHA (orange) are also shown. Figure 6.4 shows volunteer's 10 VFA T_1 maps with the ROIs indicated in red. Figure 6.5 shows the MOLLI and SASHA T_1 maps for the same acquisition as well as the histograms of the VFA T_1 maps for the 3 runs and the alternative T_1 mapping methods.

Table 6.1 shows the inaccuracy of the B_1^+ corrected VFA T_1 relative to the gold standard T_1 method (STEAM) and two alternative T_1 methods (SASHA and MOLLI). VFA T_1 for all the ROIs across the 10 volunteers was on average 3% above STEAM and 5% below SASHA and MOLLI. Using only the VFA pixels matching the spectroscopy voxel, the VFA T_1 values were on average 9% above STEAM. The VFA T_1 values for the slice matching the SASHA slice location were on average 4% below SASHA T_1. For the VFA slice matching the MOLLI slice location, the forward simulated MOLLI T_1 from the VFA data was on average 5% below MOLLI T_1. The good agreement between whole liver VFA inaccuracies (columns 4 and 6) and inaccuracies for VFA slices matching the SASHA or MOLLI slice locations (columns 5 and 7) is an indication of T_1 homogeneity across the liver volume.

The variability of T_1 across the liver was measured by the dispersion of the weighted

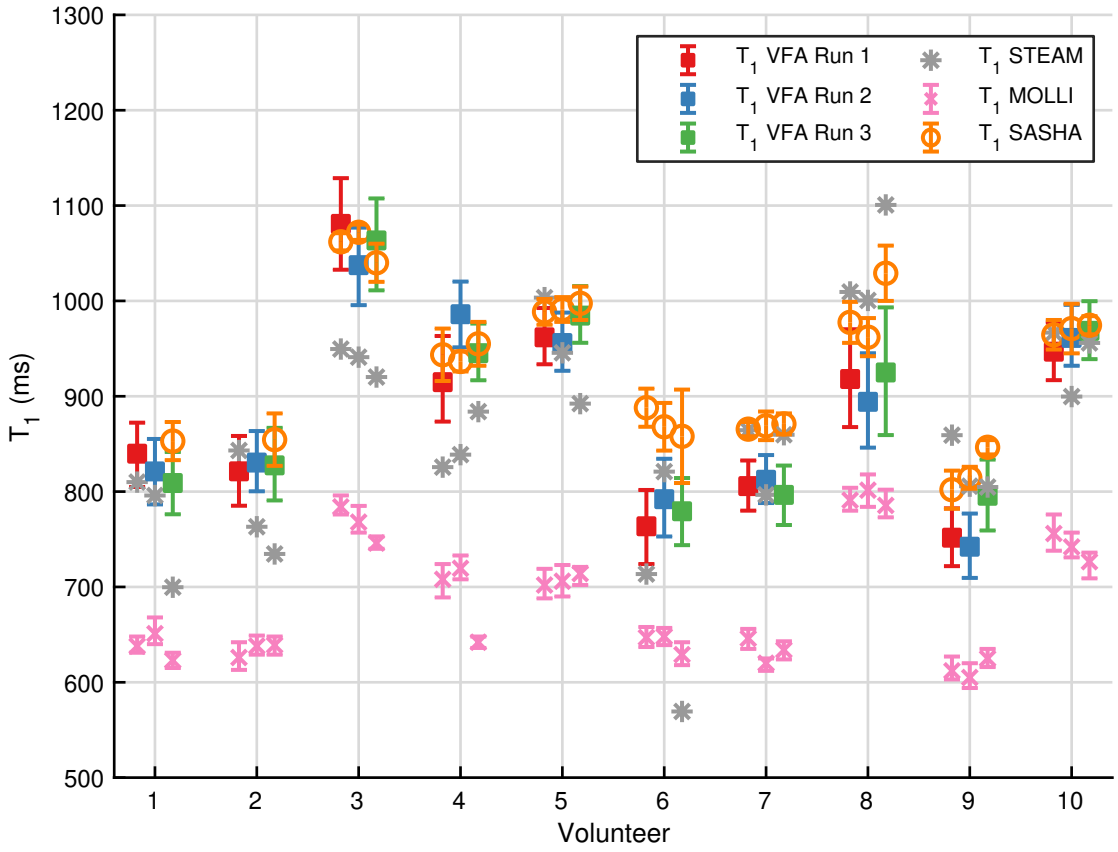


Figure 6.3: Median and interquartile (IQR) range of VFA T_1 in ms, corrected for B_1^+ inhomogeneities, for the three runs acquired for each volunteer. Run 1 (red) and run 2 (blue) are a scan-rescan, run 3 (green) is a second visit approximately one week later. Gold standard STEAM T_1 (grey stars) and alternative T_1 methods: MOLLI (pink crosses) and SASHA (orange circles) are plotted as median±IQR.

Table 6.1: Inaccuracy of VFA T_1 calculated using the gold standard STEAM method and two alternative T_1 methods: SASHA and MOLLI. The mean relative error, the mean absolute relative error and the interquartile range, [25$^{\text{th}}$ 75$^{\text{th}}$], of relative errors are reported in percentage. Columns 4 and 6 used the weighted mean VFA T_1 across all slices with ROIs, while columns 5 and 7 used only VFA slices matching the SASHA and MOLLI slice locations.

	STEAM	STEAM[a]	SASHA	SASHA[b]	MOLLI	MOLLI[c]
Mean Error (%)	3	9	−5	−4	−5	−5
Mean Absolute Error (%)	9	12	5	5	7	7
Interquartile Range (%)	[−4 10]	[1 14]	[−7 −1]	[−7 −1]	[−10 2]	[−8 1]

[a] pixel-wise differences between VFA T_1 and STEAM restricted to the spectroscopy voxel location in the VFA acquisition
[b] VFA slice matching SASHA slice
[c] VFA slice matching MOLLI slice

mean T_1s calculated for each ROI (purple bars in Figure 6.6) for each run. On average the T_1 variability across the liver was $34\,\text{ms}$. This value was compared to the standard

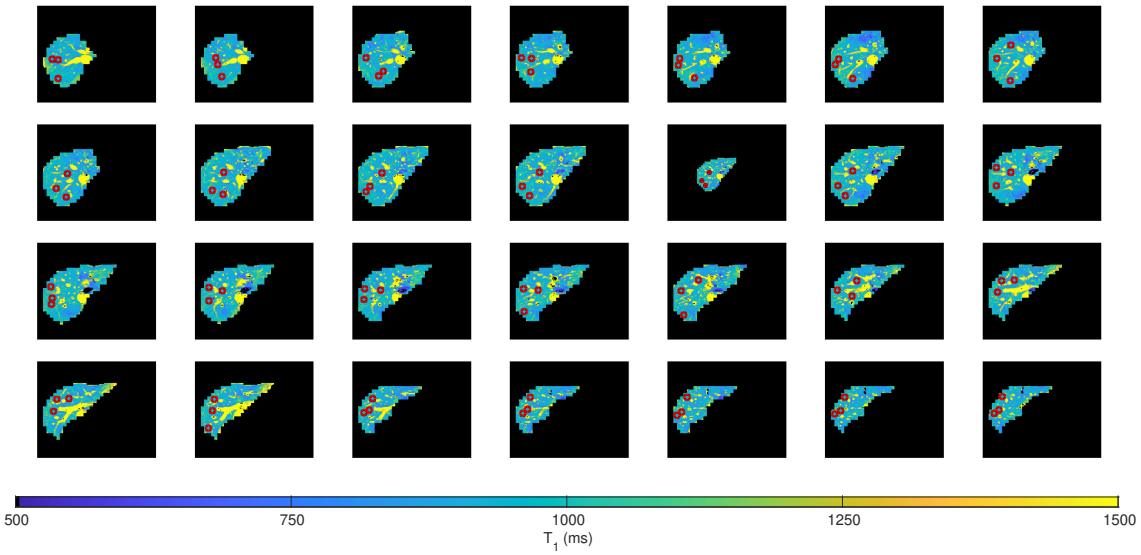


Figure 6.4: VFA T_1 maps for volunteer 10 run 1 overlaid with the red ROIs used in the statistical analysis.

deviation from all the T_1 pixels selected for all the ROIs (green bars in Figure 6.6) to estimate the proportion of the variance (right axis) due to non-Gaussian noise (pink squares) and Gaussian noise (dark blue squares). The variance arising from non-Gaussian noise was generally lower than the variance due to Gaussian noise.

One source of systematic errors in T_1 are errors in determining B_1^+ inhomogeneities. Figure 6.7 shows the B_1^+ induced variation in T_1 across the liver for each run and subject. The null hypothesis that there is no correlation between T_1 and B_1^+ factor was rejected for 10 out of 30 cases. These cases corresponded to a B_1^+-related variation in T_1 larger than $34\,\mathrm{ms}$, with the exception of volunteer 7 run 1 ($-21\,\mathrm{ms}$). For the cases where the null hypothesis was not rejected, the absolute B_1^+-related variation in T_1 was $17 \pm 14\,\mathrm{ms}$ ($\mu \pm \sigma$).

Intra-session (Figure 6.8) and inter-session (Figure 6.9) repeatability are illustrated using both correlation and Bland Altman plots. The VFA T_1 intra-session repeatability coefficient was $62\,\mathrm{ms}$ and the inter-session repeatability coefficient was $49\,\mathrm{ms}$. Table 6.2 presents repeatability metrics for the alternative T_1 methods for comparison with the VFA T_1 method.

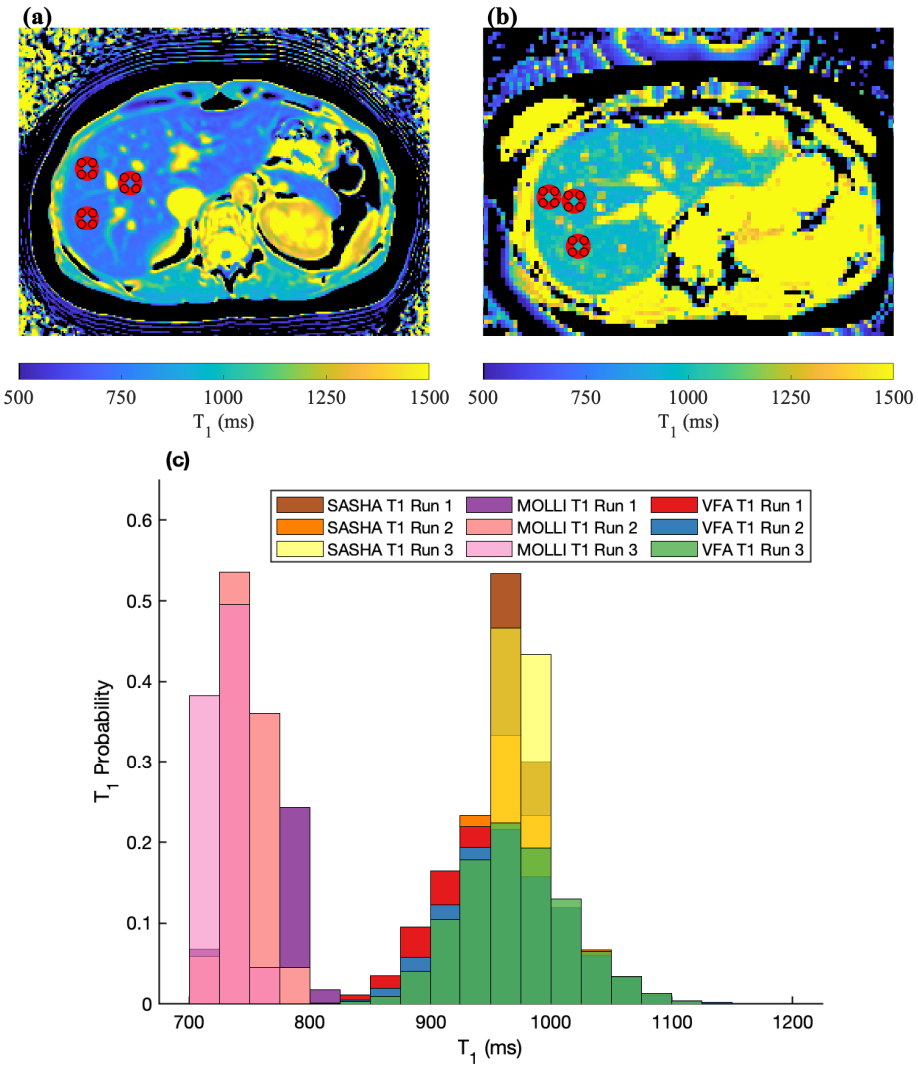


Figure 6.5: (a) MOLLI and (b) SASHA T_1 maps for volunteer 10 run 1. (c) Histograms of the T_1s extracted from all the ROIs drawn for the 3 runs of volunteer 10. There are 3 different T_1 methods: single slice MOLLI represented by the pink colour scheme demonstrating T_1 underestimation; VFA T_1 for runs 1/2/3 using 28/27/26 slices respectively, represented by the primary colour scheme and single slice SASHA T_1s represented by the warm colour scheme. 3D VFA T_1s have broader histogram widths compared to MOLLI or SASHA, but the 3 runs overlap showing the high repeatability of the developed method. The VFA T_1 histogram modes agree well with SASHA.

6.4 Discussion

Using an optimised image acquisition and processing pipeline for 3D T_1 mapping, a high accuracy was achieved characterised by a mean error of $+9\%$ relative to the gold standard *in vivo* STEAM method. The mean relative difference between VFA T_1 and SASHA T_1 was -5%. A difference of -5% was also obtained between the VFA forward

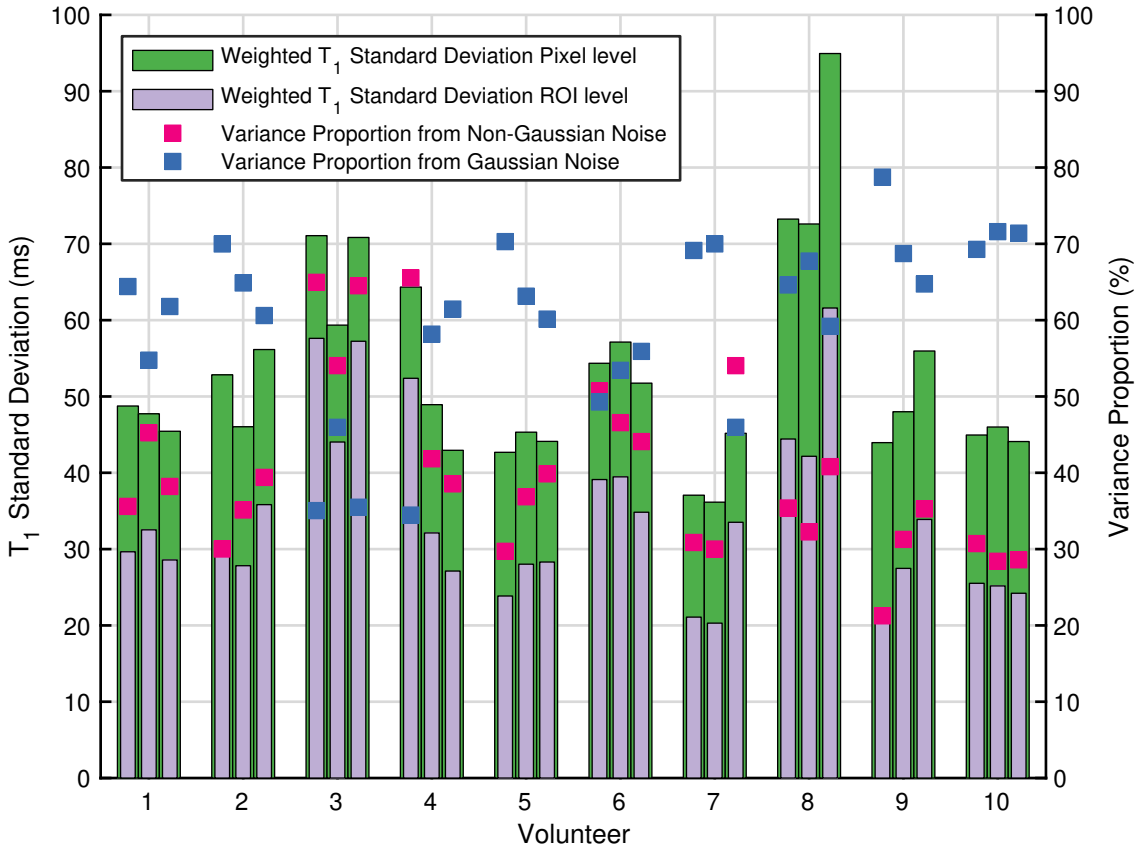


Figure 6.6: T_1 weighted standard deviations in ms calculated at the pixel level for all pixels selected across all the ROIs for each run and volunteer are illustrated by the green bars. The standard deviations of the weighted mean T_1 within each ROI across all the ROIs for each run and volunteer are illustrated by the purple bars. The proportion of the variance (right y axis) from non-Gaussian noise is plotted as pink squares and due to random Gaussian noise as dark blue squares.

simulated MOLLI T_1 and the acquired MOLLI T_1. The liver T_1 variability at an ROI level was characterised by a median T_1 standard deviation over all runs and volunteers of $31\,\mathrm{ms}$, an IQR of [27 39] ms and extreme values of $20\,\mathrm{ms}$ and $62\,\mathrm{ms}$. The method showed a high repeatability, with a T_1 standard deviation within-subject of $21\pm5\,\mathrm{ms}$ resulting in a repeatability coefficient of $60\,\mathrm{ms}$. The T_1 differences between scan and rescan had on average a $3\,\mathrm{ms}$ bias (95% CI [-20 26] ms, $p = 0.772$) with LoA between $-59\,\mathrm{ms}$ and $65\,\mathrm{ms}$ and a correlation coefficient of 0.95. The T_1 difference between the two visits, approximately 1 week apart, had an average T_1 bias of $8\,\mathrm{ms}$ (95% CI [-10 26]ms, $p = 0.338$) and a tighter 95% LoA between $-41\,\mathrm{ms}$ and $57\,\mathrm{ms}$. Consequently, a higher correlation coefficient of 0.97 and a smaller repeatability coefficient of $49\,\mathrm{ms}$

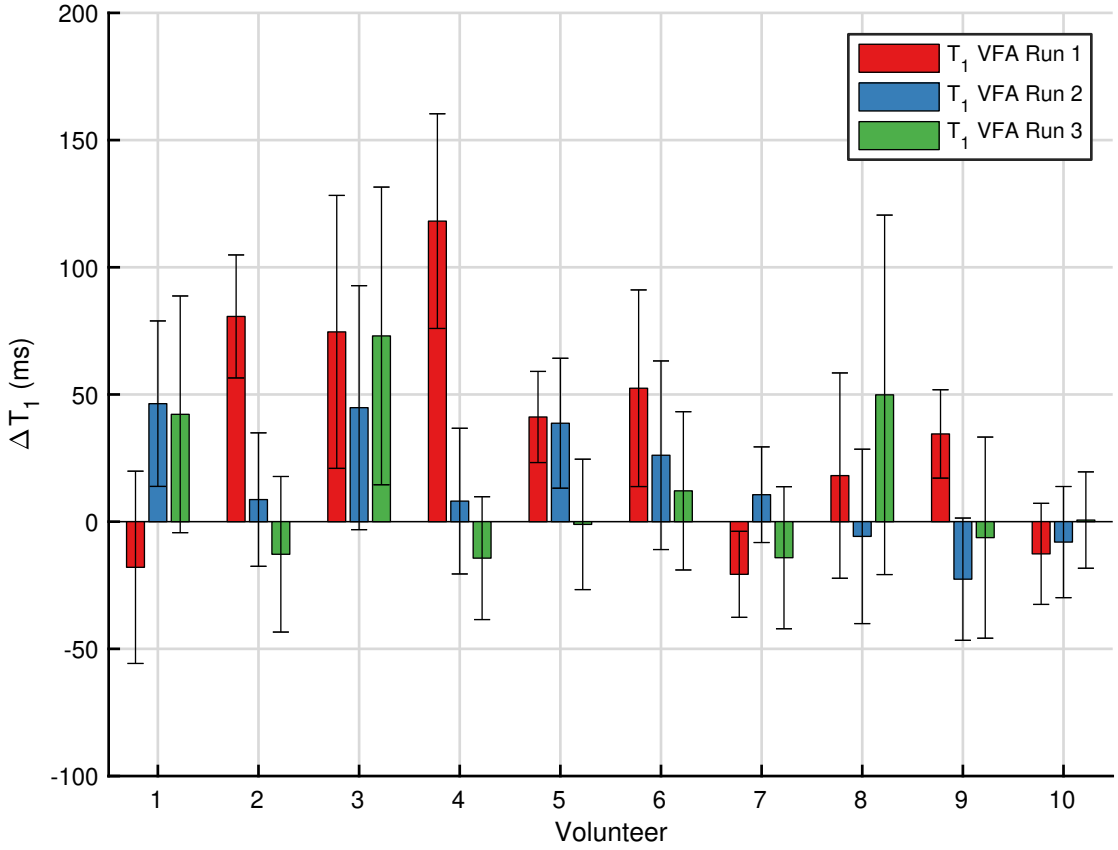


Figure 6.7: T_1 variation across the liver for each subject and run due to a residual correlation between T_1 and the B_1^+ factor. The slope of the linear fit between the mean T_1 and the mean B_1^+ factor in each ROI times the range of B_1^+ factors across the liver gives the B_1^+-related T_1 variation (Equation (6.6)) plotted as bars for run 1 (red), run 2 (blue) and run 3 (green) for each volunteer. The error bars represent the 95% CI of the slope, using a t-test with 0.05 significance level, times the B_1^+ factor range.

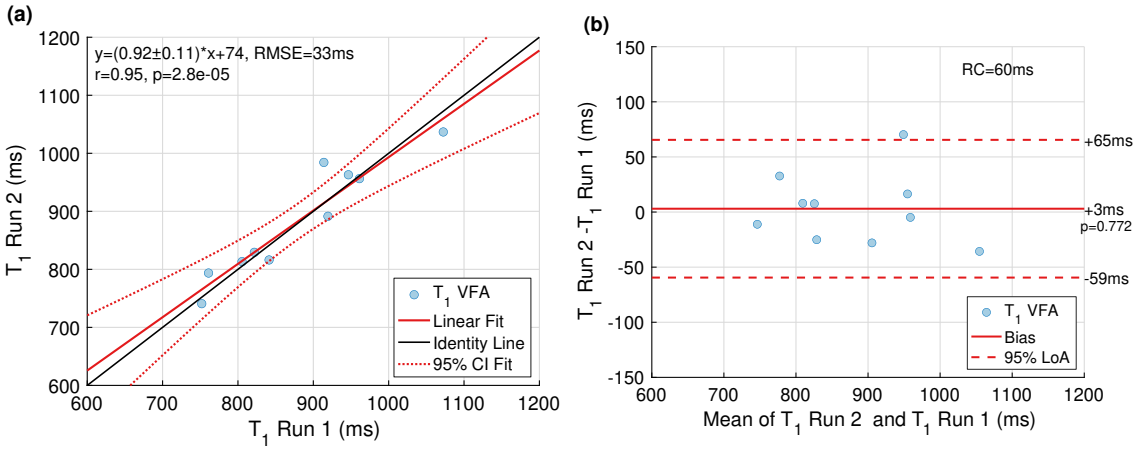


Figure 6.8: VFA T_1 intra-session (a) correlation and (b) Bland Altman plots using the weighted mean T_1 for each subject.

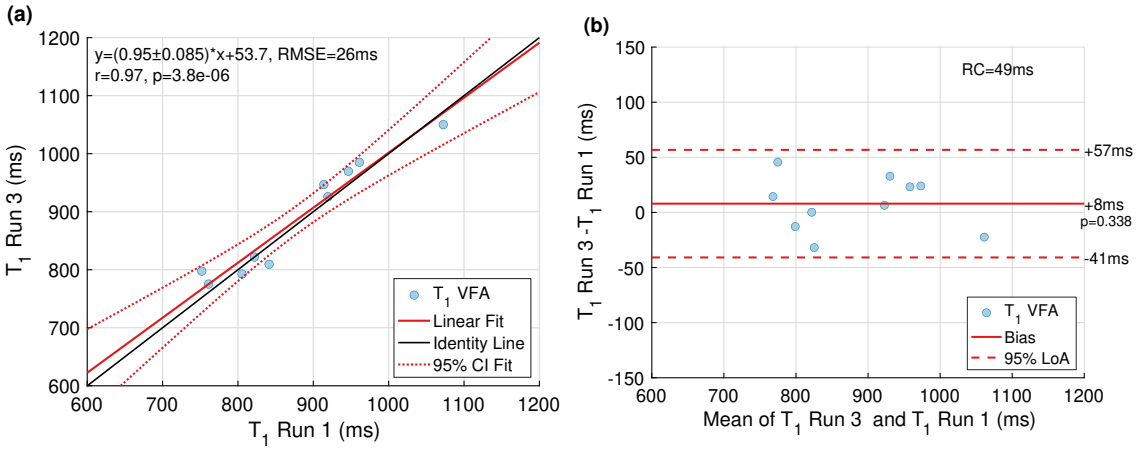


Figure 6.9: VFA T_1 inter-session (a) correlation and (b) Bland Altman plots using the weighted mean T_1 for each subject.

Table 6.2: Intra-session and inter-session repeatability metrics for VFA T_1 and alternative T_1 methods: STEAM, MOLLI and SASHA. Correlation plot metrics (columns 2-4) include Pearson correlation coefficient with the associated p-value, and regression slope with the associated standard error. Bland Altman plot metrics (columns 5-7) include bias with the associated p-value and 95% limits of agreement.

T_1 Method	Pearson Correlation Coefficient	p-value	Regression Slope (ms)	Bias (ms)	p-value	95% Limits of Agreement (ms)
VFA[d]	0.95	2.8e-5	0.92 ± 0.11	$+3$	7.7e-1	62
STEAM[d]	0.81	4.5e-3	0.68 ± 0.17	-24	2.1e-1	110
SASHA[d]	0.99	8.2e-7	0.99 ± 0.048	-6	1.2e-1	19
MOLLI[d]	0.98	5.8e-7	0.97 ± 0.068	$+1$	8.3e-1	26
VFA[e]	0.97	3.8e-6	0.95 ± 0.085	$+8$	3.4e-1	49
STEAM[e]	0.88	6.8e-4	1.4 ± 0.26	-42	1.2e-1	153
SASHA[e]	0.94	5.8e-4	0.92 ± 0.14	$+5$	6.5e-1	56
MOLLI[e]	0.93	9.0e-5	0.83 ± 0.11	-14	1.1e-1	49

[d] Intra-session: Run 1 - Run 2
[e] Inter-session: Run 1 - Run 3

were obtained. Neither the $3\,\mathrm{ms}$ or $8\,\mathrm{ms}$ average bias are statistically significant thus it cannot be concluded that there was a bias.

Very few studies have reported the accuracy of the VFA T_1 mapping *in vivo* [85], [86]. Phantom accuracy is usually measured with a widely acceptable T_1 gold standard sequence: IR SE. However, this sequence takes approximately $20\,\mathrm{min}$ per slice for a matrix of 144×192, making it inadequate as a gold standard method for measuring T_1 in the liver within one breath-hold. Nevertheless, implemented with an EPI readout, IR

SE can be run in a single breath-hold in the liver. Preibisch et al. [85] and Baudrexel et al. [86] both used a multi-slice IR-EPI as the reference T_1, without breath-holding as it was applied to the brain, and obtained an inaccuracy in WM VFA T_1 of 6.5% and 4.5%, respectively. Both WM VFA T_1 values reported used an incomplete spoiling correction for an RF phase increment of $50°$. These mean absolute errors are smaller than those obtained in this work with STEAM, but comparable to SASHA and MOLLI. Stikov et al. [100] demonstrated both in phantom and across 10 healthy volunteers an overestimation of VFA B_1^+ corrected T_1 relative to IR or IR Look-Locker. *In vivo* differences in T_1 larger than 30% were observed in WM. The authors put forward the hypothesis that inaccurate B_1^+ mapping or incomplete spoiling may explain this overestimation. They call attention to the need for a 'universal calibration scheme', necessary to harmonise T_1 mapping across scanners and advise that T_1 mapping techniques should be validated against the gold standard IR. The fact that we obtained a high accuracy in the IR SE validation in the phantom (Chapter 3) with our optimised pipeline, and *in vivo* VFA T_1 relative differences assessed with the forward-simulated VFA MOLLI and SASHA were on average -5% (Table 6.1), well below the 30% overestimation reported by Stikov et al. [100], confirms we have been able to successfully correct for the main systematic errors affecting VFA T_1 mapping. Whether the pipeline we developed is accurate, repeatable and reproducible across different scanners and vendors, which would make it a 'universal calibration scheme', remains as future work.

In MRI liver imaging we are generally limited by the duration of one breath-hold, thus we cannot apply the same protocol of 11:40 min that Baudrexel et al. [86] used in the brain. Instead, each slice in the IR-EPI would need to be acquired within 1 breath-hold. An attempt of a single slice IR-EPI scan was performed, but the poor performance of fat saturation resulted in large chemical shifts as well as distortions from B_0 inhomogeneities. For these reasons, we chose to use a spectroscopy based multi-TR multi-TE B_1^+ insensitive sequence [141] as the gold standard T_1 *in vivo*. In principle, a spectroscopy measurement of the water T_1 in the liver should not suffer from any of the biases that affect MOLLI [26].

In addition, given the spectroscopy voxel spanned approximately 7 VFA slices, STEAM would offer a better coverage of liver T_1, in the foot-head direction, than a single slice technique. However, a large variability of the STEAM T_1 was observed within-subjects of up to $252\,\mathrm{ms}$ (Figure 6.3). This was confirmed by the large T_1 biases and 95% LoA of $-24\,\mathrm{ms}$ [-133 86] ms for the intra-session, and $-42\,\mathrm{ms}$ [-195 111]ms for the inter-session (Table 6.2). The large disagreement between STEAM T_1 measurements within each individual make it an unacceptable gold standard T_1 method *in vivo*. Several reasons could have contributed to the low repeatability and inaccuracy of STEAM liver T_1 such as the confirmed presence of vessels within the spectroscopy voxel (Figure 6.10), inadequate shimming, different RF power amplitudes. Therefore, we had to rely on SASHA and MOLLI which are single slice acquisition T_1 methods.

Assessing repeatability is important as we expect the sequence to be robust to the different positioning of the volunteer on the scanner bed, different coil positioning, shimming and any changes in the B_1^-/B_1^+ field due to the different position of the patient within the receive and transmit RF coils, respectively. To ensure the repeatability conditions, the same sequences were acquired by the same scanner operator, in the same $3\,\mathrm{T}$ Prisma Siemens scanner within a short period of time [133]. We are also assuming that the time between scan-rescan is short enough that no biological change should occur in the liver T_1.

MOLLI cT_1 repeatability measurements reported *in vivo* across 22 healthy volunteers had a mean bias of $-7.5\,\mathrm{ms}$ and 95% LoA [-53.6 38.5] ms with a repeatability coefficient of $46.1\,\mathrm{ms}$ [134]. Another MOLLI cT_1 repeatability study [120] showed a mean bias of $-13\,\mathrm{ms}$ and 95% LoA [-81 56] ms. The VFA T_1 achieved a smaller mean bias of $-3\,\mathrm{ms}$ and 95% LoA [-59 65] ms (Figure 6.8), which gives a repeatability coefficient intermediate to the two MOLLI cT_1 studies. This is consistent with literature comparing different T_1 mapping methods and reporting larger *in vivo* imprecisions for VFA compared to IR or IR Look-Locker [100], [136]. MOLLI and VFA T_1 should be seen as two complementary tools. The VFA T_1 will be useful in applications where whole liver T_1 mapping is required

or where MOLLI is not available on the scanner. Increasing the VFA precision is also possible by optimising and increasing the number of excitation FAs, averaging pixels together, or decreasing the SPGR resolution.

This is the first time a non-contrast *in vivo* liver VFA T_1 repeatability study was conducted, thus we compare our results to literature VFA T_1 measurements applied to other organs. We achieved better repeatability than VFA T_1 measurements in the prostate. Zhong et al. [150] reported LoA with the 'Reference Region VFA' T_1 mapping method applied to the prostate approximately 3.7 times higher. However, our T_1 repeatability coefficient is larger compared to brain WM T_1 measurements obtained on two different MR vendors [102] using a B_1^+ correction. T_1 biases and 95% LoA of $-4\,\mathrm{ms}$ [-23 15] ms were obtained with a Siemens scanner, and $-3\,\mathrm{ms}$ [-13 20] ms with a Philips scanner. The median percentage differences reported by Lee et al. [102] were converted into ms using the average WM IR-EPI T_1 measurement from Baudrexel et al.[86] as the mean WM T_1. A recent repeatability and reproducibility study [30] achieved similar T_1 repeatability coefficient WM values to Lee et al. [102] on a Prisma scanner with a small bias of $-0.4\,\mathrm{ms}$ and LoA [-32 31] ms. However, a larger bias of $-12\,\mathrm{ms}$ and LoA of [-46 23] ms were obtained on a Trio scanner. These results show that there is some inherent bias related to the scanner hardware and software even though care was taken by Gracien et al. [30] to apply the same protocol and sequences for B_0, B_1^+ and T_1-W on both scanners.

Larger inter-sessions variations (Figure 6.9) compared to intra-session (Figure 6.8) were expected. A closer look at the data in Figure 6.8 shows that one data point (above the $+65\,\mathrm{ms}$ LoA) had an intra-session difference that was twice as large as the second largest difference. When eliminating this data point, the repeatability coefficient decreased from $60\,\mathrm{ms}$ to $43\,\mathrm{ms}$. This volunteer reported difficulty in hearing the automatic breath-hold instructions and holding the breath consistently at the same position for all scans. The method's sensitivity to breath-hold mismatches is one of its main disadvantages compared to MOLLI or SASHA where the T_1 map is acquired in a single breath-hold, provided there is no breathing during the single breath-hold.

On average, we achieved an ROI-based T_1 standard deviation of $34\,\mathrm{ms}$ across 10 volunteers (Figure 6.6). This is higher than VFA WM T_1 measurements reported in the brain by Baudrexel et al.[86] with a standard deviation of $26\,\mathrm{ms}$ using ROIs with $10\,\mathrm{mm}$ diameter across 5 healthy subjects. The T_1 variance on a pixel level, across all slices with ROIs, has contributions from non-Gaussian noise as well as random Gaussian noise (finite SNR of the VFA SPGR acquisitions). Averaging the T_1 within the $11.2\,\mathrm{mm}$ diameter (46 pixels) ROI reduces the variance due to random noise. Given 25 VFA pixels fit within one pixel in the B_1^+ map, the B_1^+ noise between the VFA pixels will be correlated. This can be one reason why the variance at the ROI level did not decrease by the number of pixels averaged. Other reasons include partial volume effects from blood or bile, breath-hold misalignments or noise correlations due to under-sampling of k-space data. Nonetheless, the random Gaussian noise contribution of the VFA signal into the T_1 map variance should still be reduced by a factor of 46. Using this factor, the non-Gaussian noise was generally lower than the Gaussian noise (Figure 6.6). This is important as it shows that a higher precision can be achieved by averaging T_1 pixels together. Sources of non-Gaussian noise are small vessels present in the ROIs due to partial volume effects, residual B_1^+ biases in the T_1 maps, or breath-hold mismatches between the different FAs either in the B_1^+ map acquisition and/or the VFA acquisition. In particular, the liver deforms non-rigidly with respiration which can result in different vessel/liver tissue proportions within an ROI for the different FAs.

Systematic errors arising from remaining B_1^+ inhomogeneities in the T_1 maps were statistically significant for $1/3$ of the cases (Figure 6.7). One reason for a correlation between T_1 and B_1^+ factor is an inaccurate determination of the B_0 values used to correct the through slice dephasing affecting the DAM ratio and thus the B_1^+ map. The edges of the liver or tissue boundaries, such as the bile ducts, portal vein or gall bladder, are regions susceptible to large dephasing and thus phase wraps as well as low spin density, resulting in a large variance in the B_0 maps. Improvements in the B_0 map acquisition by using more than two echoes [151] could reduce the variance and phase wrapping. In

addition, a higher spatial resolution along the slice direction would also be beneficial to interpolate more accurately B_0 values across the slice direction, essential for an accurate calculation of the B_1^+ factor using the 2D multi-slice GRE-EPI acquisition. Another source of B_1^+ factor inaccuracy arises from breath-hold inconsistencies between the two FAs acquired using the GRE-EPI sequence. While the large B_1^+-related variation in T_1 (Figure 6.7) seems to explain the large ROI-by-ROI T_1 standard deviation (Figure 6.6) for all runs of volunteer 3 as well as run 1 of volunteer 4 and 6, volunteer 8 showed no statistically significant correlation between T_1 and B_1^+ factor for the intra-session runs despite displaying the highest standard deviations in T_1 at the pixel level of $73\,\mathrm{ms}$, $73\,\mathrm{ms}$, $94\,\mathrm{ms}$, for the 3 runs respectively. This volunteer reported falling asleep during the scan, and analysis of the raw data confirmed breath-hold misalignments of at least 1 slice ($8\,\mathrm{mm}$) between the GRE-EPI FAs and approximately 2 slices ($6\,\mathrm{mm}$) between the VFA. However, the misalignment is likely not to be a fixed shift in the slice direction as free breathing during sleep will result in unpredictable liver dome positions for the different FAs, i.e., not easily aligned by a rigid transformation.

The T_1 in WM is less variable across individuals compared to the liver T_1 as shown by an IR-EPI standard deviation of $17\,\mathrm{ms}$ in mean WM T_1 across 6 subjects [85] and of $13\,\mathrm{ms}$ across 5 subjects [86]. In the liver, Banerjee et al. [19] measured with MOLLI cT_1 standard deviations about three to four times larger ($48\,\mathrm{ms}$) in 7 healthy volunteers. The heterogeneity of liver T_1 in a healthy population was also observed in our study with mean VFA T_1s varying between $741\,\mathrm{ms}$ and $1073\,\mathrm{ms}$ (Figure 6.3). In our case, the group standard deviation was $96\,\mathrm{ms}$ and the within-subject standard deviation was $21\,\mathrm{ms}$. Paul Tofts [60] noted that when the method's standard deviation is less than 30% of the measured group standard deviation, the contribution of the method's imprecision to the overall variance is only 9%. He considers this 9% level negligible for a group comparison study. This level was achieved in the present study. However, we had a very heterogeneous healthy volunteer liver T_1 population.

Liver T_1 has been explored as a biomarker for the diagnosis and stratification of

different liver diseases. Stratification of liver fibrosis using shMOLLI cT_1 with 90% power at a significance level of 5% is possible for all fibrosis scores (Table 6.3), except between diseased groups Ishak stage 1-2 and 3-4 according to data from Banerjee et al. [19]. The maximum VFA standard deviation (Figure 6.2) allowing the differentiation of a liver with a mean T_1 equal to the mean value of Ishak 1-2 patients from the healthy group is $40\,\mathrm{ms}$, and to differentiate between the mean T_1 values of Ishak 5-6 and Ishak 3-4 the maximum standard deviation is $38\,\mathrm{ms}$ (Table 6.3). The median dispersion in VFA T_1 at an ROI level was $31\,\mathrm{ms}$ (Figure 6.6). Out of the 30 VFA measurements, only 9 were above $38\,\mathrm{ms}$. A similar approach was applied to other liver diseases such as cirrhosis, autoimmune hepatitis and portal hypertension (Table 6.4). Portal hypertension results in the smallest VFA T_1 standard deviation requirement of $28\,\mathrm{ms}$. Overall, the majority of VFA T_1 measurements at an ROI level had sufficient precision to diagnose and stratify liver diseases that require a standard deviation of $35\,\mathrm{ms}$ or greater to distinguish healthy from diseased groups or two diseased groups with 90% power at a 5% significance level.

To assess patchy liver diseases such as PSC, the liver heterogeneity is characterised by the cT_1 IQR. MOLLI cT_1 IQR in a cohort of 50 PSC patients was significantly higher than cT_1 IQR in healthy volunteers ($88.5\,\mathrm{ms}$ vs $63.6\,\mathrm{ms}$, p$<$0.0001) [152]. Median VFA T_1 IQR measured in our healthy volunteer cohort at the voxel level was $68.1\,\mathrm{ms}$, for all the slices with ROIs drawn. This is comparable to cT_1 IQR measured in the healthy volunteers and lower than the PSC cT_1 IQR [152], demonstrating that VFA T_1 IQR could be used to identify PSC patients. Note that the cT_1 IQRs were obtained from vessel segmented MOLLI T_1 slices, thus including more pixels within one slice compared to the ROI-selected T_1s in VFA. In compensation, on average 23 slices across the 10 volunteers and 3 runs are included in the VFA compared to only 5 or 6 MOLLI slices in [152].

One underlying assumption in this study was that liver T_1 did not vary during the intra-session repeatability scans. It has been reported that even large changes in hydration and glycogen levels [153] result in variations in median shMOLLI liver T_1 that lie within scan-rescan repeatability coefficients [134]. Our study included several limitations. Firstly,

the number of volunteers was limited to 10. Secondly, the proposed *in vivo* gold standard method had poor repeatability confirming it should not be used as a gold standard method for VFA T_1 in future studies. Perhaps a more adequate *in vivo* liver T_1 gold standard would have been IR-EPI implemented with acquisition parameters that minimised chemical shift artefacts and EPI distortion. Nevertheless, the good agreement between the VFA T_1 forward simulated to MOLLI T_1 and the acquired MOLLI T_1 is a reassurance of the development of an accurate VFA T_1 method. Another limitation is the number of ROIs placed in the liver. Ideally, a segmentation of liver T_1 excluding vessels, bile ducts, and T_1 values where the fit was not reliable would provide a more robust performance of the VFA T_1 method developed. Nevertheless, three ROIs per slice are a standard practice in the literature to derive liver function metrics [134].

Table 6.3: MOLLI cT_1 (ms) measured at different fibrosis stages reported as $\mu \pm \sigma$, median(IQR) or [95% CI]. The T_1 standard deviation (σ_{T_1}) to differentiate between the several stages with 90% power and 5% significance level characterises the minimum precision necessary for the VFA T_1 method.

	No Fibrosis (NF)	Fibrosis Stage$_{1\text{-}2}$ ($F_{1\text{-}2}$)	σ_{T_1} (NF vs $F_{1\text{-}2}$)	Fibrosis Stage$_{3\text{-}4}$ ($F_{3\text{-}4}$)	σ_{T_1} ($F_{1\text{-}2}$ vs $F_{3\text{-}4}$)	Fibrosis Stage$_{5\text{-}6}$ ($F_{5\text{-}6}$)	σ_{T_1} ($F_{3\text{-}4}$ vs $F_{5\text{-}6}$)
Banerjee et al. [19]	750 ± 42	870 ± 104	40	873 ± 63	NA	1025 ± 102	38
McDonald et al. [120]	787(109)	[800 875]	NA	[875 950]	34	[950 1025]	34

NA: T_1 standard deviation was not calculated as the T_1 is not a good biomarker to differentiate the two groups, i.e., power less than 50% at 5% significance level.

Table 6.4: T_1 measured in ms for different liver diseases reported as $\mu \pm \sigma$ or median(IQR). The T_1 standard deviation to differentiate between healthy and diseased with 90% power and 5% significance level characterises the minimum precision necessary for the VFA T_1 method.

	Liver disease	T_1 Healthy	T_1 Diseased	σ_{T_1} (Healthy vs Diseased)
Bradley et al. [121] ($1.5\,\mathrm{T}$, IR-EPI)	Compensated Cirrhosis	637 ± 32	748 ± 108	46
Bradley et al. [121] ($1.5\,\mathrm{T}$, IR-EPI)	Decompensated Cirrhosis	637 ± 32	864 ± 127	NA
Janowski et al. [154] ($1.5\,\mathrm{T}$, MOLLI)	Autoimmune Hepatitis	715(94)	877(115)	37
Levick et al. [125] ($3\,\mathrm{T}$, MOLLI)	Portal Hypertension	874(159)	1104 (289)	28

NA: T_1 standard deviation was not calculated as the T_1 is not a good biomarker to differentiate the two groups, i.e., power less than 50% at 5% significance level. T_1 increases with field strength, thus T_1 values at $1.5\,\mathrm{T}$ are expected to be lower than at $3\,\mathrm{T}$.

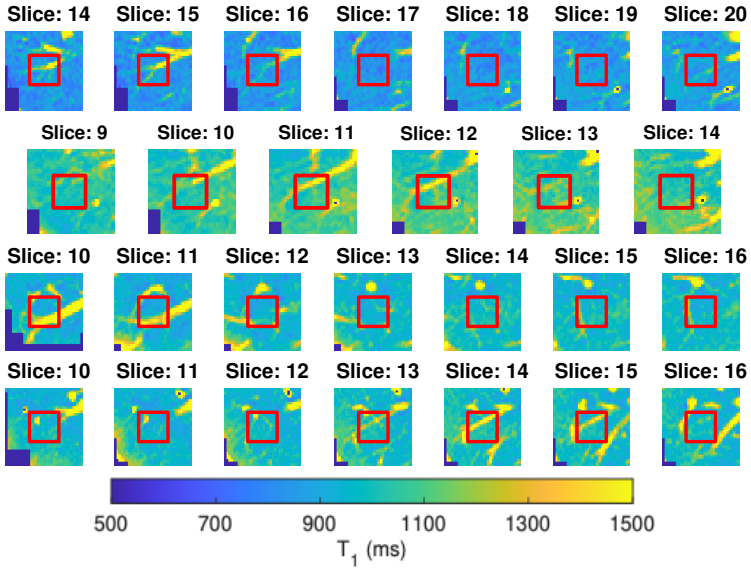


Figure 6.10: VFA T_1 maps for the voxel defined in the spectroscopy sequence for 4 different volunteers. The spectroscopy voxel is illustrated by the red rectangle. The presence of vessels within the red rectangle is clear. The spectroscopy voxel has $203\,\mathrm{mm}^3$ volume, spanning 6 to 7 VFA slices. The slice numbers above each image refer to the VFA SPGR acquisition.

6.5 Conclusion

In conclusion, a method for 3D VFA T_1 mapping in the liver at $3\,\mathrm{T}$ on a Prisma scanner was developed, using only widely available pulse sequences, that is accurate, precise and shows high repeatability for both intra- and inter-session studies. With a total scan time of 7 breath-holds, sufficient precision was achieved to measure the biological changes observed in liver T_1 for the majority of liver diseases. The results from this *in vivo* validation study should generate confidence in hepatologists for clinical adoption of the method. In addition, the outlined method using widely available pulse sequences should increase the clinical availability of robust liver T_1 mapping methods. This method also provides a template for deployment of T_1 mapping across different scanners and vendors, thus facilitating multicentre studies, essential in consortium research studies and clinical trials of pharmaceutical liver drugs.

7 Conclusions and Future Work

7.1 Summary

Developing an accurate and precise T_1 mapping method that uses pulse sequences widely available on any scanner, independent of vendor, is a first step towards developing a universal measure of T_1. Whole liver T_1 maps will allow better characterisation of the liver, the largest internal organ in the human body, leading to advances in the diagnosis and treatment of liver diseases. Measuring the *in vivo* precision of T_1 maps is also important to build protocols that allow for stratification or long-term monitoring of liver diseases.

This work confirmed that the main factor affecting the accuracy of *in vivo* T_1 maps acquired using the VFA SPGR pulse sequence at $3\,\mathrm{T}$ are B_1^+ inhomogeneities. At $3\,\mathrm{T}$, the B_1^+ factor reaches values as low as 0.5, which induces an error in T_1 of 75% if uncorrected. Consequently, construction of an accurate B_1^+ map is of foremost importance. Chapter 3 investigated the main factors affecting the B_1^+ map accuracy. Using the DAM with a 2D multi-slice GRE-EPI implementation and applying formulas from the literature resulted in median T_1 errors of 10.5% and 29% in phantom data depending on the RF excitation pulse used, the Hamming Windowed Sinc or the Water Excitation spectral-spatial pulse, respectively. In the absence of a gold standard T_1 map *in vivo*, an average difference of 7% and 44% was observed between the T_1 values corrected and uncorrected for slice

profile effects using a Hamming Windowed Sinc or Water Excitation B_1^+ map, respectively. Deviations of the slice profile from an ideal rectangle together with imperfect refocusing of the magnetisation, aggravated by B_0 inhomogeneities through slice, are two key confounders affecting the B_1^+ map accuracy. Corrections for these two confounders decreased the median T_1 error in phantom data to -0.3% and -3.9% with the Hamming Windowed Sinc and Water Excitation pulses, respectively. The proximity of the liver to the lung makes it susceptible to large B_0 inhomogeneities. *In vivo* B_0 variations through slice up to $12\,\mathrm{Hz/cm}$ were measured at $3\,\mathrm{T}$. With our B_1^+ mapping method, the error in the B_1^+ factor scales by approximately 3.8% for every $10\,\mathrm{Hz/cm}$ variation in B_0 along the slice direction. Failure to consider the impact of B_0 gradients on the B_1^+ map acquisition resulted in T_1 variations between the top and the bottom of the liver of $221\,\mathrm{ms}$, while after correcting for B_0 gradients the T_1 variations decreased to $4\,\mathrm{ms}$.

B_0 inhomogeneities cause additional confounders in EPI-based B_1^+ maps. Distortion correction is necessary in the liver at $3\,\mathrm{T}$ to reduce in-plane T_1 variations. Using the minimum echo spacing of $0.3\,\mathrm{ms}$ without correcting for distortions is not sufficient. Differences in T_1 up to 15.7% were observed between uncorrected and distortion corrected *in vivo* T_1 maps. Fat suppression is also crucial to avoid chemical shift artefacts. When residual fat signal remains, it is important to identify its imprint on the B_1^+ map and adapt the acquisition parameters to reduce its impact. When such measures are insufficient, it may be necessary to construct post-processing algorithms to remove the chemical shift artefacts. Overall, more homogeneous T_1 maps were obtained after correcting EPI-based confounders in the B_1^+ map.

Finally, the SPGR sequence is affected by incomplete spoiling resulting in median T_1 errors in phantom data of 7.4%; after correction the error decreased to -0.7%. Spatial saturation also affects the steady-state SPGR signal and should be switched off if possible. Respiration is an additional confounder to both the GRE-EPI and the SPGR signal that deforms the liver non-rigidly. Caution should be taken with state-of-the-art image registration approaches as they were found to change the B_1^+ map and T_1 map values

even in cases of no visual indication of misregistration between images.

A theoretical framework was presented in Chapter 5 to calculate the T_1 variance taking into account both the noise in the B_1^+ map and in the SPGR signal together with the range of B_1^+s and T_1s observed *in vivo* in the liver at $3\,\mathrm{T}$. This framework can be easily adapted for other T_1 mapping applications using the SPGR signal under a different range of T_1s and B_1^+ factors, such as liver T_1 mapping at $1.5\,\mathrm{T}$, liver imaging with contrast agents or brain T_1 mapping. Validation of this framework was achieved *in vivo*, demonstrating good agreement, within 0.5% on average, between simulations and *in vivo* data.

The optimal FAs that resulted in the minimum variance in T_1 in the simulations were $2°$,$3°$,$15°$,$15°$ for physiological liver ranges of T_1 and B_1^+ factors at $3\,\mathrm{T}$. From this set, a standard FA set with values of $2°$,$2°$,$15°$,$15°$ was adopted *in vivo*. This standard FA set was robust to a large range of SNRs (12.5-50, at nominal FA$=2°$). In addition, a minimal increase in T_1 CoV compared to the optimal FA set was predicted. An average whole-liver T_1 CoV of 6.2 ± 1.7% using the set of 4 standard FAs was obtained across 10 volunteers. This cohort had B_1^+ factors ranging between 0.52 and 1.16, mean T_1 values varying between $775\,\mathrm{ms}$ and $1050\,\mathrm{ms}$, SPGR SNRs between 19 and 59 (measured at nominal FAs of $2°$) and B_1^+ factor noise values between 0.8% and 4.6%.

Optimising the FA choice minimises the T_1 variance and saves breath-holds. A better T_1 CoV was achieved *in vivo*, for all 10 volunteers, when using 4 standard FAs compared to 5 uniformly spaced FAs. The choice of 2 low and 2 high FAs by the CRLB algorithm is linked to determining the M_0 and T_1 values, respectively. Low FAs are least sensitive to T_1 while FAs above the Ernst angle have larger absolute values of the first derivative of the SPGR signal with respect to T_1. In addition, it is also important to minimise the variance propagated from the B_1^+ map to the T_1 map. The optimal pair of FAs that achieved the smallest variance in the B_1^+ map was $65°/130°$. Too low FAs are affected by the SNR and the upper bound in the FA is limited by three factors: the maximum B_1^+ bias, the lack of phase data and the maximum FA available at the scanner interface.

The theoretical framework also answered the question of whether a higher return

in T_1 CoV is obtained by investing extra breath-holds in the SPGR or the B_1^+ map. Simulations and experimental data showed that it is best to invest breath-holds in the SPGR acquisition. Only at very high SPGR SNRs, did it become more advantageous to invest in B_1^+ map FAs. This agrees with simulations showing that the B_1^+ factor variance only dominated the T_1 variance at high SPGR SNRs (above 50, at a true FA$=2^\circ$).

Testing the performance of the method *in vivo* was carried out in Chapter 6. STEAM was the initially preferred method to test accuracy as the spectroscopy voxel extended through 6-7 VFA SPGR slices. However, large intra-subject variability of up to $252\,\mathrm{ms}$ invalidated its use as a gold-standard T_1 method *in vivo*. SASHA and MOLLI were used as alternative comparison methods, despite being single slice techniques. VFA SPGR T_1 values were on average 5% lower than SASHA T_1 values. VFA forward simulated MOLLI T_1 values were also on average 5% lower than MOLLI T_1 values. Intra and inter-session repeatability coefficients of $60\,\mathrm{ms}$ and $49\,\mathrm{ms}$ were achieved, respectively. Moreover, the regression slope for both sessions was consistent with a unity slope within its standard error. The median standard deviation of the VFA T_1 values, at an ROI level, was $31\,\mathrm{ms}$ across the 10 volunteers. This value offers enough precision to distinguish between a healthy and a fibrotic liver with 90% power at a 5% significance level.

In summary, a 3D T_1 mapping method was successfully built using only widely available MRI methods and requiring a total of 7 breath-holds. The primary objective of developing unbiased and repeatable T_1 maps of the liver with sufficient precision to stratify important liver diseases was achieved. The CRLB-based T_1 variance offers additional scope to further hone the T_1 map precision through increasing the total number of FAs or possibly changing the TR.

7.2 Future Work

Although the objectives set in this work were largely accomplished, a few areas remain where further work could improve the T_1 map robustness and precision. The 3D T_1 maps obtained in healthy volunteers were homogeneous over a large extension of the liver. Nevertheless, there are problematic areas where the T_1 variability exceeds the method's precision, notably the top slices near the diaphragm where large B_0 inhomogeneities exist. The discovery of the B_0 gradient through slice confounding factor was key to improve the homogeneity of T_1 maps. To correct this confounder, an accurate knowledge of the B_0 field along the slice direction is crucial. When there is no information on B_0 values in slices above the target pixel where the B_1^+ factor is being calculated, the B_0 extrapolation may not be accurate, propagating errors into the B_1^+ map. This lack of B_0 information occurs for slices near the diaphragm. Investing in a higher resolution B_0 map sequence extending beyond the B_1^+ map FoV coverage along the slice direction should help. However, areas with low signal and susceptible to respiratory motion, such as the lungs, will always be prone to inaccurate and imprecise B_0 map values. Changing from a gradient echo to a spin echo EPI sequence could result in more accurate B_1^+ map values.

Better fat suppression methods are also key for further deployment of the method in the clinic, especially for obese patients. Water excitation acquisitions suppressed better the fat but were found to be less accurate in measuring water T_1 in phantom data. Spectral-spatial pulses are more sensitive to B_0 inhomogeneities, thus higher resolution and more accurate B_0 maps may make water excitation a feasible alternative to fat saturation schemes.

Finally, another area to explore is the impact of breath-hold misalignment on the B_1^+ field. Does the B_1^+ field change significantly between a breath-hold at end-inspiration compared to end-expiration? How sensitive is the B_1^+ field to the amount of air in the lungs? It would be important to answer these questions before embarking upon the challenging task of registration. If two liver domes acquired at different end-expiratory positions encode the same B_1^+ field, registration would avoid taking the ratio between areas of lung tissue and liver tissue. Registration could in principle align the proton

density between the two images. However, because the coils do not move in the foot-head direction, registration would provoke a mismatch in the B_1^- field which would not cancel when taking the ratio in the B_1^+ map calculation. In this work, I opted not to register to preserve the B_1^- cancellation. The trade-off is that areas with mismatching proton density due to breath-hold misalignments, generally at the edges of the liver, will not have an accurate B_1^+ or T_1 map.

The leverage in using only scanner agnostic sequences would be the deployment of the method in a Philips or GE scanner. This will require harmonising the MRI parameters in Philips or GE sequences that mirror the sequences in Chapter 4. The algorithms developed for correcting the B_1^+ or SPGR confounding factors may also need adaptation depending on the specific implementation of the pulse sequences, e.g., RF phase increment, RF excitation pulse and gradients along the slice direction. Careful testing in both phantom and *in vivo* will be essential. Repeatability studies similar to those described in Chapter 6 will be necessary for each vendor as well as inter-vendor reproducibility studies.

Comparing the performance of the native B_1^+ maps adopted by each vendor against the optimised 2D DAM GRE-EPI proposed in this work would be useful to infer what costs in T_1 accuracy and precision would be incurred if the native B_1^+ map method was used. Initial work was done comparing the preconditioning RF pulse B_1^+ map method [53], available in some Siemens scanners such as the $3\,\mathrm{T}$ Prisma, against the optimised 2D DAM [155]. Characterising B_1^+ inhomogeneities in a $1.5\,\mathrm{T}$ scanner, assessing its impact on the T_1 map and comparing it to the magnitude of the confounders quantified at $3\,\mathrm{T}$ in Chapter 3 would also be useful.

Another area of interest is to apply the developed 3D T_1 mapping method to patients with liver cancer or heterogeneous liver diseases. This should allow for a better characterisation of healthy versus diseased liver tissue compared to single slice techniques such as SASHA and MOLLI. An example of this application in both HCC (Figure 7.1) and PSC (Figure 7.2) patients was tested on the Prisma scanner at OCMR. Further testing in large cohorts and statistical analysis remains as future work.

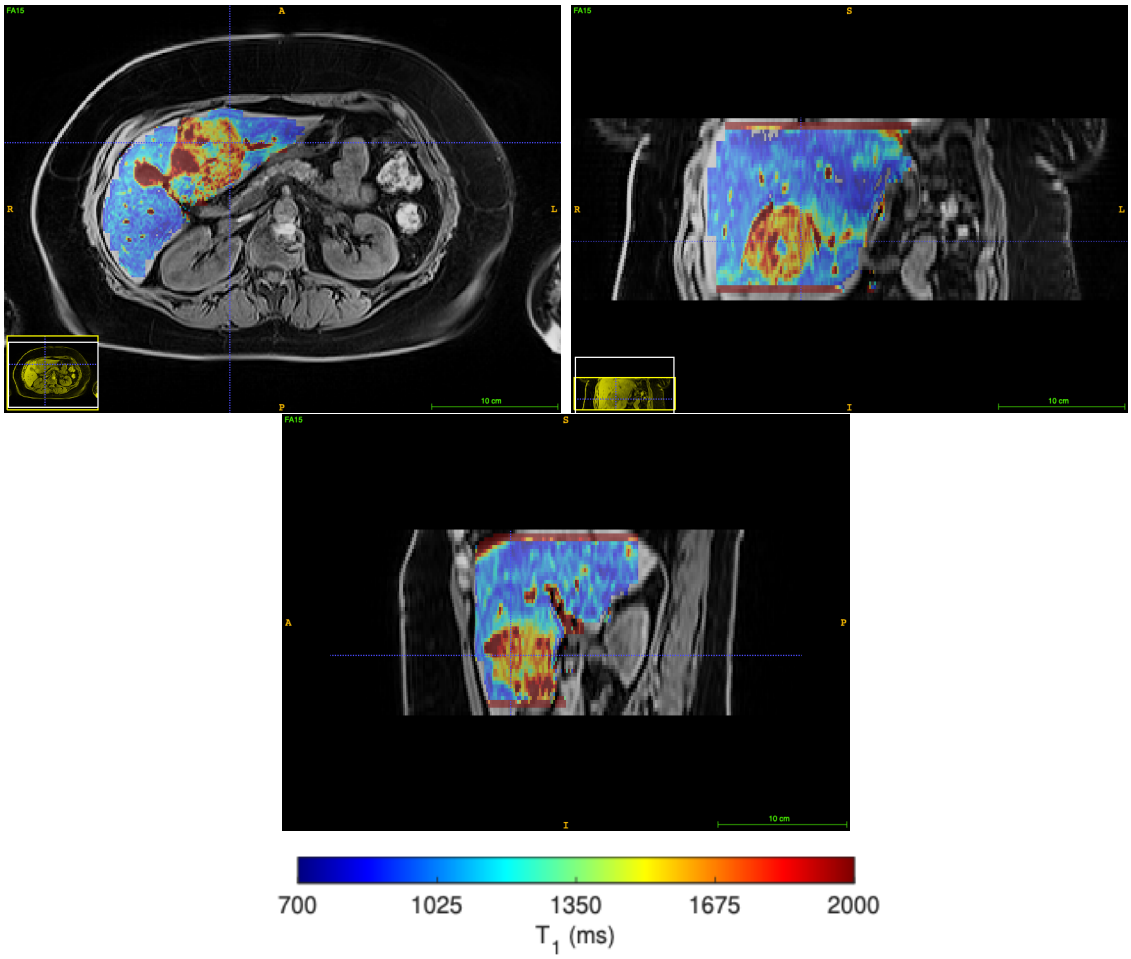


Figure 7.1: 3D T_1 maps with the method proposed in this thesis applied to a patient with hepatocellular carcinoma. The tumour corresponds to the donut-shaped mass with T_1 values above $1500\,\mathrm{ms}$ while the healthy liver has T_1 values below $1000\,\mathrm{ms}$. The tumour spans several slices as can be seen in the coronal and sagittal planes.

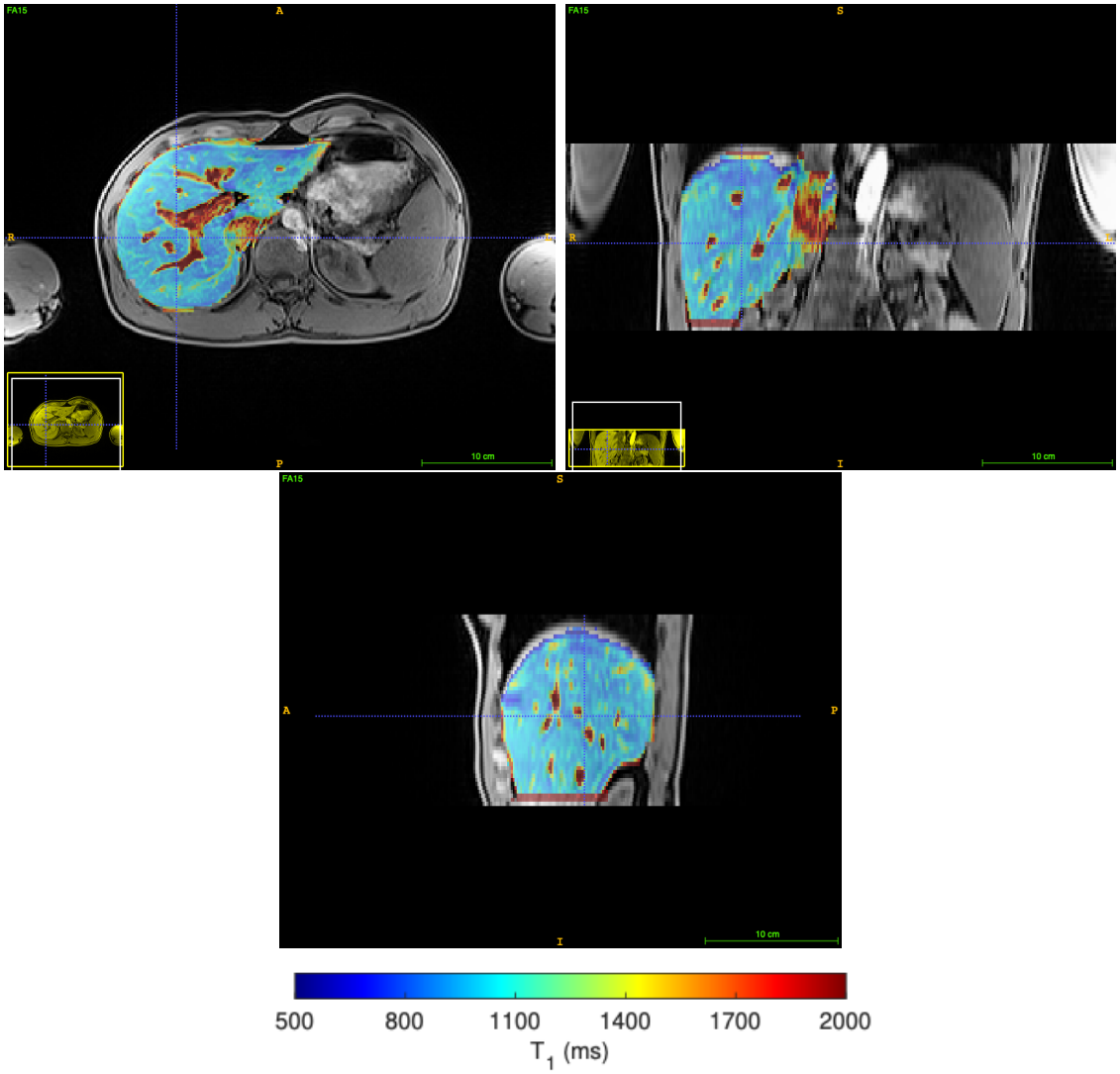


Figure 7.2: 3D T_1 maps with the method proposed in this thesis applied to a patient with primary sclerosing cholangitis. This is a heterogeneous liver disease characterised by areas of elevated T_1, especially surrounding the bile ducts, next to areas of healthy tissue.

References

[1] S. Cheemerla and M. Balakrishnan, "Global Epidemiology of Chronic Liver Disease," *Clinical Liver Disease*, vol. 17, no. 5, pp. 365–370, May 2021.

[2] A. B. Rogers and R. Z. Dintzis, "Hepatobiliary System," in *Comparative Anatomy and Histology (Second Edition)*, Cambridge, MA, USA: Academic Press, Jan. 2018, pp. 229–239.

[3] A. Kalra, E. Yetiskul, C. J. Wehrle, and F. Tuma, "Physiology, Liver," in *StatPearls [Internet]*, StatPearls Publishing, May 2021. [Online]. Available: `https://www.ncbi.nlm.nih.gov/books/NBK535438`.

[4] S. R. Z. Abdel-Misih and M. Bloomston, "Liver Anatomy," *Surg. Clin. North Am.*, vol. 90, no. 4, p. 643, Aug. 2010.

[5] N. Toshikuni, M. Tsutsumi, and T. Arisawa, "Clinical differences between alcoholic liver disease and nonalcoholic fatty liver disease," *World J. Gastroenterol.*, vol. 20, no. 26, p. 8393, Jul. 2014.

[6] S. K. Asrani, H. Devarbhavi, J. Eaton, and P. S. Kamath, "Burden of liver diseases in the world," *J. Hepatol.*, vol. 70, no. 1, pp. 151–171, Jan. 2019.

[7] D. Berger, V. Desai, and S. Janardhan, "Con: Liver Biopsy Remains the Gold Standard to Evaluate Fibrosis in Patients With Nonalcoholic Fatty Liver Disease," *Clinical Liver Disease*, vol. 13, no. 4, pp. 114–116, Apr. 2019.

[8] R. Bataller and D. A. Brenner, "Liver fibrosis," *J. Clin. Invest.*, vol. 115, no. 2, p. 209, Feb. 2005.

[9] R. A. Standish, E. Cholongitas, A. Dhillon, A. K. Burroughs, and A. P. Dhillon, "An appraisal of the histopathological assessment of liver fibrosis," *Gut*, vol. 55, no. 4, pp. 569–578, Apr. 2006.

[10] J. E. Kim, H. O. Kim, K. Bae, D. S. Choi, and D. Nickel, "T1 mapping for liver function evaluation in gadoxetic acid-enhanced MR imaging: comparison of look-locker inversion recovery and B 1 inhomogeneity-corrected variable flip angle method," *Eur. Radiol.*, vol. 29, no. 7, pp. 3584–3594, Jul. 2019.

[11] M. Haimerl, M. Schlabeck, N. Verloh, *et al.*, "Volume-assisted estimation of liver function based on Gd-EOB-DTPA-enhanced MR relaxometry," *Eur. Radiol.*, vol. 26, no. 4, pp. 1125–1133, Apr. 2016.

[12] J. H. Yoon, J. M. Lee, E. Kim, T. Okuaki, and J. K. Han, "Quantitative Liver Function Analysis: Volumetric T1 Mapping with Fast Multisection B 1 Inhomogeneity Correction in Hepatocyte-specific Contrast-enhanced Liver MR Imaging," *Radiology*, vol. 282, no. 2, pp. 408–417, Feb. 2017.

[13] C. W. Hong, A. Mamidipalli, J. C. Hooker, *et al.*, "MRI proton density fat fraction is robust across the biologically plausible range of triglyceride spectra in adults with nonalcoholic steatohepatitis," *J. Magn. Reson. Imaging*, vol. 47, no. 4, pp. 995–1002, Apr. 2018.

[14] W. M. Haufe, T. Wolfson, C. A. Hooker, *et al.*, "Accuracy of PDFF estimation by magnitude-based and complex-based MRI in children with MR spectroscopy as a reference," *J. Magn. Reson. Imaging*, vol. 46, no. 6, pp. 1641–1647, Dec. 2017.

[15] Z. M. Younossi, A. B. Koenig, D. Abdelatif, Y. Fazel, L. Henry, and M. Wymer, "Global epidemiology of nonalcoholic fatty liver disease-Meta-analytic assessment of prevalence, incidence, and outcomes," *Hepatology*, vol. 64, no. 1, pp. 73–84, Jul. 2016.

[16] J. M. Paik, P. Golabi, Y. Younossi, A. Mishra, and Z. M. Younossi, "Changes in the Global Burden of Chronic Liver Diseases From 2012 to 2017: The Growing Impact of NAFLD," *Hepatology*, vol. 72, no. 5, pp. 1605–1616, Nov. 2020.

[17] T. G. S. Pierre, P. R. Clark, and W. Chua-Anusorn, "Single spin-echo proton transverse relaxometry of iron-loaded liver," *NMR Biomed.*, vol. 17, no. 7, pp. 446–458, Nov. 2004.

[18] J. C. Wood, C. Enriquez, N. Ghugre, *et al.*, "MRI R2 and R2$*$ mapping accurately estimates hepatic iron concentration in transfusion-dependent thalassemia and sickle cell disease patients," *Blood*, vol. 106, no. 4, pp. 1460–1465, Aug. 2005.

[19] R. Banerjee, M. Pavlides, E. M. Tunnicliffe, *et al.*, "Multiparametric magnetic resonance for the non-invasive diagnosis of liver disease," *J. Hepatol.*, vol. 60, no. 1, pp. 69–77, Jan. 2014.

[20] C. L. Hoad, N. Palaniyappan, P. Kaye, *et al.*, "A study of T1 relaxation time as a measure of liver fibrosis and the influence of confounding histological factors," *NMR Biomed.*, vol. 28, no. 6, pp. 706–714, Jun. 2015.

[21] M. Pavlides, R. Banerjee, E. M. Tunnicliffe, *et al.*, "Multiparametric magnetic resonance imaging for the assessment of non-alcoholic fatty liver disease severity," *Liver Int.*, vol. 37, no. 7, pp. 1065–1073, Jul. 2017.

[22] T. Heye, S.-R. Yang, M. Bock, *et al.*, "MR relaxometry of the liver: significant elevation of T1 relaxation time in patients with liver cirrhosis," *Eur. Radiol.*, vol. 22, no. 6, pp. 1224–1232, Jun. 2012.

[23] D. R. Messroghli, A. Radjenovic, S. Kozerke, D. M. Higgins, M. U. Sivananthan, and J. P. Ridgway, "Modified Look-Locker inversion recovery (MOLLI) for high-resolution T1 mapping of the heart," *Magn. Reson. Med.*, vol. 52, no. 1, pp. 141–146, Jul. 2004.

[24] E. M. Tunnicliffe, R. Banerjee, M. Pavlides, S. Neubauer, and M. D. Robson, "A model for hepatic fibrosis: the competing effects of cell loss and iron on shortened modified Look-Locker inversion recovery T1 (shMOLLI-T1) in the liver," *J. Magn. Reson. Imaging*, vol. 45, no. 2, pp. 450–462, Feb. 2017.

[25] P. Khoshpouri, R. R. Habibabadi, B. Hazhirkarzar, *et al.*, "Imaging Features of Primary Sclerosing Cholangitis: From Diagnosis to Liver Transplant Follow-up," *Radiographics*, Oct. 2019.

[26] P. Kellman and M. S. Hansen, "T1-mapping in the heart: accuracy and precision," *J. Cardiovasc. Magn. Reson.*, vol. 16, no. 1, p. 2. Jan. 2014.

[27] M. D. Robson, S. K. Piechnik, E. M. Tunnicliffe, and S. Neubauer, "T1 measurements in the human myocardium: the effects of magnetization transfer on the SASHA and MOLLI sequences," *Magn. Reson. Med.*, vol. 70, no. 3, pp. 664–670, Sep. 2013.

[28] S. C. L. Deoni, B. K. Rutt, and T. M. Peters, "Rapid combined T1 and T2 mapping using gradient recalled acquisition in the steady state," *Magn. Reson. Med.*, vol. 49, no. 3, pp. 515–526, Mar. 2003.

[29] H.-L. M. Cheng and G. A. Wright, "Rapid high-resolution T(1) mapping by variable flip angles: accurate and precise measurements in the presence of radiofrequency field inhomogeneity," *Magn. Reson. Med.*, vol. 55, no. 3, pp. 566–574, Mar. 2006.

[30] R.-M. Gracien, M. Maiworm, N. Brüche, *et al.*, "How stable is quantitative MRI? - Assessment of intra- and inter-scanner-model reproducibility using identical acquisition sequences and data analysis programs," *Neuroimage*, vol. 207, p. 116364. Feb. 2020.

[31] R. W. Brown, Y.-C. N. Cheng, E. M. Haacke, M. R. Thompson, and R. Venkatesan, *Magnetic Resonance Imaging: Physical Principles and Design Sequence*, Second Edition. John Wiley & Sons, Apr. 2014.

[32] D. W. McRobbie, E. A. Moore, M. J. Graves, and M. R. Prince, *MRI from Picture to Proton*. Cambridge, England, UK: Cambridge University Press, Apr. 2017.

[33] M. A. Bernstein, K. F. King, and X. J. Zhou, *Handbook of MRI Pulse Sequences*. Elsevier, Academic Press, 2004.

[34] W. A. Edelstein, G. H. Glover, C. J. Hardy, and R. W. Redington, "The intrinsic signal-to-noise ratio in NMR imaging," *Magn. Reson. Med.*, vol. 3, no. 4, pp. 604–618, Aug. 1986.

[35] M. Zaitsev, J. Maclaren, and M. Herbst, "Motion artifacts in MRI: A complex problem with many partial solutions," *J. Magn. Reson. Imaging*, vol. 42, no. 4, pp. 887–901, Oct. 2015.

[36] N. Balu, B. Chu, T. S. Hatsukami, C. Yuan, and V. L. Yarnykh, "Comparison between 2D and 3D high-resolution black-blood techniques for carotid artery wall imaging in clinically significant atherosclerosis," *J. Magn. Reson. Imaging*, vol. 27, no. 4, pp. 918–924, Apr. 2008.

[37] E. L. Hahn, "Spin Echoes," *Phys. Rev.*, vol. 80, no. 4, pp. 580–594, Nov. 1950.

[38] D. C. Look and D. R. Locker, "Time Saving in Measurement of NMR and EPR Relaxation Times," *Rev. Sci. Instrum.*, vol. 41, no. 2, pp. 250–251, Feb. 1970.

[39] R. Deichmann and A. Haase, "Quantification of T1 values by SNAPSHOT-FLASH NMR imaging," *Journal of Magnetic Resonance*, vol. 96, no. 3, pp. 608–612, Feb. 1992.

[40] K. Chow, J. A. Flewitt, J. D. Green, J. J. Pagano, M. G. Friedrich, and R. B. Thompson, "Saturation recovery single-shot acquisition (SASHA) for myocardial T(1) mapping," *Magn. Reson. Med.*, vol. 71, no. 6, pp. 2082–2095, Jun. 2014.

[41] R. K. Gupta, "A new look at the method of variable nutation angle for the measurement of spin-lattice relaxation times using fourier transform NMR," *Journal of Magnetic Resonance*, vol. 25, no. 1, pp. 231–235, Jan. 1977.

[42] R. Venkatesan, W. Lin, and E. M. Haacke, "Accurate determination of spin-density and T1 in the presence of RF-field inhomogeneities and flip-angle miscalibration," *Magn. Reson. Med.*, vol. 40, no. 4, pp. 592–602, Oct. 1998.

[43] S. B. Bulumulla, S. K. Lee, and D. T. B. Yeo, "Conductivity and permittivity imaging at 3.0 t," *Concepts Magn. Reson.*, vol. 41B, no. 1, pp. 13–21, Feb. 2012.

[44] M. Alecci, C. M. Collins, M. B. Smith, and P. Jezzard, "Radio frequency magnetic field mapping of a 3 Tesla birdcage coil: Experimental and theoretical dependence on sample properties," *Magn. Reson. Med.*, vol. 46, no. 2, pp. 379–385, Jul. 2001.

[45] C. M. Collins, W. Liu, W. Schreiber, Q. X. Yang, and M. B. Smith, "Central brightening due to constructive interference with, without, and despite dielectric resonance," *J. Magn. Reson. Imaging*, vol. 21, no. 2, Feb. 2005.

[46] Q. X. Yang, J. Wang, X. Zhang, *et al.*, "Analysis of wave behavior in lossy dielectric samples at high field," *Magn. Reson. Med.*, vol. 47, no. 5, pp. 982–989, May 2002.

[47] D. Andreuccetti, R. Fossi, and C. Petrucci. "Dielectric Properties of Body Tissues: Output data." (), [Online]. Available: `http://niremf.ifac.cnr.it/tissprop/htmlclie/uniquery.php?func=stsffun&tiss=Liver&freq=127700000&outform=disphtm&tisname=on&frequen=on&conduct=on&permitt=on&losstan=on&wavelen=on&pendept=on&freq1=1000000&tissue2=Air&frqbeg=10&frqend=100e9&linstep=100&mode=log&logstep=5&tissue3=Liver&freq3=127700000`. (accessed: 29.11.2019).

[48] J. G. Sled and G. B. Pike, "Standing-wave and RF penetration artifacts caused by elliptic geometry: an electrodynamic analysis of MRI," *IEEE Trans. Med. Imaging*, vol. 17, no. 4, pp. 653–662, Aug. 1998.

[49] A. G. Webb and C. M. Collins, "Parallel transmit and receive technology in high-field magnetic resonance neuroimaging," *Int. J. Imaging Syst. Technol.*, vol. 20, no. 1, pp. 2–13, Mar. 2010.

[50] E. K. Insko and L. Bolinger, "Mapping of the Radiofrequency Field," *J. Magn. Reson., Ser. A*, vol. 103, no. 1, pp. 82–85, Jun. 1993.

[51] R. Stollberger and P. Wach, "Imaging of the active B1 field in vivo," *Magn. Reson. Med.*, vol. 35, no. 2, pp. 246–251, Feb. 1996.

[52] V. L. Yarnykh, "Actual flip-angle imaging in the pulsed steady state: A method for rapid three-dimensional mapping of the transmitted radiofrequency field," *Magn. Reson. Med.*, vol. 57, no. 1, pp. 192–200, Jan. 2007.

[53] S. Chung, D. Kim, E. Breton, and L. Axel, "Rapid B1+ mapping using a preconditioning RF pulse with TurboFLASH readout," *Magn. Reson. Med.*, vol. 64, no. 2, pp. 439–446, Aug. 2010.

[54] K. Nehrke and P. Börnert, "DREAM–a novel approach for robust, ultrafast, multislice xn–B-hnn mapping," *Magn. Reson. Med.*, vol. 68, no. 5, pp. 1517–1526, Nov. 2012.

[55] L. I. Sacolick, F. Wiesinger, I. Hancu, and M. W. Vogel, "B1 mapping by Bloch-Siegert shift," *Magn. Reson. Med.*, vol. 63, no. 5, pp. 1315–1322, May 2010.

[56] G. R. Morrell, "A phase-sensitive method of flip angle mapping," *Magn. Reson. Med.*, vol. 60, no. 4, pp. 889–894, Oct. 2008.

[57] G. J. M. Parker, G. J. Barker, and P. S. Tofts, "Accurate multislice gradient echo T1 measurement in the presence of non-ideal RF pulse shape and RF field nonuniformity," *Magn. Reson. Med.*, vol. 45, no. 5, pp. 838–845, May 2001.

[58] F. Schmitt, M. K. Stehling, and R. Turner, *Echo-Planar Imaging*. Berlin, Germany: Springer, 1998.

[59] MATLAB, *9.10.0.1739362 (R2021a)*. Natick, Massachusetts: The MathWorks Inc., 2021.

[60] M. Cercignani, N. Dowell, and P. Tofts, *Quantitative MRI of the Brain: Principles of Physical Measurement*. CRC Press, 2018.

[61] N. T. Roberts, L. A. Hinshaw, T. J. Colgan, T. Ii, D. Hernando, and S. B. Reeder, "B 0 and B 1 inhomogeneities in the liver at 1.5 T and 3.0 T," *Magn. Reson. Med.*, vol. 85, no. 4, pp. 2212–2220, Apr. 2021.

[62] G. Helms, H. Dathe, and P. Dechent, "Quantitative FLASH MRI at 3T using a rational approximation of the Ernst equation," *Magn. Reson. Med.*, vol. 59, no. 3, pp. 667–672, Mar. 2008.

[63] G. J. Stanisz, E. E. Odrobina, J. Pun, *et al.*, "T1, T2 relaxation and magnetization transfer in tissue at 3T," *Magn. Reson. Med.*, vol. 54, no. 3, pp. 507–512, Sep. 2005.

[64] P. J. Keller, W. W. Hunter Jr., and P. Schmalbrock, "Multisection fat-water imaging with chemical shift selective presaturation.," *Radiology*, Aug. 1987.

[65] C. H. Meyer, J. M. Pauly, A. Macovskiand, and D. G. Nishimura, "Simultaneous spatial and spectral selective excitation," *Magn. Reson. Med.*, vol. 15, no. 2, pp. 287–304, Aug. 1990.

[66] F. Schick, J. Forster, J. Machann, R. Kuntz, and C. D. Claussen, "Improved clinical echo-planar MRI using spatial-spectral excitation," *J. Magn. Reson. Imaging*, vol. 8, no. 4, pp. 960–967, Jul. 1998.

[67] G. E. Gold, E. Han, J. Stainsby, G. Wright, J. Brittain, and C. Beaulieu, "Musculoskeletal MRI at 3.0 T: Relaxation Times and Image Contrast," *Am. J. Roentgenol.*, Nov. 2012.

[68] B. A. Hargreaves. "Bloch equation simulator." (), [Online]. Available: `http://mrsrl.stanford.edu/~brian/blochsim/`. (accessed: 27.06.2019).

[69] C. M. J. de Bazelaire, G. D. Duhamel, N. M. Rofsky, and D. C. Alsop, "MR Imaging Relaxation Times of Abdominal and Pelvic Tissues Measured in Vivo at 3.0 T: Preliminary Results1," *Radiology*, Mar. 2004.

[70] J. D'Errico. "Slm - shape language modeling." (), [Online]. Available: `https://www.mathworks.com/matlabcentral/fileexchange/24443-slm-shape-language-modeling`. (accessed: 15.04.2021).

[71] A. Mojtahed, C. J. Kelly, A. H. Herlihy, *et al.*, "Reference range of liver corrected T1 values in a population at low risk for fatty liver disease - a UK Biobank sub-study, with an appendix of interesting cases," *Abdom. Radiol.*, vol. 44, no. 1, pp. 72–84, Jan. 2019.

[72] P. Jezzard and R. S. Balaban, "Correction for geometric distortion in echo planar images from B0 field variations," *Magn. Reson. Med.*, vol. 34, no. 1, pp. 65–73, Jul. 1995.

[73] S. M. Smith, M. Jenkinson, M. W. Woolrich, *et al.*, "Advances in functional and structural MR image analysis and implementation as FSL," *Neuroimage*, vol. 23, no. Suppl, p. 1, 2004.

[74] M. Jenkinson, C. F. Beckmann, T. E. J. Behrens, M. W. Woolrich, and S. M. Smith, "FSL," *Neuroimage*, vol. 62, no. 2, pp. 782–790, Aug. 2012.

[75] J. L. R. Andersson, S. Skare, and J. Ashburner, "How to correct susceptibility distortions in spin-echo echo-planar images: application to diffusion tensor imaging," *Neuroimage*, vol. 20, no. 2, pp. 870–888, Oct. 2003.

[76] C. Aguilera. "Extrema.m, extrema2.m." (), [Online]. Available: `https://www.mathworks.com/matlabcentral/fileexchange/12275-extrema-m-extrema2-m`. (accessed: 01.04.2021).

[77] "inpaint_nans - MATLAB CentralFile Exchange." (), [Online]. Available: `https://www.mathworks.com/matlabcentral/fileexchange/4551-inpaint_nans?s_tid=srchtitle`. (accessed: 15.04.2021).

[78] K. P. Pruessmann, M. Weiger, M. B. Scheidegger, and P. Boesiger, "SENSE: Sensitivity encoding for fast MRI," *Magn. Reson. Med.*, vol. 42, no. 5, pp. 952–962, Nov. 1999.

[79] A. Deshmane, V. Gulani, M. A. Griswold, and N. Seiberlich, "Parallel MR imaging," *J. Magn. Reson. Imaging*, vol. 36, no. 1, pp. 55–72, Jul. 2012.

[80] M. A. Griswold, P. M. Jakob, R. M. Heidemann, *et al.*, "Generalized autocalibrating partially parallel acquisitions (GRAPPA)," *Magn. Reson. Med.*, vol. 47, no. 6, pp. 1202–1210, Jun. 2002.

[81] J. Hamilton, D. Franson, and N. Seiberlich, "Recent advances in parallel imaging for MRI," *Prog. Nucl. Magn. Reson. Spectrosc.*, vol. 101, pp. 71–95, Aug. 2017.

[82] A. Haase, J. Frahm, D. Matthaei, W. Hanicke, and K.-D. Merboldt, "FLASH imaging. Rapid NMR imaging using low flip-angle pulses," *Journal of Magnetic Resonance*, vol. 67, no. 2, pp. 258–266, Apr. 1986.

[83] C. H. Cunningham, J. M. Pauly, and K. S. Nayak, "Saturated double-angle method for rapid B1+ mapping," *Magn. Reson. Med.*, vol. 55, no. 6, pp. 1326–1333, Jun. 2006.

[84] Y. Zur, M. L. Wood, and L. J. Neuringer, "Spoiling of transverse magnetization in steady-state sequences," *Magn. Reson. Med.*, vol. 21, no. 2, pp. 251–263, Oct. 1991.

[85] C. Preibisch and R. Deichmann, "Influence of RF spoiling on the stability and accuracy of T1 mapping based on spoiled FLASH with varying flip angles," *Magn. Reson. Med.*, vol. 61, no. 1, pp. 125–135, Jan. 2009.

[86] S. Baudrexel, U. Nöth, J.-R. Schüre, and R. Deichmann, "T 1 mapping with the variable flip angle technique: A simple correction for insufficient spoiling of transverse magnetization," *Magn. Reson. Med.*, vol. 79, no. 6, pp. 3082–3092, Jun. 2018.

[87] M. Weigel, "Extended phase graphs: Dephasing, RF pulses, and echoes - pure and simple," *J. Magn. Reson. Imaging*, vol. 41, no. 2, pp. 266–295, Feb. 2015.

[88] S. J. Malik, R. P. A. G. Teixeira, and J. V. Hajnal, "Extended phase graph formalism for systems with magnetization transfer and exchange," *Magn. Reson. Med.*, vol. 80, no. 2, pp. 767–779, Aug. 2018.

[89] J. P. Felmlee and R. L. Ehman, "Spatial presaturation: a method for suppressing flow artifacts and improving depiction of vascular anatomy in MR imaging.," *Radiology*, Aug. 1987.

[90] F. A. Breuer, M. Blaimer, R. M. Heidemann, M. F. Mueller, M. A. Griswold, and P. M. Jakob, "Controlled aliasing in parallel imaging results in higher acceleration (CAIPIRINHA) for multi-slice imaging," *Magn. Reson. Med.*, vol. 53, no. 3, pp. 684–691, Mar. 2005.

[91] B. Lena, C. Bos, C. J. Ferrer, C. T. W. Moonen, M. A. Viergever, and L. W. Bartels, "Rapid 2D variable flip angle method for accurate and precise T1 measurements over a wide range of T1 values," *NMR Biomed.*, vol. 34, no. 8, e4542, Aug. 2021.

[92] M. Soellradl, A. Lesch, J. Strasser, *et al.*, "Assessment and correction of macroscopic field variations in 2D spoiled gradient-echo sequences," *Magn. Reson. Med.*, vol. 84, no. 2, pp. 620–633, Aug. 2020.

[93] A. Lutti, C. Hutton, J. Finsterbusch, G. Helms, and N. Weiskopf, "Optimization and validation of methods for mapping of the radiofrequency transmit field at 3T," *Magn. Reson. Med.*, vol. 64, no. 1, pp. 229–238, Jul. 2010.

[94] S. Klein, M. Staring, K. Murphy, M. A. Viergever, and J. P. W. Pluim, "elastix: A Toolbox for Intensity-Based Medical Image Registration," *IEEE Trans. Med. Imaging*, vol. 29, no. 1, pp. 196–205, Nov. 2009.

[95] D. P. Shamonin, E. E. Bron, B. P. F. Lelieveldt, M. Smits, S. Klein, and M. Staring, "Fast Parallel Image Registration on CPU and GPU for Diagnostic Classification of Alzheimer's Disease," *Front. Neuroinf.*, vol. 0, 2014.

[96] W. Huizinga, D. H. J. Poot, J.-M. Guyader, *et al.*, "PCA-based groupwise image registration for quantitative MRI," *Med. Image Anal.*, vol. 29, pp. 65–78, Apr. 2016.

[97] K. F. Stupic, M. Ainslie, M. A. Boss, *et al.*, "A standard system phantom for magnetic resonance imaging," *Magn. Reson. Med.*, vol. 86, no. 3, pp. 1194–1211, Sep. 2021.

[98] W. T. Dixon, "Simple proton spectroscopic imaging," *Radiology*, vol. 153, no. 1, pp. 189–194, Oct. 1984.

[99] S. C. L. Deoni, "Correction of main and transmit magnetic field (B0 and B1) inhomogeneity effects in multicomponent-driven equilibrium single-pulse observation of T1 and T2," *Magn. Reson. Med.*, vol. 65, no. 4, pp. 1021–1035, Apr. 2011.

[100] N. Stikov, M. Boudreau, I. R. Levesque, C. L. Tardif, J. K. Barral, and G. B. Pike, "On the accuracy of T1 mapping: searching for common ground," *Magn. Reson. Med.*, vol. 73, no. 2, pp. 514–522, Feb. 2015.

[101] M. Boudreau, C. L. Tardif, N. Stikov, J. G. Sled, W. Lee, and G. B. Pike, "B 1 mapping for bias-correction in quantitative T 1 imaging of the brain at 3T using standard pulse sequences," *J. Magn. Reson. Imaging*, vol. 46, no. 6, pp. 1673–1682, Dec. 2017.

[102] Y. Lee, M. F. Callaghan, and Z. Nagy, "Analysis of the Precision of Variable Flip Angle T1 Mapping with Emphasis on the Noise Propagated from RF Transmit Field Maps," *Front. Neurosci.*, vol. 11, p. 106. Mar. 2017.

[103] R. P. A. G. Teixeira, S. J. Malik, and J. V. Hajnal, "Joint system relaxometry (JSR) and Crámer-Rao lower bound optimization of sequence parameters: A framework for enhanced precision of DESPOT T 1 and T 2 estimation," *Magn. Reson. Med.*, vol. 79, no. 1, pp. 234–245, Jan. 2018.

[104] H. Z. Wang, S. J. Riederer, and J. N. Lee, "Optimizing the precision in T1 relaxation estimation using limited flip angles," *Magn. Reson. Med.*, vol. 5, no. 5, pp. 399–416, Nov. 1987.

[105] L.-C. Chang, C. G. Koay, P. J. Basser, and C. Pierpaoli, "Linear least-squares method for unbiased estimation of T1 from SPGR signals," *Magn. Reson. Med.*, vol. 60, no. 2, pp. 496–501, Aug. 2008.

[106] C. M. Lewis, S. A. Hurley, M. E. Meyerand, and C. G. Koay, "Data-driven optimized flip angle selection for T1 estimation from spoiled gradient echo acquisitions," *Magn. Reson. Med.*, vol. 76, no. 3, pp. 792–802, Sep. 2016.

[107] G. Nataraj, J.-F. Nielsen, and J. A. Fessler, "Optimizing MR Scan Design for Model-Based T_1 , T_2 Estimation From Steady-State Sequences," *IEEE Trans. Med. Imaging*, vol. 36, no. 2, pp. 467–477, Feb. 2017.

[108] H. Bruder, H. Fischer, R. Graumann, and M. Deimling, "A new steady-state imaging sequence for simultaneous acquisition of two MR images with clearly different contrasts," *Magn. Reson. Med.*, vol. 7, no. 1, pp. 35–42, May 1988.

[109] G. H. Welsch, K. Scheffler, T. C. Mamisch, *et al.*, "Rapid estimation of cartilage T2 based on double echo at steady state (DESS) with 3 Tesla," *Magn. Reson. Med.*, vol. 62, no. 2, pp. 544–549, Aug. 2009.

[110] R. R. Ernst and W. A. Anderson, "Application of Fourier Transform Spectroscopy to Magnetic Resonance," *Rev. Sci. Instrum.*, vol. 37, no. 1, pp. 93–102, Jan. 1966.

[111] A. Ben-Tal and A. Nemirovski, "Robust solutions of uncertain linear programs," *Oper. Res. Lett.*, vol. 25, no. 1, pp. 1–13, Aug. 1999.

[112] S. M. Kay, *Fundamentals of statistical signal processing: estimation theory*. Prentice-Hall, Inc., Mar. 1993.

[113] M. C. Schabel and G. R. Morrell, "Uncertainty in T(1) mapping using the variable flip angle method with two flip angles," *Phys. Med. Biol.*, vol. 54, no. 1, pp. 1–8, Jan. 2009.

[114] S. C. L. Deoni, T. M. Peters, and B. K. Rutt, "Determination of optimal angles for variable nutation proton magnetic spin-lattice, T1, and spin-spin, T2, relaxation times measurement," *Magn. Reson. Med.*, vol. 51, no. 1, pp. 194–199, Jan. 2004.

[115] J. Wolberg, *Data Analysis Using the Method of Least Squares*. Springer, 2006.

[116] O. Dietrich, J. G. Raya, S. B. Reeder, M. F. Reiser, and S. O. Schoenberg, "Measurement of signal-to-noise ratios in MR images: influence of multichannel coils, parallel imaging, and reconstruction filters," *J. Magn. Reson. Imaging*, vol. 26, no. 2, pp. 375–385, Aug. 2007.

[117] H. Olsson, M. Andersen, J. Lätt, R. Wirestam, and G. Helms, "Reducing bias in dual flip angle T1-mapping in human brain at 7T," *Magn. Reson. Med.*, vol. 84, no. 3, pp. 1347–1358, Sep. 2020.

[118] C. Besa, O. Bane, G. Jajamovich, J. Marchione, and B. Taouli, "3D T1 relaxometry pre and post gadoxetic acid injection for the assessment of liver cirrhosis and liver function," *Magn. Reson. Imaging*, vol. 33, no. 9, pp. 1075–1082, Nov. 2015.

[119] O. Dietrich, M. Freiermuth, L. Willerding, M. F. Reiser, and M. Peller, "Flip angle-optimized fast dynamic T1 mapping with a 3D gradient echo sequence," *Magn. Reson. Med.*, vol. 73, no. 3, pp. 1158–1163, Mar. 2015.

[120] N. McDonald, P. J. Eddowes, J. Hodson, *et al.*, "Multiparametric magnetic resonance imaging for quantitation of liver disease: a two-centre cross-sectional observational study - Scientific Reports," *Sci. Rep.*, vol. 8, no. 9189, pp. 1–10, Jun. 2018.

[121] C. R. Bradley, E. F. Cox, R. A. Scott, *et al.*, "Multi-organ assessment of compensated cirrhosis patients using quantitative magnetic resonance imaging," *J. Hepatol.*, vol. 69, no. 5, pp. 1015–1024, Nov. 2018.

[122] A. N. A. Jayaswal, C. Levick, E. A. Selvaraj, *et al.*, "Prognostic value of multiparametric magnetic resonance imaging, transient elastography and blood-based fibrosis markers in patients with chronic liver disease," *Liver Int.*, vol. 40, no. 12, pp. 3071–3082, Dec. 2020.

[123] A. N. A. Jayaswal, C. Levick, J. Collier, *et al.*, "Liver cT 1 decreases following direct-acting antiviral therapy in patients with chronic hepatitis C virus," *Abdom. Radiol. (NY)*, vol. 46, no. 5, pp. 1947–1957, May 2021.

[124] M. Pavlides, R. Banerjee, J. Sellwood, *et al.*, "Multiparametric magnetic resonance imaging predicts clinical outcomes in patients with chronic liver disease," *J. Hepatol.*, vol. 64, no. 2, pp. 308–315, Feb. 2016.

[125] C. Levick, J. Phillips-Hughes, J. Collier, *et al.*, "Non-invasive assessment of portal hypertension by multi-parametric magnetic resonance imaging of the spleen: A proof of concept study," *PLoS One*, vol. 14, no. 8, Aug. 2019.

[126] N. Palaniyappan, E. Cox, C. Bradley, *et al.*, "Non-invasive assessment of portal hypertension using quantitative magnetic resonance imaging," *J. Hepatol.*, vol. 65, no. 6, pp. 1131–1139, Dec. 2016.

[127] J. R. Dillman, S. D. Serai, A. T. Trout, *et al.*, "Diagnostic performance of quantitative magnetic resonance imaging biomarkers for predicting portal hypertension in children and young adults with autoimmune liver disease," *Pediatr. Radiol.*, vol. 49, no. 3, pp. 332–341, Mar. 2019.

[128] N. Yoshimura, K. Saito, T. Saguchi, *et al.*, "Distinguishing hepatic hemangiomas from metastatic tumors using T1 mapping on gadoxetic-acid-enhanced MRI," *Magn. Reson. Imaging*, vol. 31, no. 1, pp. 23–27, Jan. 2013.

[129] Z. Peng, C. Li, T. Chan, *et al.*, "Quantitative evaluation of Gd-EOB-DTPA uptake in focal liver lesions by using T1 mapping: differences between hepatocellular carcinoma, hepatic focal nodular hyperplasia and cavernous hemangioma," *Oncotarget*, vol. 8, no. 39, pp. 65 435–65 444, Jul. 2017.

[130] U. L. Fahlenkamp, K. Ziegeler, L. C. Adams, S. M. Böker, G. Engel, and M. R. Makowski, "Native T1 mapping for assessment of the perilesional zone in metastases and benign lesions of the liver," *Sci. Rep.*, vol. 10, no. 1, p. 12889. Jul. 2020.

[131] J. R. Dillman, S. D. Serai, A. G. Miethke, R. Singh, J. A. Tkach, and A. T. Trout, "Comparison of liver T1 relaxation times without and with iron correction in pediatric autoimmune liver disease," *Pediatr. Radiol.*, vol. 50, no. 7, pp. 935–942, Jun. 2020.

[132] E. Selvaraj, G. Ridgway, E. Culver, *et al.*, "Combination of quantitative 3D MRCP and multi-parametric MRI demonstrates increased periductal iron-corrected T1 in large-duct primary sclerosing cholangitis," *J. Hepatol.*, vol. 73, S86, Aug. 2020.

[133] L. G. Kessler, H. X. Barnhart, A. J. Buckler, *et al.*, "The emerging science of quantitative imaging biomarkers terminology and definitions for scientific studies and regulatory submissions," *Stat. Methods Med. Res.*, vol. 24, no. 1, pp. 9–26, Feb. 2015.

[134] V. Bachtiar, M. D. Kelly, H. R. Wilman, *et al.*, "Repeatability and reproducibility of multiparametric magnetic resonance imaging of the liver," *PLoS One*, vol. 14, no. 4, Apr. 2019.

[135] S. Roujol, S. Weingärtner, M. Foppa, *et al.*, "Accuracy, precision, and reproducibility of four T1 mapping sequences: a head-to-head comparison of MOLLI, ShMOLLI, SASHA, and SAPPHIRE," *Radiology*, vol. 272, no. 3, pp. 683–689, Sep. 2014.

[136] T. Tirkes, X. Zhao, C. Lin, *et al.*, "Evaluation of variable flip angle, MOLLI, SASHA, and IR-SNAPSHOT pulse sequences for T 1 relaxometry and extracellular volume imaging of the pancreas and liver," *MAGMA*, vol. 32, no. 5, pp. 559–566, Oct. 2019.

[137] F. E. Mozes, E. M. Tunnicliffe, M. Pavlides, and M. D. Robson, "Influence of fat on liver T1 measurements using modified Look-Locker inversion recovery (MOLLI) methods at 3T," *J. Magn. Reson. Imaging*, vol. 44, no. 1, pp. 105–111, Jul. 2016.

[138] F. E. Mozes, E. M. Tunnicliffe, A. Moolla, *et al.*, "Mapping tissue water T 1 in the liver using the MOLLI T 1 method in the presence of fat, iron and B 0 inhomogeneity," *NMR Biomed.*, vol. 32, no. 2, e4030. Feb. 2019.

[139] E. F. Cox, C. E. Buchanan, C. R. Bradley, *et al.*, "Multiparametric Renal Magnetic Resonance Imaging: Validation, Interventions, and Alterations in Chronic Kidney Disease," *Front. Physiol.*, vol. 8, p. 696. Sep. 2017.

[140] C. Bradley, R. A. Scott, E. Cox, *et al.*, "Short-term changes observed in multiparametric liver MRI following therapy with direct-acting antivirals in chronic hepatitis C virus patients," *Eur. Radiol.*, vol. 29, no. 6, pp. 3100–3107, Jun. 2019.

[141] G. Hamilton, A. N. N Schlein, and C. B. Sirlin, "Flip angle corrected multi-tr, multi-te 1h mr spectroscopy," in *Proceedings of Intl. Soc. Mag. Reson. Med. 26*, 2018.

[142] L. A. B. Purvis, W. T. Clarke, L. Biasiolli, L. Valkovič, M. D. Robson, and C. T. Rodgers, "OXSA: An open-source magnetic resonance spectroscopy analysis toolbox in MATLAB," *PLoS One*, vol. 12, no. 9, e0185356. Sep. 2017.

[143] L. Vanhamme, A. Van den Boogaart, and S. Van Huffel, "Improved method for accurate and efficient quantification of MRS data with use of prior knowledge," *J. Magn. Reson.*, vol. 129, no. 1, pp. 35–43, Nov. 1997.

[144] H. Yu, A. Shimakawa, C. D. G. Hines, *et al.*, "Combination of complex-based and magnitude-based multiecho water-fat separation for accurate quantification of fat-fraction," *Magn. Reson. Med.*, vol. 66, no. 1, pp. 199–206, Jul. 2011.

[145] A. T. Bagur, C. Hutton, B. Irving, M. L. Gyngell, M. D. Robson, and M. Brady, "Magnitude-intrinsic water-fat ambiguity can be resolved with multipeak fat modeling and a multipoint search method," *Magn. Reson. Med.*, vol. 82, no. 1, pp. 460–475, Jul. 2019.

[146] S. K. Piechnik, V. M. Ferreira, E. Dall'Armellina, *et al.*, "Shortened Modified Look-Locker Inversion recovery (ShMOLLI) for clinical myocardial T1-mapping at 1.5 and 3 T within a 9 heartbeat breathhold," *J. Cardiovasc. Magn. Reson.*, vol. 12, no. 1, p. 69. Nov. 2010.

[147] D. G. Altman, *Practical Statistics for Medical Research*. Chapman & Hall/CRC, 1999.

[148] *Introduction to Medical Statistics*. Oxford, England, UK: Oxford University Press, Sep. 2015.

[149] J. M. Bland and D. G. Altman, "Measuring agreement in method comparison studies," *Stat. Methods Med. Res.*, vol. 8, no. 2, pp. 135–160, Jun. 1999.

[150] X. Zhong, S. Shakeri, D. Liu, *et al.*, "Repeatability and reproducibility of variable flip angle T 1 quantification in the prostate at 3 T," *J. Magn. Reson. Imaging*, vol. 49, no. 6, pp. 1730–1735, Jun. 2019.

[151] A. Matakos, J. M. Balter, and Y. Cao, "A Robust Method for Estimating B0 Inhomogeneity Field in the Liver by Mitigating Fat Signals and Phase-Wrapping," *Tomography*, vol. 3, no. 2, pp. 79–88, Jun. 2017.

[152] E. Selvaraj, A. Jayaswal, T. E. M., *et al.*, "Quantifying the Heterogeneity of Liver Inflammation and Fibrosis in Primary Sclerosing Cholangitis using the Interquartile Range of iron-corrected T1 from Multi-parametric MRI.," vol. 70, Oct. 2019, 798A–799A. [Online]. Available: `https://www.rdm.ox.ac.uk/publications/1064244`.

[153] F. E. Mózes, L. Valkovič, M. Pavlides, M. D. Robson, and E. M. Tunnicliffe, "Hydration and glycogen affect T 1 relaxation times of liver tissue," *NMR Biomed.*, vol. 34, no. 7, e4530. Jul. 2021.

[154] K. Janowski, E. Shumbayawonda, A. Dennis, *et al.*, "Multiparametric MRI as a Noninvasive Monitoring Tool for Children With Autoimmune Hepatitis," *J. Pediatr. Gastroenterol. Nutr.*, vol. 72, no. 1, pp. 108–114, Jan. 2021.

[155] G. Belsley, D. J. Tyler, M. D. Robson, and E. M. Tunnicliffe, "A comparison of two b1+ mapping methods for 3d vfa t1 mapping in the liver at 3t," in *Proceedings of Intl. Soc. Mag. Reson. Med. 29*, 2021.